THE INTERPLAY AMONG MIXING, FLOW STRUCTURE AND REACTION IN CONTINUOUS TAYLOR COUETTE REACTORS

A Dissertation

Presented to the Faculty of the Graduate School

of Cornell University

In Partial Fulfillment of the Requirements for the Degree of

Doctor of Philosophy

by

Mohammad Fuad Aljishi

August 2018

THE INTERPLAY AMONG MIXING, FLOW STRUCTURE AND REACTION IN CONTINUOUS TAYLOR COUETTE REACTORS

Mohammad Fuad Aljishi, Ph. D.

Cornell University 2018

Understanding mixing characteristics and influence of flow behavior on mass-transport is critical to enhancing performance in reactive flows, where the interaction between fluid dynamics and chemical reactions is important. As a model reactor system, the Taylor-Couette Reactor (TCR) allows for examining a range of hydrodynamic instabilities, while stimulating vortex motion, offering a highly active extensive interface for mass transfer, and multiphase mixing. Specifically, this dissertation assesses the effect of changing flow structure and mixing patterns in TCR on mass transport, for a range of multiphase flow reactions including crystal formation, particle functionalization and gas-liquid absorption. Overall, this dissertation confirms that it is not just the increase of energy of dissipation that is critical towards enhancing the mixing but rather the structure of the flow regimes, which if elaborately understood and characterized, enables us to exercise more effective control over the mass transfer in reactions. The first part of this work focused on studies involving the precipitation of barium sulfate which revealed that the emergence of vortex motion plays a critical role in fine-tuning crystal properties such as particle size. The second part focused on examining the influence of the onset of the primary Taylor vortex instability, as well as secondary instabilities, in tailoring the coating layer during the surface modification of metallic filler particles with methacryloxypropyltrimethoxysilane (MPS). The surface of aluminum fillers was modified

with specific ($H_2C=C$) functionality, offering a more uniform degree of coating, lower degree of aggregation, smoother surface and higher MPS coupling efficiency after the emergence of Taylor vortices, especially after the onset of modulated wavy vortex flow regime. The last part focused on investigating the variety of flow patterns in a three-phase system, reacting gaseous carbon dioxide (CO_2) with aqueous calcium hydroxide ($Ca(OH)_2$) to precipitate solid calcium carbonate crystals ($CaCO_3$) in a TCR, to assess the influence of the corresponding flow dynamics, CO_2 gas bubble size and interfacial area on the properties of the resulting $CaCO_3$ crystals. It was found that identifying the emergence of the "ring flow" structure was critical to optimizing the interfacial area and fine-tuning crystal properties such as internal crystal pore structure, surface area, particle size and morphology.

BIOGRAPHICAL SKETCH

Mohammad was born in the Eastern province of Saudi Arabia and grew up in the city of Qatif. After graduating from high school with outstanding honors, he joined the highly competitive Saudi Aramco College Preparatory Center (CPC) and completed the program while making it to the top 10, with special honors in Chemistry, English and Math. After receiving his Bachelor's degree in Chemical Engineering from Rice University with the T.W. Moore distinguished award, Mohammad began his work with Saudi Aramco's Research & Development Center in Dhahran, Saudi Arabia. His work focused on developing catalytic post-treatment process for Supercritical Water Technology, co-authoring five US granted patents.

To my beloved parents, Hanna and Fuad, for their unconditional love, inspiring character, and endless support.

ACKNOWLEDGMENTS

I would like to start by expressing my sincere gratitude to my advisor, Professor Yong Lak Joo, for his generous support and valuable mentorship . I truly appreciate and respect the time and diligence he devoted in guiding me along this journey. His dedicated teaching, committed advising and attentive guidance have been critical in expanding my knowledge, developing my research skills and giving me the methodology and momentum to reach my academic goals and complete this work.

Special thanks to Professor Jeff W Tester for his continuous support throughout my academic years at Cornell. Under his great leadership, and as a member of Cornell's Earth-Energy Systems Integrated Graduate Education and Research Training (IGERT), I had the opportunity to share my work and interact with students and faculty across various engineering fields and to appreciate the value of interdisciplinary work, inspiring me to explore my research from wider perspectives. Special acknowledgments to Professor Mingming Wu for her insightful suggestions and valuable discussions related to my dissertation work.

I acknowledge Cornell Center for Materials Research (CCMR) and the Nanobiotechnology Center (NBTC) for Shared Research Facilities. Funding for various parts of this research was partially provided by Samsung, Axium Nano, LLC, and KETEP (Korea Institute of Energy Technology Evaluation and Planning). I am grateful to Saudi Aramco for providing me the opportunity to pursue academic research at Cornell and for funding my graduate studies. Particular thanks to Dr. Ki-Hyouk Choi and Dr. Ali al-Somali for their support and encouragement.

I would like to thank the members of the Joo research group for their help and constant support. Special acknowledgements to professor Woo-Sik Kim, Dr. An-Cheng Ruo and Glenn Swan for helping me in establishing the Taylor Couette research competency from scratch. Particular thanks to Hanna Won, Jeongmin Shin and Mayank Jhalaria for their contributions to my thesis research. Linh Nguyen, Bader al-Nasser for assisting me in arranging experiments. I am grateful to have enjoyed the pleasant company of the Joo Group, namely: Nate Hansen, Jay Park, Bryan Rolfe, Brian Williams, Joe Carlin, Ghazal Shoorideh, Soshana Smith, Yevgen Zhmayev and Andrew Shah.

Last but not least, I would like to express genuine gratitude to my precious family: my mother Hana, my father Fuad, my brothers Ali, Hussain, Eyad and Ayman for their unconditional love, great inspiration and unlimited support. My appreciation to the legacy of my late grandfather, my generous grandmother, loving aunts and the rest of my family.

TABLE OF CONTENTS

LIST OF FIGURES

LIST OF TABLES

LIST OF EQUATIONS

LIST OF ABBREVIATIONS

TCF	Taylor-Couette Flow
TCR	Taylor Couette Reactor
PFR	Plug Flow Reactor
CSTR	Continuous Stirred Tank Reactor
TCPF	Taylor Couette Poiseuille Flow
LTVF	Laminar Taylor Vortex Flow
LTCF	Laminar Taylor Couette Flow
WVF	Wavy Vortex Flow
MWVF	Modulated Wavy Vortex Flow
WTVF	Weakly Turbulent Vortex Flow
TTVF	Turbulent Taylor Vortex Flow
PTV	Propagating Taylor Vortices
SHV	Stationary Helical Vortices
SSV	Stationary Spiral Vortices
MPS	Methacryloxypropyltrimethoxysilane
PCC	Precipitated Calcium Carbonate
PMMA	Poly(methyl methacrylate)
RT	Residence Time

LIST OF SYMBOLS

Ta	Taylor Number
Ta_c	Critical Taylor Number
Ta_r	Reduced Taylor Number
a_z	Axial wave number
a_{z_c}	Critical Axial wave number
a_θ	Azimuthal wave number
λ	Axial wave length (vortex pair)
Re_θ	Azimuthal Reynolds number
$Re_{\theta c}$	Critical Azimuthal Reynolds number
Re_z	Axial Reynolds number
V_z	Axial velocity within the annulus
η, r_1/r_2	Gap ratio
r_1	Inner cylinder radius
r_2	Outer cylinder radius
d	Gap thickness
Lr	Reactor length
$\Gamma = Lr/d$	Aspect ratio of reactor length
Ω_1, ω	Angular velocity of inner cylinder
ν	Kinematic viscosity
ϕ_{sl}	Solids fraction of the slurry (state by mass)
ρ_s	Solids density
ρ_{sl}	Slurry density
ρ_l	Liquid density
μ_s	Dynamic viscosity of slurry
μ_l	Dynamic viscosity of liquid
μ_r	Relative viscosity
t	Time
Q_L	Liquid Flow Rate
Q_G	Gas Flow Rate
G	Axial flow mass flux (kg/m^2s)

$Re_{z\text{-}L}$	Axial Reynolds number for Liquid Flow
$Re_{z\text{-}G}$	Axial Reynolds number for Gas Flow
V_L	Liquid space velocity
V_G	Gas space velocity
$\beta = V_G/V_L$	Gas/liquid flow ratio
ρ_G	Gas Phase density
μ_G	Gas Phase viscosity
v_L	Liquid Phase Kinematic Viscosity
ε	Energy of disssipation (W/kg)
a	Interfacial area (m^{-1})
d_b	Bubble diameter
α_g	Gas volume fraction
d_{32G}	Sauter diameter
Ha	Hatta Number
u_{Slip}	Average slip velocity
k	Kinetic constant of the chemical reaction
$C^{bulk}_{Ca(OH)_2}$	Solubility of calcium hydroxide, $(mol \cdot m^{-1})$
D_{co_2}	Diffusivity of carbon dioxide, $(m^2 \cdot s^{-1})$
$D_{Ca(OH)_2}$	Diffusivity of calcium hydroxide, $(m^2 \cdot s^{-1})$
$C^{int}_{CO_2}$	Solubility of carbon dioxide, $(mol \cdot m^{-1})$
$k_L a$	Overall mass transfer coefficient
k_L	Individual mass transfer coefficient
t_{macro}	Macromixing time
t_{meso}	Mesomixing time
t_{micro}	Micromixing time
Pe	Peclet Number
D_{ax}	Axial dispersion
Sh	Sherwood number

CHAPTER 1

INTRODUCTION

1.1 Importance of Mixing and Process Intensification

Designing efficient reactors with optimum process intensification is of great importance to many industrial applications. Intensified processes, with higher mass transfer rates, can lead to lower energy costs and capital costs, due to compact equipment size [1] , as well as increased efficiency and higher product yields of better quality [2]. Enhanced intensification can be approached through increasing the input of energy through external force fields, enhancing the reactor surface configuration, or by operating in high throughput continuous-flow mode [3]. Although continuous stirred tank reactors (CSTR) provide significant mixing intensity, they lack the advantage of tightly controlling the process history as in the plug flow reactor (PFR), where narrow residence time distribution allow all fluid elements to spend equivalent time in the reactor [1].

To overcome rate limiting steps associated with conventional reactor configurations, it is critical to develop reaction environments that can combine the advantages of different conventional reactors (such as PFR and CSTR) , offering more significant mixing, higher surface-to-volume ratio and increased mass-transfer efficiency [4]. In addition to reactor design, understanding mixing characteristics and influence of flow behavior on mass-transport is critical to enhancing performance in reactive flows, where the interaction between fluid dynamics and chemical reactions is important [1]. This thesis explores the use of vortex flow in a continuous Taylor-Couette Reactor (TCR) in applications that require enhanced mixing and process intensification, as a unique approach to overcome the technical barrier in multiphase reactions.

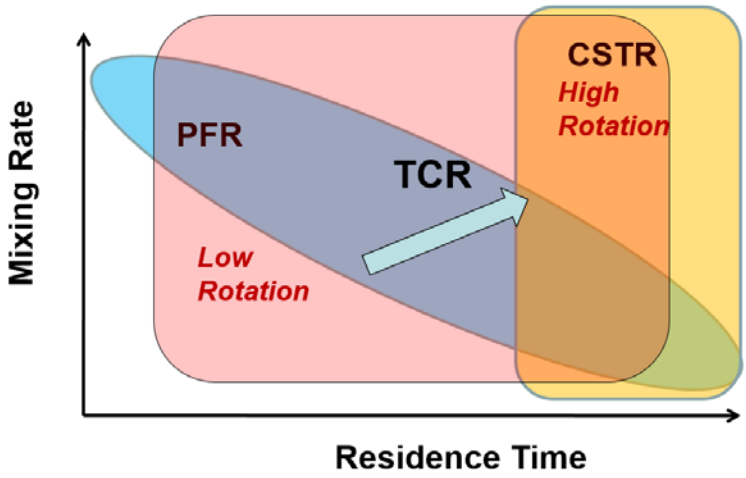

Figure 1.1.1 Mixing rate vs. residence rime in various reactors

As a form of novel intensified plug flow reactors, the Taylor-Couette reactor has recently been explored as an intensified reactor on commercial scales [1], as it offers the opportunity to have enhanced control on the final properties of products due to its higher mass transfer efficiency, together with good mixing properties and large contact area [5]. Specifically, Taylor-Couette flow allows for examining hydrodynamic instabilities while stimulating vortex motion, offering a highly active interface for mass transfer, and phase mixing. Through the use of secondary flow regimes, the TCR provides high mass transfer rates and enhanced mixing properties, including a high surface-to-volume ratio, which makes it preferable for highly exothermal or endothermal reactions. In addition, narrow residence time distribution (reaching the behavior of PFR) and homogeneous distribution of mixing intensity in the TCR volume (compared to a CSTR), combined with mild but effective shear rates [6], makes TCR an attractive reactor for a range of chemical reactions. Unlike mixing in typical PFR configuration, which is almost entirely dependent on the reactant-feed flow, micromixing times in the Taylor Couette reactor are influenced by the inner cylinder rotation. This offers the possibility of independently controlling the mixing intensity and decoupling it from the feed flow-rate. The intense local

mixing combined with the ability to control axial dispersion in the reactor [7], allows the TCR to offer mixing on multiple scales ranging from macro-fluid motion, mesomixing all the way to mixing on the microscale, which can be possible through turbulent hydrodynamic conditions that enable faster attainment of the fluid state where molecular diffusion can be dominant [3].

1.2 Introduction to Taylor Couette Reactors

As depicted in Figure 1.2.1, the reactor vessel consists of two coaxial cylinders, with the inner cylinder rotating while the outer cylinder is fixed together with inlets and outlets for continuous operation. When the flow is driven solely by cylinder rotation, a transition of purely azimuthal laminar flow to an axisymmetric cellular fluid motion occurs beyond a critical rotation speed where the destabilizing centrifugal force exceeds the stabilizing viscous force. This hydrodynamic instability marks the Taylor-Couette flow (TCF) regime, as determined by the critical Taylor number (Ta_c) [8]. Uniformly spaced counter-rotating cellular vortices, with each pair forming an axial wave in TCF is characterized by critical wavenumber (a_c) and wavelength (λ) [9].

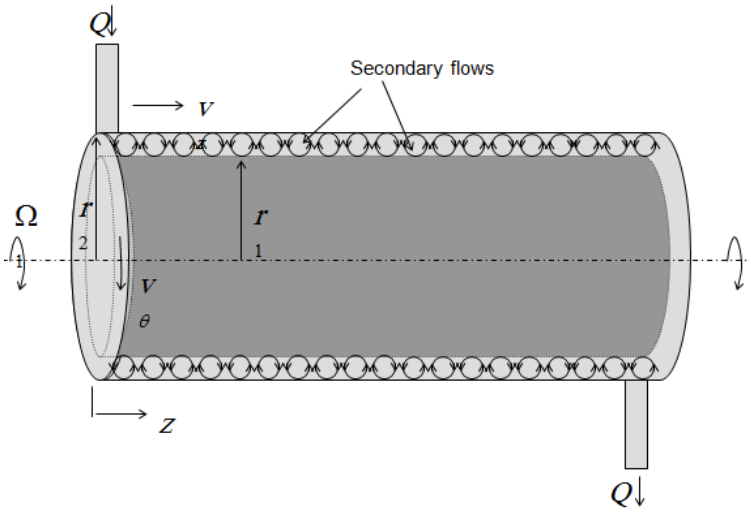

Figure 1.2.1 General schematic of Taylor Couette flow.

Equation 1.2.1 Azimuthal Reynolds number

$$\mathrm{Re}_\theta = \frac{r_1 \Omega_1 d}{\nu}$$

Equation 1.2.2 Taylor number

$$Ta = \frac{2 r_1^{\,2} d^4}{r_2^2 - r_1^2}\left(\frac{\Omega_1}{\nu}\right)^2 = \mathrm{Re}_\theta^{\,2}\left(\frac{2d}{r_2 + r_1}\right)$$

Equation 1.2.3 Axial wavelength

$$a = \frac{2\pi d}{\lambda}$$

As specified by the Taylor number (Ta), the onset of instability depends on reactor geometry and fluid properties including the ratio of the inner cylinder radius to the outer one ($\eta = r_1/r_2$), the gap width ($d = r_2 - r_1$), and the aspect ratio ($\Gamma = L/d$). As the inner cylinder rotation increases further beyond the critical speed, higher order harmonics become important [10], leading to a second instability that is marked by non-axisymmetric periodic flow, known as wavy vortex flow (WVF). Flow transitions towards turbulence occur through a progression of flow instabilities, each of which represent a flow regime transition, such as modulated wavy vortex flow (MWVF) [11] and turbulent Taylor vortex flow (TTVF) [12]. The onset of secondary instabilities and the corresponding flow regimes has been comprehensively characterized and mapped out by Mizushina [13] for flow with the outer cylinder fixed, and by Andereck [14] for flows with co-rotating and counter-rotating cylinders. TCF can be extended to operate as a continuous reactor by imposing Poiseuille flow within the annulus. Extensive studies on Taylor Couette Poiseuille flow (TCPF) have shown that axial flow tends to delay the onset of Taylor instability. Increasing axial flow diminishes the dominance of centrifugal forces, resulting in a proportional increase in Ta_c, while it gives rise to time dependent vortex flow. The

superimposed axial flow is characterized by the axial Reynolds number (Re_z), as described by (4).

Equation 1.2.4 Axial Reynolds number

$$\mathrm{Re}_z = \frac{\nu_m d}{\upsilon} = \frac{Q(r_2 - r_1)}{A\upsilon} = \frac{Q}{\pi(r_2 + r_1)\upsilon}$$

Generation of periodically spaced toroidal vortex cells is a distinctive advantage of Taylor Couette flow. The flow between the concentric cylinders is divided into cellular elements, each of which consists of counter-rotating vortices. Because these vortex pairs are usually equal in size, it is assumed that mixed fluid is uniformly distributed along the vortices, so that it spends identical residence time in each cellular element. Because of these characteristics, Taylor Couette flow is modeled as steady state flow within a number of continuous stirred reactors in series. Assuming that no more than one vortex is generated within the radial direction, the length of each vortex is assumed to be equivalent to the annular gap width. Thus the number of vortices and the volume of each vortex are estimated as below.

Equation 1.2.5 Vortex size

$$\lambda = 2 * d \;\; ; \; V_{vortex} = \pi(r_2^2 - r_1^2)(r_2 - r_1) = \pi(r_2 + r_1)d^2 \;\; ;$$

Equation 1.2.6 Number of vortex pairs

$$N_{Vortex\,pairs} \; = \; N_{CSTRs} = \frac{Lr}{2 * d}$$

Such assumptions neglect the possibility of back mixing and exchange of fluid elements between vortices, which can be considerable if axial flow is relatively large [15]. Also, the assumption that vortices have uniform composition has experimentally been proven wrong, especially in intermediate or low rotational velocities of the inner cylinder, or in low volume fraction of dispersed phase. In addition, in certain regime flow, especially in cases where large

rotational speeds are combined with considerable axial flow, vortex oscillation becomes significant. Therefore, under such conditions, flow within vortices becomes highly transient with variable vortex volume [16]. In these regimes, toroidal vortices lose their "ideal behavior", and they begin to behave as circumferential waves [17].

1.3 Literature Review

Theoretical studies of TCPF flow were explored first by Chandrasekhar [18], followed by Di Prima [19] [20], whose results were experimentally verified by Donnelly and Fultz [21], and Snyder [22]. Mixing characteristics and mass transport, for both macro- and micromixing patterns (i.e. inter- and intra-vortex mass transport) has been well documented in TC and TCP flow configurations using tracer techniques. Because vortex pairs in TC are usually equal in size, Kataoka *et al.* assumed that mixed fluid is uniformly distributed along the vortices, so that it spends identical residence time in each cellular element. Introducing weak axial flow and assuming a well-defined flow structure, they suggested ideal-plug flow in TCP by studying radial and circumferential mixing in the absence of back-mixing [23]. When axial flow is relatively large, Kataoka *et al.* found that there exists a small degree of exchange of fluid elements between neighboring vortices [15]. By measuring inter-vortex flux independently and decoupling it from dispersion enhancing/reducing effects, Desmet *et al.* confirmed the existence of inter-vortex fluxes even though the experiments were done in batch mode (TC) [24]. While earlier studies modeled the flow as a series of CSTR's with one-dimensional dispersion [25] [26] [27], Desmet's work offered a two-zone mathematical model to account for intra-vortex mixing during TCF. This multi-zone model has been extended to different derivatives [16] [28]. While expansive literature exists on mass transport in one-phase TCF, studies tailored towards mass transport and reactions in two phases still need to be addressed. The effect of the presence

of a second immiscible liquid phase on the hydrodynamics of TCF can be divided into two categories: layered/stratified flow at low rotational speed, and banded/emulsified flow patterns at high inner cylinder rotation rates. While radially stratified flow patterns can be generated in systems with co-rotating cylinders, banded/emulsified flow patterns appear only in systems where the outer cylinder is fixed [29]. Though less than stratified liquid-liquid flows, emulsified flow patterns were first detected by Joseph *et al.* in 1984 [30]. Several investigators have performed experiments on hydrocarbon-water mixing in TCF and TCPF configurations, in which they have identified three distinct flow patterns that emerge upon changing operating conditions. While banded flow structure consisted of alternating water and organic-rich vortices that appear at higher Ta, spatially homogeneous structure that is marked by phase inversion appeared at moderate Ta. Campero and Vigil developed empirical correlations that describe the transition from inverted to banded flow patterns, and they identified an axially oscillatory flow regime with alternating regions of banded and inverted structures that appeared at the lowest Ta [31]. In a subsequent study, the same group investigated axial mass transport in these flow patterns using standard tracer-response techniques, and developed a simple criterion for predicting when banded flow patterns arise by assuming that centrifugally-driven droplet migration to vortex cores compete with turbulent diffusion [32]. A recent study concerning hydrocarbon-water mixing in vertical TCF have shown that flow patterns are either in the form of homogeneous dispersion, banded dispersion, segregated or in the form of stratified flow with both phases retaining individual integrity [33].

Reported studies of hydrocarbon-water mixing in TCF coupled with reaction are scarce. Extraction of benzoic acid from toluene to water carried out in the model Taylor column has been demonstrated by Forney *et al.*, and they obtained a single-stage efficiency that conformed

to the pattern of data previously measured for much larger CSTR [34]. The wide range of rotation rates in a TC vessel allows it to imitate performance of PFR and CSTR at low and higher rotation rates, respectively [16].The combination of intense local mixing with axial dispersion is of great interest in two phase immiscible interactions, where mass transport is usually diffusion limited. The reactor's high surface-to-volume ratio makes it advantageous for highly exothermic or endothermic reactions. These advantages have made TCF a flow device that is widely used in many industrial and research processes, such as emulsion studies [35] [36] [37] [38], interfacial polycondensation [39], catalytic [40], photochemical [41], electrochemical [42] [17, 43] [44],, and enzymatic reactions [45], [46], precipitation [47], algal growth [48], blood heparin neutralization [49], flocculation for wastewater treatment [50], monodisperse silica-particle synthesis [51], membrane filtration [52], and microparticle classification [53].

In contrast to micromixing in PFR, such as T-mixer reactors, where faster mixing generated by smaller flow structures is mainly driven by the increase of dissipation of kinetic energy (due to flowrate) [54] [55]., flow structures in the TCR can be fine-tuned with various orderly patterns through smaller changes in the energy of dissipation. In comparison with changing the flow-mode of a tank reactor from batch to continuous flow, the changes of the flow-structure in the TCR are more substantial, especially at higher flowrates, where the axial flow dampens the influence of the centrifugal forces. Still, precise control over the maintenance and transition among diverse range of hydrodynamic flow regimes can be achieved in the TCR [56], where the nature of toroidal flow, the size and shape of vortices and their behavior, can vary from being orderly to wavy all the way to the generation of turbulence which can further decompose the vortices into smaller eddies. Particle trajectories, generated by the Taylor cortices, transition

between the inner and outer cylinder at frequencies that increase with increasing cylinder rotation [48].

1.4 Scope of Research

This thesis investigates the impact of flow structure and the corresponding changes in the shape of the fluid streamlines on reactions ranging from single-phase (homogenous), two-phase (heterogeneous solid-liquid) to multiple phases (solid-liquid-gas). The characteristics of the flow in the TCR is first assessed experimentally via flow visualization. Different reactor geometries were studied to select a reactor configuration that allows for optimum control over the flow hydrodynamics. This was done by performing fluid dynamic experiments investigating the change in flow structure characteristics when operating the reactor in the TCP continuous flow arrangement. Hydrodynamic similarities of different experiments is mainly achieved by operating within the same reduced Taylor numbers , which require estimating the range of changes in the critical Taylor number (Ta_c) when axial flow is introduced to the system. Identical flow regimes are replicated through this scaling factor ($Ta_r=Ta/Ta_c$), in spite of changes in the axial flow or composition.

By discerning the different flow patterns in the Taylor Couette reactor, we apply changes in the flow structure to model chemical reactions in homogeneous single phase, heterogeneous and multiple phase environments. First, as presented in chapter 3, we explored the role of the vortex motion near the onset of the primary instability in fine-tuning crystal properties such as internal crystal structure, particle microstructure and morphology during the homogeneous aqueous phase precipitation of barium sulfate (BaSO4). In this study, we investigated the change of crystal size and distribution before and after the onset of primary instability in ranges of similar energy consumption. By doing this, the influence of shear energy of rotation is decoupled to

exclusively manifest the effect of vortex flow structure on precipitations. In chapter 4, we extend our findings in homogeneous phase reactions to the heterogeneous-phase silanization reaction which involves the functionalization of submicron aluminum spherical particles with MPS. In this case, understanding mixing characteristics and influence of flow behavior on mass-transport during such functionalization reaction is critical for the development of polymer-metal hybrid fillers with uniform, reproducible and well-characterized coating layer. The work in chapter 4 was focused on exploring the role of the vortex motion near the onset of the primary instability in fine-tuning the surface functionality of aluminum particles. Monodispersed fine submicron spheres were selected for this study due to their well-characterized size and morphology and their potential for nano-composite applications. The change in mass transport was characterized by assessing the coupling efficiency (TGA), degree of coating and functionality (FTIR, XPS), coating morphology (SEM) and change in particle dispersion (DLS) and oxidation behavior (XRD) due to change in surface energy after functionalization (zeta potential). By investigating the coating properties before and after the onset of primary instability in ranges of similar energy consumption. , the influence of shear energy of rotation is decoupled to exclusively manifest the effect of vortex flow structure on the MPS coupling on filler surface [57].

In an effort to scale-up the process to industrially relevant applications, we explored the effect of secondary instabilities on the same functionalization reaction, but with larger micron sized particles, as explained in chapter 5. This chapter outlines the development of a scalable continuous flow surface modification process for the functionalization of disk-shaped micron-sized aluminum fillers with MPS monomer surface functionality, designed for industrial applications that aim at overcoming misalignment of disk shape fillers in polymer composites.

Due to the effect of flow and filler shape, the disk fillers tend to align along the thickness direction of the mold. Thus, providing resistance to orientation via controlling interaction between disk fillers and matrix can reduce misalignment.

Finally, to have a comprehensive understanding of the impact of changing flow structure on complex reactions, we focused on studying the multiphase precipitation of calcium carbonate crystals by reacting gaseous carbon dioxide with aqueous suspensions of slurry calcium hydroxide solutions in a Taylor Couette crystallizer. The objective of this study was to investigate the variety of flow patterns in this three-phase system and to examine the influence of the corresponding flow dynamics, CO_2 gas bubble size and interfacial area on calcium carbonate crystal properties. Recent studies [58] [6] [59] [60] revealed that the interfacial area in a gas–liquid system in a Taylor-Couette reactor varies substantially depending on the flow regime, since a variety of flow states can be observed due to the interaction between centrifugal and buoyancy forces. While previous studies on Taylor-Couette reactors in horizontal configuration only focused on the influence of dissipated energy, in this study we extend our understanding of changes in two phase interfacial transport with variation in flow regime behavior, by assessing vortex dynamics using flow visualization tools. The first part of this study included an experimental characterization of flow patterns by assessing gas bubble dispersion and bubble size, while identifying flow-patterns with highest interfacial area. In the second part, the ideal mixing flow regimes identified from flow-visualization experiments were used as conditions for $CaCO_3$ production. It was found that the evolution of certain flow-patterns, particularly “ring flow”, can compromise the interfacial transport despite higher energy of dissipation. Such observations confirmed that crystal properties, such as internal crystal structure, particle microstructure and morphology, are more dependent on the interfacial

area, which is determined by the flow-structure, than on the intensity of mixing or degree of turbulence. In addition to influencing the degree of interfacial transport between the gas-liquid phases, the Taylor Couette reactor offered macro and micro fluid motion that further enhanced the degree of mixing intensity, affecting the crystallization process and $CaCO_3$ properties, such as particle size distribution [1], crystallite size, surface area and pore volume as demonstrated in this study.

CHAPTER 2

FLOW CHARACTERIZATION

2.1 Introduction

This chapter details the Taylor Couette reactor setup, the flow visualization technique, image analysis approach and sample images of the flow-structures observed at various flow transitions that mainly occur in single phase environments. Preliminary results on mixing flow regimes among two immiscible liquid phases are also presented.

2.2 Experimental Setup

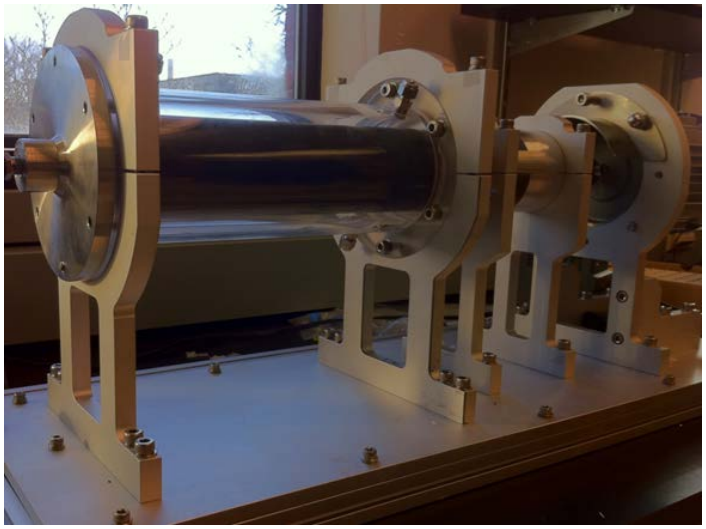

Figure 2.2.1 Taylor Couette reactor in geometry A.

The experimental setup, illustrated in Figure 2.2.1, consists of two coaxial cylinders, with the aluminum inner cylinder rotating while the Plexiglas outer cylinder is fixed. The inner cylinder rotation rate is controlled by a phase inverter, connected to a motor drive that provides rotation rates in the range of 30-1500 RPM. Reactors of various lengths and gap sizes have been fabricated. Specifically, experiments involved four different cylindrical geometries whose physical specifications are displayed in Table 2.2.1. Kinematic viscosity (ν) of circulating fluid influences the stability of the TCF, as it corresponds to dynamic parameters such as Ta_c and

Re_z [61]. The kinematic viscosity of the glycerol-water mixtures at 25◦C were estimated in reference to [62] . Temperature was assumed to be constant in the range of 20°C. Axial flow for TCPF experiments was provided by a peristaltic pump with two coupled pump heads, which allowed a wide range of axial flowrates. Variation in fluid viscosity can affect the pumping flowrate, resulting in an uncertainty in axial flow of about ± Re_z = 2.7%. Similarly, the limited control over the accuracy of the inner cylinder rotation rate results in an uncertainty of ±Ta = 4.4% (±1RPM).

Table 2.2.1 Geometries of various Taylor Couette reactors used

	System Geometry			
	A	**B**	**C**	**D**
r_1 (cm)	**4.05**	**2.01**	**2.27**	**2.27**
r_2 (cm)	**5.05**	**2.53**	**2.53**	**2.53**
d (cm)	**1.00**	**0.52**	**0.26**	**0.26**
r_1/r_2	**0.80**	**0.80**	**0.90**	**0.90**
Lr (cm)	**30**	**15**	**15**	**30**
Lr/d	**30**	**29**	**58**	**116**

2.3 Flow Visualization Technique

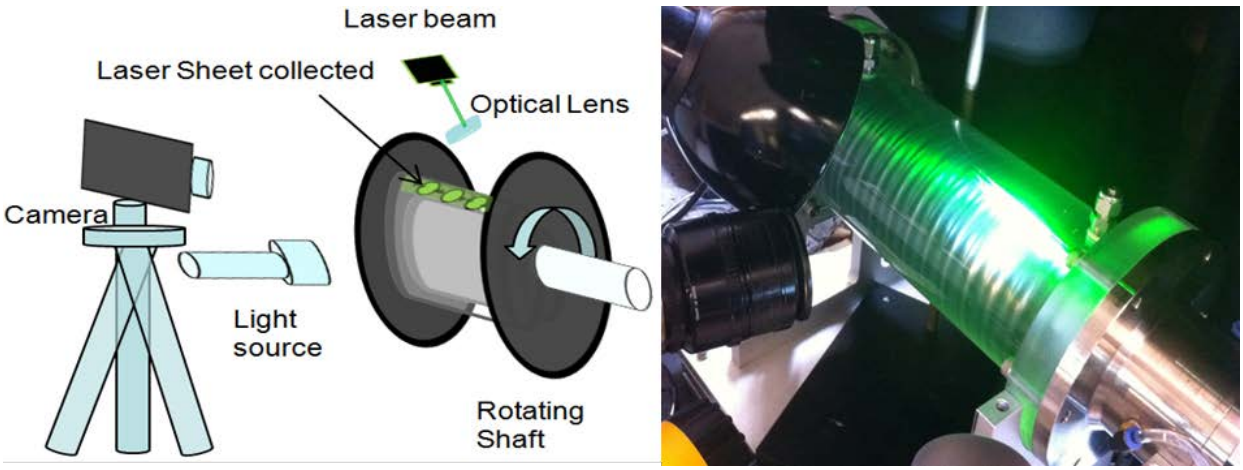

Figure 2.3.1 Layout of flow visualization setup

Flow visualization was the primary technique used to determine the onset of TCF. Small superfine reflective anisotropic particles were seeded in the given fluid. The pigmented titanium dioxide coated mica flakes (4x32 microns, 3.1 g/ml, from Kalliroscope Corporation) align themselves with the local shear stress direction, and light reflectance off the particles makes the flow field visible. The onset of instability is marked by alternating light and dark bands indicating the presence of counter-rotating Taylor vortices. To create an opaque and highly light scattering solution, the flakes were added to the fluids at a volume fraction of 2 $x10^{-5}$, as suggested in other studies [63]. The observer incident light will be reflected back resulting in the white coloring of the local fluid, when the face of the mica flakes is oriented towards the observer [64]. The spacing of each white fluid region corresponds to differences in the orientation of the flow-aligned mica particles [63], which characterize the shape and length of the formed vortices. Different flow regimes were identified via flow visualization using a high speed CCD video camera, which acquired and stored the images directly in 256 shades of gray. The on-board memory is sufficient for 3300 images, which can be captured at any rate up to 1000 Hz. To adjust image quality for different operating conditions, parameters, such as, exposure, image capturing rate (Hz), and movie playing speed (frames per second) were modified accordingly. Spectral image analysis is done through a procedure that is applied using a software written on the basis of Matlab. By applying a fast Fourier transform (FFT) algorithm to the intensity profile [65], a discrete Fourier transform is then adjusted to obtain a_c. As displayed in Figure 2.3.2, images include ruler measurements to accurately adjust the intensity domain.

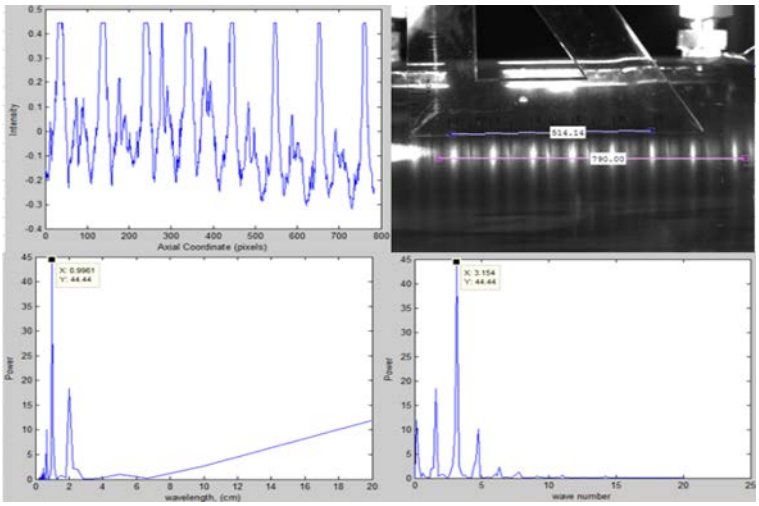

Figure 2.3.2 Estimation of the axial wavenumber.

In most experimental systems, Taylor vortices first appear near the ends of the cylinders at lower than expected values of Ta [64]. Because the end-caps of the Couette cell are stationary (*i.e.* coupled to the outer cylinder), friction-driven secondary flow can be induced as a result of the imbalance between pressure and centrifugal forces. This pressure gradient near the boundaries drives a radial flow [66]. The extent of the flow domain dominated by Taylor vortices then spreads from the end rings toward the center of the cell, until the vortices meet at mid-length at what we expect to correspond to the theoretical Ta_c for fully developed TCF (Figure 2.4.1 b-d). Besides referring to axisymmetric stability analysis, as provided by Chandrasekhar, results obtained from experiments with axial flow were compared with non-axisymmetric mode stability analysis results, done by Dr. An-Cheng through numerical integration of flow governing equations. The loss of symmetry due to axial flow introduces disturbances that may be traveling in both the circumferential and axial directions, reflecting a non-zero azimuthal wavenumber (m).

To provide more qualitative information of the flow field, laser sheet illumination of the flow in the r-θ plane as well as r-z plane was used along a cross-section of the annulus (see Figure

2.3.3). A 50mW Argon-ion laser beam is expanded into a laser sheet by a simple rod-shaped cylindrical lens. When the laser sheet is coplanar with the axis of the cylinders, the interface is clearly visible, and qualitative details about the fluid motion are obtainable. Probed by illuminating the gap, the axial and radial structure of the disturbance flow in the highlighted cross-section can be determined. For flow visualization, the camera is placed orthogonal to the illuminated section.

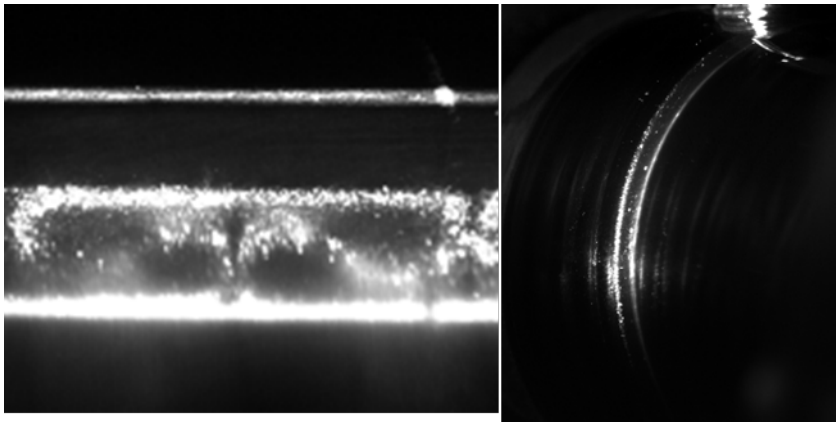

Figure 2.3.3 Laser-sheet visualization in the *r*-θ plane and *r*-*z* plane

Laser sheet visualization is important in accurately determining the instantaneous formation of Taylor vortices. As reported in previous studies, at exactly Ta_c, the circulation of the cells is small and more difficult to detect visually. A slight increase in Ta up to 1.03 Ta_c (+1RPM) corresponded to an increase in the amplitude of circulation, resulting in more sharply defined cells. However, at around 1.07 Ta_c toroidal vortex structure is altered by the formation of "split" Taylor vortices. Such double-vortex formation is indicative of post TC flow [10]. Laser illumination was also used along the azimuthal direction to detect possible cross-sectional streamlines that are associated with non-axisymmetry.

2.4 Results

2.4.1 Flow-Regimes in Single Phase Flow

2.4.1.1 **Taylor-Couette Flow (TCF)**

The scope of this work included experiments operated in both batch mode (TCF) and continuous mode (TCPF). The processing variables included using a range of working fluids, different cylindrical geometries and variations in axial flowrates. The details of these experiments, and corresponding flow visualization, and image analysis results are presented for each reactor configuration. As summarized in Table 2.4.1, experimental results, using 70% vol. glycerol solution, revealed that Ta_c decreased from 2084 to 1896 as the radius ratio increased from 0.8 to 0.9, while a_c remained the same with an average value of a_c=3.13, indicating that the height of each vortex is comparable to the gap width [63]. The onset of the second instability, WVF, corresponded to Ta=4575, 5302 for the vessels of radius ratio~ 0.8 (geometries A and B, respectively). As found in earlier studies, WVF in Figure 2.4.1(e) emerged in the range of Ta/Ta_c ~2.2-2.4 ($Re_\theta/Re_{\theta c}$~1.48) [67]. The observed period of oscillation of 1.2 seconds for the WVF regime corresponded to an oscillation frequency of nearly half of the inner cylinder, as reported before [68]. Experiments in the large reactor (geometry A) confirmed that the flow phase transition from WVF regime to modulated wavy vortex flow (MWVF) occurs around Ta/Ta_c ~40, as cited in other studies [31]. Meanwhile, the onset of secondary instabilities within the realm of wavy flow, such as chaotic vortex flow occurred around Ta/Ta_c ~93, similar to values reported in earlier experiments, which is Ta/Ta_c ~100. The chaotic vortex flow regime includes various flow patterns that were previously studied [69]. In particular, as depicted in Figure 2.4.1 (f), a transition to weakly turbulent vortex flow (WTVF) was found at Ta/Ta_c ~ 178.

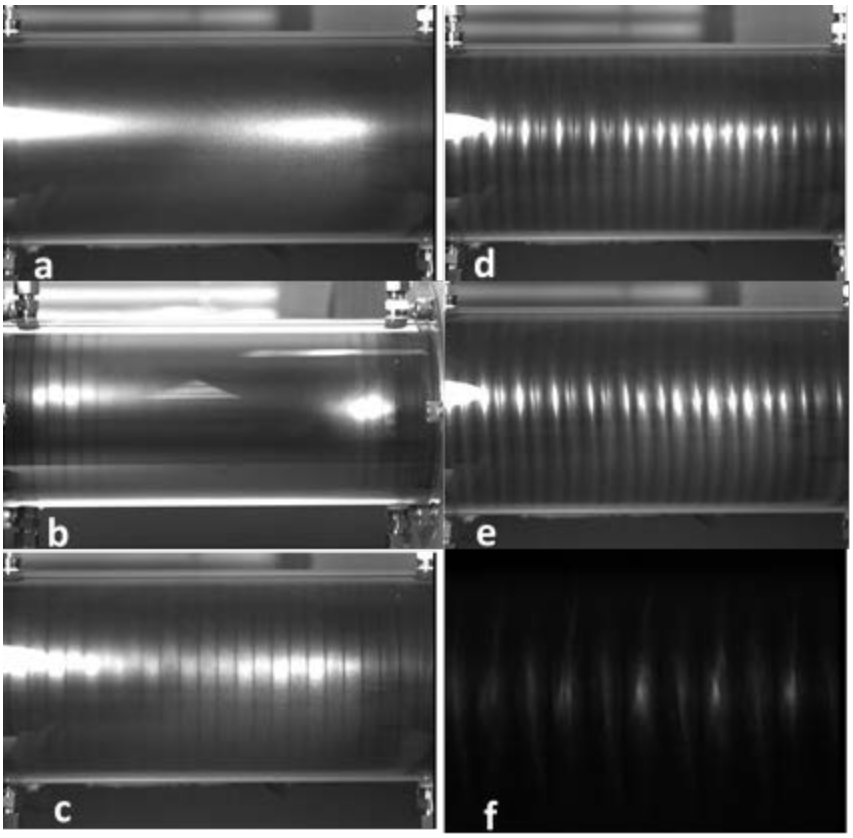

Figure 2.4.1 Flow visualization of various flow regimes.

Table 2.4.1 Onset of Taylor vortices.

System Geometry		**A**	**B**	**C**	**D**
Theoretical	**Ta_c**	**1994**	**1994**	**1823**	**1823**
Observed		**2084**	**2054**	**1896**	**1878**
% error		**4.50**	**2.97**	**3.98**	**2.99**
Theoretical	**a_c**	**3.13**	**3.13**	**3.13**	**3.13**
Observed		**3.16**	**3.11**	**3.12**	**3.14**
% error		**0.96**	**-0.64**	**-0.32**	**0.32**

2.4.1.2 Taylor-Couette with Weak Poiseuille Flow (Re_z <10)

When applying axial flow for geometry A at a rate of 630ml/min (Re_z~1.966), the vortex velocity was estimated to be 0.432cm/sec, which is larger than the mean axial flow velocity

(0.354cm/sec) by a ratio of 1.22, close to the theoretical value of 1.17 [70], and almost matching with values measured by Snyder (1.19-1.21) [22], and Donnelly and Fultz (1.2-1.3) [21]. For such weak axial flow, only a slight increase in Ta_c was observed (from 2084 to 2115), while the increase in a_c seemed negligible (3.16 to 3.19). Vortex cellular pattern resembled the toroidal patterns when no flow is applied, except Taylor vortices were drifting downstream (i.e. Propagating Taylor Vortices, PTV). Because of the large gap size, axial flow for geometry A remained weak (Re_z <10) even for extremely high flowrates, up to 4000ml/min. To avoid the circulation of large quantities of fluid, axial flow experiments were conducted in a vessel with geometry B. As shown in Figure 2.4.2, the axial flow rates were increased up to 1500 ml/min (Re_z ~9.2), corresponding to an increase in Ta_c. When compared to values obtained from Chandrasekhar's axisymmetric stability analysis [18], the experimentally observed values are considerably higher. However, the observed trend is similar to stability results based on non-axisymmetric instability and what Donnelly & Fultz observed. The difference in magnitude is partially due to the higher radius ratio that they used, η~0.95. The measured a_c were in the range of anticipated values, except at Re_z ~4.6, where the cellular structure appeared as fixed spirals with double helix topology, corresponding to the two counter-rotating helical vortices.

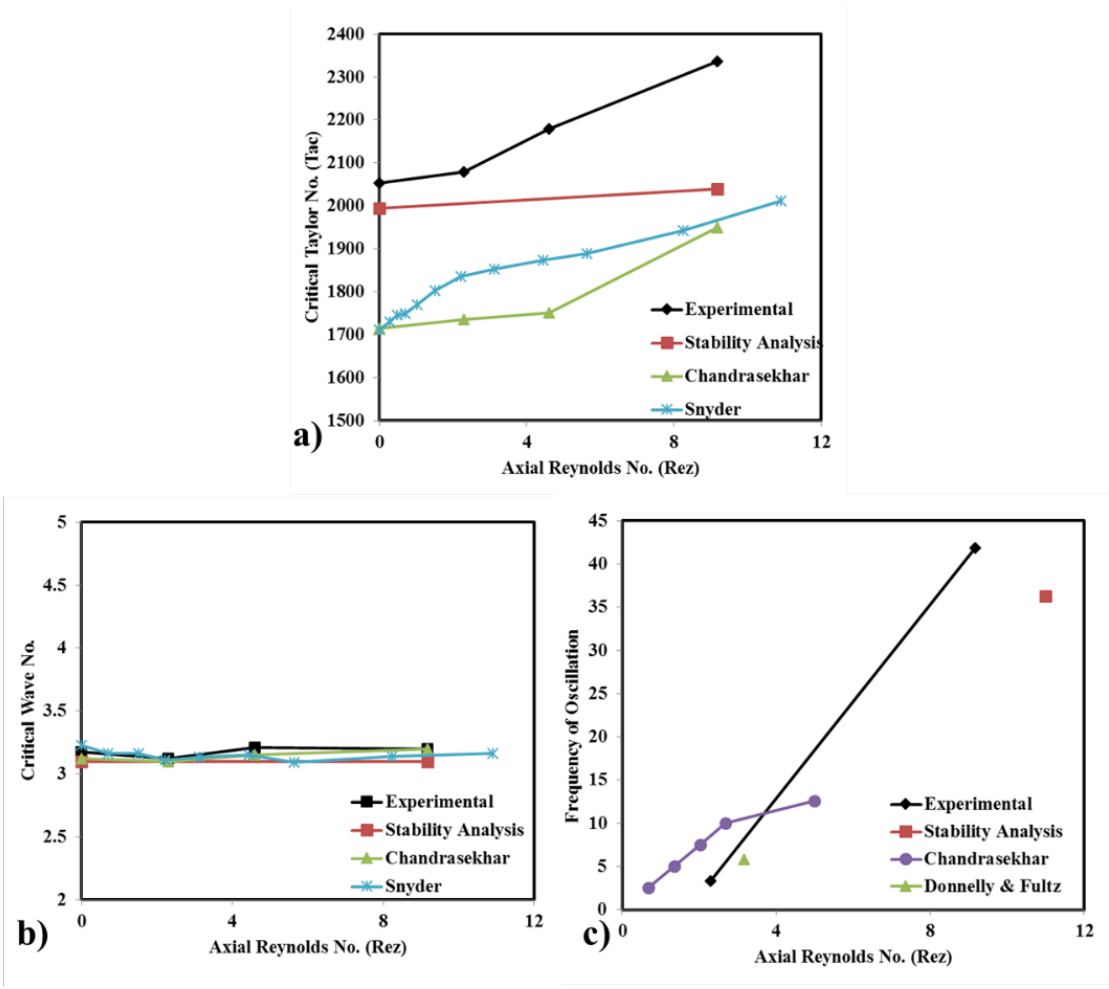

Figure 2.4.2 Comparison of non-axisymmetric stability analysis with flow visualization experiments with increasing axial flow. a) Critical Taylor number, Ta_c, vs. Re_z, b) critical axial wavenumber, a_c, vs. Re_z

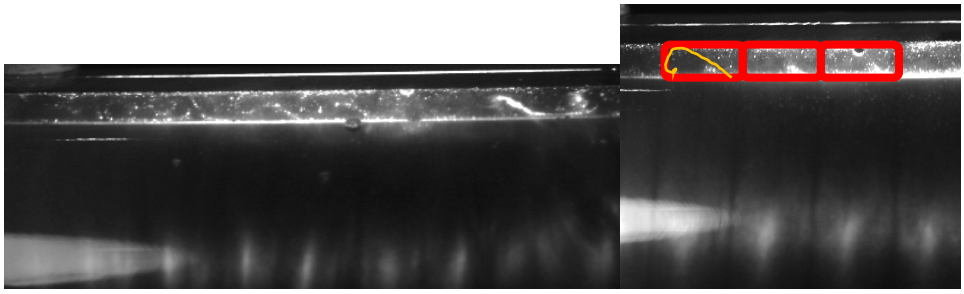

Figure 2.4.3 Stationary helical vortex flow developed at Re_z ~9 (right) and Re_z ~ 4 (left).

As seen in Figure 2.4.3, laser sheet visualization indicated the presence of vortices that were asymmetric in size, with the larger vortex appearing in a pattern similar to a cat's eye while the

smaller one enclosed in a cell bounded to the outer cylinder wall. Tsameret and Steinberg [71] constructed a flow-regime map, for cylindrical geometry similar to geometry A (η=0.77), and they indicated a flow transition from propagating Taylor vortices (PTV) to stationary helical (or spiral) vortices (SHV or SSV) taking place at Re_z ~4 [72]. As the SSV mode replaces the PTV mode, the counter-rotating pair of toroidal vortices changes its topology to asymmetric helical counter-rotating vortices. This transition from the axisymmetry to stationary helical symmetry could have caused the deviation in the measured a_c, which indicates, on a linear theory basis, the width of the cells that form when the interface becomes unstable. For a_c~3.1, the vortex cells are nearly square, the outflow is substantially stronger than the inflow, and there is negligible cross flow between vortices. With increasing axial flow a_c increases, which indicates that the vortices become thinner and more rectangular [10]. Therefore, the reduction in a_c implies an increase in the axial wavelength, indicating that the size growth in one of the vortices exceeds the reduction in the other vortex. Though full numerical analysis supports this observation, according to Raguin and Georgiadis [72], such asymmetry in vortex size has not been experimentally observed in the available literature. This is probably due to the scarcity in studies dealing with the structure and/or the size of vortices for small axial Reynolds number [73]. In reference to Figure 2.4.2 (c), for low axial flow (Re_z ~2.2), the observed frequency of oscillation was in the range of values calculated by Chandrasekhar, and experimentally observed by Donnelly and Fultz. While observed frequency of oscillation at higher axial flow (Re_z =9.2) was a bit high relative to non-axisymmetric numerical predictions. At Re_z ~9.2, it was observed that the vortices collapse periodically as they move. Such contraction and expansion affects fluid mass in the vicinity, and can be detected visually through laser sheet illumination. As depicted in Figure 2.4.3, the emergence of vortices and their corresponding

merging appeared to indicate as if the flow was transitioning from SSV, near the entrance, to PTV, near the exit. For a system with η=0.77, Tsameret *et al* identified a transitional regime between SSV and PTV, which they observed to be dominant around Re~12 [71].

2.4.1.3 Entry Effects in TCPF

Experiments with 30 vol. % glycerol solution were performed to examine the effect of axial flow at larger axial Reynolds number values. Though the increase in axial flow corresponded with an increase in Ta_c and the critical axial wavenumber, results from these experiments had major uncertainty, as the flow was complicated by turbulence due to entry and end effects. Therefore, another set of experiments were performed to assess the influence of the inner cylinder rotation rate and axial flow rate on entry affects, using water as working fluid.

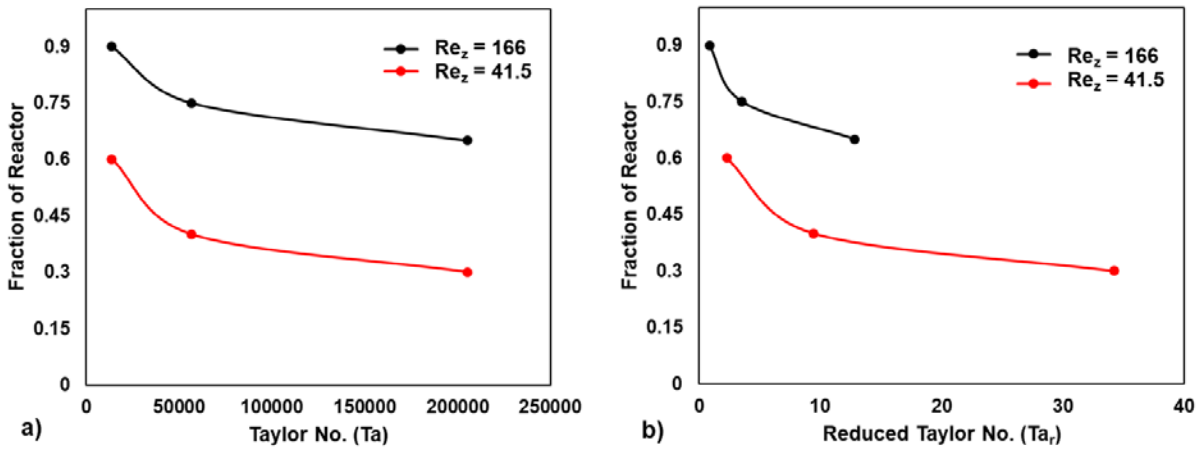

Figure 2.4.4 Fraction of reactor length occupied by entry effects for geometry B.

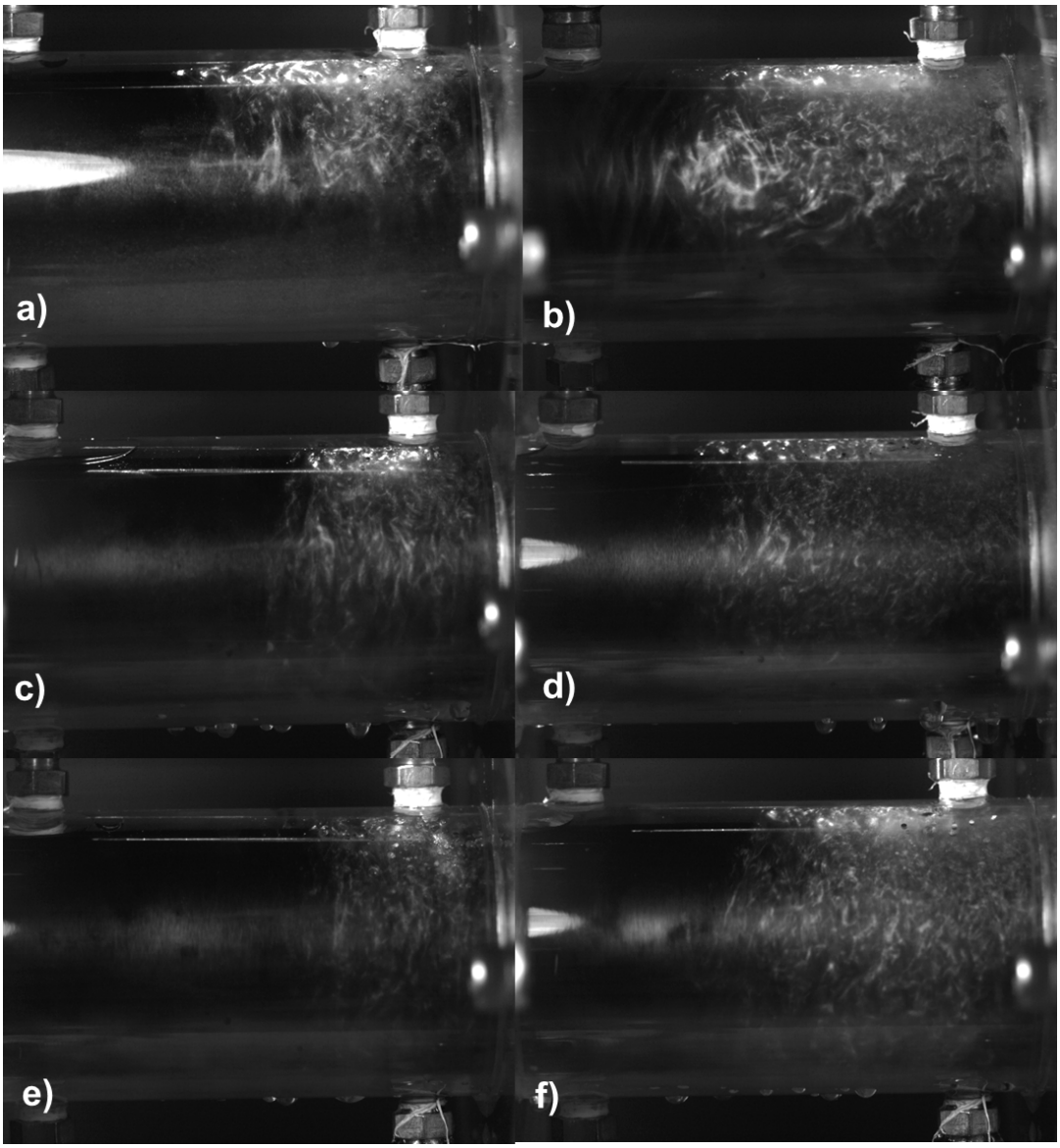

Figure 2.4.5 Demonstration of entry effects for geometry B taken at Rez = 41.6 at a) 35 RPM (Ta_r ~ 2.3), c) 71 RPM (Ta_r ~ 9.5) and a) 135 RPM (Ta_r ~ 34) and at Rez=166 at b) 35 RPM (Ta_r ~ 0.85), d) 71 RPM (Ta_r ~3.5) and f) 135 RPM (Ta_r ~13)

As demonstrated in Figure 2.4.5 and Figure 2.4.4, it was found that the entrance length required to develop stable laminar flow increases with increasing axial flowrate. The results illustrated that experiments with low rotation rates exhibit significant entry affects, covering more than 75% of the vessel, both at high and low flow rates, while at high flow rates (Re_z ~166) increasing inner-cylinder rotation had little effect on reducing the extent of the entry affects.

Overall, geometry D was able to extend the range of reproducing consistent flow-structures while minimizing entry effects up to Re_z =200 (4L/min in the case of 30 vol. % glycerol solution).

2.4.1.4 Taylor-Couette with Moderate Poiseuille Flow (10< Re_z <30)

In an attempt to make the axial component of flow more stabilized and developed, experiments were carried out using a 50% vol. glycerol solution as working fluid. A double-head pumping configuration was used to maximize flow. From Figure 2.4.6, Ta_c and a_c were observed to increase with axial flow with trends that resemble numerical simulation results. Yet, it is important to note that, at Re_z ~31, vortices were difficult to detect visually due to overlapping, as a result of the imposed axial flow which winded around the vortices overwhelming their cellular structure. Studies that utilize velocity field measurement techniques, such as LDV (Laser Doppler Velocimetry) and PIV (Particle Image Velocimetry), have indicated that vortices retain their structure, but with some distortion [70].

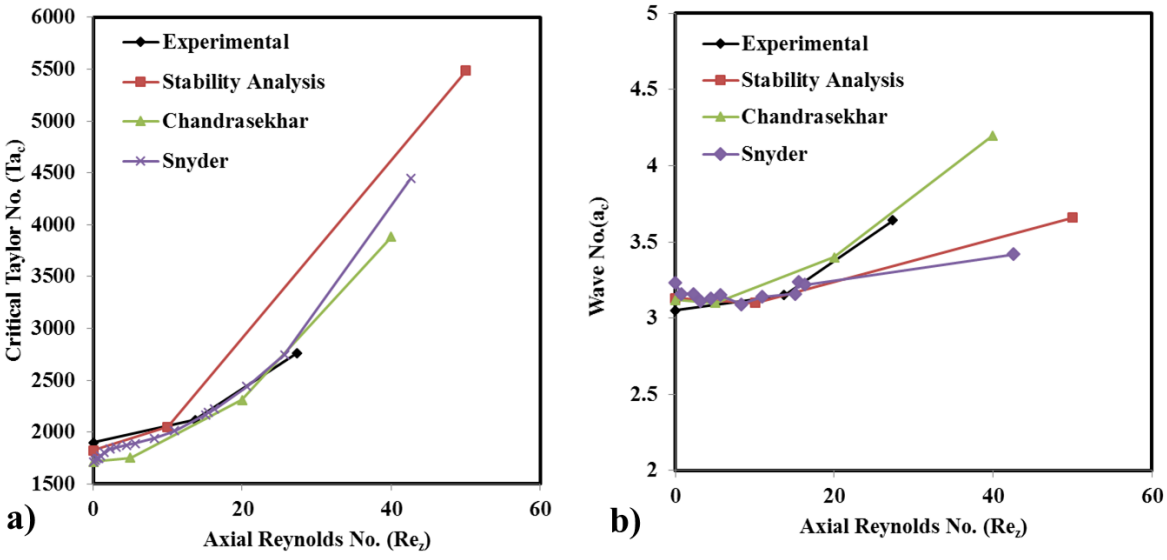

Figure 2.4.6 Comparison of non-axisymmetric stability analysis with flow visualization experiments with increasing axial flow. a) Critical Taylor number, Ta_c, vs. Re_z, b) critical axial wavenumber, a_c, vs. Re_z.

2.4.1.5 Taylor-Couette with Strong Poiseuille Flow ($30 < Re_z < 120$)

To be able to test flows of higher Re_z, while minimizing entry effects, the inner cylinder were modified to provide a smaller radial gap width. Shifting to geometry C, where the gap ratio is 0.9, provided a higher aspect ratio, and proved helpful in minimizing the extent of entry affects, while reaching up to Re_z ~60 with reasonable reliability.

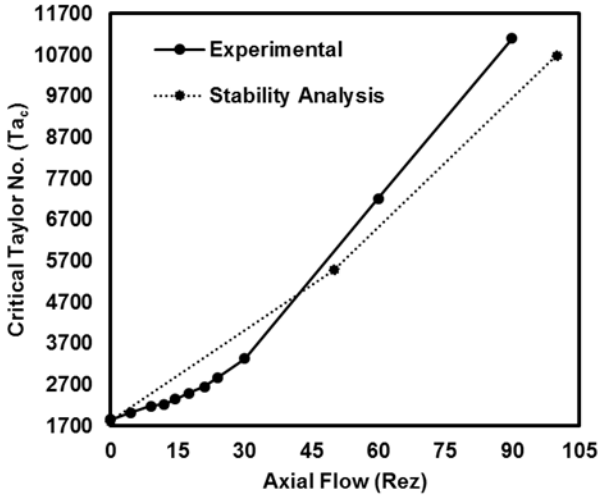

Figure 2.4.7 Estimated critical Taylor number, Ta_c, values obtained via non-axisymmetric stability analysis and via flow visualization experiments.

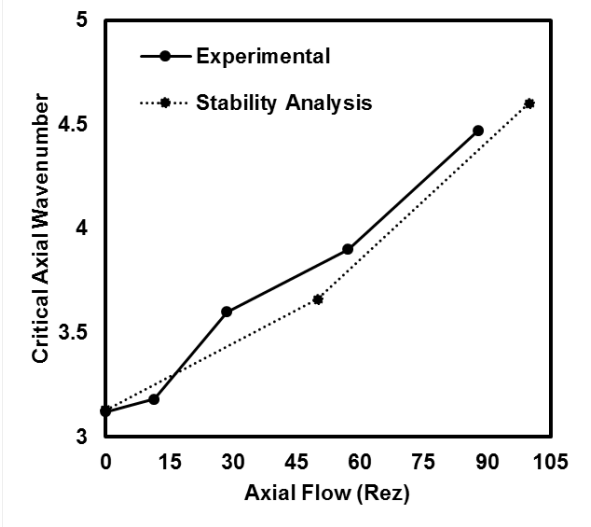

Figure 2.4.8 Estimated critical axial wavenumber, a_c, values obtained via non-axisymmetric stability analysis and via flow visualization experiments.

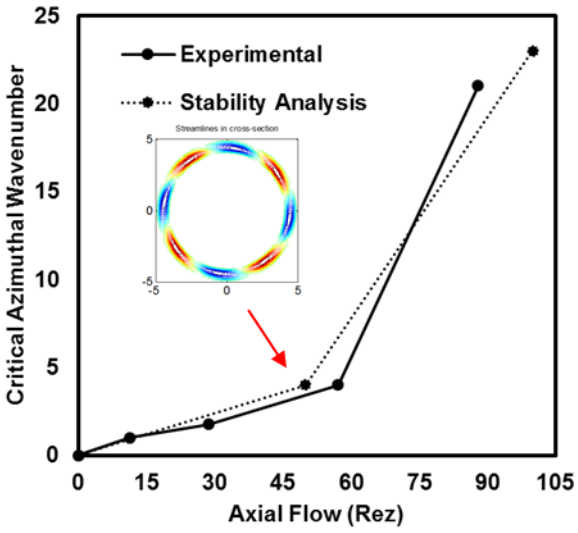

Figure 2.4.9 Estimated critical azimuthal wavenumber, *m*, values obtained via non-axisymmetric stability analysis and via flow visualization experiments.

As shown in Figure 2.4.7 and Figure 2.4.8, the values for Ta_c and a_c were very near to the ones obtained from non-axisymmetric numerical simulation, except for $Re_z > 60$, where discrepancy is due to the dominance of entry affects in this region. From the azimuthal wavenumber graph, displayed in Figure 2.4.9, the first shift to the non-axisymmetric disturbance was viewed at Re_z ~27.4, with $m = 2$. The value of $m = 4$ observed Re_z ~54.7 agrees with stability predictions. The high axial flow caused the vortex boundaries to tilt so that they form an angle with the axis of the inner cylinder, resulting in moving spiral (MS) topology for both Re_z =27.4, Re_z =54.7, as sampled in Figure 2.4.10. While the vortices in Re_z =27.4 were easier to discern visually than for Re_z =54.7, the cellular structure was better observed than in the case of Re_z =31 for geometry B. This demonstrates that gap reduction stabilizes the flow.

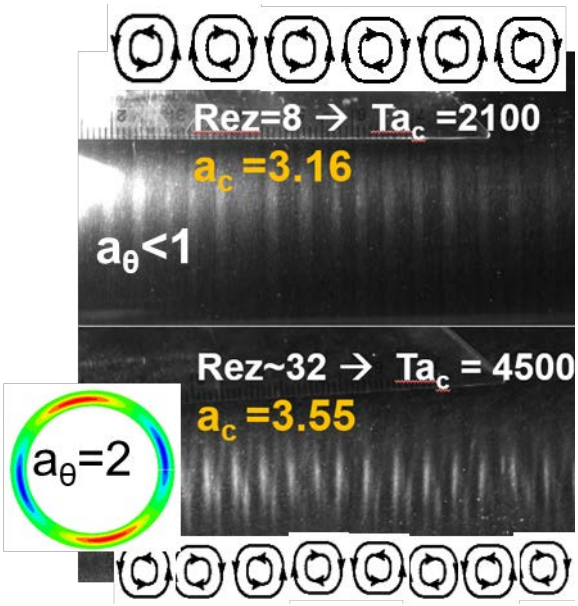

Figure 2.4.10 Change in number of vortices and evolution of spiral topology with increasing axial flow.

2.4.1.6 **Conclusion**

Overall, any discrepancy between theoretical predictions (numerical estimation) and experimental results could be due to the fact that numerical estimation assumes axial flow to occur evenly along the entire circumferential cross section, while the experimental setup is designed so that the flow enters and exits the reactor at ports along the radial directions. A transient delay to laminar Taylor-vortex flow is probable for non-integer aspect ratios (which is the case in all geometries), as there may be an initial mismatch of the converging vortices from the right and left of the vessel [74]. In addition, because of non-axisymmetry, spiral cells were actually observed rather than toroidal cells, and thus it is expected that experimentally measured values differ from those predicted by Chandrasekhar, and are in better agreement with the stability results based on non-axisymmetric modes.

These above experiments helped in designing better vessel geometry suited for the purpose of phase-mixing. Also, the observations reinforce the enormous complexity and variety of patterns

that TCPF may assume. The observed increase of the axial wavenumber indicates that the number of vortices was found to increase with a reduction in the annulus gap width [75] and with the increase in axial flow.

2.5 Immiscible Phase Mixing Experiments

2.5.1 Immiscible Phase Mixing without Axial Flow

To assess immiscible phase mixing effects in TCF, a series of experiments were done on kerosene-water mixtures in geometry C (η=0.9, Γ=58) with no axial flow. Since the mica flakes used in these experiments were hydrophilic, they initially placed in the water phase (bottom). Therefore, the presence of any mica in the kerosene phase will be the result of mass-transfer across the water-hydrocarbon interface. To investigate the effect of changing the relative density of the continuous and dispersed phases while keeping constant viscosity, experiments were also conducted in moderate (40%) and high kerosene (75%) volume fractions. As summarized in

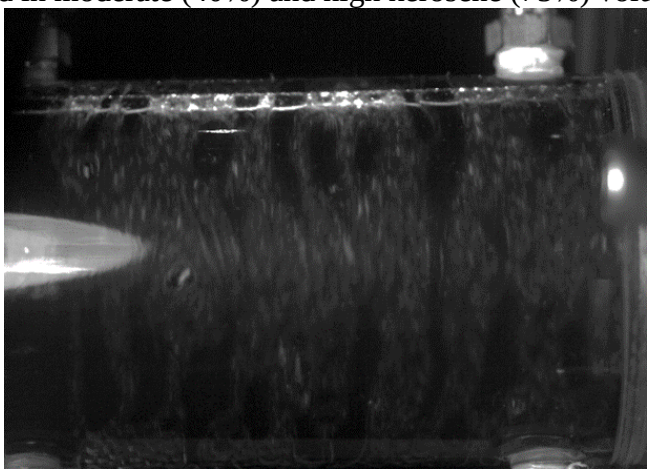

Figure 2.5.2 Laser sheet visualization of vortices formed when mixing two immiscible phases at Ta/Ta_c=18.6.

Table 2.5.1, for moderate organic-phase volume (40%), various flow patterns were observed depending on the inner cylinder rotation. These experiments were repeated with kerosene dyed with Red Oil O (1.6×10^{-4}M) to better visually describe the dispersed phase. Bulk dying of one phase allowed any waviness in the interface to be visually observed as the color intensity of the fluid is related to the fluid depth. The same flow patterns and qualitative mixing (mica mass transfer to the kerosene phase) was observed.

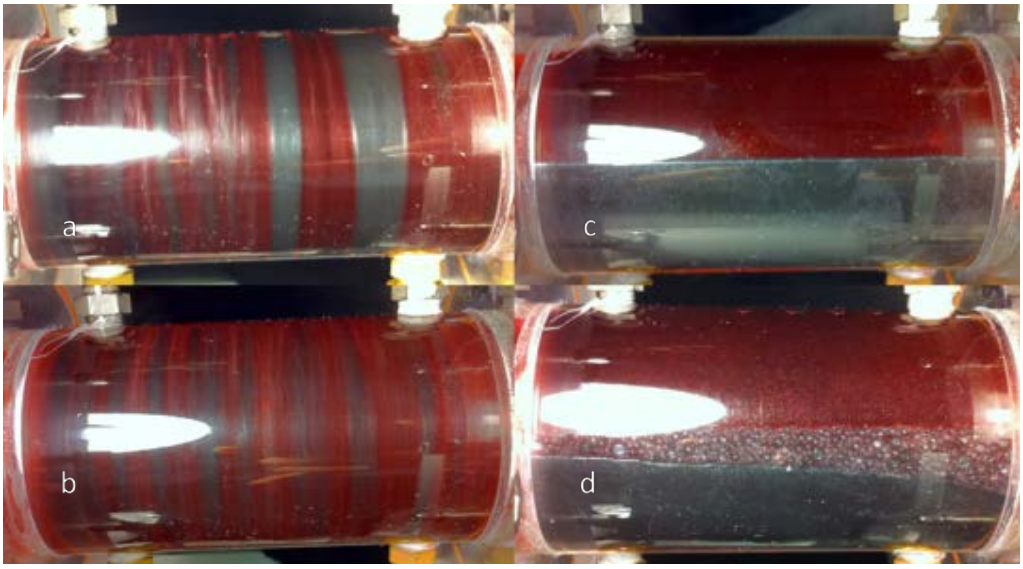

Figure 2.5.1 a) Ta/Ta_c=18.6, b)Ta/Ta_c = 47.6, c)phases before mixing, d) phases after mixing

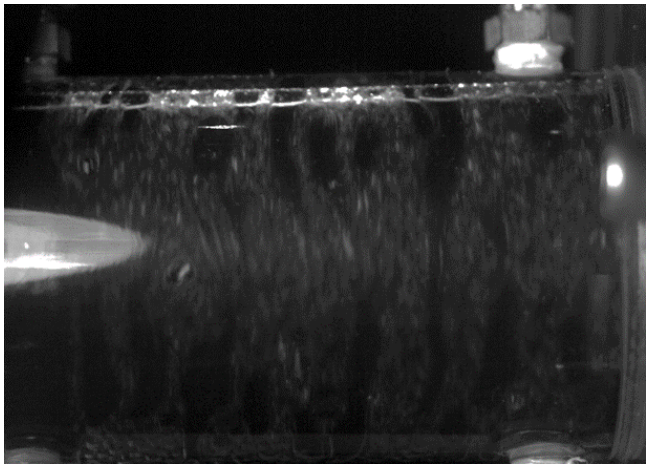

Figure 2.5.2 Laser sheet visualization of vortices formed when mixing two immiscible phases at Ta/Ta_c=18.6.

Table 2.5.1 Flow Regimes for 40 vol% Kerosene

Ta/Ta_c	**Dispersion Regime**
0.36	**Segregated**
0.48	**Segregated-water droplet disturbance**
4.28	**Discontinuous phase stratification**
7.80	**Discontinuous (dynamic) Rollers**
18.58	**Separate water & hydrocarbon rollers**
36.41	**Bulk water Roller**

107.02	**Homogenous with thin oscillatory bands**
145.66	**Fully homogeneous**

Table 2.5.2 Flow Regimes for 75 vol% Kerosene

Ta/Ta_c	**Dispersion Regime**
3.7	**Segregated-water droplet disturbance**
5.7	**Water dispersed in Kerosene**
7.1	**Formation of larger water droplets**
18.6	**Thin water & hydrocarbon rollers**
36.4	**Oscillatory water & hydrocarbon rollers**
47.6	**Homogenous with thin oscillatory bands**
145.7	**Homogeneous**

Initially, though the two phases were segregated, the hydrocarbon phase was dragged into the water phase, resulting in the formation of water-in-oil emulsion at the interface. At Ta/Ta_c=0.48, phase segregation was disturbed by shear-dragged water droplets flowing into the hydrocarbon phase. Such water crossovers took place at time intervals ranging from 1.25-1.56 seconds. We note that laser sheet visualization indicated Taylor vortex formation at lower Ta_c than expected (0.87 Ta_c of Kerosene only), and that water droplets stratify toward the outer cylinder as they travel in the kerosene phase. Such stratification made the vortices more difficult to detect visually. Beyond $4.28Ta_c$, the phases were no longer segregated, and instead, discontinuous phase stratification is observed. The stratified phases begin to form larger regions that resemble broken rollers at around Ta/Ta_c=7.8. As seen in Figure 2.5.1 (a), separate kerosene and water rollers were observed at Ta/Ta_c=18.58. The water rollers merged together at Ta/Ta_c=36.41, forming a larger 'bulk' roller. As depicted in Figure 2.5.1 (b), at Ta/Ta_c=47.6 a unique flow structure emerges consisting of kerosene-rich (more red) regions separated by clear water bands, with each kerosene region being further subdivided by thin water bands. The kerosene and water emulsified forming a pseudo-homogeneous mixture, and this transition was observed to take place at Ta/Ta_c=107. Mass transfer of mica flakes was influenced by rotation

rate and the corresponding residence time. As seen in Figure 2.5.1 (c-d), qualitative estimation indicated an overall transfer of 40% of mica flakes from water by increasing rotation rates up to $Ta/Ta_c=107$, with a cumulative residence time of about half an hour. As summarized in Table 2.5.2, similar flow patterns were observed for experiments with 75 vol% kerosene volume fraction, except that the banded structure was not observed. Rather, an earlier transition to pseudo-homogeneous dispersed flow pattern with oscillatory bands was observed at $Ta/Ta_c=47.6$ (compared to $Ta_c=107$ for moderate volume fractions). Moreover, no mass transfer of mica flakes was visually detected. . In addition, quasi-static acceleration rates of the inner cylinder were found to be critical for generating specific flow patterns at their corresponding rpm.

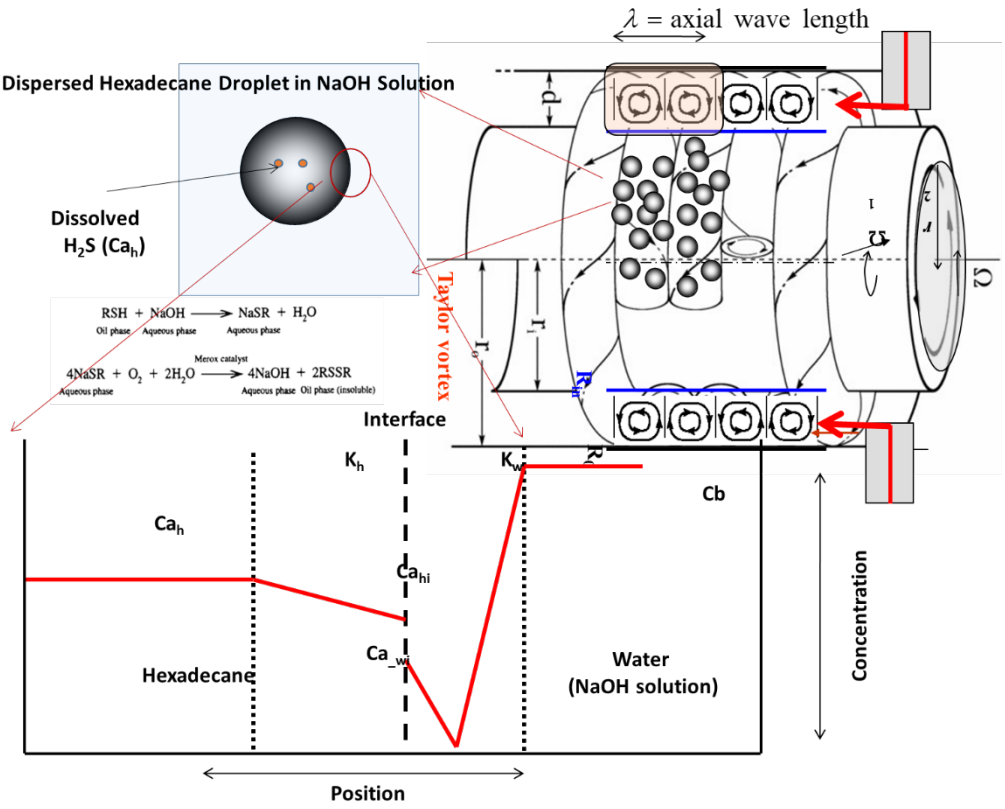

Figure 2.5.3 Interfacial mass transfer among two immiscible liquid phases.

Behavior of immiscible liquid droplets strongly influences mass transfer limitations in the dispersed phase. At all flow-regimes observed for the mixing of two immiscible fluids in the TCR, there exists a thin film around the interface where molecular diffusion is dominant rather than turbulent diffusion. The thickness of the thin film is influenced by the viscosities of the two phases and the degree of mixing when stirring rates are due to either axial or rotational motion. As illustrated in Figure 2.5.3, in order for the species to pass from the hydrocarbon organic phase and be absorbed into the aqueous phase or vice versa, it has to diffuse from the bulk to the thin film that surrounds the interface between the hydrocarbon and water.

As observed in previous experiments, formation of boundary layers of water surrounding vortex cores that are heavily concentrated in dispersed phase (kerosene) reduces the degree of dispersion, and therefore, the interfacial area between the dispersed and continuous phases is kept to a minimum. Such phenomena is usually labeled as banded structure formation [76], as opposed to homogenous phase regime, in which the organic phase is highly, almost "perfectly" mixed with the water phase. Such conditions are possible only with very high rotational speeds. These experiments demonstrate that mass transport in immiscible liquid-liquid TCF depends strongly on the flow patterns, which in turn depend upon operational parameters, such as rotation rate, residence time and volume fraction. Other factors, such as surface tension and the introduction of axial flow, could also influence mass-transport. It has been demonstrated that the reduction in interfacial tension, done by adding an emulsifier, has a dramatic effect on droplet size [29] [76].

Experiments confirming the onset of flow-transitions and flow characteristics of single phase behavior of hydrocarbons in TCF were performed through monitoring the alignment of hydrophobic aluminum flakes suitable for organic phase flow visualization [10]. The onset of

instability in these experiments were found to be consistent with the results derived above for the single aqueous phase glycerol solutions.

2.5.2 Immiscible Phase Mixing with Axial Flow

To further examine the influence of axial flowrate, mixing between immiscible hydrocarbon-water mixtures in the continuous TCR was examined by considering the mixing of water and kerosene at equal volume fractions. In these experiments, the water phase was dyed with methylene blue at concentration of 0.91×10^{-5} M, with mica flakes suspended at 0.0062 wt%, while the kerosene phase was seeded with superfine reflective anisotropic Aluminum particles at concentration of 0.0065wt%, as displayed in Figure 2.5.4.

Figure 2.5.4 water phase was dyed with methylene blue, with mica flakes, while the kerosene phase was seeded with superfine reflective anisotropic Aluminum particles.

With the introduction of Flow is 3 L/min (at 1455rpm), corresponding Re_z~200 for kerosene (Ta~1750Ta_c) and Re_z~340 for the water phase (Ta~4560Ta_c), it was observed that the wavelength between the alternating water rich and hydrocarbon rich bands increased from 0.53 cm (a_z=2.95) to 1.1cm (a_z=1.47), as seen in Figure 2.5.5. The consistent reproducible formation of this flow pattern can be classified as bifurcation point with quasiperiodic stable flow regime

[74], as the banded flow regime (at 1455rpm) did not exhibit hysteresis within the resolution of the experiments.

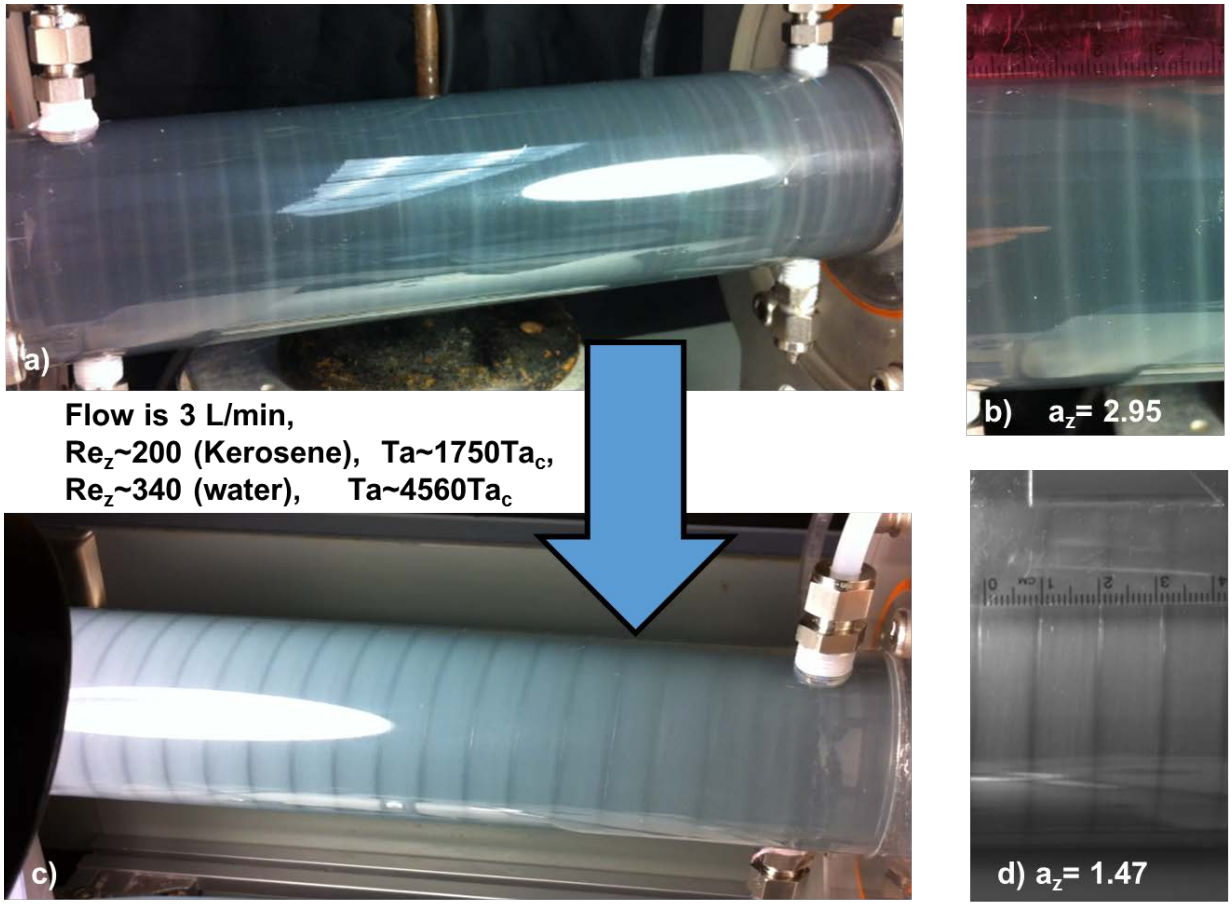

Figure 2.5.5 Mixing of two immiscible liquids in TCR a) without axial flow and c) with axial flow of 3L/min.

With the emergence of such distinct banded patterns under strong axial flow, the contact area between the hydrocarbon and water phases can be increased significantly, forming donut-shaped toroidal waves of alternating concentration (hydrocarbon-rich vs. water-rich). For enhanced interfacial dispersion among the immiscible phases, the inertial forces must be greater than the surface tension. Studies have also confirmed that intercell exchange velocity, which is proportional to the increase in axial flow, must be high enough to disperse the phases into droplets across the entire annulus, suggesting a minimum of Ta_r= Ta/Ta_c =1000 is required to

satisfy the criterion of inertial force being greater than the surface tension, with which the dispersion of one liquid into another is achieved [33].

CHAPTER 3

EFFECT OF FLOW STRUCTURE AT THE ONSET OF INSTABILITY ON BARIUM SULFATE PRECIPITATION IN TAYLOR-COUETTE CRYSTALLIZERS

3.1 Introduction

Formation of inorganic powders via precipitation is a critical step for the production of solids with ultrafine size, and fine-tuned morphology. Controlling the flow dynamics of the feed mixing before and during the irreversible reaction can assist in controlling particle properties such as particle size, morphology, crystallinity and product purity, all of which determine the quality of the final product. Due to the importance of barium sulfate ($BaSO_4$) crystalline powders in a wide array of industrial applications, such as paper coatings, pigments, nanocomposites, radiocontrast agents, it has been chosen as a model substance to study the influence of mixing conditions on particle formation during precipitation [77].

Fluid dynamics can play a significant role in determining crystal size, microstructure and morphology during precipitation. In particular, variation in mixing intensity, reactor configuration and geometry are important in determining crystal size distribution [78]. For example, in semi batch configuration, it was observed that the mean crystal size decreased dramatically when the two feed streams were located near the impeller rather than far away from it, which produced larger crystals [79]. Overall, the precipitation of $BaSO_4$ has been examined in several reactor configurations including continuous mixed suspension-mixed product removal (MSMPR) [80] [81], semi batch mode [82], stirred tank reactor [83], Y-mixer [84], T-mixer [85], Impinging Jets [86] and cavitational and conical chambers with ultrasonic sound as a mixing accelerator [87].

Supersaturation is generated by mixing, while it is reduced by nucleation and growth. For complete solid formation, precipitation time-scales range from less than milliseconds at intense mixing up to fractions of a second at slow mixing. Such variation is possible because the rates of nucleation and growth depend on supersaturation. For $BaSO_4$ precipitated from $BaCl_2$ and H_2SO_4 solutions in an applied T-mixer with a *step50*-profile, the whole precipitation process is complete after about 1 ms, when the supersaturation is reduced to saturation and the primary particles are formed. Secondary processes such as aggregation start to dominate changes in the particle size distribution ending within a timescale of one second [88]. Since the precipitation of $BaSO_4$ is a very fast process, such reactors attempt to reduce mixing time scale with shortened contact to create $BaSO_4$ nanoparticles. The main shortcoming with such configurations is that they heavily depend on feed flow conditions. Such dependence can be lessened in Taylor Couette (TC) reactor configuration where micromixing times are mainly influenced by the inner cylinder rotation rather than reactant-feed flow. The uniformity in the fluid dynamic conditions is another important advantage that TC crystallizers can offer. Reduction in mean crystal size due to an increased rotation of the inner cylinder in a TC crystallizer has been reported for the crystallization of Guanosine 5-monophosphate (GMP) under different concentrations [89]. A similar observation was observed by Judat *et al.* for barium sulfate precipitation in Taylor Couette reactor configuration with large axial flow under turbulent flow conditions [90]. Also, Marchisio *et al.* examined the precipitation of barium sulfate in the Taylor-Couette reactor solely driven by cylinder rotation after injection the reactants under turbulent vortex and fully turbulent flow, and they observed a decrease of the mean crystal size with increasing rotation rate [91]. Particle size distribution (PSD) of

precipitated barium sulfate in TC crystallizers under much milder axial flow rates was examined by Scargiali *et al.,* where they found that higher flow rates resulted in smaller crystals [92].

The common aspect of the former studies on $BaSO_4$ precipitation in TC crystallizers is that they operate with very high energy of dissipation, and at excessive rotational speeds, in ranges that are certainly beyond the onset of primary instability and rather close to turbulent flows. Although those studies demonstrated the successful production of small $BaSO_4$ crystals in TC crystallizers, they did not fully explain the interplay between fluid dynamics and $BaSO_4$ crystallization, and studies tailored towards examining the role of flow transition from laminar to vortex flow in determining crystal properties have not been yet reported. In the current study, we have explored the role of the vortex motion near the onset of the primary instability in fine-tuning crystal properties such as internal crystal structure, particle microstructure and morphology in TC crystallizers. We investigated the change of crystal size and distribution before and after the onset of primary instability in ranges of similar energy consumption. By doing this, the influence of shear energy of rotation is decoupled to exclusively manifest the effect of vortex flow structure on precipitations. To explain the observed phenomena, we also performed a particle trajectory analysis, borrowing the linear instability results, to calculate the contour length of particles traveling in the TC crystallizer. Through this study, we expect to provide a guide towards the production of finer crystal size at minimum energy consumption.

3.2 Experimental Procedure

3.2.1 Experimental Setup

The experimental setup of the TC crystallizer, illustrated in Figure 3.2.1, consisted of two coaxial cylinders, with the aluminum inner cylinder rotating while the Plexiglas outer cylinder

is fixed. The inner cylinder rotation rate is controlled by a phase inverter, connected to a motor drive that provides rotation rates in the range of 30-1500 RPM. Table 3.2.1 includes the physical specifications of the TC crystallizer used in the current study.

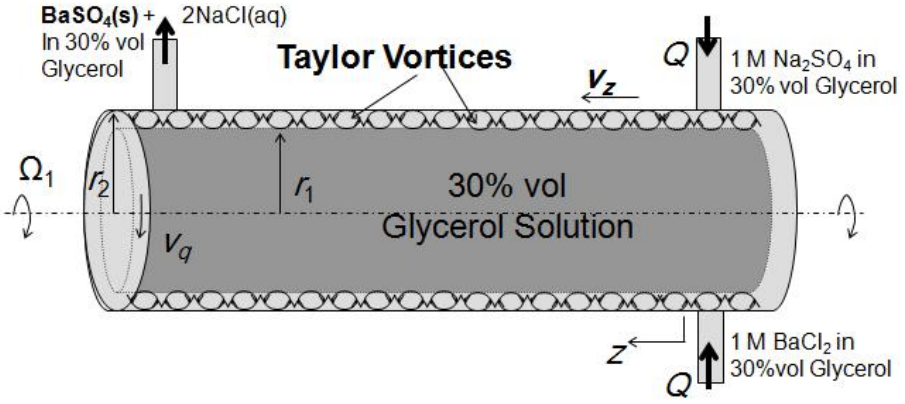

Figure 3.2.1 . Schematic of precipitation of barium sulfate in Taylor Couette crystallizer

Table 3.2.1 Dimensions of Taylor Couette Crystallizer

r_1(cm)	r_2 (cm)	$d(r_2\text{-}r_1)$ (cm)	L_r (cm)	$d/\,r_1$	$r_1/\,r_2$	$L_r/\,d$
2.275	2.533	0.2584	15	0.114	0.898	58.039

The primary hydrodynamic instability marks the Taylor-Couette flow (TCF) regime, as determined by the critical Taylor number (Ta_c). Uniformly spaced counter-rotating cellular vortices, with each pair forming an axial wave, is characterized by critical wavenumber (a_c) and wavelength (λ_c).

The scope of this work involved the precipitation of barium sulfate under laminar flow (Ta < Ta_c) and Taylor vortex flow (Ta > Ta_c) with three different flow rates: Re_z = 3.3 (mean residence time ~ 48 s), Re_z = 14 (mean residence time ~ 12 s) and Re_z = 42 (mean residence time ~ 3.8 s).

The overall precipitation process occurs through a combination of parallel and successive mechanisms that involve nucleation, growth, and secondary processes such as agglomeration, attrition, breakage and ripening. The barium sulfate precipitation was performed when non-premixed solutions of barium chloride ($BaCl_2$) and sodium sulfate (Na_2SO_4) were fed to the reactor, producing sodium chloride as a byproduct. Nucleation and growth are primarily driven by supersaturation which can be estimated using a concentration-based ratio. An initial supersaturation of 95,000 is obtained for 1M solutions of $BaCl_2$ and Na_2SO_4 assuming instantaneous mixing [84].

$$BaCl_{2(aq)} + Na_2SO_{4(aq)} \rightarrow BaSO_{4(s)} + 2NaCl_{(aq)}$$

The kinematic viscosity of the glycerol-water mixtures viscosity were determined in the usual manner with Ostwald capillary viscometer using water as the reference liquid and are shown in Table 3.2.2. Temperature was assumed to be constant in the range of 20°C. Axial flow in TC crystallizers was provided by a peristaltic pump with two coupled pump heads, which allowed a wide range of axial flow rates. Variation in fluid viscosity can affect the pumping flow rate, resulting in an uncertainty in axial flow of about ± Re_z= 2.7%. Similarly, the limited control over the accuracy of the inner cylinder rotation rate results in an uncertainty of ±Ta = 4.4% (±1RPM). The solutions were prepared from reagent grade anhydrous salts and 30% glycerol solution, made with de-ionized water. The addition of sodium sulfate and barium chloride to the 30% glycerol solution resulted in an increase in the viscosities of the feed solutions. While the estimation of the axial Reynolds number, Re_z, of the entering fluids was done through averaging the viscosities of the 1M $BaCl_2$ and 1M Na_2SO_4 solutions (~$4.18 \times 10^{-6} m^2/s$), the determination of the Taylor number was more complex due to the gradual change in viscosity of the fluid medium in the TC reactor. Though the viscosity of the TC fluid medium is that of

30% glycerol solution initially, it changes as the feed solutions enter the reactor. To calculate the relevant Taylor number, an estimated viscosity of 3.58 $x10^{-6}$ (m^2/s) was obtained by assuming a fluid medium of that consists of 50% of the entering fluid (4.18 $x10^{-6}$ m^2/s) and remaining half of 30% glycerol solution.

Table 3.2.2 Viscosities of solutions used in the BaSO4 precipitation experiments

Fluid	30%Glycerol Solution	1M Na_2SO_4	1M $BaCl_2$	Entering Fluid Mixture	Entering Fluid				
					10%	25%	50%	75%	100%
Kinematic viscosity (m^2/s) $x10^{-6}$	2.84	4.78	3.58	4.18	2.97	3.18	3.58	3.85	4.18

Phase structure and crystallite size of $BaSO_4$ was identified using a Scintag Theta-Theta X-ray Diffractometer (XRD) (Cu K_ radiation, λ = 1.5418A°), while the crystal size and morphology were examined using a LEICA 440 Scanning Electron Microscope (SEM) and FEI T12 Tecnai Spirit transmission electron microscopy (TEM). Analysis of the microstructure of barium sulfate was possible through size measurements performed in the Malvern Zetasizer instrument (measures between 0.6 nm – 6 μm), which works on Dynamic Light Scattering (DLS) principle.Particles in Brownian motion are subject to laser illumination while the resulting intensity fluctuations in the scattered light are related to the size.

For sample preparation, the collected product was centrifuged for 15 minutes under 5000RPM, washed in deionized water, and centrifuged again. Two washes with deionized water were deemed sufficient to dissolve all the sodium chloride co-produced in the reaction as well as the

glycerol medium. The products were then dried in a vacuum oven at around 200°C for four hours. The dried products were subject to slight grinding, before XRD and SEM analysis. After treatment in ultrasonic bath for one hour, samples were filtered in a 0.5µm filter before performing measurments in the Malvern Zetasizer.

3.3 Results and Discussion

3.3.1 Linear Stability Analysis and Flow Visualization

Since the performance of the Taylor-Couette reactor can significantly be improved by the presence of vortex structure, understanding the general stability characteristics becomes a necessary task. The flow in the Taylor-Couette reactor which consists of two coaxial cylinders, with the inner cylinder rotating together with inlets and outlets for continuous operation is called spiral Poiseuille flow [93], [94] or Taylor Couette Poiseuille flow (TCPF). Theoretical studies of TCPF flow were explored first by Chandrasekhar [18], followed by Di Prima [19] [20], whose analyses, focusing on the approximation of small-gap limit ($\eta = r_1/r_2 \to 1$) and axisymmetric assumption, were later experimentally verified by Donnelly and Fultz [21], and Snyder [22]. Subsequent extensive studies for arbitrary finite gap and non-axisymmetric analysis provided more comprehensive instability characteristics [94] [93] [95] [96]. To provide comprehensive comparison with flow visualization and sufficient critical information required for the present barium sulfate precipitation experiments, a three-dimensional linear stability analysis has been revisited in our recent study [97]. As specified by the Taylor number (*Ta*), the onset of Taylor vortex flow by the centrifugal instability depends on reactor geometry and fluid properties including the gap width and the radii of inner and outer cylinders. As the inner cylinder rotation increases further beyond the critical speed, higher order harmonics become important, leading to a second instability that is marked by non-axisymmetric periodic flow,

known as wavy vortex flow (WVF). Flow transitions towards turbulence occur through a progression of flow instabilities, each of which represents a flow regime transition, such as modulated wavy vortex flow (MWVF) and turbulent Taylor flow (TTF). The onset of secondary instabilities and the corresponding flow regimes has been comprehensively characterized and mapped out by Mizushina [13] for flow with the outer cylinder fixed, and by Andereck [14] for flows with co-rotating and counter-rotating cylinders. In the present study, we focus on the effect of Taylor vortex flow by the primary instability on crystallization and precipitation of $BaSO_4$.

When the axial flow is present, the system becomes more stable and the onset of instability is significantly delayed because increasing axial flow diminishes the dominance of centrifugal forces. As Re_z increases, the critical mode may shift from axisymmetric to non-axisymmetric disturbance, which causes the vortices to time-dependently travel both in the circumferential and axial directions. The loss of symmetry reflects a non-zero azimuthal wavenumber (*m*). As shown in Figure 3.3.1 (a) and (b), a nonaxisymmetric critical mode of an azimuthal wavenumber *m*=4presences at the onset of instability (Ta_c =5483) for TCPF with Re_z=50 and the radius ratio $\eta = 0.9$. An-Cheng *et al.* study included a set of flow visualization experiments in TC crystallizers to validate their numerically predicted flow structures in both longitudinal and transverse cross-sections. In particular, the presence of non-axisymmetric mode is confirmed by laser-sheet flow visualization experiments based on glycerin/water mixture solutions with light-reflecting mica flakes. In Figure 3.3.1 (c), the influence of axial flow on vortex structures was examined by laser illumination in the *r*-*z* plane, along a cross-section of the annulus. Laser sheet illumination was also applied in the *r*-θ plane, along the azimuthal

direction, to detect possible cross-sectional streamlines that are associated with non-axisymmetry, see Figure 3.3.1 (d).

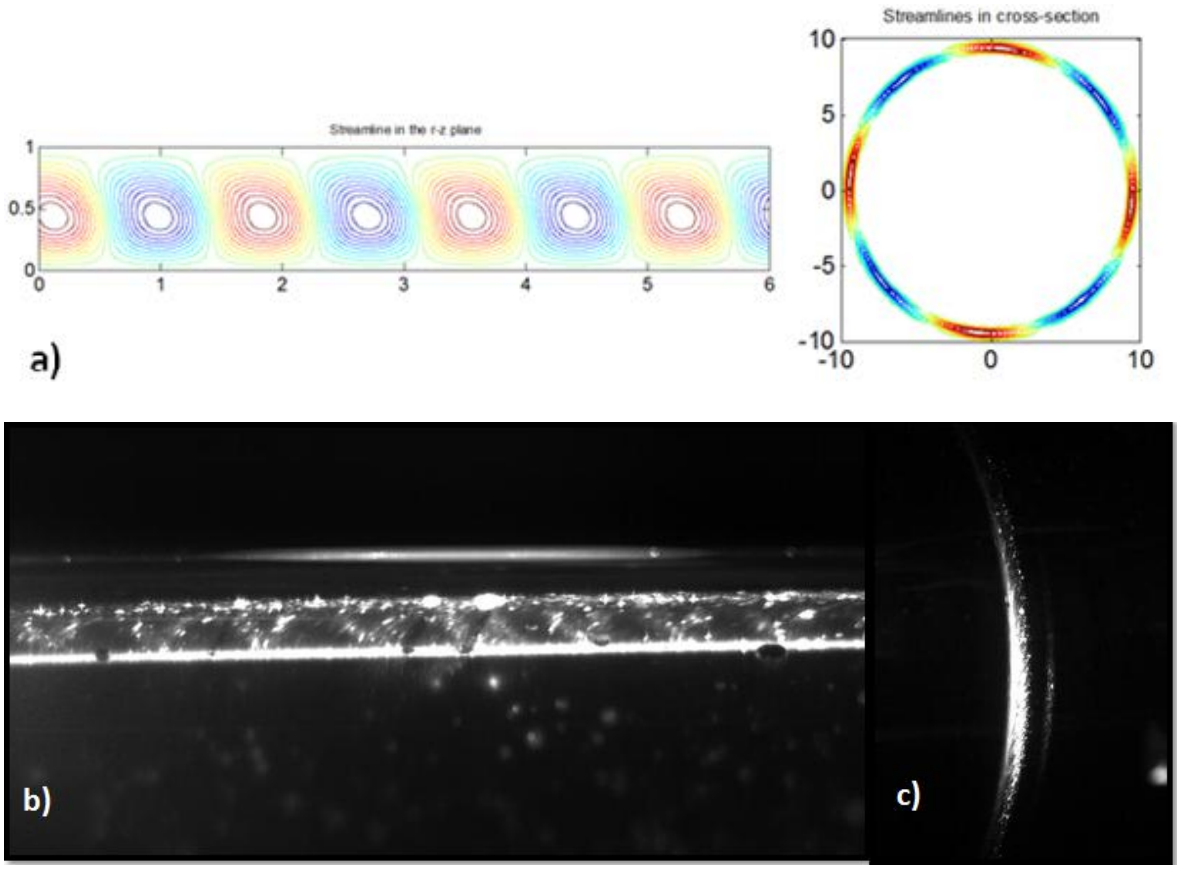

Figure 3.3.1 a) Streamlines in the *r*-*z* and *r*-Θ planes for Taylor Couette Poiseuille flow at Ta_c=5,483 with Re_z = 50 and $\eta = 0.9$. Laser sheet flow visualization at Re_z = 28 b) Axial (*r*-*z*) plane c) Azimuthal (*r*-θ) plane.

Mixing characteristics and mass transport, for both macro- and micromixing patterns (*i.e.* inter- and intra-vortex mass transport) has been well documented in TC and TCPF flow configurations using tracer techniques. Because vortex pairs in TC are usually equal in size, Kataoka *et al.* assumed that mixed fluid is uniformly distributed along the vortices, so that it spends identical residence time in each cellular element. Introducing weak axial flow and assuming a well-defined flow structure, they suggested ideal-plug flow in TCPF by studying radial and circumferential mixing in the absence of back-mixing [23]. When axial flow is

relatively large, Kataoka *et al.* found that there exists a small degree of exchange of fluid elements between neighboring vortices [15]. By measuring inter-vortex flux independently and decoupling it from dispersion enhancing/reducing effects, Desmet *et al.* confirmed the existence of inter-vortex fluxes even though the experiments were done in batch mode (TC) [24]. While earlier studies modeled the flow as a series of CSTR's with one-dimensional dispersion [25] [26] [27], Desmet's work offered a two-zone mathematical model to account for intra-vortex mixing during TCF. This multi-zone model has been extended to different derivatives [16] [28]. As shown in Figure 3.3.2, increasing axial flow diminishes the dominance of centrifugal forces, resulting in a proportional increase in the critical Taylor number (Ta_c), and critical wavenumber (a_c) and thus the vortex size decreases with increasing axial flow. Although Ta_c and a_c were observed to increase with axial flow with trends that resemble the ones obtained from non-axisymmetric numerical stability analysis, the experimentally observed values were found to be higher. This may be due to the fact that axial flow was locally introduced through inlets whereas circumferentially uniform axial flow was applied in the stability analysis. A similar difference is observed when comparing axisymmetric stability analysis, as provided by Chandrasekhar [18], with results obtained from experiments with circumferentially uniform axial flow performed by Snyder. From the azimuthal wavenumber graph, the first shift to the non-axisymmetric disturbance was viewed at Re_z ~13, with m = 2. The value of m = 4 observed at Re_z~54.7 agrees with stability predictions. As shown in Figure 3.3.1 (a), the high axial flow caused the vortex boundaries to tilt so that they form an angle with the axis of the inner cylinder, resulting in moving spiral (MS) topology for both Re_z =27.4 and Re_z=54.7.

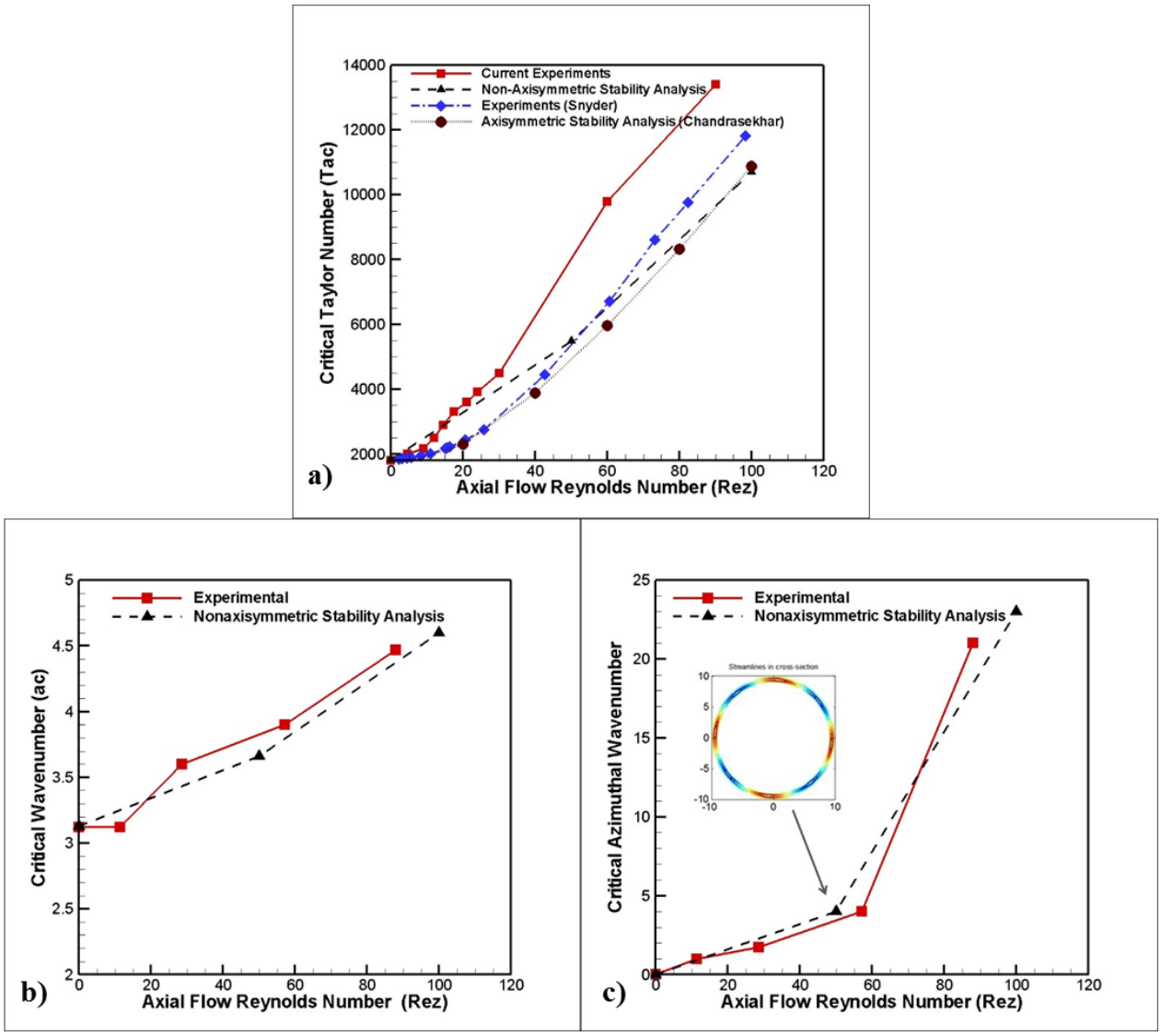

Figure 3.3.2 Comparison of non-axisymmetric stability analysis with flow visualization experiments with increasing axial flow. a) Critical Taylor number, Ta_c, vs. Re_z, b) critical axial wavenumber, a_c, vs. Re_z, and c) critical azimuthal wavenumber a_θ, vs. Re_z

3.3.2 Barium Sulfate Precipitation

3.3.2.1 Effect of Initial Supersaturation

According to Li *et al.* varying the initial supersaturation ($Sc_{,0}$) allows for a controlled morphology of the barium sulfate crystals [98]. They observed that crystal morphology can range from dendrite shape to spherical particles as the initial supersaturation is varied from

$Sc_{,0}$=100 to $Sc_{,0}$=9,500. In our TC crystallizer, while similar results were observed for $Sc_{,0}$=200, we observed spheroidal rods for $Sc_{,0}$=9,500. As seen in Figure 3.3.3, spherical particles were observed at higher initial supersaturation ($Sc_{,0}$=24,000) in TC crystallizers than in the membrane dispersion mini-reactor ($Sc_{,0}$=9,500). Because the initial supersaturation is high (95,000), the characteristic time for the nucleation process will be extremely short (~1 x 10^{20} hr/m^3) [5], especially when compared with the micromixing time. According to Judat *et al.* correlation, the micromixing time in the range of Taylor numbers and axial flowrates was in the range of 0.6-1.5 seconds [90]. This means that flow hydrodynamics should have negligible influence on the nucleation step of $BaSO_4$.

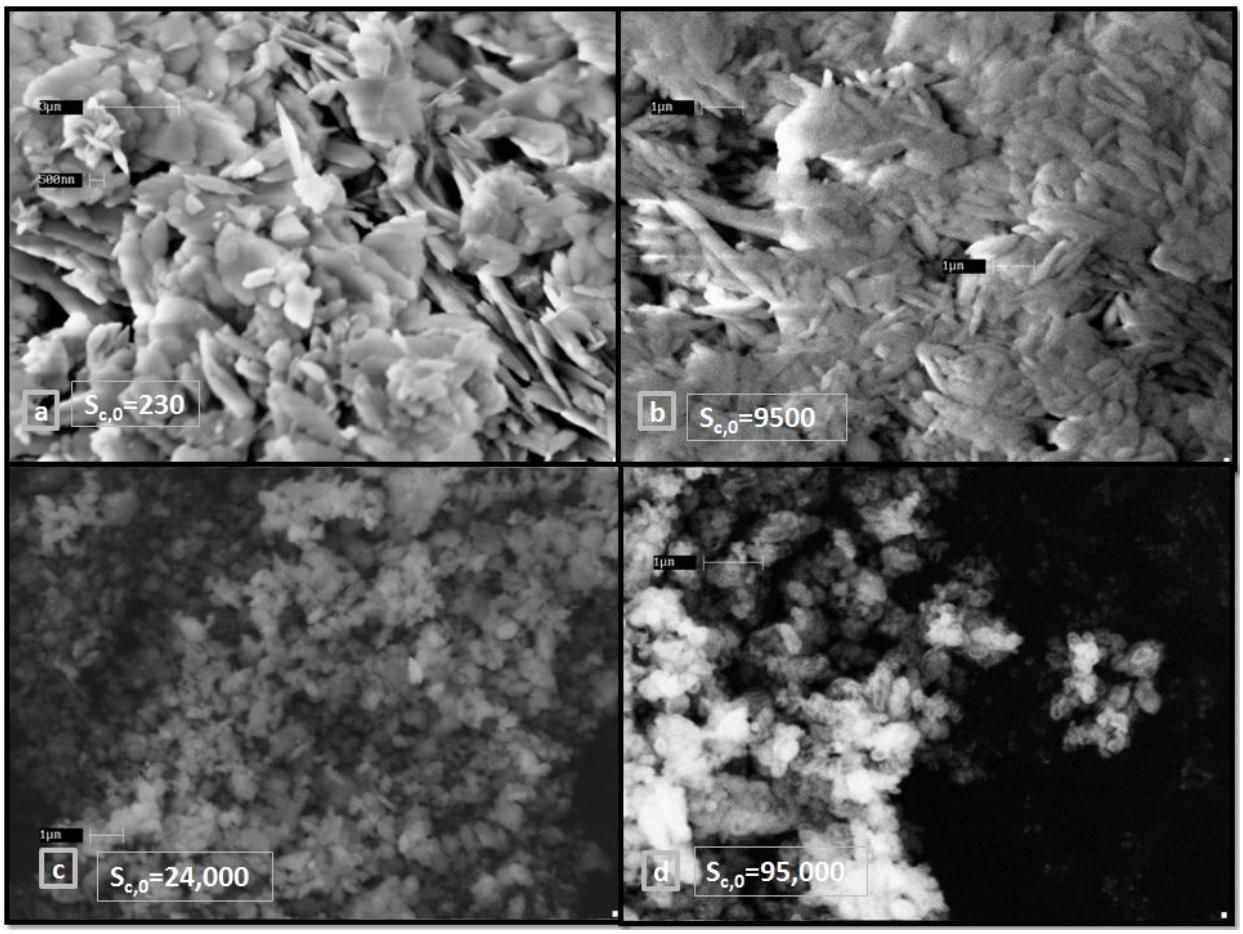

Figure 3.3.3 $BaSO_4$ formed in Taylor-Couette flow at different initial supersaturation ratios a) Re_z =2.4, Ta=1.3Ta_c , b) Re_z =13.5, Ta=1.07Ta_c , c) Re_z ~ 4, Ta~1.2Ta_c , d) Re_z =3.3, Ta= 0.86Ta_c

3.3.2.2 Crystal Internal Structure

Atoms in crystalline solids are arranged in an ordered three-dimensional array, forming a lattice that is described as a unit cell defined by non-coplanar vectors ***a***, ***b***, and ***c*** with inter-edge angles of **α**, **β**, and **γ.** These unit cells form the building blocks that makeup crystallites, which can contain many thousands of unit cells stacked in a three dimensional matrix. As a result, each crystallite contains multiple two dimensional planes lattice planes, each with a distinctive orientation that is defined by miller indices (***hkl***).

The X-ray diffraction (XRD) pattern, as displayed in Figure 3.3.4 (a) revealed the crystalline structure and phase composition of $BaSO_4$ particles. All of the peaks can be indexed as a typical orthorhombic structure of $BaSO_4$ ($\boldsymbol{\alpha} = \boldsymbol{\beta} = \boldsymbol{\gamma} = 90°$), within the range of reported values in the JCPDS Card Files No. 80-0512 (lattice parameters: $\boldsymbol{a}$ = 7.162, $\boldsymbol{b}$ = 8.876 and $\boldsymbol{c}$ = 5.343 Å). No characteristic peaks of other impurities were observed, which indicated that the product had a high purity. The average crystalline size estimated by using the Scherrer formula from the broadening of the XRD are revealed in Figure 3.3.4 (a) according to the (**2 1 0**) plane diffraction peak. A TEM image, shown in Figure 3.3.4 (b) indicates that the ions forming the crystallites possess spheroidal shape with average sizes in the range of 12 ~ 19 nm. The overall shape implies that the superstructure is composed of spheroidal crystallites aligned along the orthorhombic planes.

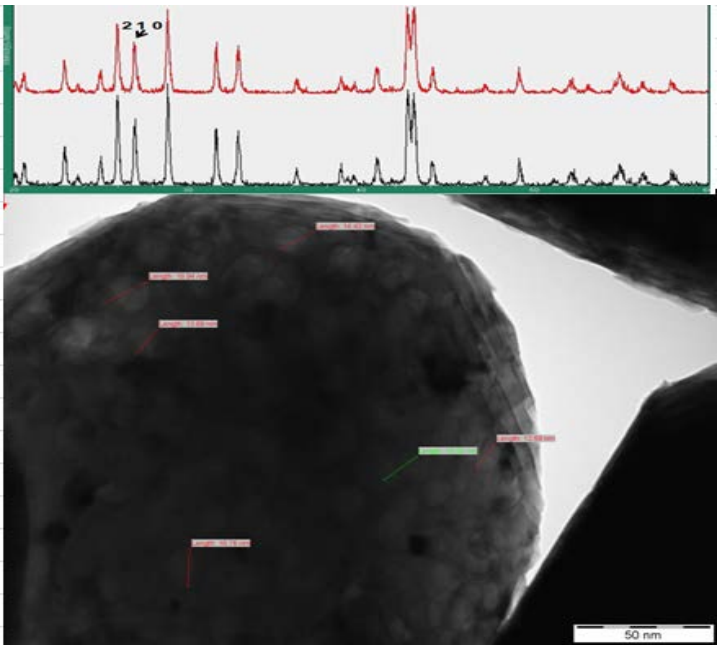

Figure 3.3.4 a) typical XRD diffraction patterns and b) TEM image $BaSO_4$ crystals

At the onset of instability the hydrodynamics of the system allow for the formation of Taylor vortices. The results indicate an influence of the vortex mixing on the $BaSO_4$ crystalline powder. A small change in the unit cell dimensions of the orthorhombic lattice strucutre was observed around the onset of instability, correpsonding to a reduction of 1.82%, 0.62%, 3.24%, in the dimesnions *a,b,c*, respectively in the case of Re_z = 42, and 1.11%, 0.65%, 1.79%, in the dimesnions *a,b,c*, respectively in the case of Re_z = 3.3, as displayed in Figure 3.3.5 (a).

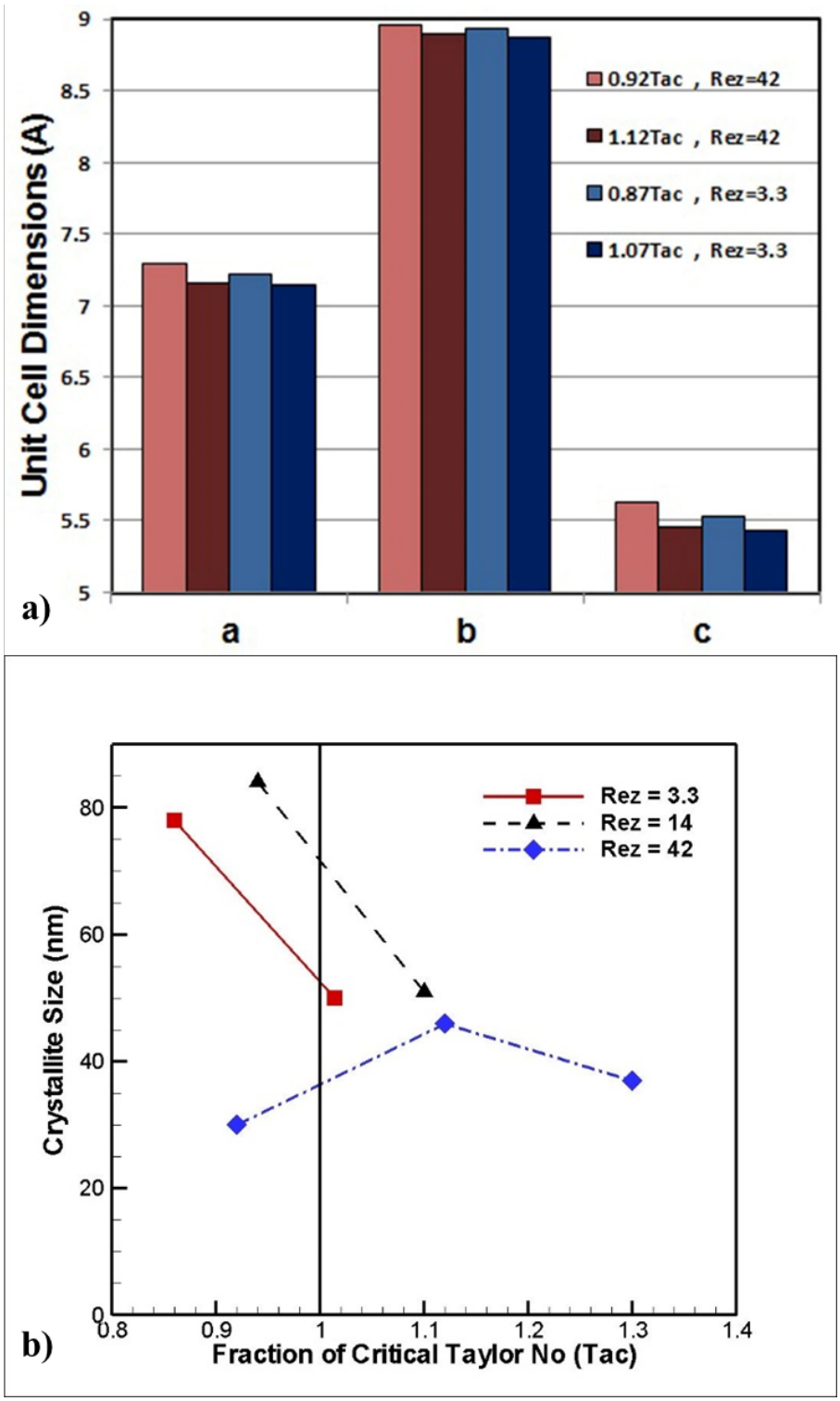

Figure 3.3.5 a) Reduction in Unit Cell Dimensions due to the onset of instability observed for Re_z=3.3 and Re_z = 42. b) Crystallite size broadening in plane (2 1 0)

Figure 3.3.5 shows results obtained via X-ray diffraction, which characterizes the average bulk structure of crystalline material. As seen in Figure 3.3.5 (b), before the onset of Taylor vortex flow, higher flowrate (Re_z = 42) produced much smaller crystallites (30nm) than flowrates Re_z =3.3 and 14, which produced crystallites of similar sizes: 79nm and 85nm respectively. This means that greater axial dispersion (caused by increasing axial flow) before the instability results in shorter macromixing times allowing for the control of the extent of nuclei growth. At the onset of instability, all flowrates resulted in crystalline sizes that ranged between 40-50 nm reflecting the limited effect of macromixing in the presence of Taylor vortex micromixing. Such small variation also suggests that Taylor vortices provide mixing conditions that allow us to accommodate a range of residence time, while still producing similar crystallite sizes. In particular, asubstantial reduction in crystallite size broadening (plane 2 1 0) was observed from 79nm to 50nm, and 85nm to 51nm for Re_z=3.3 and 14, respectively.Specifically, the reduction at Re_z =3.3 complements the decrease in lattice parameters of individual unit cells within the crystallite (observed in Figure 3.3.5-a). However, at Re_z=42 crystallites grew larger at the onset of instability (from 30nm to 46nm) while the unit cell lattice parameters still decreased, indicating that the number of unit cells that makeup the crystallites has increased. This difference is likely due to flow entry effectsnear the local region of inlets, which becomes increasingly signficant with higher flowrates. This explains the reduction in crystallite size from 46nm to 37nm when Taylor number is increased from $1.12Ta_c$ to $1.3Ta_c$, respectively, as entry effects are dampened with higher inner cylinder rotation.

3.3.2.3 Crystal Microstructure

The size of particles, defined by the harmonic intensity averaged particle diameter, was observed to grow larger across the instability resulting in trends that are inversely proportional

to the observed crystallite reduction. Figure 7a presents a typical particle size (secondary grain), which may consist of one or more crystals ("primary grains"). The different crystals may be separated by large angle boundaries, and amorphous or crystalline interfaces. These observed particle microstructures are a result of an aggregative growth mechanism, where particles are formed by the aggregation of small building blocks rather than by the commonly accepted molecular growth mechanism. This is more true in this case, since the diffusion coefficient of $BaSO_4$ in 35%wt glycerol (30%vol) is 0.19 $x10^{-5}$ cm^2/sec, which is much lower than $BaSO_4$ diffusion in water is (0.5 $x10^{-5}$ cm^2/sec).

Comparing Figure 3.3.6 (a) with Figure 3.3.5 (b), reveals the contrasting response of crystallite and particle formation to the change of flow hydrodynamics (including probable influence of entry effects), from which it is found that secondary aggregation of crystals made of smaller primary crystallites is more likely to take place than for larger ones. Overall, the generation of smaller crystallites is more likely to facilitate the formation of secondary random aggregates, which combine arbitrarily without any preferential direction of growth. This has been suggested by Judat and Kind who confirmed that secondary processes which can further alter product properties occur more quickly when crystallites are of smaller size, to the extent of competing with primary processes, such as nucleation, crystallite growth and self-assembled aggregation of crystals [84]. Additionally, high supersaturation enhances the availability of crystallites remaining in the submicron range and therefore increases the probability of crystallite-colloidal interactions [99].

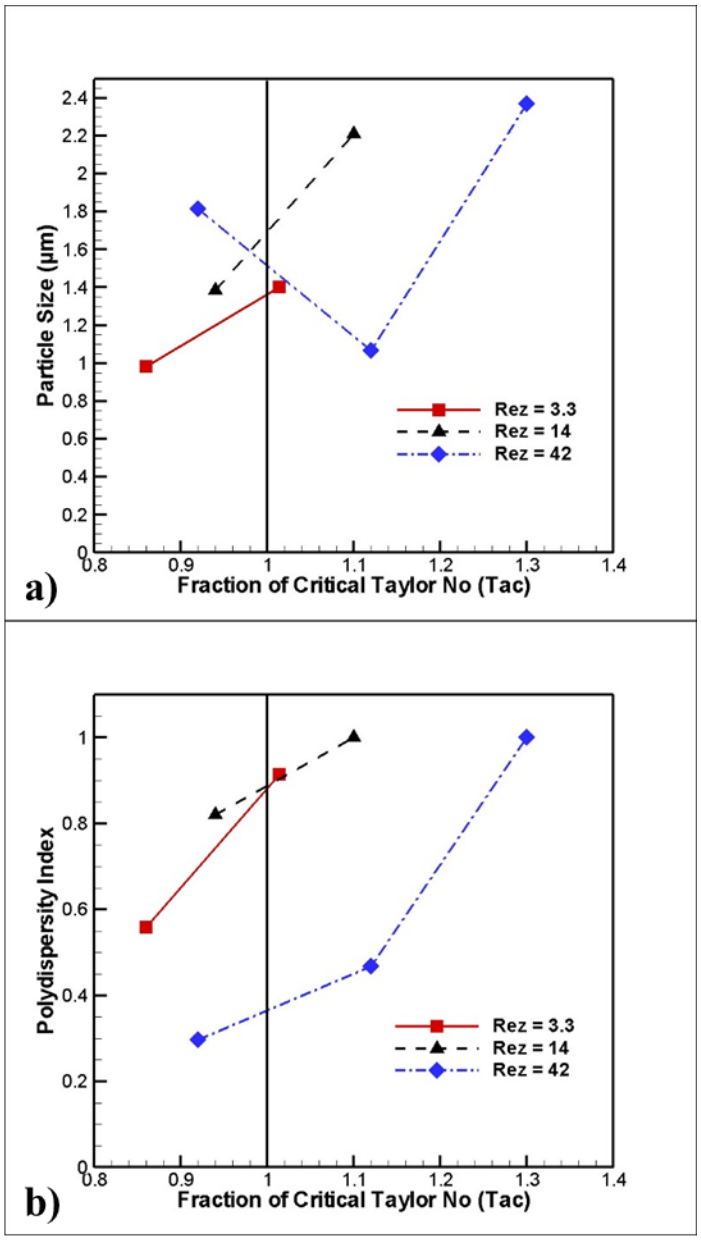

Figure 3.3.6 a) Particle size (secondary grain), and b) polydispersity index of $BaSO_4$ crystals

Figure 3.3.6 (b) shows that the increase in particle size is accompanied by an increase in the polydispersity index (PDI), which is a measure of the width of dispersion, and an indicator of the extent of crystallite aggregation. The increase in PDI across the instability reflects the role of vortex mixing in creating broader dispersions. In general, smaller crystallite size results in

higher number of smaller crystals. Consequently, crystallite-crystallite collisions will be larger in number. With the onset of instability, shear-induced crystallite-crystallite collisions contribute to a larger degree of secondary aggregation in Taylor Vortex flow. The increase in polycrystallinity suggests that these secondary particles are of colloidal nature [84], aggregating arbitrarily leading to grain boundaries that are visible by TEM, as in Figure 3.3.8 (d).

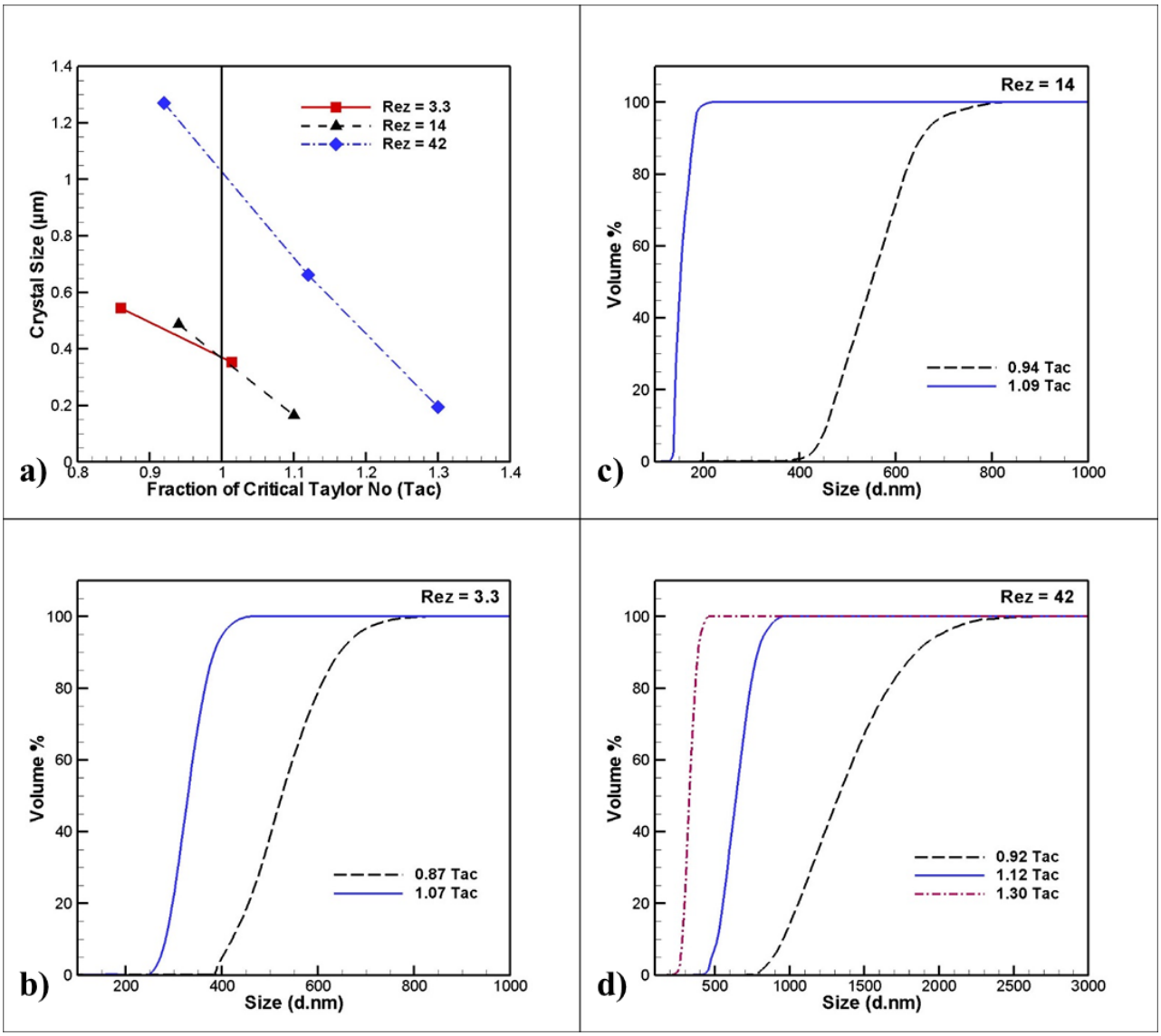

Figure 3.3.7 a) Crystal size (primary grain) for $BaSO_4$ powders, b), c) and d) Crystal Size Distribution (CSD) by volume fraction (%) for Re_z = 3.3, Re_z = 14 and Re_z = 42, respectively.

Self-assembled aggregation of crystallites results in the formation of crystals (primary grains). Crystal size was observed to be smaller at shorter residence time of 12 seconds (Re_z=14) relative to 48 seconds (Re_z=3.3), as depicted in Figure 3.3.7(a). However, for a much shorter residence time (~3.8 seconds, at Re_z=42) the crystal size increased. It is possible that there exists a minimum residence time needed for a finite self-assembly of crystallites. Specifically, a threshold axial flow is needed for the formation of smallest crystals without compromising the contribution of macromixing due to Taylor vortices. In all flowrates, a significant reduction in crystal size was observed at the onset of primary instability. The furthur decrease in crystal is observed for higher Taylor numbers can be explained by the increase in azimuthal micromixing rate resulting into higher local super-saturations, due to higher micromixing. As observed by Judat *et al.*, the crystal size was found to decrease when increasing the cylinder rotational speed (Taylor number) at the same axial flow rate when operating in regions beyond Taylor vortex flow [90].

Under all flow rates, the crystal size distribution was found to be much broader in the case of laminar flow when compared to the narrow range observed for Taylor-vortex flow. Comparing Figure 3.3.7 (b) and (c) shows that an increase in axial flow from Re_z =3.3 to Re_z =14 was observed to result in size distributions between 250-500 nm and 50-200nm, respectively. The size distribution at much higher flowrates (Re_z =42) was less narrow for 1.12Ta_c but decreased to similar levels to Re_z =3.3 at 1.3Ta_c. However, the crystal size distribution is definitely much narrower at 1.12Ta_c (500 – 1000nm) relative to the distribution found for flow before the onset of instability (750 – 2750nm). Trends in both average crystal size and crystal size distribution suggest the existence of a threshold axial flowrate with which a minimum crystal size is achieved at the onset of instability.

3.3.2.4 **Crystal Morphology**

SEM images in Figure 3.3.8 show a morphology of barium sulfate crystals that is consisted with the crystallite, crystal and particle sizes observed. The change in morphology at the onset of instability in Re_z=3.3 shows resulted in smaller crystals with larger particle size and greater polydispersity. TEM images confirm the reduction in crystallite and crystal size, but also confirm a clear increase in particle size and more polydispersed secondary grains. Similar observations are revealed in Figure 3.3.9, which compare $BaSO_4$ morphology before and after the onset of instability for Re_z = 14 .

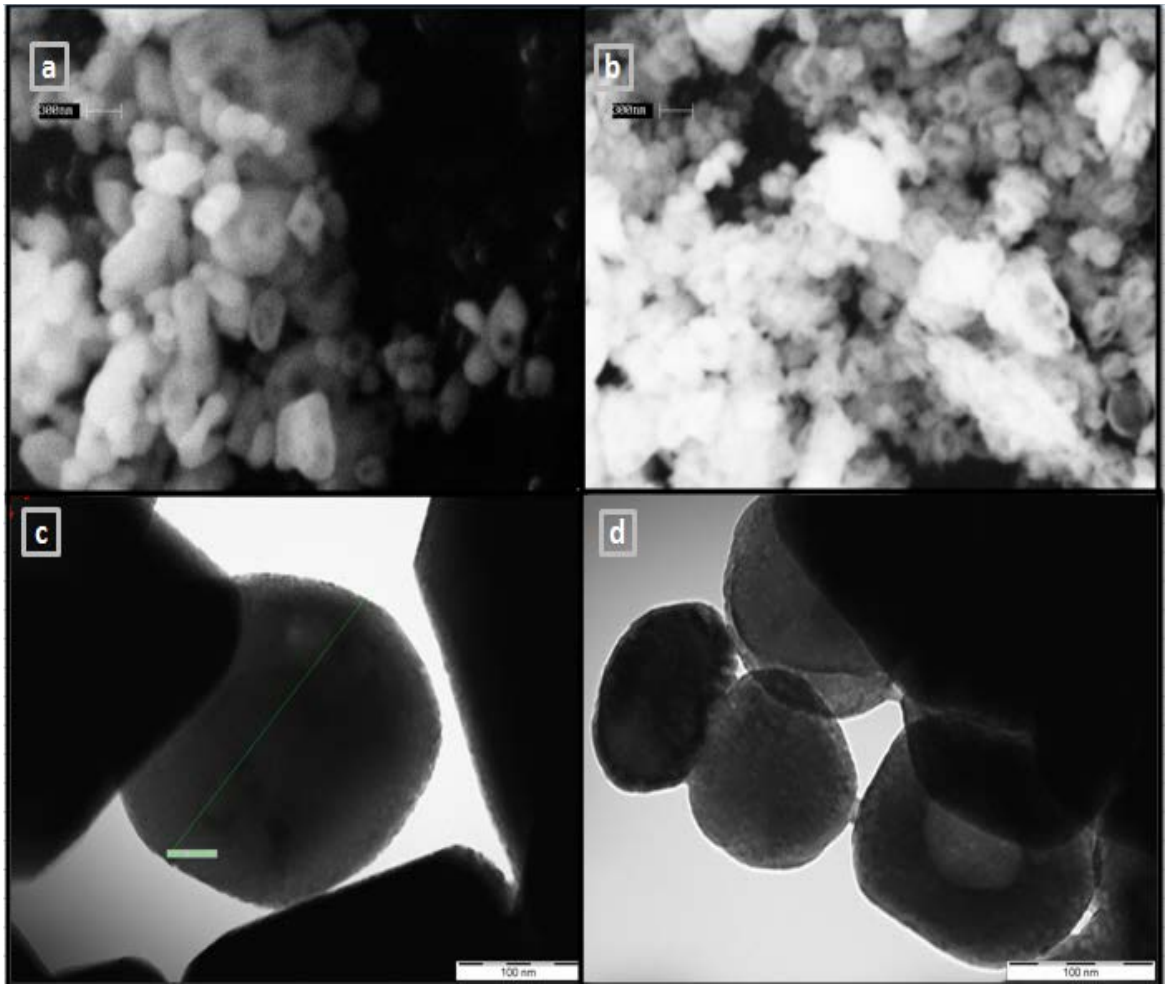

Figure 3.3.8 $BaSO_4$at Re_z = 3.3. SEM (300nm scale): (a) Ta = 0.92Ta_c, (b) Ta = 1.12Ta_c. TEM (100 nm scale): (c) Ta = 0.92Ta_c, (d) Ta = 1.12Ta_c

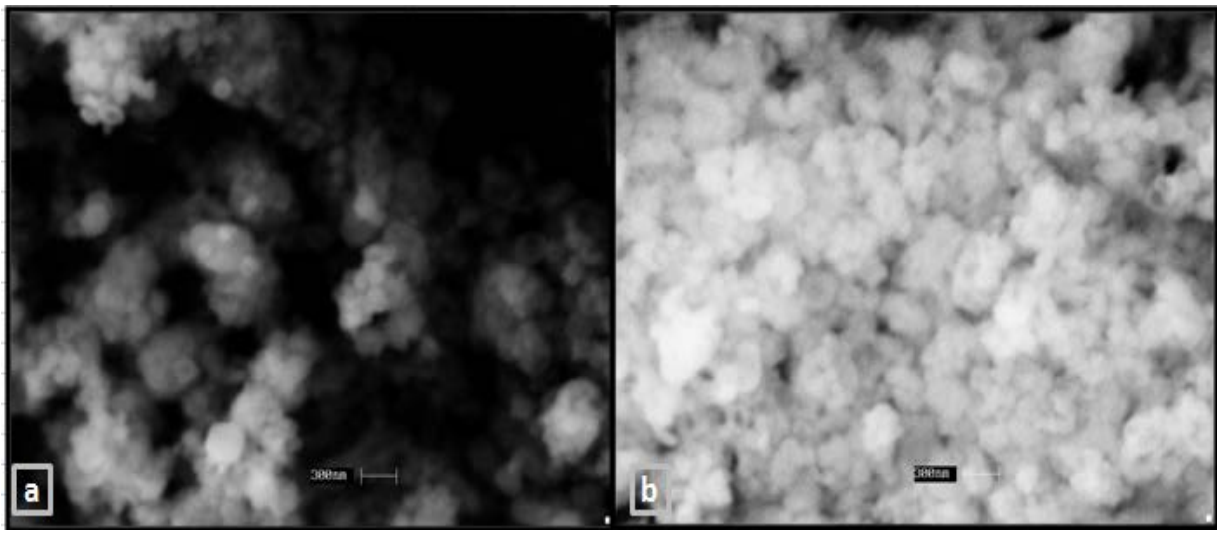

Figure 3.3.9 $BaSO_4$at Re_z = 14. SEM (300nm scale): (a) Ta = $0.92Ta_c$, (b) Ta = $1.12Ta_c$

3.3.3 Particle Trajectory Analysis

The experiments of TC crystallizer found that the process of precipitation of barium sulfate is significantly influenced by hydrodynamic conditions, where crystals in the laminar-flow state (before the onset of instability) are bigger in size than those with vortex flow. These observations can be explained by inspecting the residence time and/or the contour length of crystals during their travel in the TC crystallizer. However, unlike the complicated work presented by Marchisio *et al.*[15], we propose a simple analysis to achieve the goal without considering the detailed dynamics on the molecular level (ex. reaction kinetics and the migration of particles). Despite of losing certain accuracy, we will show that this approach is able to, at least qualitatively, elucidate the causality of the distribution of crystal size and the transition of flow structure, merely through the information borrowing from stability analysis.

In the laminar flow state, a particle initially at the near-wall region will keep flowing near the wall, especially if the particle is too small to consider its migration. Due to the non-slip

condition, the axial velocity of the near-wall particle is smaller than that of the middle particles. Accordingly, the near-wall particles will remain in the crystallizer for a much longer time than the middle ones, and thus will have a bigger size as they exit the chamber. The residence time was estimated to plot the particle trajectory (see Figure 3.3.10).

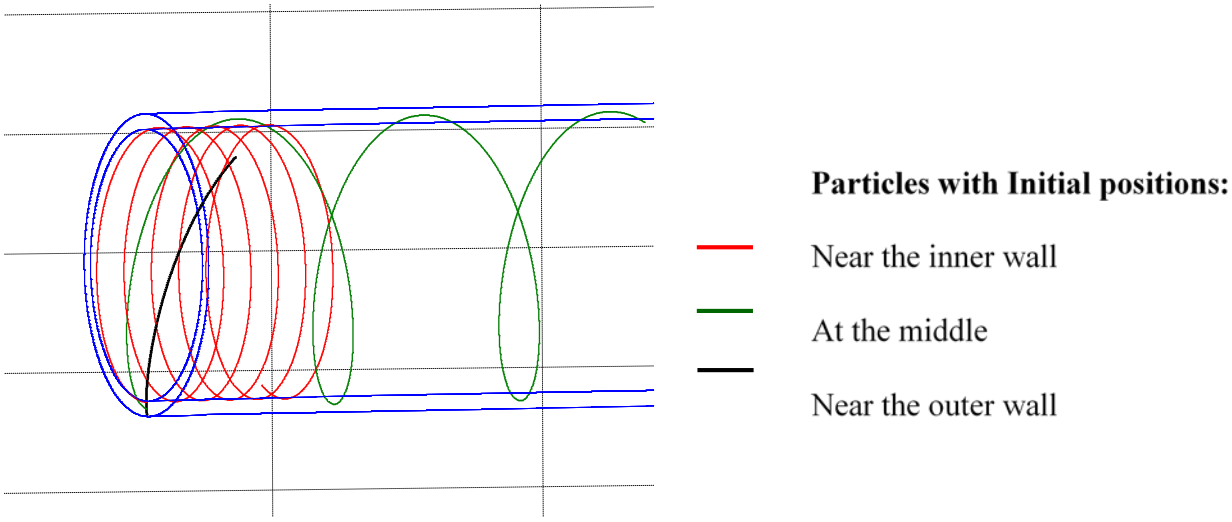

Figure 3.3.10 . Particle trajectory for three different initial positions at the laminar-flow state near the onset of instability (Re_z= 10, Ta = 1970.74< Ta_c, η= 0.9). The red curve has the longest contour length and the black one has the shortest contour length, while the green curve has the shortest residence time

The curves describe the particle trajectories for three different initial positions during the same elapse time. As we can see, the middle particle (following the green curve) run farther away from the inlet than the other ones, and thus has a smallest residence time, even though its contour length is not shortest. Accordingly, we can expect that the distribution of crystal size will be broader and non-homogenous due to large diversity of residence times.

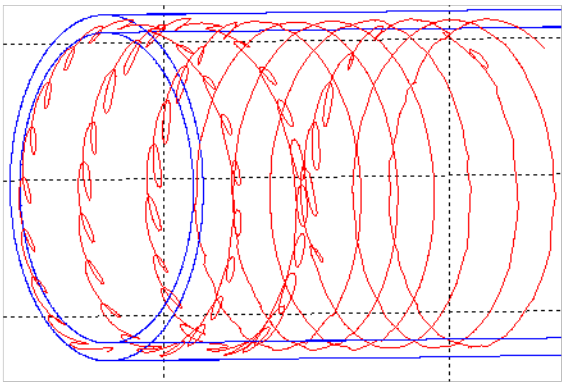

1. At the middle of gap:

$(r_0, \theta_0, z_0) = (0.024, \pi/2, 0.0)$.

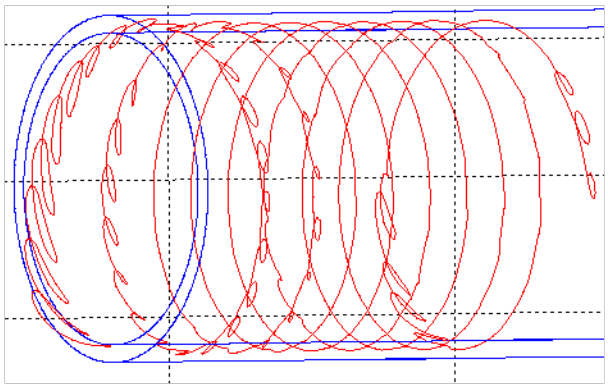

2. Near the inner cylinder:

$(r_0, \theta_0, z_0) = (0.02255, \pi/2, 0.0)$

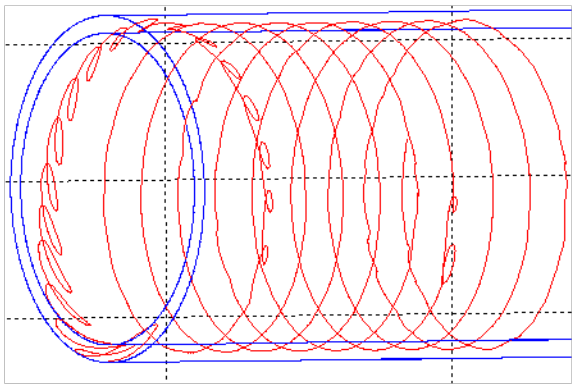

3. Near the outer cylinder:

$(r_0, \theta_0, z_0) = (0.02513, \pi/2, 0.0)$.

Figure 3.3.11 The trajectory of fluid particle for three different initial positions at the onset of instability. The existence of vortex structure enhances the momentum transport and averages out the contour length of particles. Simulation conditions: $r_1 = 0.02275\,\text{m}$, $r_2 = 0.02533\,\text{m}$, $Q = 90.65\,\text{ml/min}$, $\rho = 1000$, $\nu = 10^{-6}$, and $\varepsilon_s = 1000$

In the case of Taylor vortex flow, the cellular vortices come to interplay after the onset of instability. Figure 3.3.11 presents the case of unsteady flow with zero azimuthal wavenumber (m_c = 0), where the Taylor number is just slightly above the critical value (Ta_c). Clearly, the contour length and the axial traveling distances away from the inlet for the three initial positions

are now very close, indicating similar residence times for all particles. This happens in Taylor vortex flow because particles initially in the outer-wall boundary layer will be subject to cellular vortices, bringing them away from the viscous boundary layer towards the middle region (where the axial flow velocity is higher), providing larger axial momentum. Therefore, we can expect that the CSD will be more uniform and narrow than the laminar flow case, in which the contour lengths for different initial positions are different, and all of them are much shorter than those in the case of Taylor-vortex flow (see Figure 3.3.12).

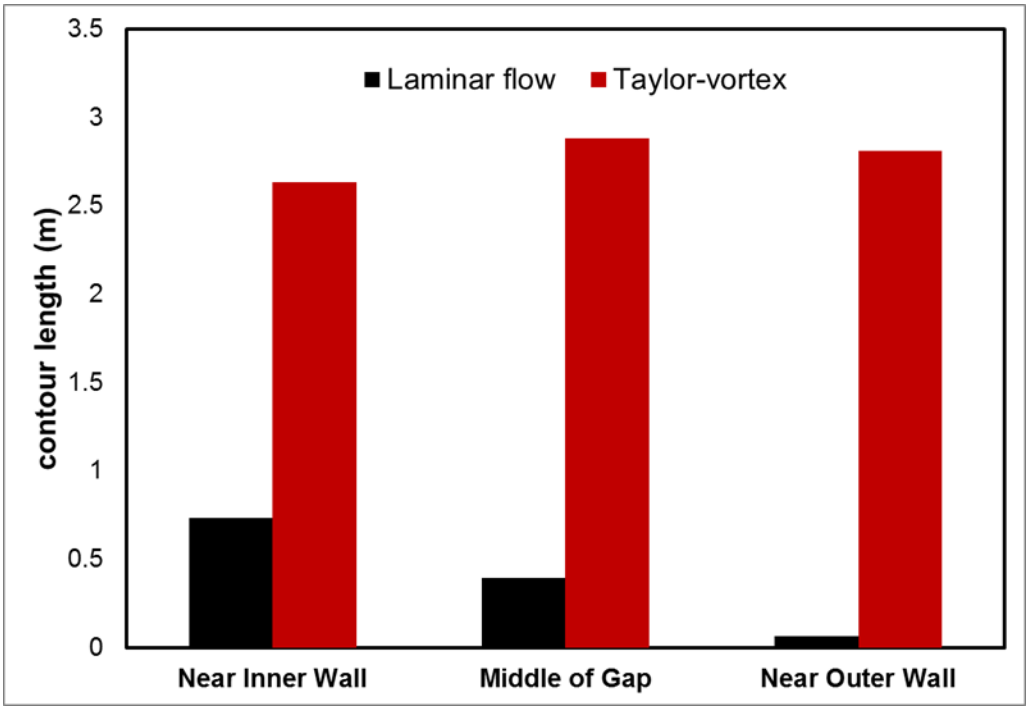

Figure 3.3.12 Comparison of estimated contour lengths before and after the onset of instability (Ta_c) at various positions across the gap

As for higher Taylor numbers or larger the axial Reynolds numbers, the mechanism is basically similar as long as vortices exists there. However, a too high rotational rate or flow rate will lead to a more complicated flow structure, usually with oscillating spiral vortices, as predicted in the linear stability analysis. In this situation, some particles could be arrested by oscillating vortices

and get a longer contour length to grow as bigger crystals. This could have contributed to the increase in crystallite size observed at the high flow rate of Re_z=42.

3.4 Conclusion

The current study on barium sulfate precipitation before and after the onset of instability elucidates the influence of vortex motion on crystal growth and self-assembled aggregation. In general, crystal size decreased with increasing flow rate and decreasing residence time. More importantly, the crystal size distribution was found to be much broader in the case of laminar flow when compared to the narrow range observed for Taylor-vortex flow under all flow rates. Particle trajectory analysis based on linear instability results was used to calculate the contour length of particles traveling in the TC crystallizer. The predicted difference in particle residence time/contour length before and after instability served as confirmation of the observed crystal size trends.

Experiments in this study produced submicron barium sulfate crystals similar to the ones produced in previous studies which operate with very high energy of dissipation, and at much higher rotational speeds. This indicates that Taylor vortex flow regime may serve as the optimum region for crystal growth rather than vortex motion with turbulent flow or secondary instabilities. Such conclusion needs to be validated by future studies that examine the response of crystal size and microstructure and distribution during the onset of secondary instabilities, spanning wavy vortex flow (WVF) all the way to turbulence, passing through a progression of flow regimes, such as modulated wavy vortex flow (MWVF) and turbulent vortex flow.

Properties of precipitated barium sulfate are shaped by the interaction of several steps involved, such as mixing, nucleation, growth, and self-assembled and arbitrary aggregation. Due to the nature of their kinetics, studying each step individually presents a challenge as they don't

necessarily take place sequentially. Rather, some steps could occur simultaneously, resulting in competition between the corresponding sub processes. In this study, it was found that primary steps, such as crystallite growth can be partially paralleled by secondary arbitrary aggregation and ripening, especially when flow hydrodynamics favor growth of smaller crystallites. Taylor Couette flow hydrodynamics had negligible influence on the nucleation step in the performed experiments with barium sulfate due to the instaneous nature of the reaction and the high initial supersaturation used. To examine the influence of Taylor vortex hydrodynamics on the nucleation and growth steps, future experiments on very low supersaturation should be performed, in which the crystal growth is very slow [84]. Working with feed solution of smaller concentrations would also help reduce uncertainties due to viscosity variation. This is due to the change of fluid medium in the TC crystallizer during precipitation. As the amount of precipitated $BaSO_4$ powder increases, colloidal interactions become more significant, leading to an increase of fluid viscosity, possibly reaching that of a non-Newtonian colloidal suspension [99]. In addition, under such low concentration, flow visualization experiments can be performed to study vortex micromixing and structure during precipitation. Specifically, particle velocimetry studies to examine the change in contour length before and after the onset of instability would help in validating the particle trajectory analysis proposed in this paper.

CHAPTER 4

INFLUENCING SURFACE FUNCTIONALIZATION OF ALUMINUM FILLERS WITH 3-METHACRYLOXYPROPYLTRIMETHOXYSILANE THROUGH THE ONSET OF INSTABILITY IN TAYLOR COUETTE FLOW

4.1 Introduction

Surface modification of metal fillers is a common approach to achieve a desired surface functionality while retaining the mechanical properties of the bulk material. Wet chemistry can be a useful to modify the surface properties of conductive fillers, and it offers an effective means to control the orientation and dispersion of such fillers into a polymer matrix [100]. A wide range of wet-chemistry methods have been employed for the surface modification and the enhancement of the interface between metallic aluminum particles and matrix. Covalent modification techniques are most commonly applied to the self-assembly of organosilanes over particle surface through the reaction with the hydroxyl-terminated surface of the thin oxide layer that protectively encompass metals such as aluminum [101].

In addition to promoting adhesion and composite reinforcement, organosilane coupling agents have demonstrated their ability to promote filler alignment [102]. Organotrialkoxysilane monomers provide organic functional radicals that can be readily co-polymerized. Chemical functionalization of aluminum fillers with organosilanes, such as acrylic monomers, is an effective approach in modifying the fillers' surface chemistry with specific (H_2C=C) functionality, leading to an increase in the affinity of the fillers to polymer matrices. Specifically, surface-treatment of metal fibers with adhesive and sealant materials such as methacryloxypropyltrimethoxysilane (MPS) can greatly enhance the attraction to the bulk

polymers such as poly carbonate (PC) and PMMA due to its strong affinity to the carbonyl or acrylic group.

Silanization of inorganic surfaces with organofunctional alkoxysilanes is typically done in either dry aprotic solvents, both polar [103] [104] [105] and non-polar [106] [107] [108] [109], protic aqueous environment [110] [111] [112] [101] [113] [114] [115] [116] [117] [118], and is occasionally done in pure water [119], [120]. MPS silanization under dry environment is sometimes carried out in polar-aprotic solvents, such as DMF [103], but is most commonly applied via non-polar aprotic solvents such as Toluene, with inert environment and reaction times that vary from 16 hours [109] all the way to 24 hours [106] [107]. Under such conditions, high temperatures that range from 55C to 70C are usually needed to promote condensation, as well as a catalyst, such as maleic anhydride [104] [105] or 2,6-dimethylpyridine [107], and an anti-polymerization radical scavenger agent, such as hydroquinone [109] [108]. Such temperatures have also been used in aqueous environments that include methanol [118], ethylene glycol [121], boiling acetone [104] [105] and water-ethanol [117] mixtures, with reaction times that vary from 2hours [104] [105] to 24hours [118]. MPS silanization under aqueous alcohol environment of either ethanol or propanol has been done under milder conditions that require no heating, and shorter residence time (varying from 3minutes [111] to 90 minutes [110]). An acidic environment of pH~4.5 is maintained to act as both a reaction catalyst, and anti-polymerization radical scavenger [102] [122].

To avoid inconvenient complex processing steps associated with silanization under aprotic environment, the grafting in this study was done by preparing separate mixtures of coupling agent (MPS) and aluminum particle suspensions in the midst of 90% 2-Propanol (IPA), with a pH of 4.5, then mixing the separate solutions within the reaction vessel. Prior to that, the MPS

is first hydrolyzed by the trace quantities of water present in the solution followed by reaction with surface silanols forming covalent bonds with the surface. Water content is minimized to avoid the formation of extensive polysiloxane bonds that can lead to the formation of silsesquioxane structures [101] [123]. In most silanization processes, the functionalization reaction is done under variable mixing environment that utilizes magnetic stirring to induce agitation and increase particle dispersion within the solvent [107] [108] [109] [110]. Though stirring speeds are rarely reported, intense stirring conditions are often desired [124]. However, no studies so far have examined the effect of rate of mixing on the degree of functionalization. Understanding mixing characteristics and influence of flow behavior on mass-transport during such functionalization reaction is critical for the development of polymer-metal hybrid fillers with uniform, reproducible and well-characterized coating layer. Studies examining the reaction kinetics of different silanes coupling on silica via concentrated high temperature silanization, highlighted that different silanes react at substantially different rates depending on their functional groups, and that, as such, control of the mixing process of silica/silane, which remains challenging, could have huge impact on improving the declustering of silica particles and hydrophobation of silica surface during the mixing process [125].

Taylor-Couette reactors (TCR) offer a well-characterized mixing environment that can be conveniently operated in a continuous-flow fashion with high-throughput [93], [94]. As a model reactor system where flow takes place in the annulus between two concentric cylinders, Taylor-Couette flow (TCF) allows for examining hydrodynamic instabilities while stimulating vortex motion, offering a highly active interface for mass transfer and phase mixing [17]. Although the flow is steady and purely azimuthal for low angular cylindrical velocities, a series of hydrodynamic instabilities emerge during the gradual increase of inertial forces against viscous

forces [13]. Emerging vortices act to increase the surface area of the interface between different and partially unmixed materials, offering a high surface-to-volume ratio [55].

This work is focused on exploring the role of the vortex motion near the onset of the primary instability in fine-tuning the surface functionality of aluminum particles. Monodispersed fine submicron spheres were selected for this study to their well-characterized size and morphology and their potential for nano-composite applications. In particular, we focused on examining the effect of change in flow structure during the onset of primary instability in Taylor Couette (TC) flow, which results in the transition from purely azimuthal laminar flow to the emergence of Taylor vortices, on mass transport by characterizing the coupling efficiency (TGA), degree of coating and functionality (FTIR, XPS), coating morphology (SEM) and change in particle dispersion (DLS) and oxidation behavior (XRD) due to change in surface energy after functionalization (zeta potential). By investigating the coating properties before and after the onset of primary instability in ranges of similar energy consumption. , the influence of shear energy of rotation is decoupled to exclusively manifest the effect of vortex flow structure on the MPS coupling on filler surface [57].

4.2 Materials & Experimental Methods:

4.2.1 Materials

Spherical aluminum powder (APS ≈ 800nm, AL-M-021M-P.800NS) was purchased from American Elements. γ-methacryloxypropyltrimethoxysilane (MPS) was purchased from Momentive under commercial name Silquest A-174®. 2-Propanol (IPA), Glacial Acetic Acid was purchased from Fisher. Deionized water was used throughout the study.

4.2.2 MPS Solution Preparation and Reaction

Acetic Acid was used to adjust pH to 4.5, which is chosen specifically to minimize the rate of condensation among silanol groups of monomeric silane molecules to larger oligomers, promoting to more stable silane solutions [112]. Higher pH values were found to produce weaker bond strengths than those obtained with silane solutions at pH = 4.5 [118]. 90% Isopropanol (IPA) was particularly chosen as a solvent because hydrolysis of MPS occurs more readily in 2-Propanol relative to ethanol [118]. Even in coupling experiments done in the medium of ethanol, 2-propanol was used to improve the solubility of the homocondensates [126]. Previous studies that involved the preparation of stable dispersions of nano-sized silica modified by MPS demonstrated the ability to control the degree of grafting of MPS on silica in 2-propanol as needed [127]. Solutions hydrolyzed at different times (up to two hours) were subject to FTIR analysis which indicated no change in the absorption spectrum, confirming that MPS hydrolyzes rapidly in 90% Iso-propanol with pH=4.5. Although traces of water have been reported to be essential for the formation of well-packed monolayers [128], water content was limited to 10vol% to help in hydrolyzing the MPS and avoid the formation of complex networks of poly-siloxane bonds that can lead to the formation of silsesquioxane structures [101].

A low silane concentration of 1.5 wt% was selected because such concentration range is known to produce thin siloxane films (with a thickness of ca. 10–50 nm) enough to promote the resin-to-metal bond [118]. Maintaining silane concentration below 5 vol.% preserves the silane–solvent system keeping the silane monomers in balance while minimizing autopolymerization [111]. Although grafting density increases with higher silane content, lower MPS concentration has been reported to give higher grafting yield [101]. The silane solutions were allowed to hydrolyze for at least 1 hour at room temperature. Such hydrolysis time of the silane/IPA

solution was selected because it was found to result in optimum coupling of MPS on the aluminum flakes. Shorter hydrolysis times were found to result in poorer MPS coupling.

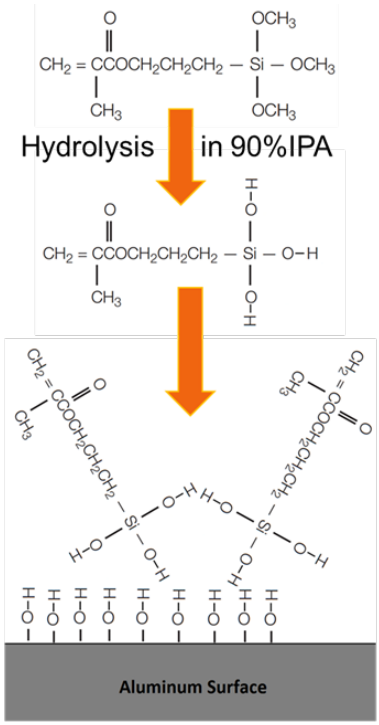

Figure 4.2.1 Functionalization of Aluminum filler with methacryloxypropyltrimethoxysilane (MPS) under pH=4.5.

The methoxy groups react in the acid catalyzed aqueous alcohol solution undergoing hydrolysis resulting in the formation of intermediate silanol groups (–Si–OH). Silanols may condense to form stable condensation products, such as dimeric cross-linked siloxane bonds (–Si –O– Si). Chemically suitable hydroxyl groups are found on the outermost surface of most metal surfaces, which form a thin and passive oxide layer. Once mixed with the filler substrate, the silanol groups will react with the hydroxylated surface of the aluminum fillers initially forming stable hydrogen bonds, which undergo condensation to form stable metallo-siloxane –Si –O– M– covalent bonds at the metal-solvent interface [109].

Once the reaction is terminated, samples are collected in centrifuge tubes, and centrifuged for 30 minutes under 6500 RPM. Bressy et al, indicated that the centrifugation step was able to remove unreacted MPS molecules effective in preventing additional MPS-homocondensed layers from bonding to the functionalized surface [1]. For more certainty, samples are washed once with IPA to remove excess silane and then filtered. Once separated, the functionalized particles are dried at 110C for 1 hour to ensure solvent/water removal and to induce further condensation for the formation of strong covalent bonds across the filler surface. Preliminary experiments in our study exploring the influence of thermal treatment revealed that heating for longer time (6 hours) was observed to slightly compromise the MPS coating layer.

4.2.3 Characterization Methods

Detail FTIR analysis of bonding mechanism during silanization reaction was done through Magna Nicolet FTIR spectrometer with a miracle ATR sampling accessory from Pike Technologies (Madison, WI), operating at $4\ cm^{-1}$ resolution. . The spectral subtraction capability of FTIR spectroscopy enables the selective monitoring of the structure of the coupling agent. External pressure was applied on ATR measurement to ensure good contact of the samples with the diamond ATR crystal. Although the inorganic part of the MPS coupling agent yields relatively strong absorbance, the quantities absorbed on the aluminum surface are very small relative to the aluminum mass. To selectively monitor the structure of the coupling reaction and emphasize the contributions of the silanization reaction, the spectrum of the non-silane treated pristine filler was used as a background spectrum. Sample single beam spectrum was obtained and ratioed against the background single-beam spectrum to yield the absorbance spectra of functionalized samples [129]. The spectra were mathematically processed (including

smoothing, baseline correction), in order to minimize noise, and to make the spectra comparable [112].

Quantitative elemental analysis as well as chemical bonding information were possible through X-ray photoelectron spectroscopy (XPS). CasaXPS software was used for curve fitting and signal interpretation. Surface imaging of particle morphology and aggregation was assessed through Tescan Mira3 Field Emission Scanning Electron Microscopy (FESEM). Energy dispersive X-ray (EDX) spectroscopy enabled elemental color mapping of MPS distribution on aluminum surface. Thermogravimetric analysis was performed on a TA Instruments TGA device, where 2 mg samples were placed on aluminum DSC pans. All data were collected in dynamic mode under flowing nitrogen (60ml/min) from room temperature to 580°C at a rate of 10°C/min.

Specific BET surface area analysis (Gemini VII 2390t, Micrometritics with nitrogen as sorbent) was done to assess the change in surface area after the functionalization of mon-dispersed fillers. The reduction in surface area, was assumed to be proportional to an increase in average particle diameter due to the self-assembly of MPS layers on the aluminum spherical surface. As a result, a hypothetical average MPS thickness could be estimated from the BET surface area analysis.

Hydrodynamic Analysis of the coating uniformity, thickness, degree of aggregation and polydispersity of functionalized aluminum spheres was possible through size measurements performed in the Malvern Zetasizer instrument (measures between 0.6 nm – 10 μm), which works on Dynamic Light Scattering (DLS) principle. Suspended particles (both in toluene and water) were subjected to laser illumination while the resulting intensity fluctuations in the scattered light due to brownian moion are related to the size. The same DLS approach was used

to measure the zeta potential of alluminum filler dispersions in water with the pH varied using 1M HCl and 1M NaOH, as done in earlier studies [102].

The enhanced miscibility of functionalized aluminum spherical fillers was assessed using Toluene as hydrophobic non-polar media, and water as polar media [109]. To determine the effectiveness of the MPS monomer coatings on the stability of spherical fillers in Toluene, 0.03g of each sample was dispersed in 10ml of Toluene in a glass vial. The mixtures were then transferred to an ultrasonic bath for 1 min to suspend the particles. Upon suspension, the vials were placed next to teach other to compare suspension stability through careful observation and image collection at different times.

Additionally, a high-temperature water oxidation test was performed, where 0.1g of functionalized aluminum powder was mixed in 10ml of water and subject to heating at 70°C for 90 minutes. Similarly, room-temperature oxidation of 0.03g of pristine and functionalized aluminum particles under 10ml of water was allowed to progress for 14days. In addition to careful observation, the rate of oxidation of aluminum fillers in water was assessed by utilizing using a Scintag Theta-Theta X-ray Diffractometer (XRD) (Cu K_ radiation, λ = 1.5418A°).

4.2.4 Taylor Couette Reactor Setup

The experimental setup of the TCR, illustrated in Figure 4.2.2, consisted of two coaxial cylinders, with the aluminum inner cylinder rotating while the Plexiglas outer cylinder is fixed. The inner cylinder rotation rate is controlled by a phase inverter, connected to a motor drive that provides rotation rates in the range of 30-1750 RPM.

Table 4.2.1 includes the physical specifications of the TC crystallizer used in the current study. The primary hydrodynamic instability marks the transition from laminar Taylor Couette Flow (TCF) to Taylor Vortex Flow (TVF), as determined by the critical Taylor number (Ta_c).

As specified by the Taylor number (Ta), the onset of Taylor vortex flow (TVF) by centrifugal instability depends on reactor geometry and fluid properties, including gap width and radii of inner and outer cylinders. From detailed flow visualization and stability analysis in this reactor configuration [57], we have determined the onset of the primary instability takes place almost instantaneously and reproducibly, since the radius ratio of the reactor is>0.71 and the length to gap ratio is above 35 [130].

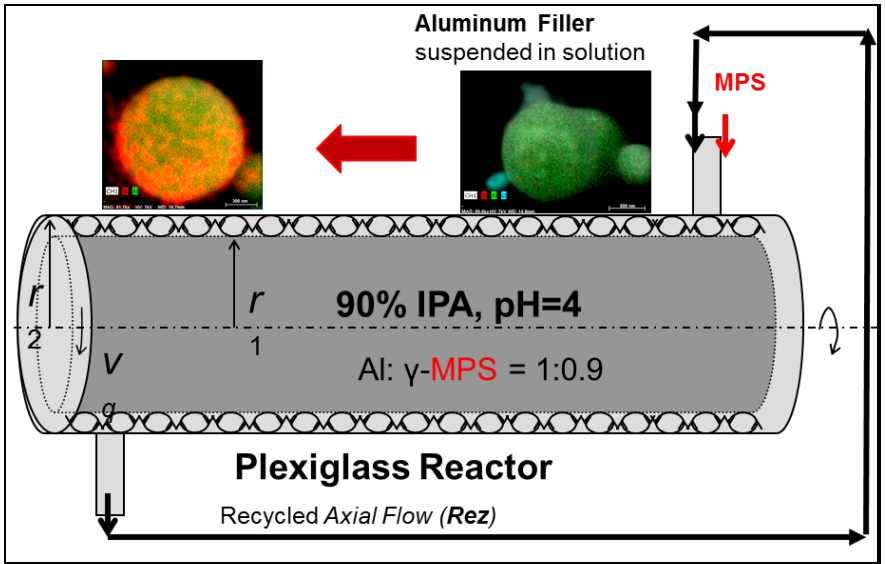

r_1 (cm)	r_2 (cm)	$d\,(r_2\text{-}r_1)$ (cm)	L_r (cm)	d/r_1	r_1/r_2	L_r/d
2.28	2.53	0.258	15	0.11	0.90	58

Figure 4.2.2 Schematic of functionalization of Aluminum in Taylor Couette reactor

Table 4.2.1 Functionalization conditions and corresponding hydrodynamic parameters.

Al (g)	**MPS (g)**	**Solvent Volume (ml)**	**Viscosity ($10^6 m^2/s$)**	**RPM range**	**Ta/Ta_c**	**Flow Rate (ml/s)**	**Re_z**	**Residence Time**
2.5	**2.2**	**150**	**3.06**	**60 to 92**	**0.85 , 1.15**	**0 , 3.5 ,14**	**0 , 8 , 32**	**1minute, 15minutes**

4.2.5 Experimental Methodology

1.7wt% MPS solutions of 90% IPA solution with pH=4.5 (1.25 vol% MPS), was mixed and hydrolyzed for 1 hour under room temperature. Directly following the addition of the MPS solution to the Plexiglas TC reactor, 2.5g of aluminum sub-micron spheres were added to the reactor, resulting in a 1.9wt% aluminum suspension, with an MPS:Al weight ratio of 0.88. The mixtures were recycled under variable axial flow rates: $Re_z = 0$, $Re_z = 8$ and $Re_z = 32$ with short and long residence time: 1 and 15 minutes, while the rotational speeds were designed to allow for the silanization under laminar flow ($Ta < Ta_c = 0.85\ Ta_c$) and Taylor vortex flow ($Ta > Ta_c = 1.15\ Ta_c$) at each flow rate and residence time. The flow-structures were determined from separate experiments [57], but utilizing the Plexiglas reactor for these experiments offered a confirmation of the flow structure during the reaction. A demonstrative visualization of the flow structure can be seen in Figure 4.2.3. The 12 samples were then analyzed with XPS, FTIR, TGA, DLS, BET, SEM and XRD.

Figure 4.2.3 Flow visualization imaging of aluminum functionalization in laminar Taylor Couette flow (0.85 Ta_c) and Taylor vortex flow (1.15Ta_c) in batch mode (Re_z =0).

4.3 Results

4.3.1 XPS Surface Analysis

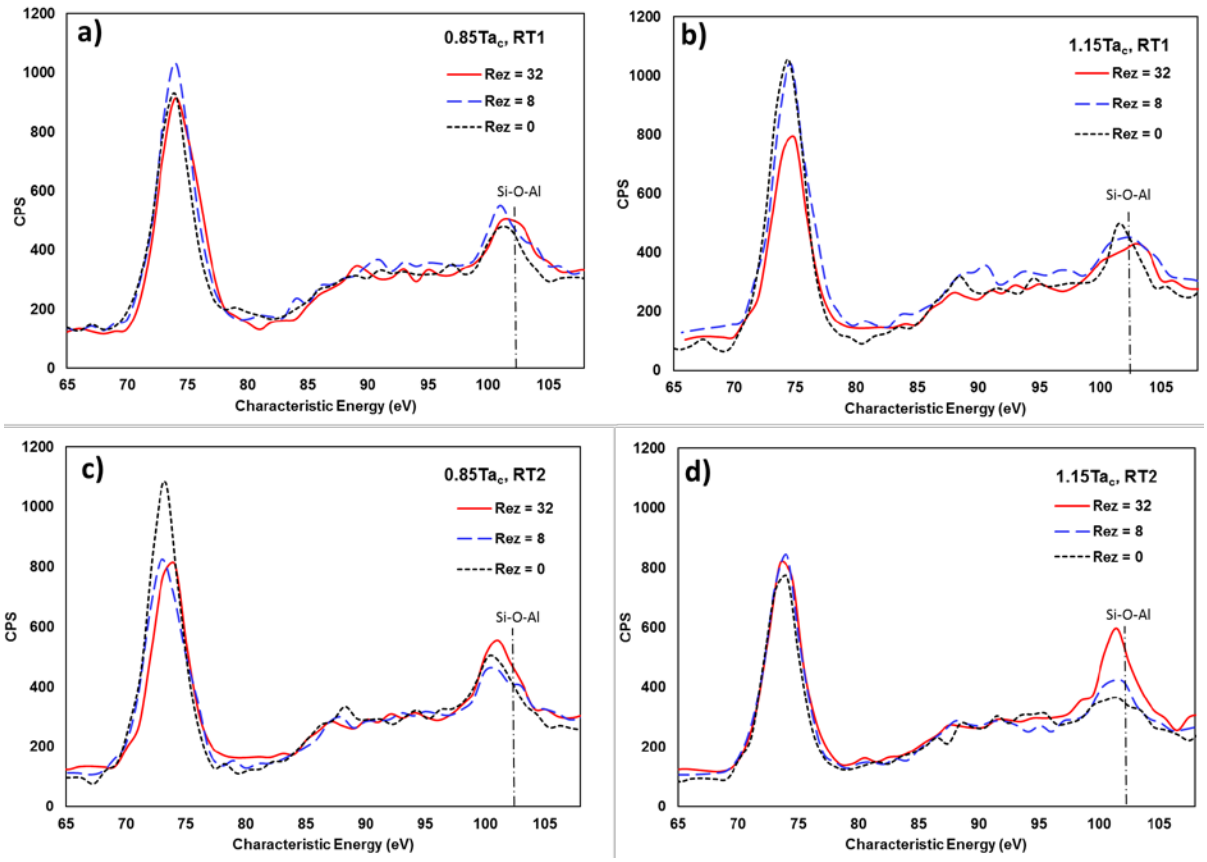

Figure 4.3.1 XPS peaks for Aluminum (70eV) and Si (95eV) for short residence time at 0.85 Ta_c (a) and 1.15 Ta_c (b) and long residence time at 0.85 Ta_c (c) and 1.15 Ta_c (d).

The impact of axial flow and onset of instability on the surface composition of functionalized aluminum particles was examined via XPS. The functionalization of the spherical fillers is confirmed by the reduction in the Aluminum binding energy, Al2p (73eV) peak, and a corresponding increase in the peak for silicon, Si2p (99eV) [109]. The reduction in aluminum and increase in Si was quantitatively assessed by Si:Al atomic ratio (Figure 4.3.4), obtained from the XPS surface elemental composition. The influence of increasing axial flow on enhancing MPS surface coverage, indicated by Si2p (99eV), was observed to be more significant under longer residence time, (Figure 4.3.1 c and d). Studies of XPS surface spectroscopy of silane coupling suggested that the center of Si $2p_{3/2}$ ionization in silane compounds ranges between 100.5 and 102.92 eV, depending on the nature of coupling [131]. Increasing the flow resulted in shifting the center of the Si2p binding energy to slightly higher values, especially after the onset of the vortex flow structure (Figure 4.3.1 4 b and d). Such higher binding energies are attributed to more bonding of the MPS monomer to the aluminum surface via the formation of covalent metallo-siloxane bonds (Si–O–Al). J.B. Bajat et al. examined the Si2p on Al substrate functionalized with vinyltriethoxysilane and attributed the peak at 103.5 eV for silicon bonded to aluminum [131]. They also indicated that the shift in aluminum Al2p to higher binding energies corresponds to more covalent bond formation between the silane and the aluminum surface, particularly peaks at 73.3 and 74.1 eV (Al–O–Si) [131]. As observed in Figure 4.3.2, the peaks for carbon C1s exhibited a similar shift in binding energy towards higher values, particularly in the range of 287.1 to 289.5 eV, which is associated with carbonyl carbon (–COO–) in the silane [131].

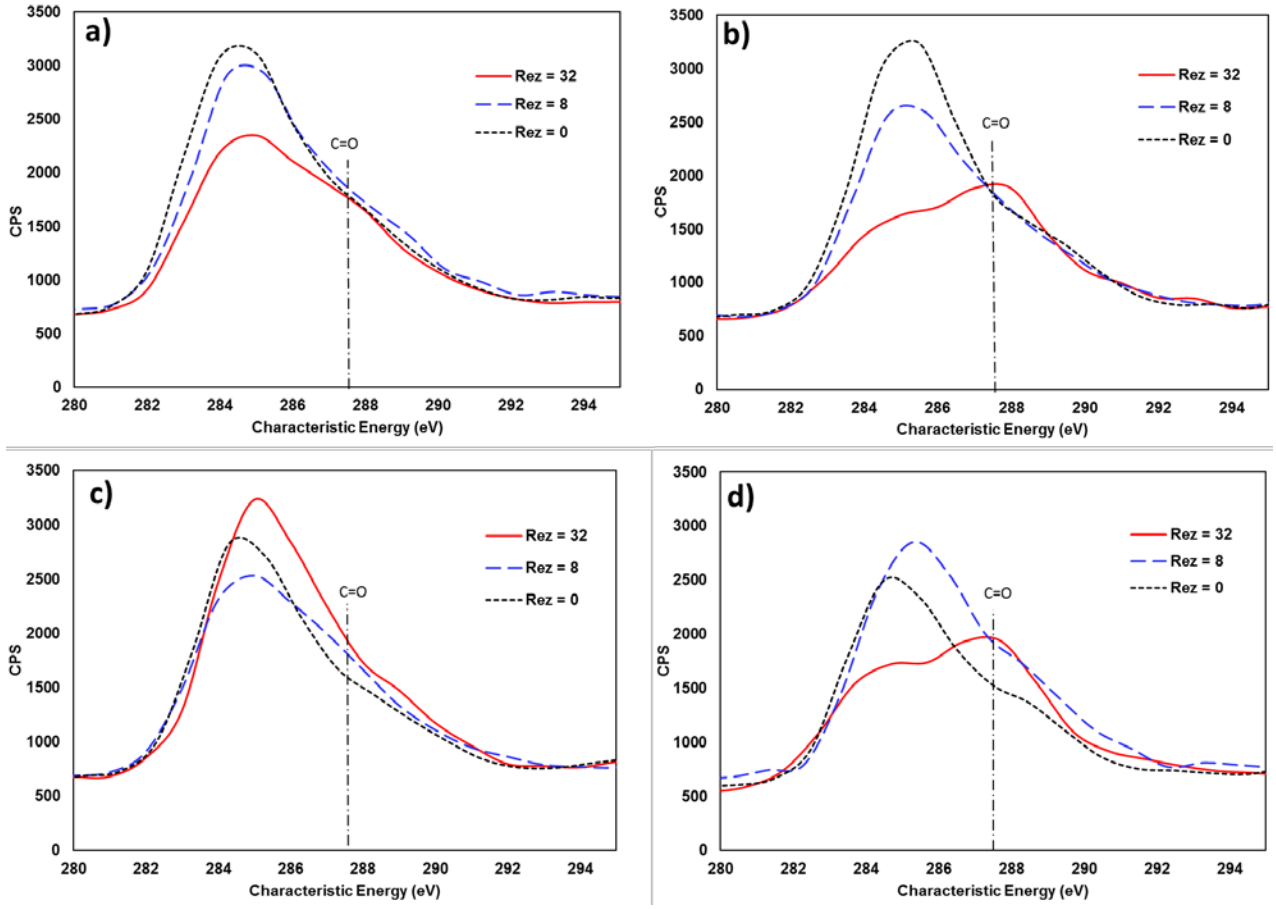

Figure 4.3.2 Analysis of the perseveration of monoacrylic surface functionality via the characterization of the Acryloyl group, where the C=C and C=O bonds are conjugated.

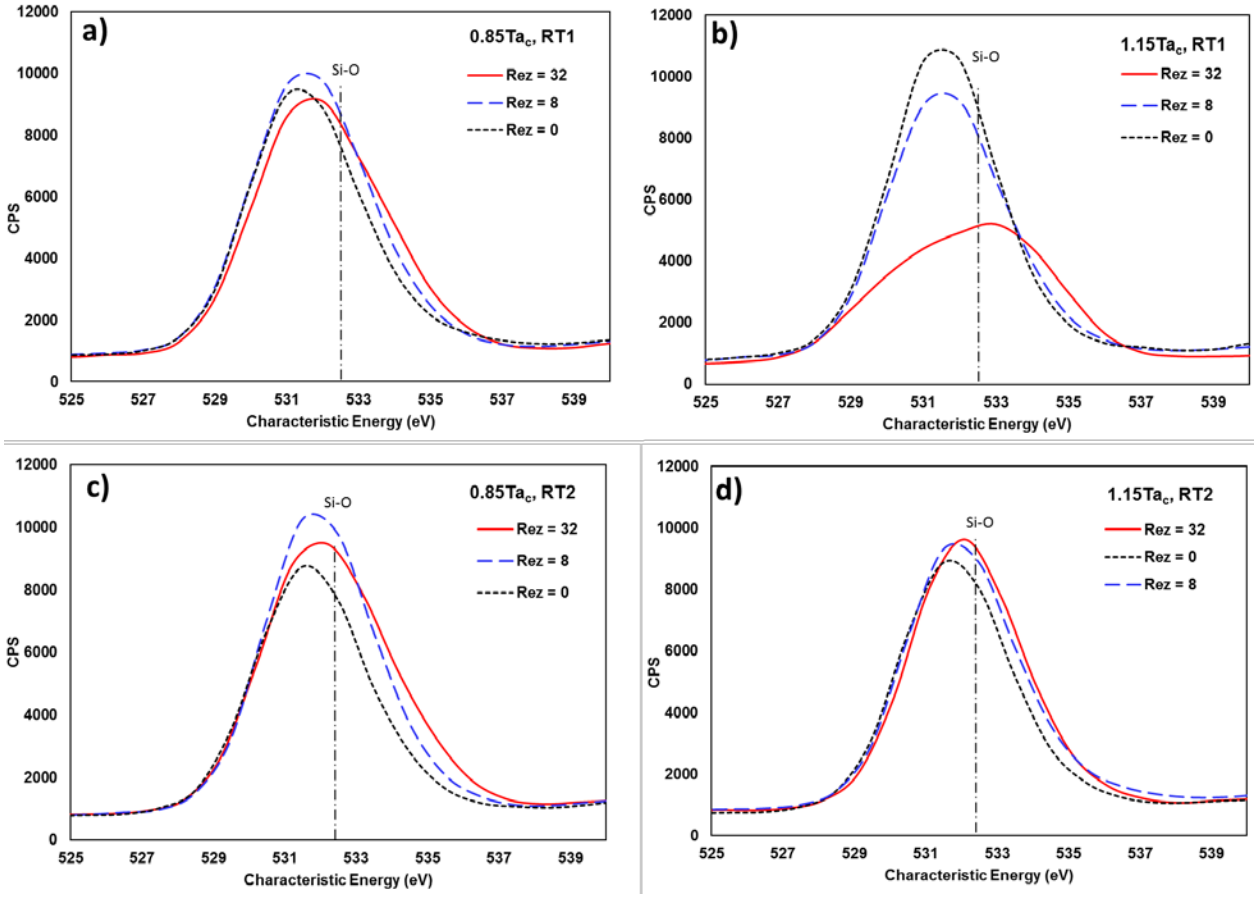

Figure 4.3.3 Analysis of the perseveration of monoacrylic surface functionality via the characterization of O 1s (532 eV), where the O–C=O bond appears at 534.8 eV.

The presence of the covalent metallo-siloxane bond (Si–O–Al) was also confirmed by examining the shape of the O 1s (532 eV) spectra. As can be seen in Figure 4.3.3, with increasing axial flow from Re_z=0 to Re_z=32, O1s showed a gradual shift of the band towards higher binding energies close to 535eV, which is associated with the presence of carboxylic bands [132].

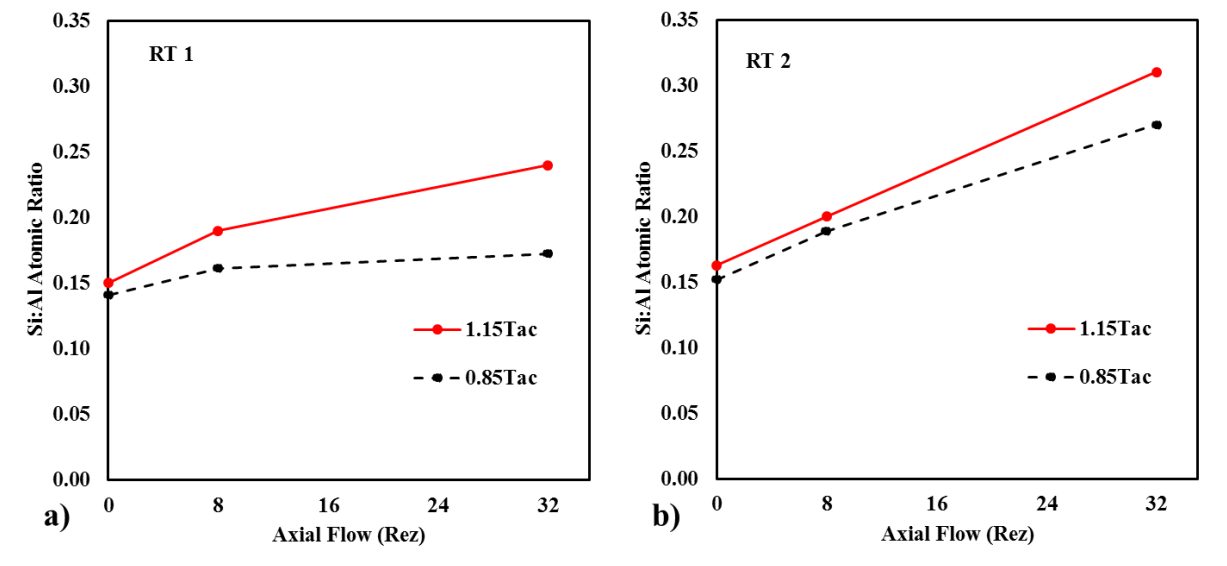

Figure 4.3.4 Si:Al Atomic Ratio obtained from XPS peak integration of short residence time (a) and long residence time (b).

4.3.2 Bond Characterization

From the FTIR analysis, sample single beam spectra were obtained and ratioed against the background single-beam spectrum for pristine aluminum to yield the absorbance spectra of MPS coating layer for samples functionalized under short residence time (1 min) and long residence time (15 mins) displayed in Figure 4.3.5 and Figure 4.3.6, respectively. The functionalized samples exhibited clearly distinctive features associated with MPS coupling, where the MPS monomeric ligands react with the surface hydroxyls present on the amorphous oxide passivated layer on the aluminum fillers, thereby covalently anchoring the monomers to the filler surface. The formation of metallo-siloxane (Al-O-Si) and siloxane networks (Si-O-Si) is confirmed by the broad absorption in the 1200-950 cm^{-1}range. The similar mass of Al and Si atoms allow the vibrational modes to overlap [133]. Previous studies on silane couplings identified bands around 800 to 900 cm^{-1} [134], and 620 to 680 cm^{-1} [120] to metallo-siloxane (Al–O–Si) bonds. Absorption bands in the range of 1400 to 1500 cm^{-1} are attributed to the

CH_2, CH_3 bending while Peaks at 1720 cm^{-1} and 1635 cm^{-1} correspond to scissor vibrations of methacrylate carbonyl and vinyl, respectively. Such peaks confirm the preservation of the desired MPS surface functionality, where the silane chains are standing perpendicular to the aluminum surface and only bounded by the silane head, forming an extended configuration [135].

Table 4.3.1 Absorption region and bond type found in MPS coating layer

Wavelength (cm^{-1})	**Bond type**
615-630	**metallo-siloxane (Al–O–Si) bonds**
680-690	
995-1025	**metallo-siloxane (Al-O-Si) and siloxane networks (Si-O-Si)**
1100-1120	
1455-1475	**CH2, CH3 bending**
1620-1660	**methacrylate vinyl**
1705-1725	**methacrylate carbonyl**

Overall, the key peaks associated with MPS coupling were found to be more strongly pronounced for spectra associated with samples functionalized under the emergence of Taylor vortex flow (1.15 Ta_c). This is most clear when it comes to examining spectra for samples functionalized under batch configuration of Re_z=0 , as displayed in Figure 4.3.5 (a) and Figure 4.3.6 (a), in which axisymmetric toroidal vortex flow (1.15 Ta_c) provides significantly sharper bands than laminar flow (0.85 Ta_c). The increase in axial flow towards Re_z=32 was distinctly advantageous to enhancing MPS coupling, as it reflected the most prominent peaks for both short and long residence times (Figure 4.3.5-c and Figure 4.3.6 -c).

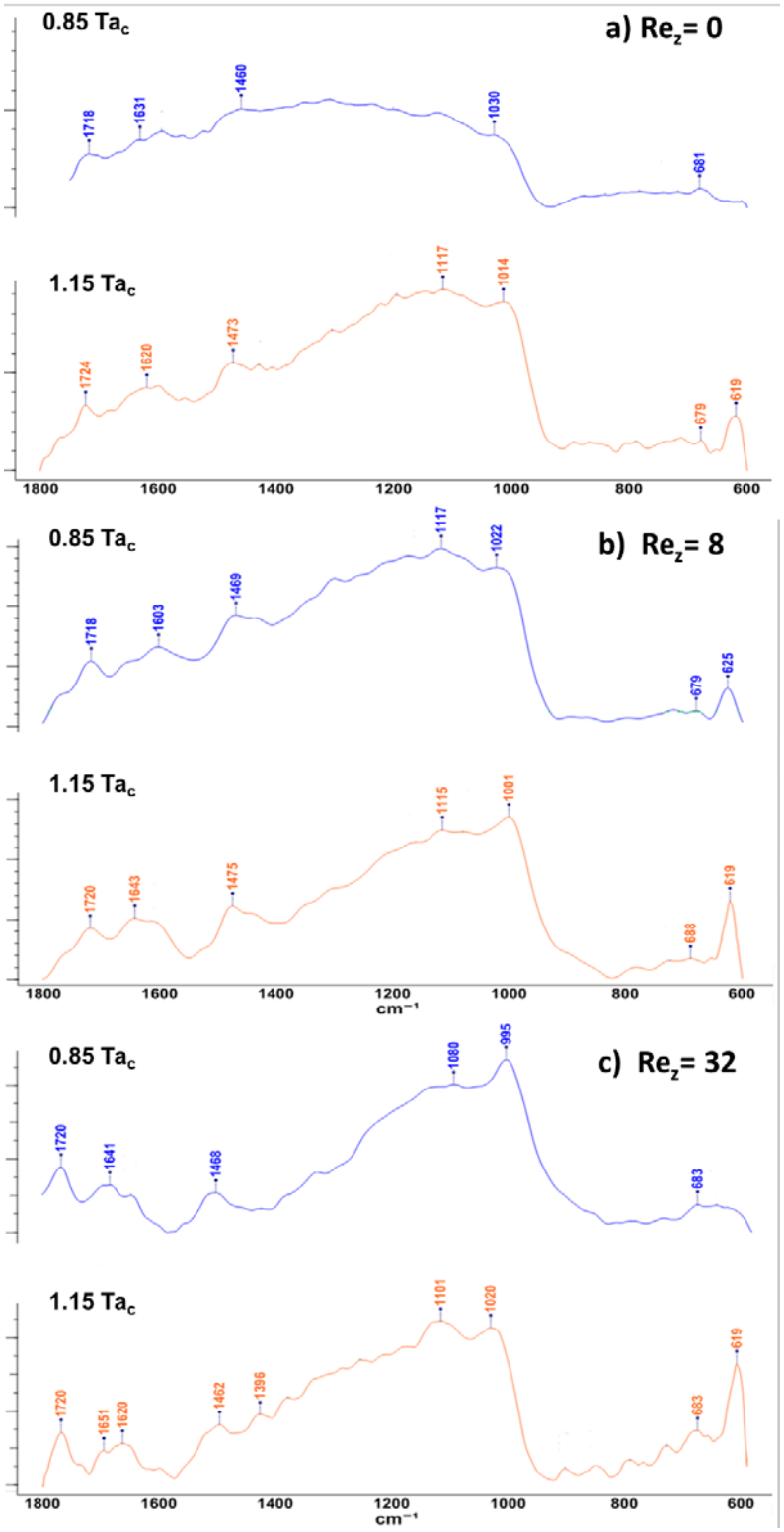

Figure 4.3.5 **.** FTIR Spectra of MPS coating on Aluminum for Re_z =0, 8, 32, reaction time =1 minute before and after the onset of instability, obtained with Aluminum background.

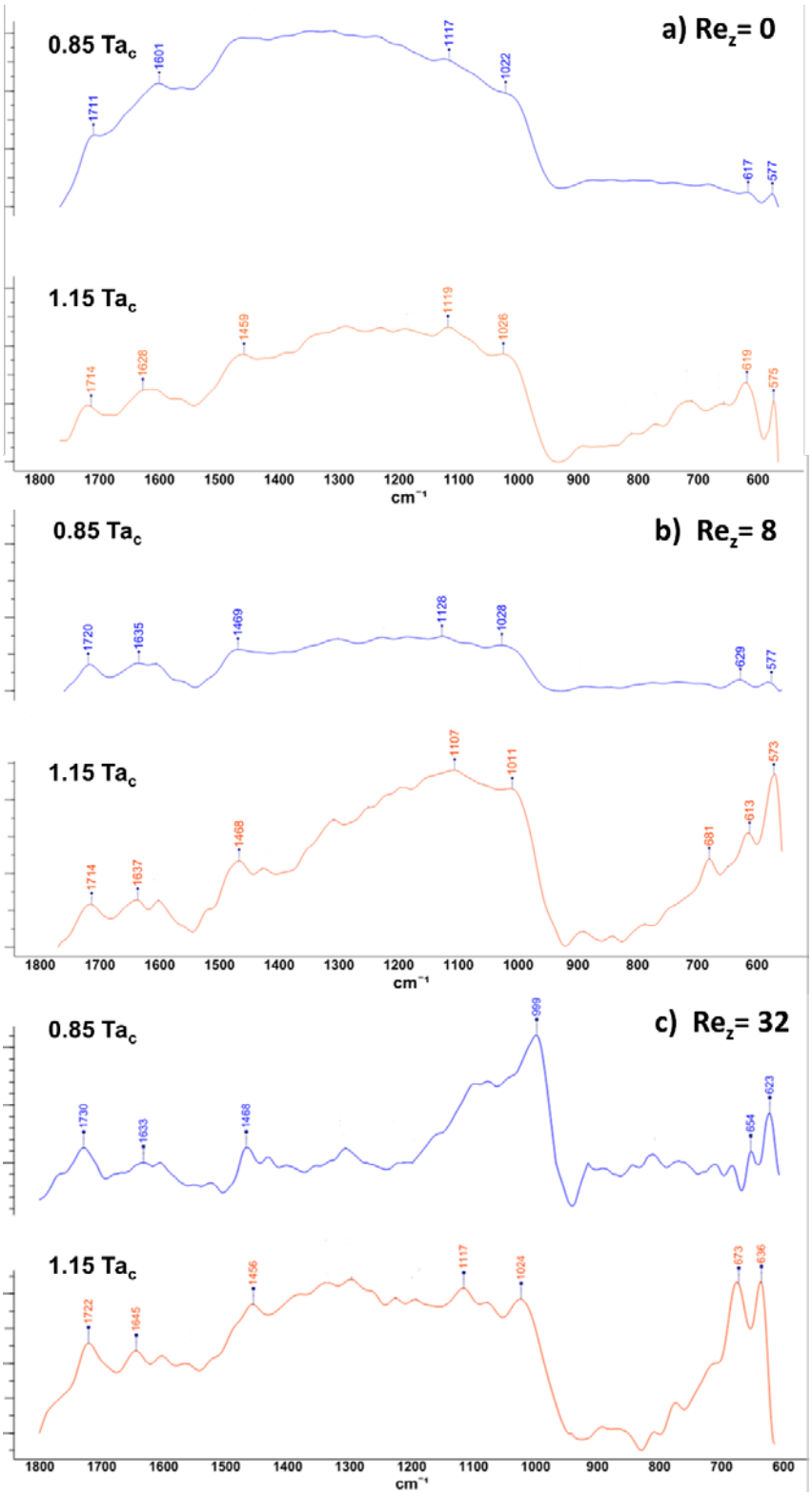

Figure 4.3.6 FTIR Spectra of MPS coating on Aluminum for Re_z =0, 8, 32, reaction time =15 minutes before and after the onset of instability, obtained with Aluminum background.

4.3.3 Thermal Analysis

The surface of aluminum particles is covered by a thin passivating oxide layer which chemisorbs water molecules to form surface hydroxyl groups on which further water molecules are adsorbed physically through hydrogen bonding [1]. Considering the mass losses found within temperature ranges from 180 to 550 °C measured in TGA (Figure 4.3.7), the amount of the chemisorbed water released from aluminum particles was determined to be equivalent to 15 OH molecules/nm^2. Such concentration of hydroxyls on aluminum surface favors a perpendicular orientation of MPS molecules under ideal conditions, since the maximum wetting surface area of the MPS is around 315m^2/g [136], with a theoretical grafting density of 7.7 molecules/nm^2 [137].

To monitor the reaction efficiency, the mass loss due to the thermal decomposition of the organic component under nitrogen atmosphere was measured via TGA for each functionalization condition. Figure 4.3.7 contains an overlay of the TGA curves acquired for samples functionalized under short reaction time (a) and 15 minute reaction time (b). These curves represent the degradation of the MPS monomer, either physisorbed, bound, or in polymer form, on the particle surface. While the loss between 100 and 200 °C is attributed to physisorbed monomer, the drastic mass loss beyond 200°C indicates the significant decomposition of any MPS that was either covalently bound to the aluminum surface or polymerized into strongly adhered MPS layer [109].

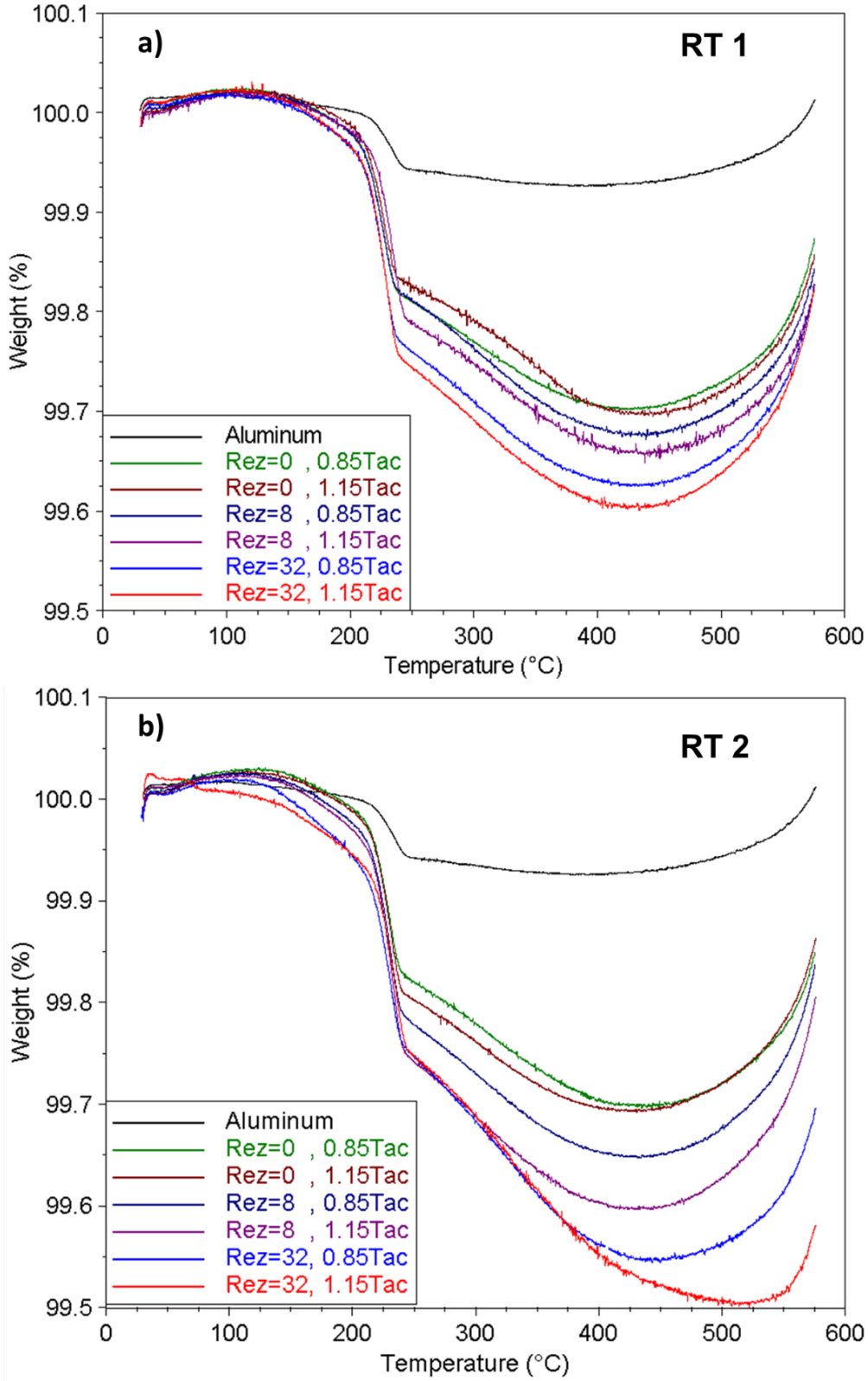

Figure 4.3.7 TGA analysis for short residence time (a) and long residence time (b).

Based on the surface area of the filler particles (2.67 m^2/g, measured via BET), the MPS molecular density on the surface was estimated from the TGA decomposition pattern. The corresponding grafting densities estimated for each reaction condition are displayed in Figure 4.3.8. Filler silanization under similar conditions [138] resulted in high grafting densities that are within the range of the ones observed in this study. Several studies have proposed a grafting density that varies between 2 molecules/nm^2 [138] to 4 molecules/nm^2 [109]to be sufficient for the creation of an MPS monolayer on silica and alumina surfaces, respectively. The grafting densities and decomposition pattern observed suggests the formation of poly-siloxane chains which may result in silane multi-layers that are mostly chemisorbed, as they can withstand temperatures beyond 200°C.

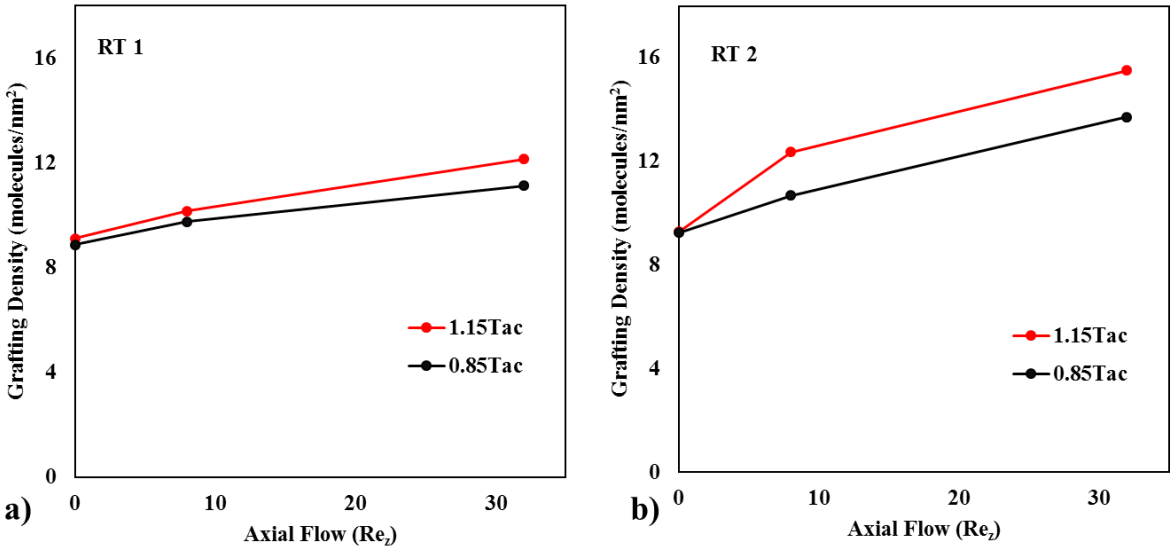

Figure 4.3.8 MPS grafting density on Aluminum obtained from TGA analysis for short residence time (a) and long residence time (b).

The surface area of functionalized particles under long residence time (15 minutes) was determined using the BET method, as displayed in Figure 4.3.9. The surface modification of aluminum particles with MPS caused a reduction in the surface area that was proportional to

the increase in axial flow, especially below the onset of vortex instability where the flow is mostly laminar (0.85 Ta_c).

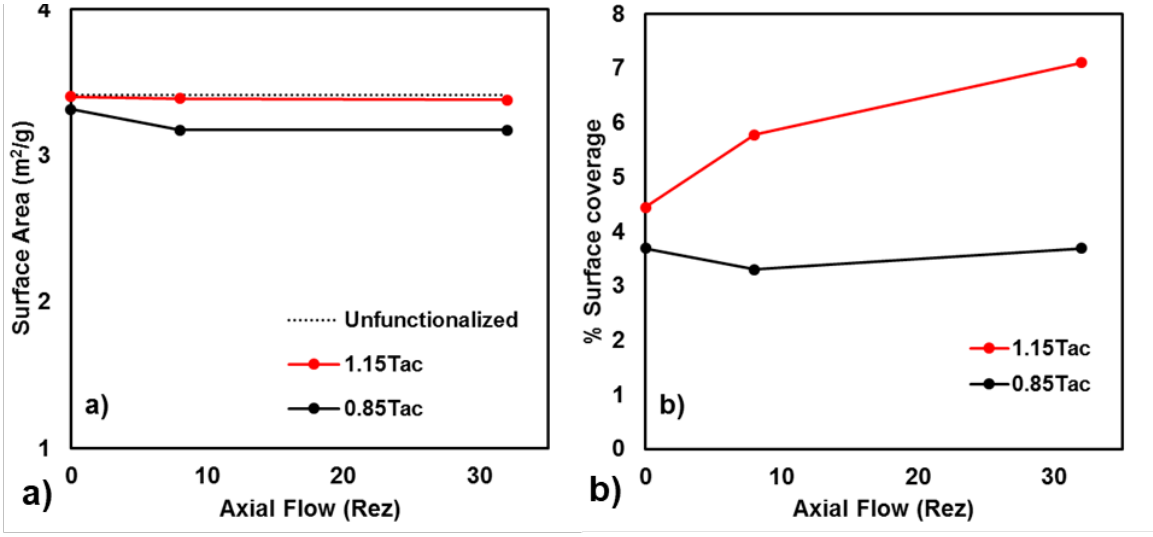

Figure 4.3.9 Change in external surface area of functionalized particles under long residence time (a). From the TGA and BET data, a hypothetical MPS surface coverage % was derived (b).

4.3.4 Surface Coverage

To investigate this further, we examined the morphology, uniformity and degree of surface coverage using FE-SEM combined with EDX to characterize the elemental content of the functionalized surface. Samples appearing in Figure 4.3.11 are for particles functionalized under axial flow of Re_z=32 with long residence time (a, b) and short residence time (c). The chemical element mapping technique revealed the relative positions of silicon which is the key element in assessing the coupling of MPS. Analyzing the Color Map image, particles functionalized in laminar Taylor-Couette flow conditions exhibited greater aggregation, with the MPS functionality being more confined to the edges. The clumping of particles in such flow structure reflects the lower BET surface area observed at 0.85 Ta_c. Such aggregation is most likely due to the increased formation of extensive polysiloxane Si-O-Si due to co-

polymerization of silane monomers to form of molecular bridges that connect particles together. On the other hand, the particles that were functionalized under the influence of vortex flow (1.15 Ta_c) retained their monodispersity (Figure 4.3.11-b). The corresponding silicon map for the vortex flow structure clearly reflects enhanced surface coverage that is more uniform and homogeneously distributed over most of the aluminum particle surface. Although the silicon color map for particles functionalized under Taylor vortex for shorter residence time, as seen in Figure 4.3.11 (c), indicate a lower concentration of silicon, they still confirm uniform distribution of MPS, minimizing the localization of MPS patches.

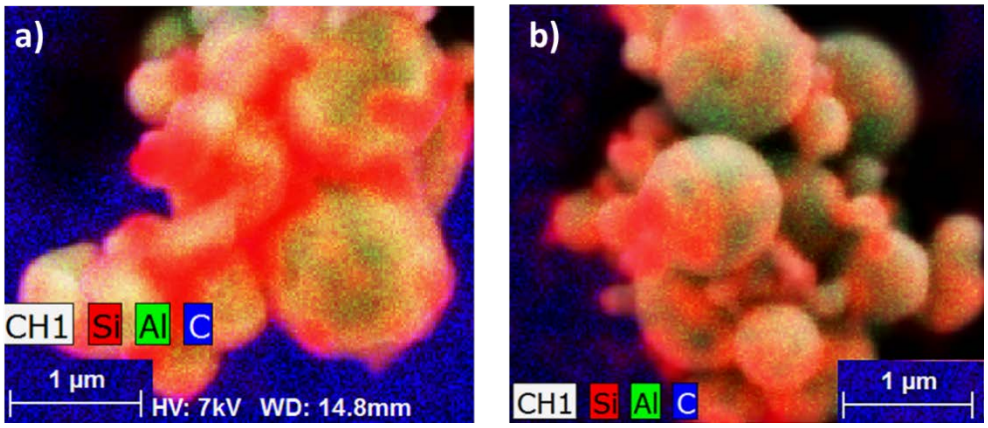

Figure 4.3.10 SEM of functionalized aluminum under Re_z=32 at 0.85 Ta_c (a) and 1.15 Ta_c (b) for 15 minutes

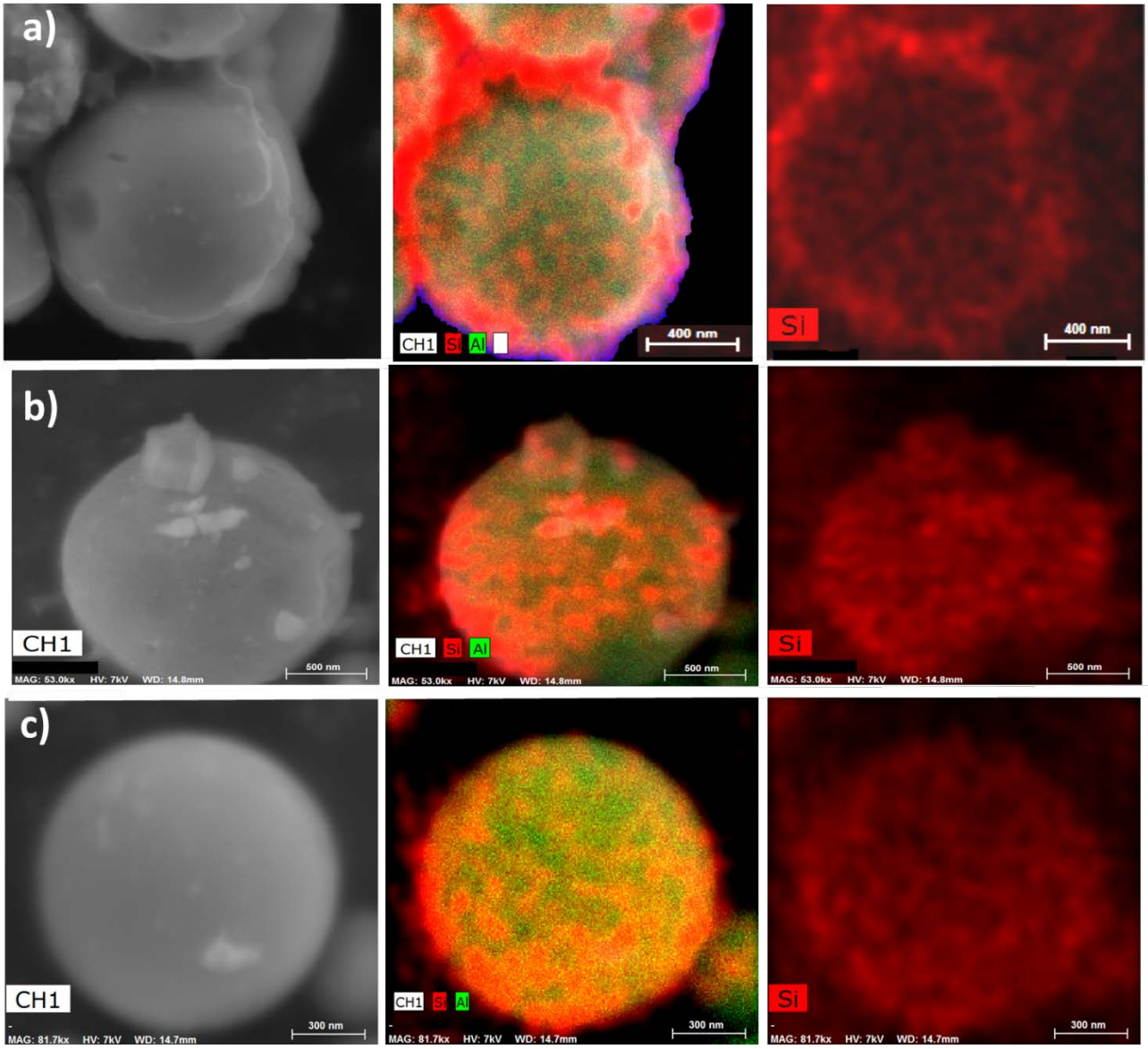

Figure 4.3.11 SEM of functionalized aluminum under Re_z=32 at 0.85 Ta_c (a) and 1.15 Ta_c (b) for 15 minutes and 1.15 Ta_c for 1 minute (c).

4.3.5 Particle Dispersion Studies

4.3.5.1 Dispersion in Toluene

The formation of covalent metallo-siloxane bonds between the MPS and aluminum surfaces, displaces the hydroxylated oxide surface, orienting the low polarity methacrylic portion of the MPS perpendicularly away from the particle surface. The resulting functionalized particles

should have a hydrophobic coating that allows them to exhibit enhanced miscibilty in nonpolar media [109]. To determine their enhanced degree of miscibility, 0.03g of unmodified aluminum and particles from each functionalization condition were suspended in 10ml of Toluene. Toluene was chosen specifically because it is a common nonpolar dispersion media that was used previously for the assessment of aluminum dispersion [109] and the DLS particle size of MPS-modified CeO_2 [103]. The mixtures were then transferred to an ultrasonic bath for 1min to suspend the particles. Upon stirring, the suspensions were placed next to each other to compare their stability through careful observation. Images of the suspensions were taken after 5 minutes (Figure 4.3.12) 15 minutes (Figure 4.3.13) and 45 minutes (Figure 4.3.14), when most of the particles settled out of the suspensions. Due to their large size (~650nm) and density, the particles were settling quickly. However, it was clear that all functionalization conditions resulted in enhanced miscibility when compared to the neat aluminum. While, increasing residence time resulted in more stable suspensions, the increase in axial flow produced particles that were more significantly stable in toluene, especially at Re_z=32. Suspensions of particles functionalized under vortex flow were only slightly more stable than those functionalized in laminar Taylor Couette flow (0.85 Ta_c). Accordingly, the degree of aluminum suspension stability was observed to be more signficant under flow conditions that favored increased MPS coating, especially for conditions that induce more uniform surface coverage.

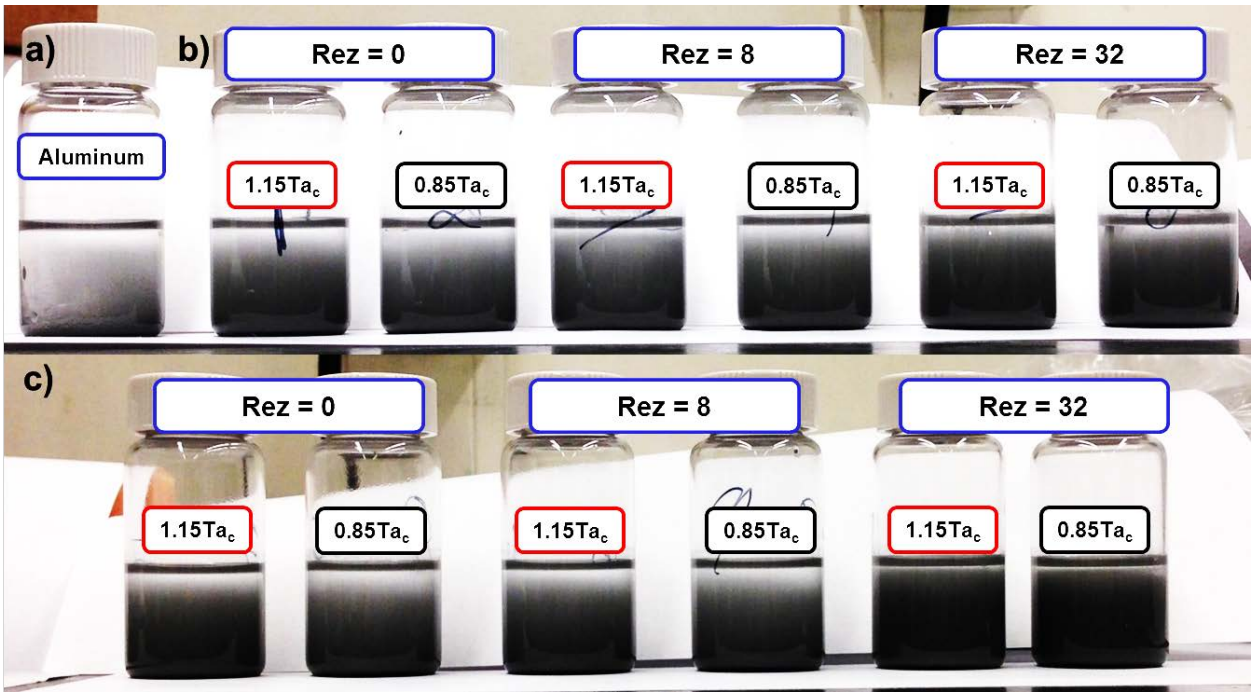

Figure 4.3.12 Aluminum miscibility test in Toluene after settling for 5 minutes for reference aluminum (a) functionalized for short residence time (b) and long residence time (c).

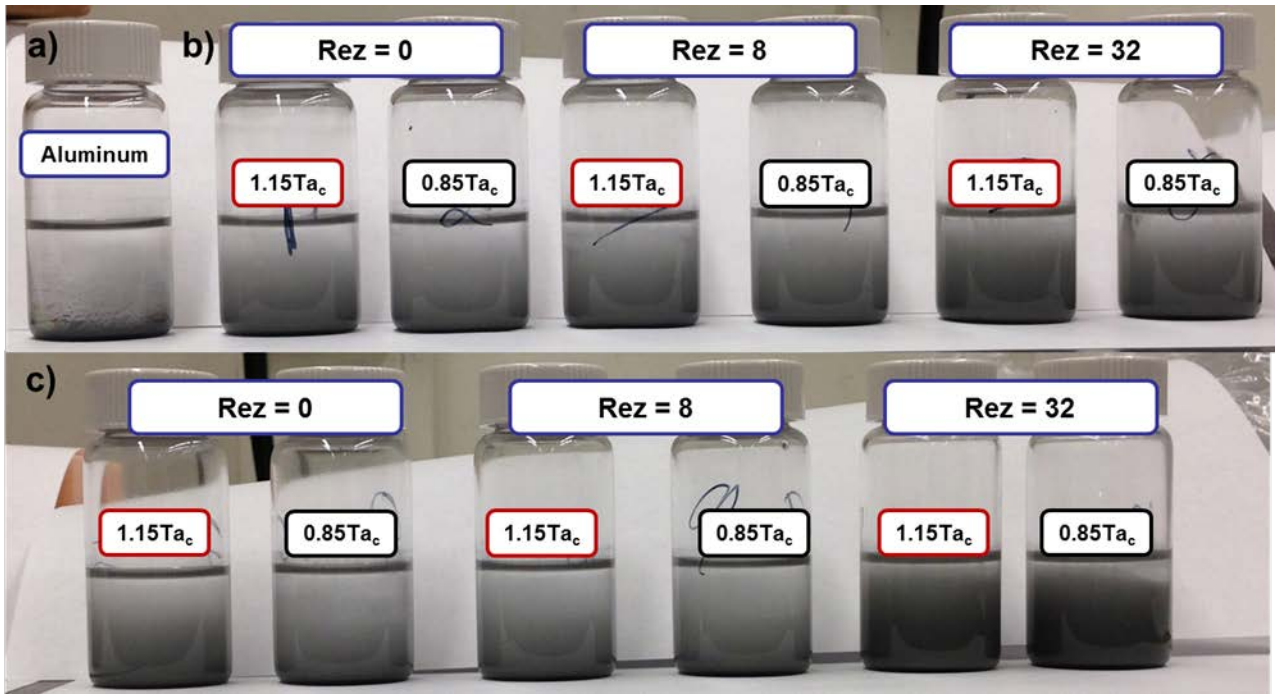

Figure 4.3.13 Aluminum miscibility test in Toluene after settling for 15 minutes for reference aluminum (a) functionalized for short residence time (b) and long residence time (d). Zeta Potential is plotted as a function of Silicon atomic % on Aluminum surface (c).

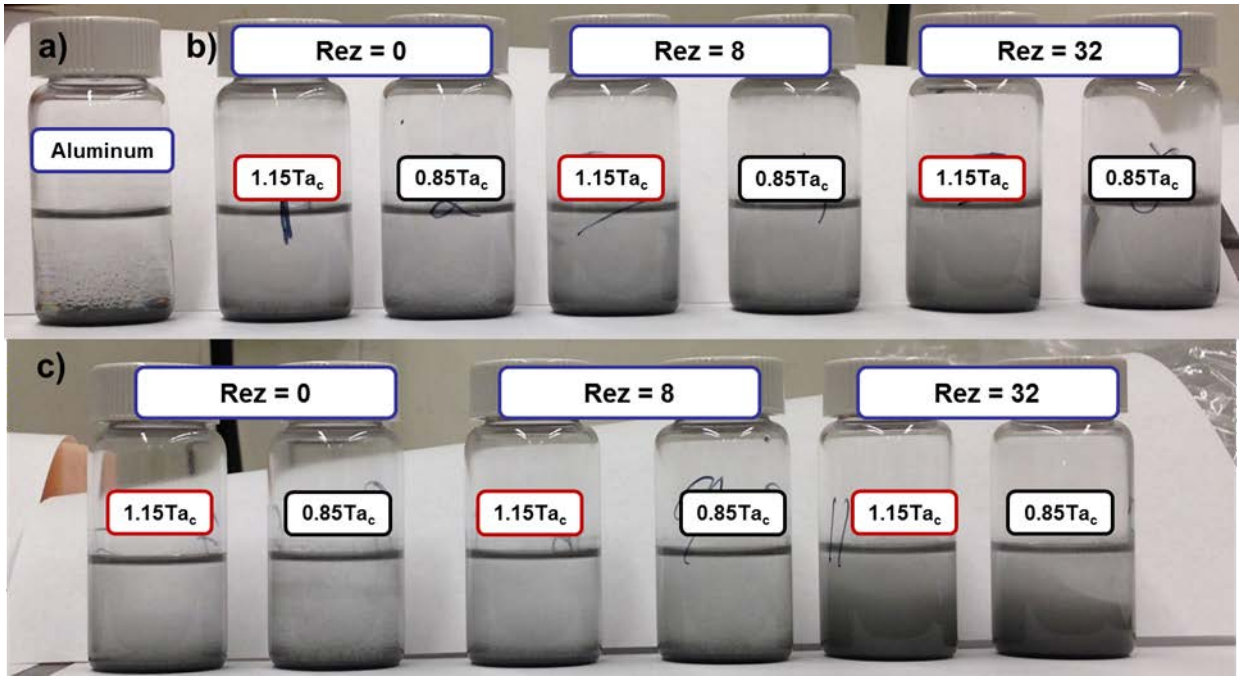

Figure 4.3.14 Aluminum miscibility test in Toluene after settling for 45 minutes for reference aluminum (a) functionalized for short residence time (b) and long residence time (d). Zeta Potential is plotted as a function of Silicon atomic % on Aluminum surface (c).

The stability of aluminum dispersions is strongly dependent on the hydrodynamic particle size. For a more quantitative assessment of the relative stability and behavior of MPS-modified particles in toluene, a series of particle size measurements were made via dynamic light scattering (DLS). As shown by the particle size distributions (PSD) in Figure 4.3.15, the average particle size of aluminum decreases proportionally with the increase in axial flow from Re_z=0 to Re_z=32. The onset of Taylor vortices helped in reducing the size of the particles even further, leading to narrower and more uniform particle size distributions. The increase in residence time from 1 minute to 15 minutes resulted in narrower PSD.

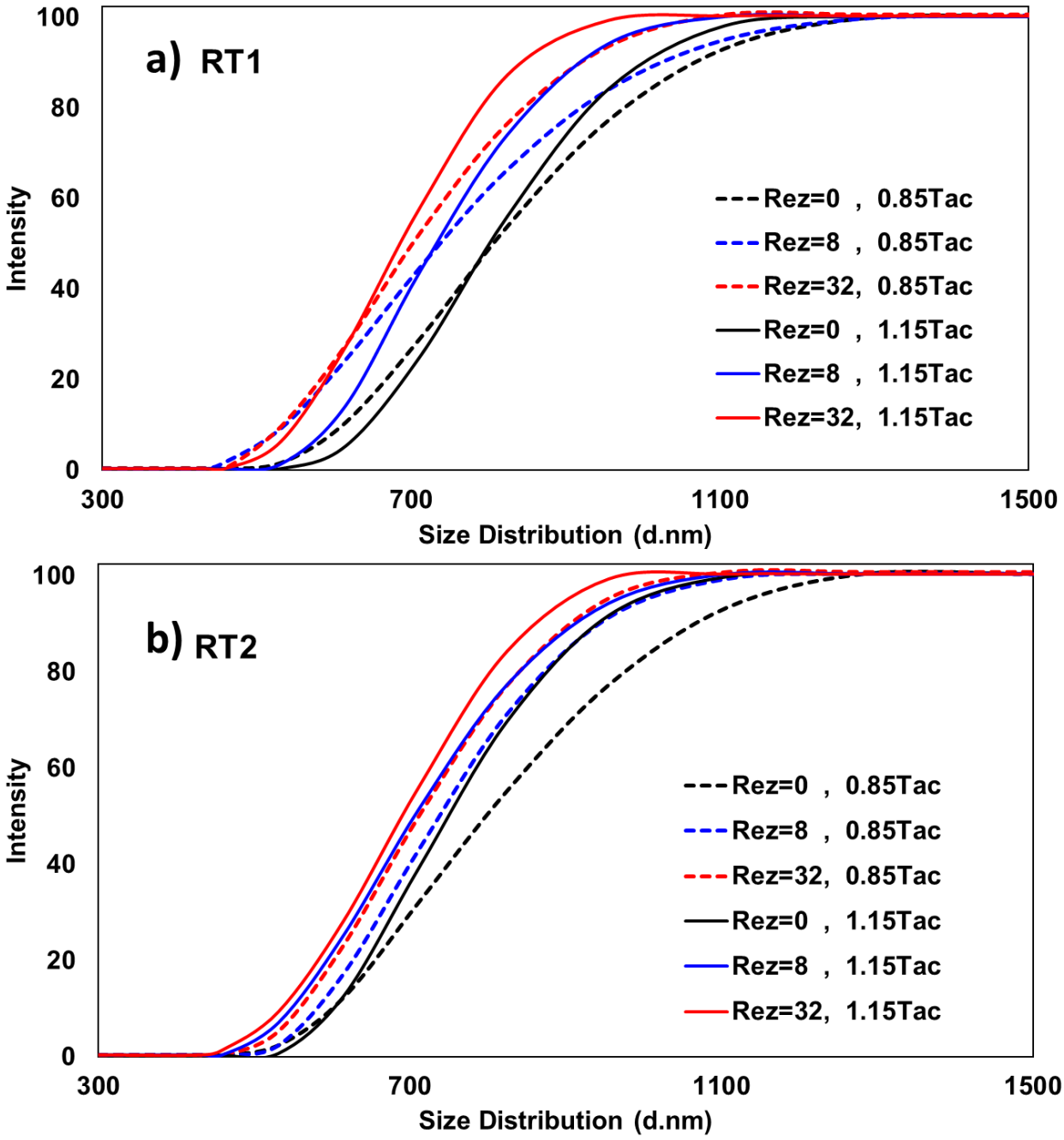

Figure 4.3.15 Particle size distribution in Toluene via DLS for short residence time (a) and long residence time (b), for below the onset of instability (dashed) and above it (solid lines).

The same characteristic trends in the PSD were also observed for the average hydrodynamic diameter (Z-avg) of the particles in Toluene, as plotted in Figure 4.3.16(a) and (b), for short and long residence time, respectively. Due to increased axial dispersion and additional MPS

coating, the particles at Re_z=32, become highly mono-dispersed with particle sizes approaching those observed via BET (measured for longer residence time, Figure 4.3.16-b). Even for this condition, the particle sizes given by DLS are slightly larger than that observed in BET because the solution-based mean hydrodynamic diameter usually includes a few solvent layers.

More aggregation and increased poly-dispersion results in particles settling out of the suspension quicker than in conditions that favor mono-dispersed behavior. By becoming more uniformly hydrophobic, the particles experience less flocculation leading to lower polydispersity and more stable suspensions (Figure 4.3.16 c and d). As observed via SEM, the onset of vortex flow structure leads to lower aggregation and allows particles to retain their monodispersed morphology.

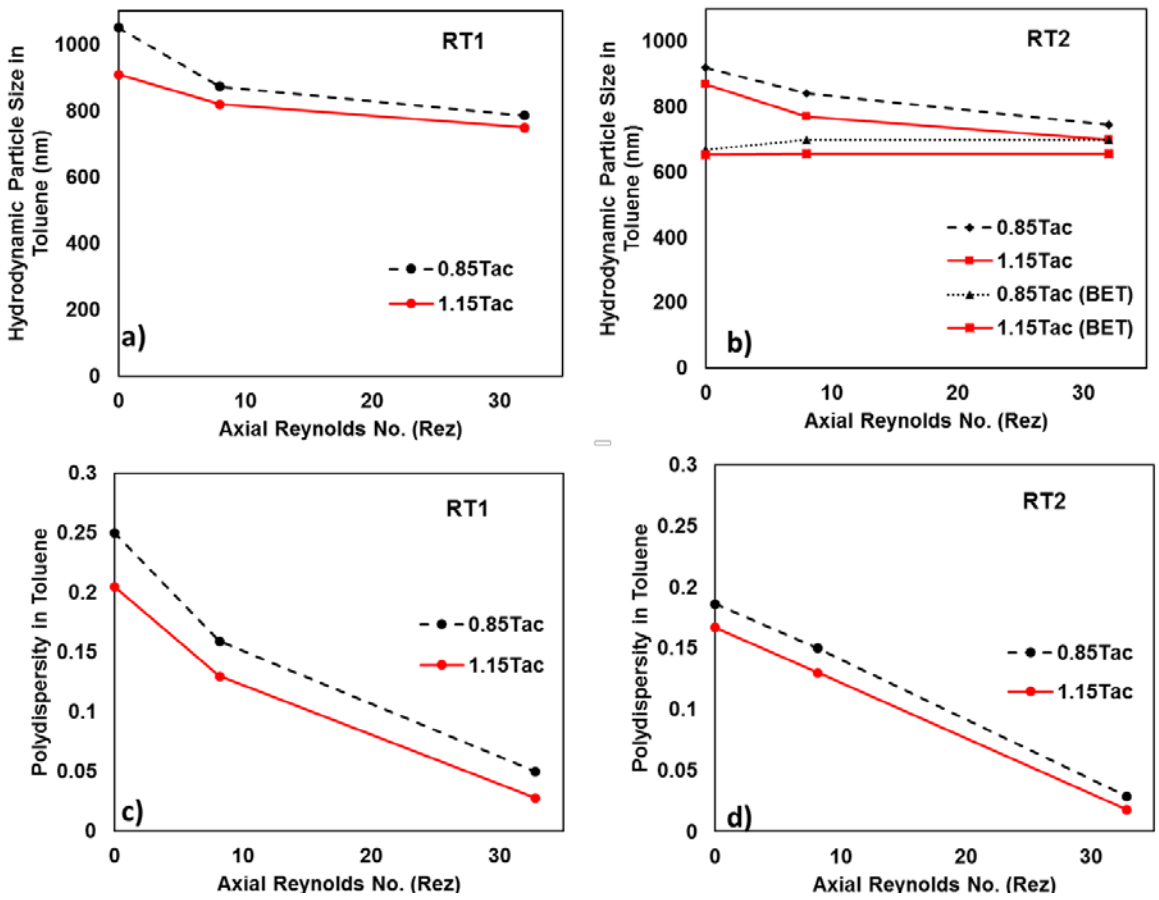

Figure 4.3.16 The average hydrodynamic size for aluminum particles in toluene (a, b) and corresponding polydispersity values (c, d) for short and long residence times, respectively

4.3.5.2 **Zeta Potential**

The hydrodynamic diameter of the dispersions is controlled primarily by the ionic strength of the dispersion media, which is a function of the electro-kinetic surface potential, known as the zeta-potential. The same DLS approach was used to assess the electrokinetic properties of functionalized aluminum particles by measuring streaming potentials at various pH's. The zeta potential profiles of particles functionalized under various flow conditions for long residence time (15 minutes) are compared with untreated aluminum and depicted in Figure 4.3.17. The pH at which the zeta potential of aluminum is zero - the isoelectric point of the surface (IEPS) – was shifted from pH between 6 and 7 to lower pH in the range of 2.5 to 4.5. Such shift to

lower pH is due to the MPS coupling agent substituting silanol sites for aluminum hydroxide sites. If the adsorbed MPS layer is hydrolytically unstable, desorption of silane in water will allow the isoelectric point to drift back to the value for untreated aluminum [102]. However, the zeta potential values showed no drift and were reproducible for at least 20 runs with only marginal error, confirming the stability of the MPS layer with no appreciable desorption of the silane from the surface. The pH range observed (2.5 to 4.5) corresponds to the region where the silane triols of neutral organofunctional silanes, RSi-(OH) exhibit maximum stability. Plueddemann suggested that point of zero-charge (IEPS) of organofunctional silanols would be about 3 [102], similar to what we observed for the functionalized samples. The shift to lower IEPS is proportional to the increase in MPS chemisorbed on the aluminum surface. With increasing axial flow to Re_z=32, the aluminum particles behaved completely anionically even in an aqueous medium of lower pH. The trends in the electro-kinetic potential confirm that the surfaces were responding to the change in H+ and OH- ion concentrations, suggesting that the particles were only partially coated with MPS given that a surface completely silanated with MPS will have no ionizable sites left and will show no surface charge, irrespective of the solution pH.

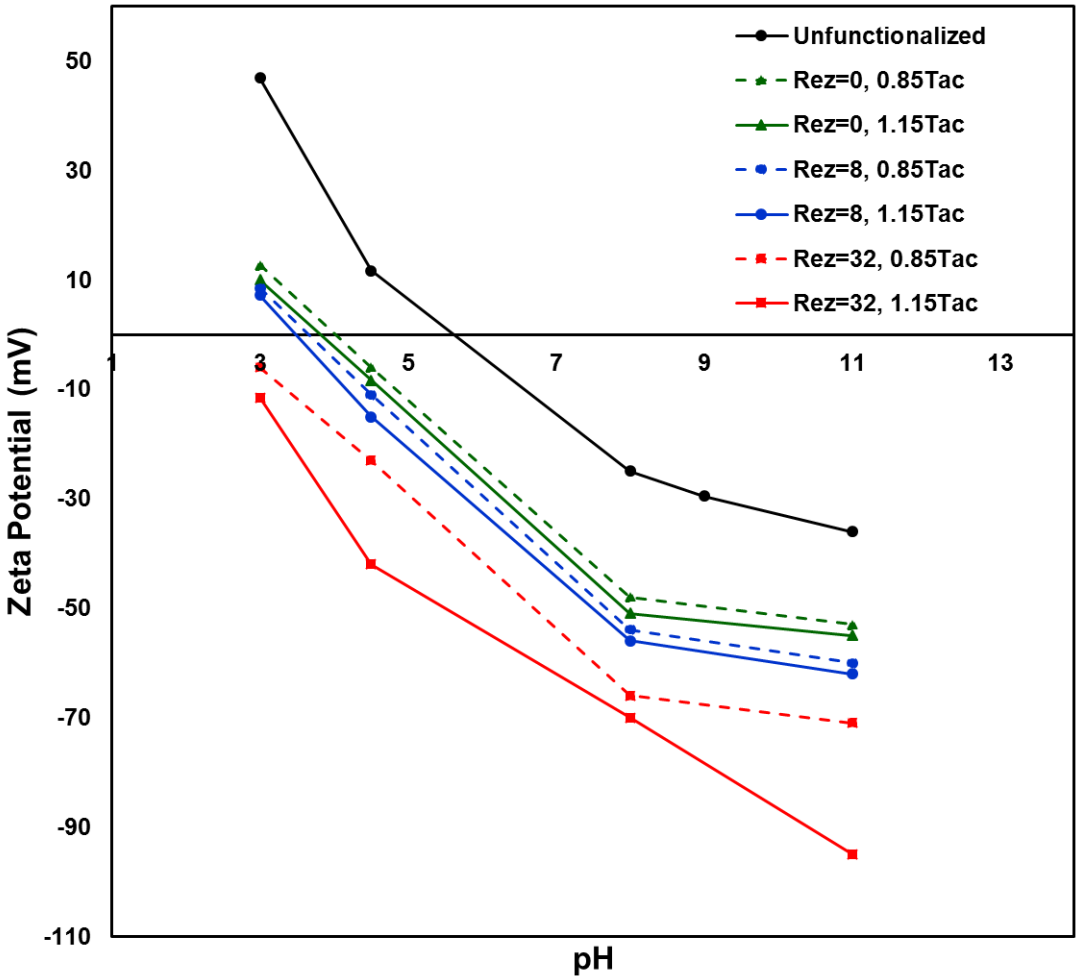

Figure 4.3.17 The change in Zeta potential of aluminum with pH, illustrates the shift in the isoelectric point of the surface (IEPS) with increasing intensity in hydrodynamic conditions for long residence time (RT2=15 minutes).

4.3.5.3 **Dispersion in Water**

Given that the functionalized particles exhibit hydrophobic properties and a shifted IEPS, their behavior while suspended in water will differ accordingly. To quantify such change, particle size measurements of MPS-modified particles were performed again via DLS, but this time in water (see supporting materials). Although the particle size distribution became narrower after the onset of instability (Figure 4.3.18 b and d), the average hydrodynamic particle size and polydispersity increased. In contrast to the trends observed for their behavior in nonpolar media,

the increase in axial flow, combined with the onset of Taylor vortices and longer residence time, resulted in an increase in a higher degree of flocculation, as evident from the particle size distribution (Figure 4.3.18), average hydrodynamic particle diameter and polydispersity index (Figure 4.3.19).

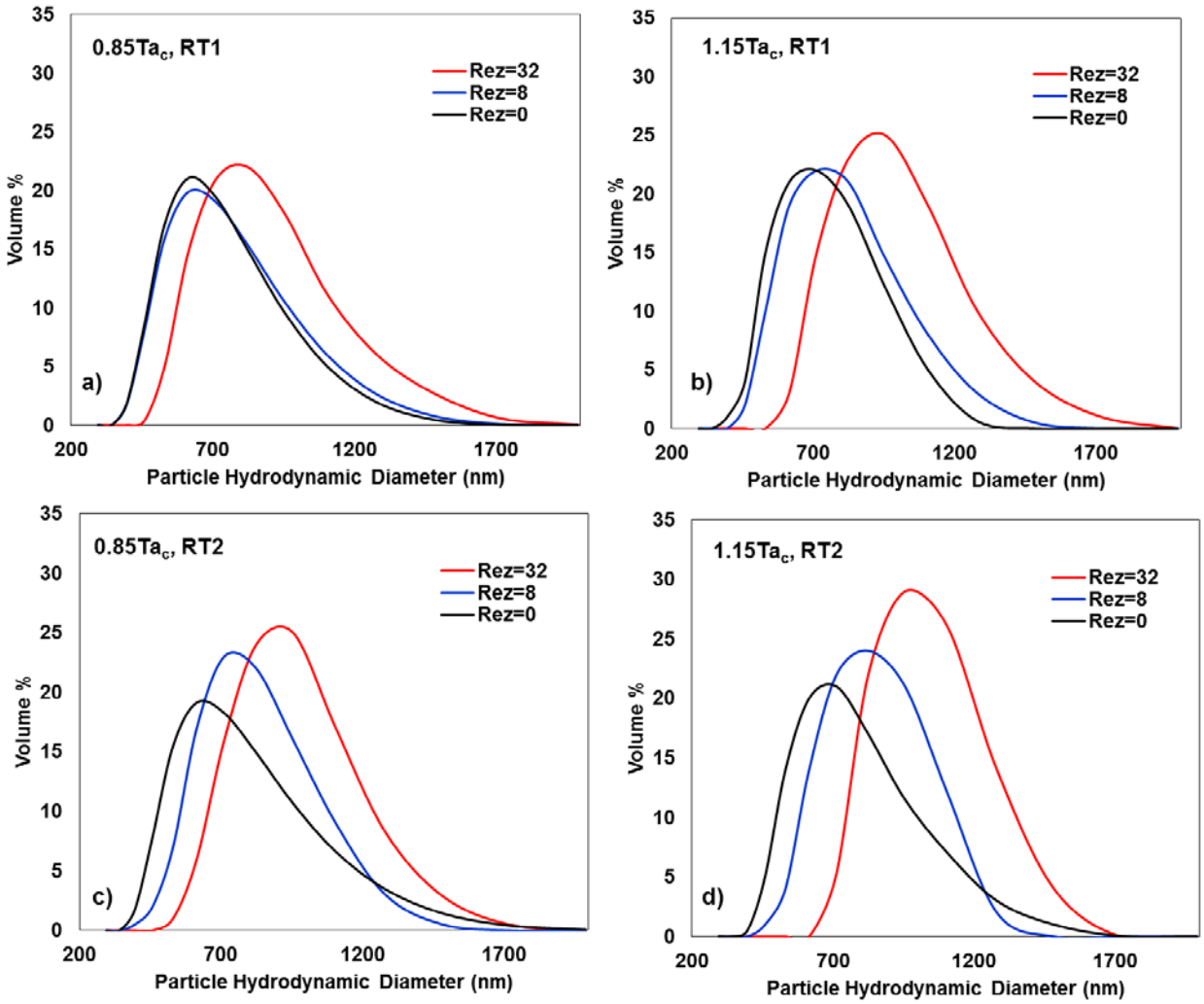

Figure 4.3.18 Particle size distribution in water via DLS for short residence time (a, b) and long residence time (c,d), for below the onset of instability and above it, respectively.

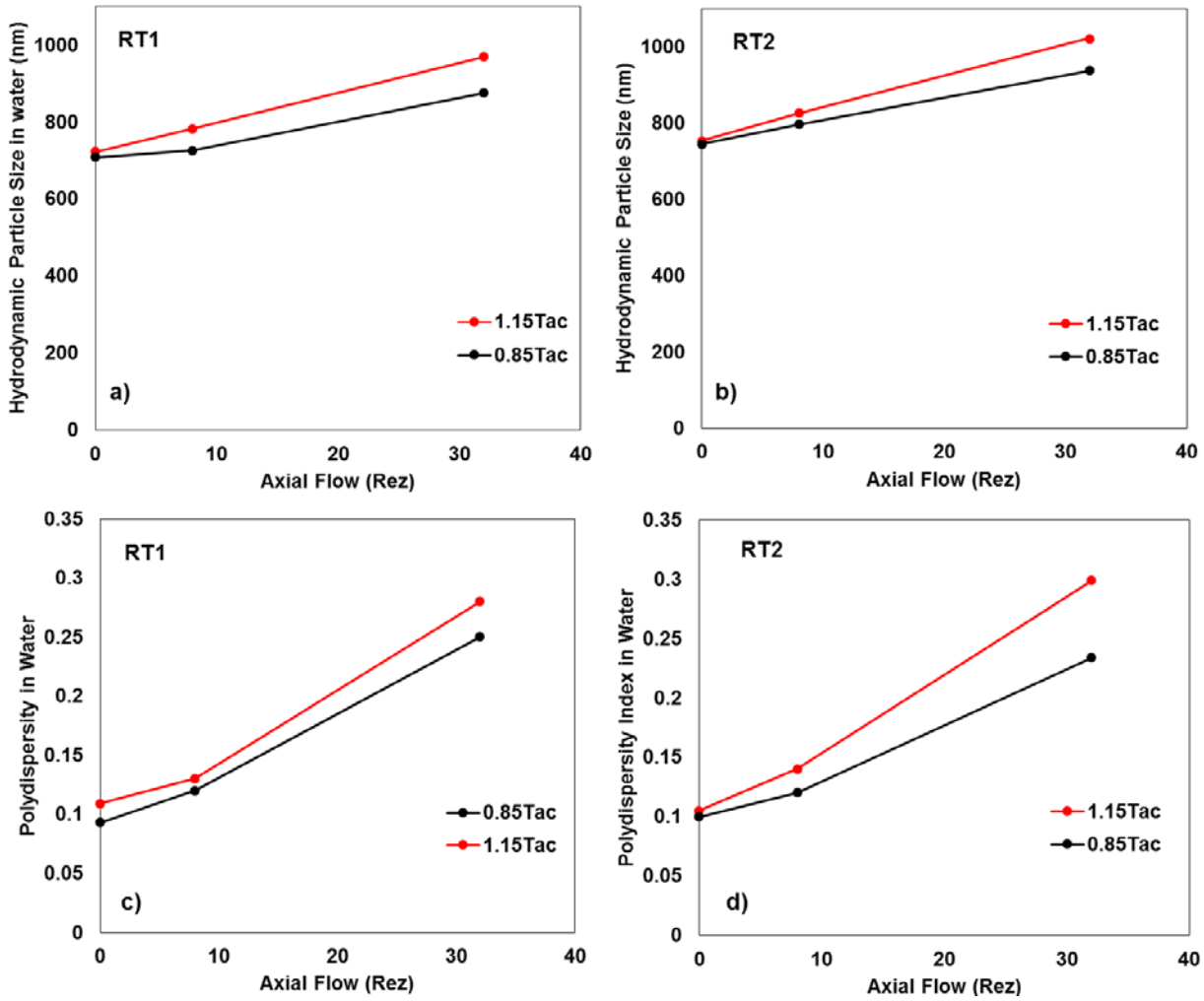

Figure 4.3.19 The average hydrodynamic size for aluminum particles in toluene (a, b) and corresponding polydispersity values (c, d) for short and long residence times, respectively.

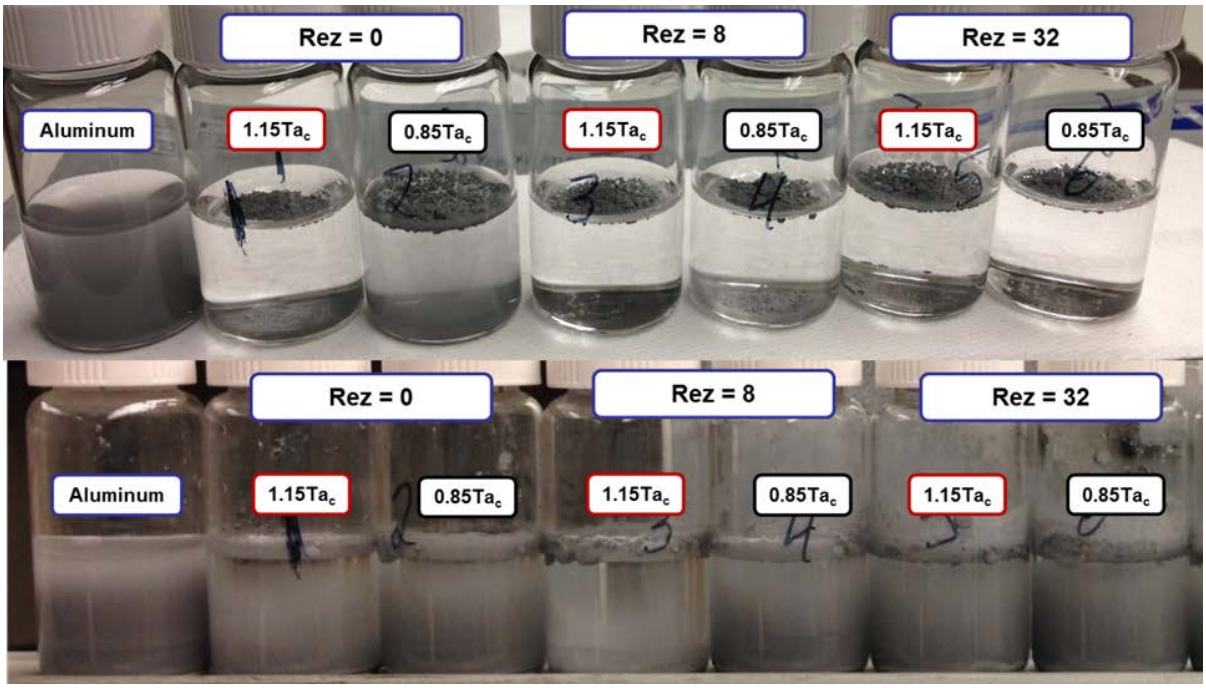

Figure 4.3.20 Change in wettability of 0.3g of aluminum in 10ml of water due to functionalization in short residence time (1min). Before mixing (top), after mixing (bottom).

To further examine the degree of hydrophobicity introduced by the MPS functionalization, and to test the stability of the coating layer in limiting the diffusion of water to the particle surface, 0.03g of functionalized particles were immersed in 10ml of water. As observed in Figure 4.3.20, the functionalized aluminum particles repelled the water forming an aluminum layer on top, while the neat aluminum powder was immediately dispersed in water. After mild mixing, the particles begin to be suspended, with the significant portion of the particles repelling the water and sticking to the side-walls of the glass vials, especially for higher axial flow (Re_z=32).

4.3.6 Oxidation Studies

4.3.6.1 Room Temperature Oxidation

The mixtures were then transferred to an ultrasonic bath for 1min to aid in suspending the particles. Upon stirring, the suspensions were placed next to each other to compare their stability and resistance to oxidation for 14 days. From the color change in the powder, the

untreated aluminum was completely oxidized within the first few days. Although the functionalized particles demonstrated far better resistance to oxidation, they were eventually fully oxidized by the end of the 14 days, except those functionalized at higher axial flow (Re_z=32), especially those treated under longer residence time (Figure 4.3.21). In addition to color change, the degree of oxidation was assessed by the change in crystal structure via XRD analysis. Figure 4.3.22 (a) shows that samples functionalized under high axial flow were only partially oxidized. Meanwhile, no oxidation was observed at the same conditions but for longer residence time. It was notable that the samples functionalized under Taylor vortices for Re_z=8 exhibited lower oxidation, particularly for longer residence time, where no oxidation took place for 336 hours.

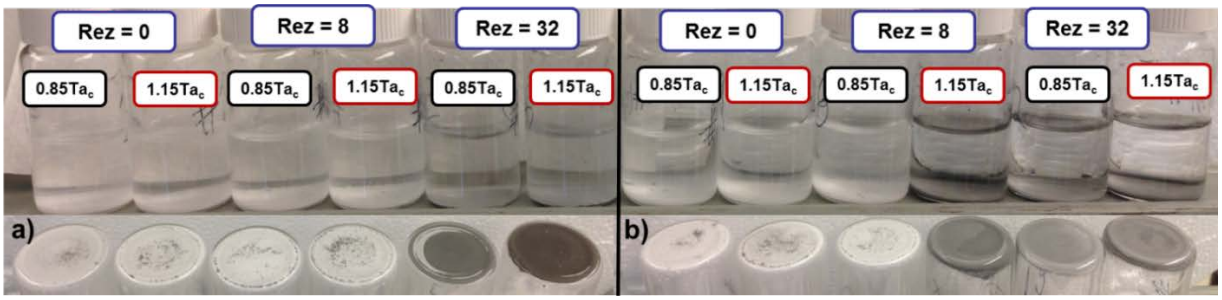

Figure 4.3.21 Functionalized samples for short (a) and long (b) residence time (a) after 14 days of room temperature oxidation.

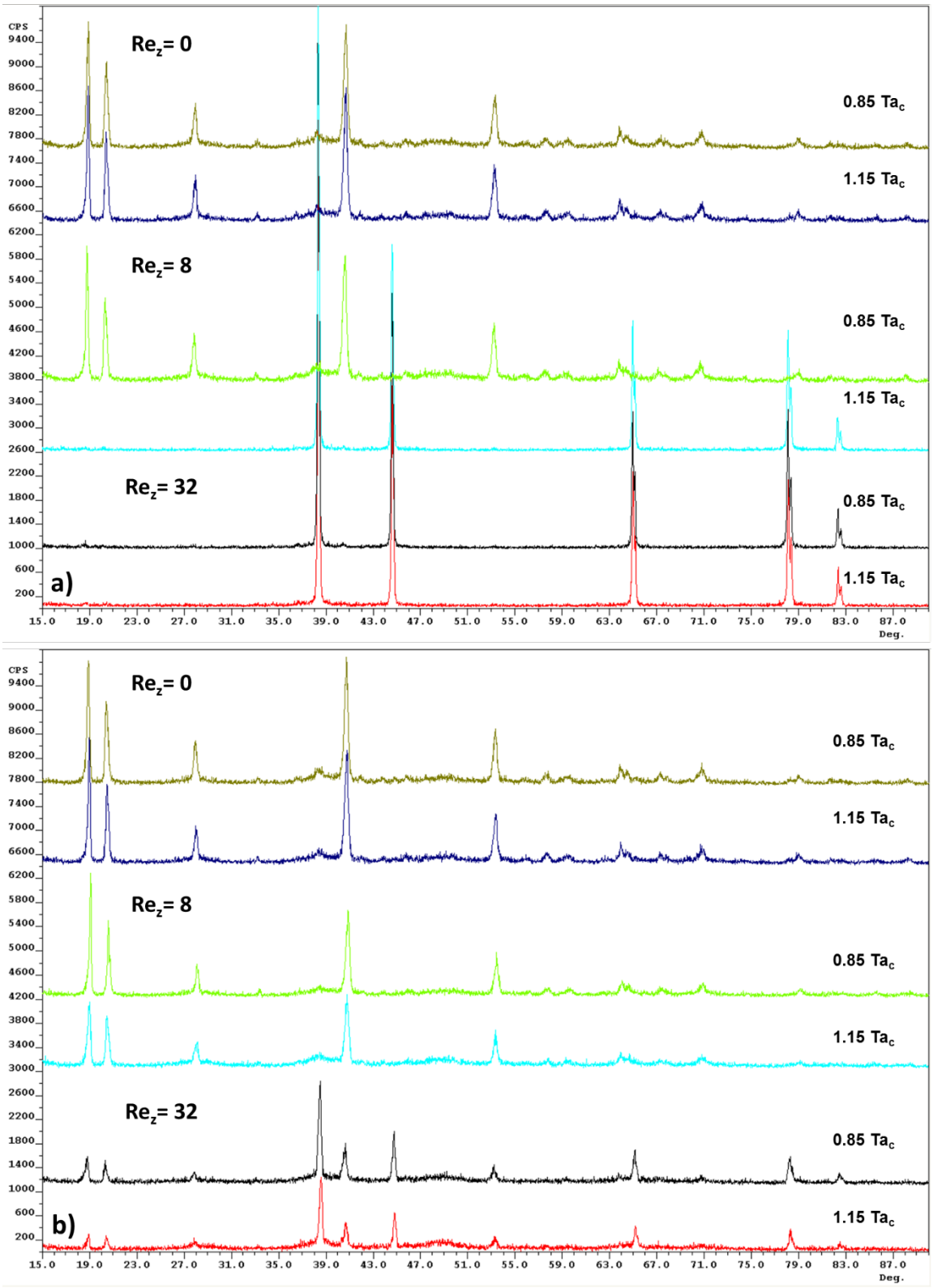

Figure 4.3.22 XRD spectra of oxidized samples under room temperature for 336 hours for functionalized aluminum under short residence time (a) and long residence time (b).

The color change after oxidation from deep gray/black to white (Figure 4.3.21) is due to the formation of aluminum oxide and is accompanied by the evolution of hydrogen gas bubbles. The degree of oxidation is marked by the slow consumption of metallic aluminum to favor the formation of oxides increasing the mass of the powder. Table 4.3.2 displays the mass gained for suspension in water, where the oxidized samples exhibited significant increase in mass while the mass of unoxidized samples remained unchanged.

Table 4.3.2 Percentage gain in mass due to Oxidation

Axial Flow (Re_z)	**T=70°C, 1.5 hours**				**T=25°C, 336 hours**			
	1 min		**15 min**		**1 min**		**15 min**	
	$0.85Ta_c$	**$1.15Ta_c$**	**$0.85Ta_c$**	**$1.15Ta_c$**	**$0.85Ta_c$**	**$1.15Ta_c$**	**$0.85Ta_c$**	**$1.15Ta_c$**
0	27%	**20%**	41%	**23%**	157%	**153%**	160%	**151%**
8	8%	**3%**	5%	**0%**	133%	**129%**	123%	**0%**
32	6%	**0%**	0%	**0%**	81%	**77%**	0%	**0%**
Pristine Aluminum	**60%**				**160%**			

4.3.6.2 High Temperature Oxidation

In parallel with room-temperature aqueous oxidation, the integrity of the silane coatings were studied under more intense conditions. To accelerate the rate of oxidation, 0.1g of the powders were mixed in 10ml, in a similar fashion to the former samples, but instead were exposed to an elevated temperature of 70°C for 90 minutes. As expected, the trends observed in this case paralleled those at room-temperature. In fact, while the aluminum particles fully oxidized, none of the functionalized samples exhibited full oxidation. Such stability suggests that the MPS coatings were not significantly affected by elevated temperatures, unlike those observed by

Crouse et al. for MPS coupled on aluminum nano-particles [109]. This is most likely due to the thicker coating layer indicated by the higher MPS grafting densities found in this study (8 to 16 molecules/nm^2) compared to their grafting density of 3.3 molecules/nm^2. In particular, those functionalized under high axial dispersion, Taylor vortex flow structure (1.15 Ta_c) and for longer residence time were able to better withstand the degree of oxidation, with markedly lower mass gained (see Figure 4.3.23 and Table 4.3.2).

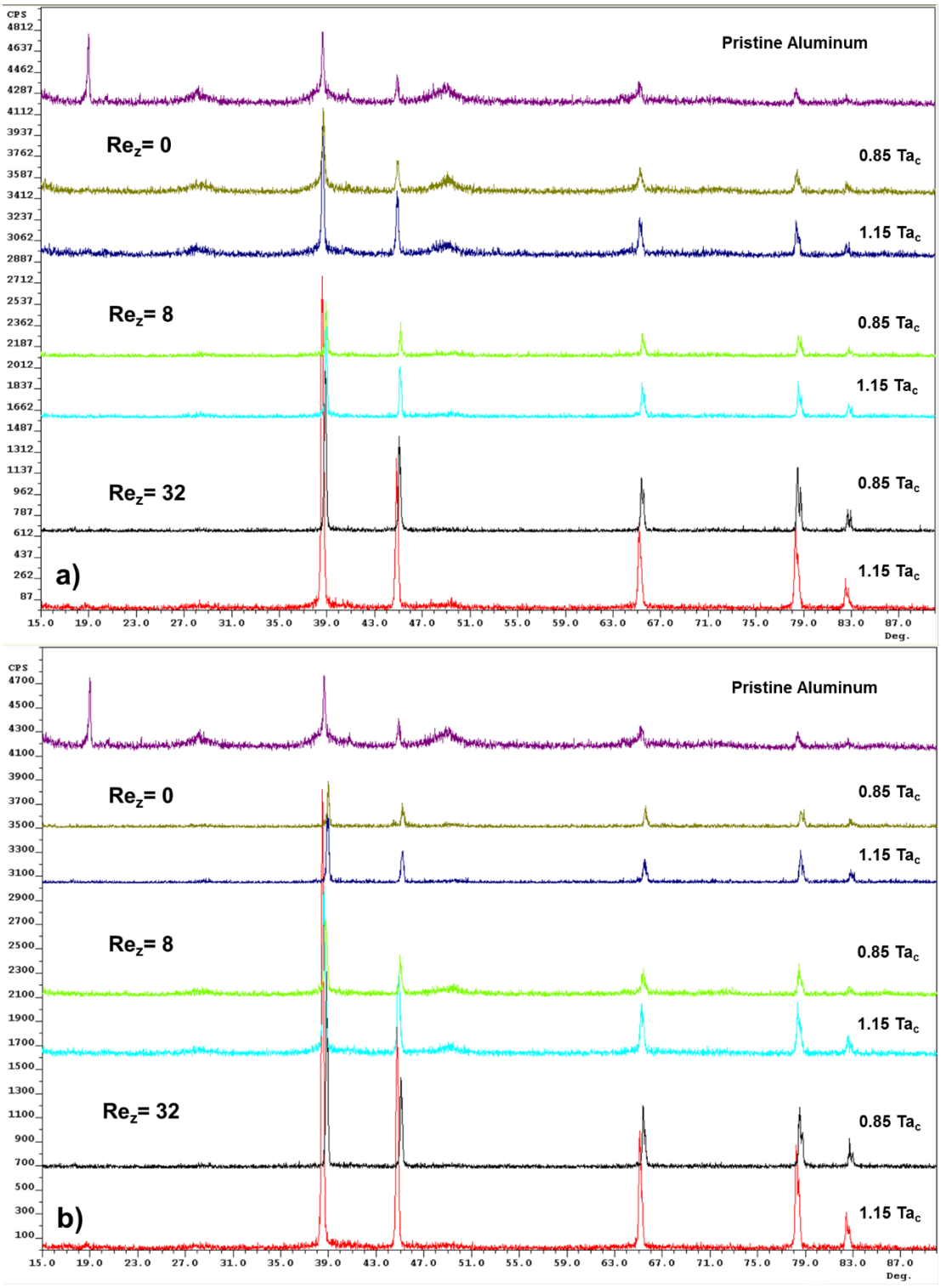

Figure 4.3.23 XRD spectra of thermally oxidized samples under 70°C for 90 minutes for functionalized aluminum under short residence time (a) and long residence time (b).

4.4 Discussion

4.4.1 General Discussion

The collection of experimental data presented above strongly suggests that the effectiveness of MPS coupling on the aluminum surface is markedly influenced by the flow structure and mixing conditions during the silanization reaction. The method of applying the organosilanes homogeneously can be as important as the chemistry of the selected silane and has an important impact on the orientation of the silane molecules and the final physical properties of the coating layer [102]. While ethanol has been reportedly applied as a homogenizer for silane reactions such as that of metals functionalized with allyltrimethoxysilane [101], 2-propanol has been used in previous studies to specifically improve the solubility of MPS homocondensate [139], and our designated pH environment has been specifically selected to minimize the rate of condensation between silanol groups of monomeric silane molecules to larger oligomers is [122]. Although the silane solution during the reaction should consist predominantly of monomeric silane triols, trialkoxy monomers, unlike monoalkyoxy silanes, still have a great capacity to form trimeric bonds and agglomerate. Vigorous stirring has been applied to specifically promote the dissolution of organotrialkoxysilanes in water [121].

Previous literature has highlighted the importance of different mixing parameters, such as reaction time and temperature [106] [107] [118]. While there are no studies that has investigated the effect of flow structure, some experiments suggested that shear rate can enhance the degree of functionalization [124]. Mcmorrow et al. developed a homogenization method to disperse ceramic nanoparticles during their treatment with acryloxypropyltrimethoxysilane. They reported that magnetic stirring and impeller mixing were not intense enough to break up aggregated particles. Instead, they applied intense shear through homogenization to break up

the particles and apply greater control over the silane hydrolysis and condensation reaction, reporting that high shear mechanical mixing proved to be more efficient for dispersing the ceramic nanoparticles to achieve adequate silane surface treatment [124].

Shear flow in Taylor Couette reactors has been utilized for the de-agglomeration and break-up of polystyrene particles into mono-dispersed spherical particles [140]. So instead of utilizing a homogenizer we utilized the effect of the onset of Taylor Vortex Instability combined with axial flow to mirror the mechanical mixing that takes place in a homogenizer. Even though the Taylor vortex flow structure doesn't necessarily offer nano-scale control, perhaps even down to molecular level like in a homogenizer, when combined with high axial shear flow the vortex structure formed offers enhanced homogeneity for the self-assembly of organosilanes over the inorganic substrate.

Under laminar Taylor coquette flow ($Ta < Ta_c$) the fluid exhibits a solid body rotation with transport occurring mainly azimuthally, with neither radial nor axial transport. With the onset of Taylor vortex flow (TVF, $Ta > Ta_c$), a series of travelling vortices emerge with a unitary vortex cell consisting of pairs of counter-rotating vortices that circulate fluid/particles from the outer-wall boundary layer into inflow boundaries that direct fluid radially inward towards the center of the vortex cell where the axial flow velocity is higher. Such effects become more prominent with axial flow, which boosts axial momentum.

Mixing characteristics and mass transport, for both macro- and micromixing patterns (i.e. inter- and intra-vortex mass transport) has been well documented in TCR configurations using tracer techniques. Because vortex pairs in TC are usually equal in size, it is assumed that the mixed fluid is uniformly distributed along the vortices, so that it spends identical residence time in each cellular element [23]. Introducing axial flow and assuming a well-defined flow structure,

Kataoka et al. suggested plug flow in continuous flow TC with a small degree of exchange of fluid elements between neighboring vortices [15]. By measuring inter-vortex flux independently and decoupling it from dispersion enhancing/reducing effects, Desmet et al. confirmed the existence of inter-vortex fluxes [24]. In reference to earlier studies [25] [26] [27] intra-vortex mixing under Taylor vortex can be modeled as a series of CSTR's with multi-dimensional dispersion [16] [28]. When the axial flow is present, the system becomes more stable and the onset of instability is significantly delayed because increasing axial flow diminishes the dominance of centrifugal forces. As Re_z increases, the critical mode may shifts from axisymmetric to non-axisymmetric disturbance, which causes the vortices to time-dependently travel both in the circumferential and axial directions. The loss of symmetry reflects a non-zero azimuthal wavenumber (m), implying increased mixing in circumferential, radial, and axial directions [57].

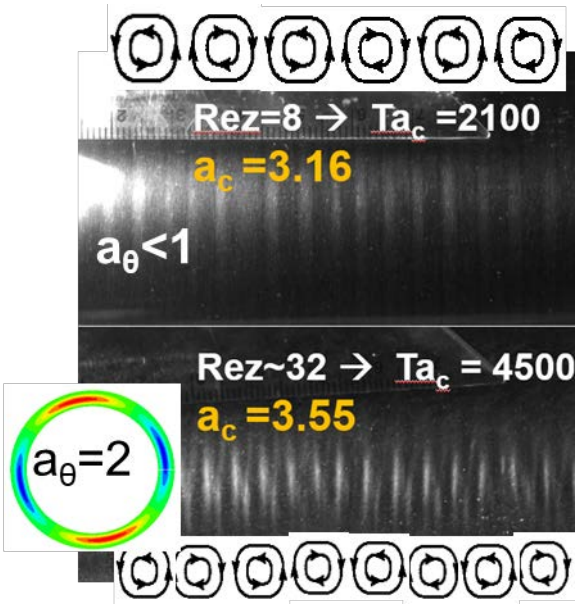

Figure 4.4.1 Change in number of vortices and evolution of spiral topology with increasing axial flow.

From detailed flow visualization imaging done in an earlier study [57], displayed in Figure 4.4.1, and given the reactor length of 15 cm, we can estimate the number of vortices present at Re_z=0 to be around 58 (29 pairs). With the increase of axial flow to Re_z=8 the number of vortices barely increases. With the maximum flow rate used in this study (Re_z=32), the number of vortices available becomes 66, resulting in four additional unitary vortex cells, each consisting of a pair of counter-rotating vortices. In addition, the increase in axial flow introduces significant enhancement in circumferential mixing due to the emergence of stronger non-axisymmetry, with the azimuthal wavenumber increasing to a_w=2 at Re_z=32 while it was negligible at Re_z=0 and Re_z=8. As summarized in Figure 4.4.1 and Figure 4.4.2, these estimations were visually verified in-situ during the functionalization experiments, as they were carried in a Plexiglas reactor. In Taylor vortex flow, while the micromixing time (intra-vortex mixing) is estimated to be around 10 milliseconds, macromixing (inter-vortex) was about 3 seconds. Given that the latter being the limiting stage for the whole mixing process in Taylor-Couette reactor (1), it is expected that the increase of axial flow can significantly enhance the whole mixing process.

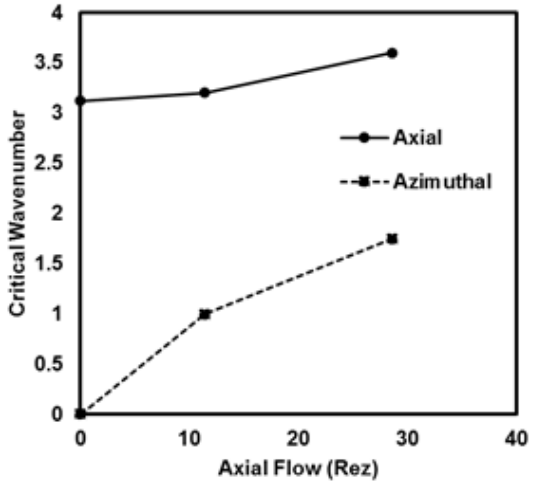

Figure 4.4.2 Change in axial and azimuthal critical wavenumbers with increasing axial flow.

4.4.2 Metallo-siloxane vs. Polysiloxane

Assessment of chemical bond formation via XPS and FTIR indicated that an increase in axial flow and the onset of instability seems to contribute to the favoring of metallo-siloxane covalent bond formation rather than the formation of homocondensates, which could result in lower surface coverage despite having high grafting density. Surface coverage is a more significant parameter when it comes to ensuring the formation of metallo-siloxane bonds and the preservation of vinyl ($C=CH_2$) methacrylate functionality. In addition, the onset of instability helps in increasing the uniformity of the coating. Such uniformity is not only expressed in terms of a reduction in surface roughness [141], but it also implies increased surface coverage.

There exists a competition between the tendency of MPS to self-polymerize and the degree of surface coupling through the formation of metallo-siloxane covalent bonds. Although MPS hydrolysis proceeds rapidly, the condensation and formation of hydrogen bonds among MPS molecules and inorganic surface proceeds at much slower rates. Although our conditions are designed to minimize this, these reactions can occur simultaneously in parallel after the initial hydrolysis step. Fine-tuning the flow structure during the silanization reaction allowed for a homogenous molecular distribution of MPS molecules or dimers over well-dispersed particles rather than the formation of homocondensates through oligomerization. From the FTIR bonding data, the onset of instability seems to provide a more homogenous environment that minimizes MPS oglimeration and limits the formation of long-chains of polysiloxane bonds, favoring metallo-siloxane cross-linking. In addition to the increase in the Si:Al atomic ratio from XPS analysis, the SEM morphological color mapping confirms the increase in MPS surface coverage under Taylor vortex flow structure.

4.4.3 Multilayer Structure

As observed via SEM, starting with island type growth configuration [142], the grafted MPS molecules assemble forming a patchy-like morphology [143]. If the MPS molecules are oriented vertically as rods aligned perpendicularly to the aluminum surface, then an estimated grafting density of 4 molecules/nm^2 is enough to form a monolayer [118]. Actual grafting densities usually diverge from such values due to the formation of multilayers. From the grating densities found in this study, we estimate the number of MPS molecular layers to vary from two to four multilayers. Such values are commonly values observed in aqueous silylation methods, with MacMillan citing that 2% silane concentration in aqueous alcohol typically produces between 3 to 8 molecular layers [123]. Such polymolecular films with thickness equivalent to ten or more monolayers can still retain the properties of a monolayer, given that the bilayers remain well-oriented [102]. In this case, head-to-head adsorption of coupling agent layers is the favored orientation and organization within the silane multilayer [102].

Since the spherical aluminum particles are non-porous, by comparing the surface area after functionalization to that of unmodified aluminum particles (2.67 m^2/g), an estimated thickness of the MPS coating was derived. Such hypothetical thickness indicates a higher degree of coating with increasing axial flow, as inferred from TGA and XPS data. But when focusing on the influence of onset of instability, we observe a significantly thicker coating at 0.85 Ta_c. When relating this BET thickness to the mass loss from TGA, the MPS functionalization under Taylor vortices appears to produce significantly more compact silane layers, especially with increasing axial flow. The thickness of monolayers of aminopropyltriethoxysilane and 3-mercaptopropyltriethoxysilane is reported to be around 0.8nm [144], and 0.7nm [145], respectively. Assuming perpendicular orientation of the MPS molecule (as inferred from the significant carbonyl (C=O) bonds detected via XPS) and assuming an expected height of an

MPS monolayer to be 0.8nm, we can interpolate the number of monolayers equivalent to the hypothetical thicknesses derived from BET surface area measurements. Then, given that the grafting density for a monolayer is ~ 4 molecules/nm^2, we estimated the percentage of aluminum surface covered with covalent bonds between the MPS and aluminum (Al-O-Si) as displayed in Figure 4.3.9 (b). As observed from examining coating morphologies from SEM-EDS analysis, functionalization under Taylor vortex flow appears to provide greater surface coverage.

Combining the particle size derived from BET with the size observed via DLS can offers a more detailed understanding of the behavior of these particles. . The BET particle size is compared with those obtained from the DLS analysis performed under different dispersants. Particle sizes derived from DLS tended to be larger, because they are based on the hydrodynamic diameter of the particles, which tend to flocculate and polydisperse depending on the dispersant. The BET surface analysis is considered to be more representative of the coating thickness, as it provides a more bulk analysis that takes into account the surface area of a larger amount of sample. However, particle size derived from BET may be affected by particle aggregation. In addition, particle size analysis from SEM was attempted via ImageJ analysis software, but did not yield any significant trends, as the resolution was less than 50nm.

Though not accurately determined, the thickness of the MPS layer is estimated to vary from 10 to 30nm. While thin siloxane films (with a thickness of ca. 10–50 nm) are sufficient for resin-to-metal coupling [118], the optimum layer thickness for applications promoting paint adhesion require a thickness varying from 50 to 150 nm [113]. Such multilayer coverage has also been deemed more effective than monolayer coverage for the reinforcement of a fiber reinforced composite [146].

Though advantageous for applications that require a uniform surface structure, monolayer cleavage is readily accomplished in high or low pH. Despite their inherently less uniform structure, multilayers tend to be more hydrolytically stable, where the cross-linked network is not dissolved if one bond is broken [123]. Higher MPS grafting densities have been associated with uniform spreading of polymer during composite formation, leading to shell-like polymer growth [142]. Matinlinna et. al noted that strongly hydrophobic MPS films tend to be tens of molecular layers thick, reducing the chance of water penetration and contact with the inorganic substrate [113]. Accordingly, our oxidation test results indicate that the MPS layer on particles functionalized under high axial flow rate (Re_z =32) exhibit higher surface coverage with a greater number of multilayers, minimizing any chance of deterioration due to water contact.

The shift in the XPS binding energies of the carbon peak towards higher peaks at C=O binding energy suggests stronger preservation of methacrylate functionality, especially after the onset of the Taylor vortices. Enhanced monolayer coverage of MPS means close-packing and perpendicular orientation on the functionalized surface. This extended configuration yields compact coating with larger grafting densities. The increased stability of suspensions of particles functionalized under higher axial flow reflects that peripheral MPS molecular layers are aligned properly, as the wettability of silane-treated fillers depends on the proper orientation of the silane on the filler surface.

4.4.4 Chemisorption vs Physisorbed MPS

While siloxane cross-linkage on the surface between neighboring silanol residues can enhance the robustness of the assembly [142], physisorbed silane layers showed low mechanical strength and poor resistance to environmental attack [147]. Although the fraction of covalently bonded to the substrate (chemisorbed) usually predominates at the base of the coating layer, there exists

an irregular fraction of peripheral MPS on the coating layer that is primarily of physisorbed structures [148].To improve the mechanical properties of composites, it is required to increase the chemisorbed silane chains, ensuring a well-entangled siloxane layer [146]. Polycondensed silane multilayers tend to be complex, and distinguishing physically adsorbed silanes from chemically conjugated self-assembled monolayers (SAM) is rather difficult [128]. Although accurate control of silane growth may be critical to systems that involve molecular devices, for most applications, the distinction between monolayer and a vaguely-defined multilayer is not a significant concern [128]. In this study, we defined physisorbed silane to be the fraction of mass loss under 200°C in the TGA curve. The very low oxidation rate and increased miscibility of particles functionalized under high axial flow conditions (at Re_z=32) indicate that much of the adsorbed MPS was strongly chemisorbed, while particles functionalized at less intense mixing conditions (Re_z=0 , Re_z=8) exhibited coatings that seemed be more loosely bound, with quicker desorption.

4.4.5 Particle Dispersion and Agglomeration

Greater particle agglomeration observed in SEM morphological studies under laminar Taylor Couette flow (<Ta_c) is also reflected in the broader particle size distributions (PSD) observed in DLS studies of suspensions in both toluene and water. Such trends have been observed in previous studies that explored crystal size change in precipitations performed below add above the onset of Taylor vortices. Aljishi et al. attributed broader PSD due to large diversity of residence times/contour lengths followed by particles depending on their relative position in the reactor annulus. In contrast, a more homogeneous PSD is observed at the onset of Taylor vortices due to the similarity in contour lengths, where particles are subjected to uniform cellular vortex motion [57]. Curran et al. reported that cells under laminar Taylor Couette flow

tend to increasingly sediment, and that introducing axial flow could help in thwarting the sedimentation, with the onset of Taylor vortices significantly reducing the likelihood of particle sedimentation [56]. Their studies of oxygen mass-transport among cells under laminar and vortex flow structures concluded that mass transfer in the Taylor vortex flow regime to be much more significant, suggesting a stepwise increase in the mass-transfer coefficient during the flow transition [130] .

4.4.6 Predictive Correlations

Although predicting the degree of functionalization in Taylor Couette flow is challenging due to the multiple parameters affecting the silanization process, empirical correlations can be developed based on experimental results presented in this study to quantify the changes in the properties of functionalized particles based on the range of axial flowrates and cylinder rotation rates used in this system. To relate the changes in functionalization to changes in the fluid flow structure, two correlations for Si:Al atomic ratio and MPS grafting density, based on XPS and TGA data, respectively, were developed via nonlinear least squares regression:

Equation 4.4.1 Correlation for predicted Si:Al atomic ratio from XPS analysis

$$Si{:}\,Al\ Atomic\ Ratio = 0.065(Ta_r + 0.48)^{0.76}(Re_z + 4.016)^{0.247}(t + 0.11)^{0.088};\ R^2 = 0.9$$

Equation 4.4.2 Correlation for predicted MPS grafting density from TGA analysis

$$Grafting\ Density\ (\frac{molecules}{nm^2}) = 5.97(Ta_r)^{0.23}(Re_z + 6.18)^{0.19}(t)^{0.049};R^2 = 0.93$$

The equations demonstrate that the change in flow structure, particularly the onset of Taylor vortices, is the dominant factor for improving the degree of functionalization. While the influence of reaction time was also important, the change in axial flow had a stronger impact on MPS deposition on the surface of aluminum particles. These observations are consistent with

studies that showed the change in mass flux of oxygen diffusing in media under vortex flow to be significantly larger, especially when dispersion effects are introduced [56].

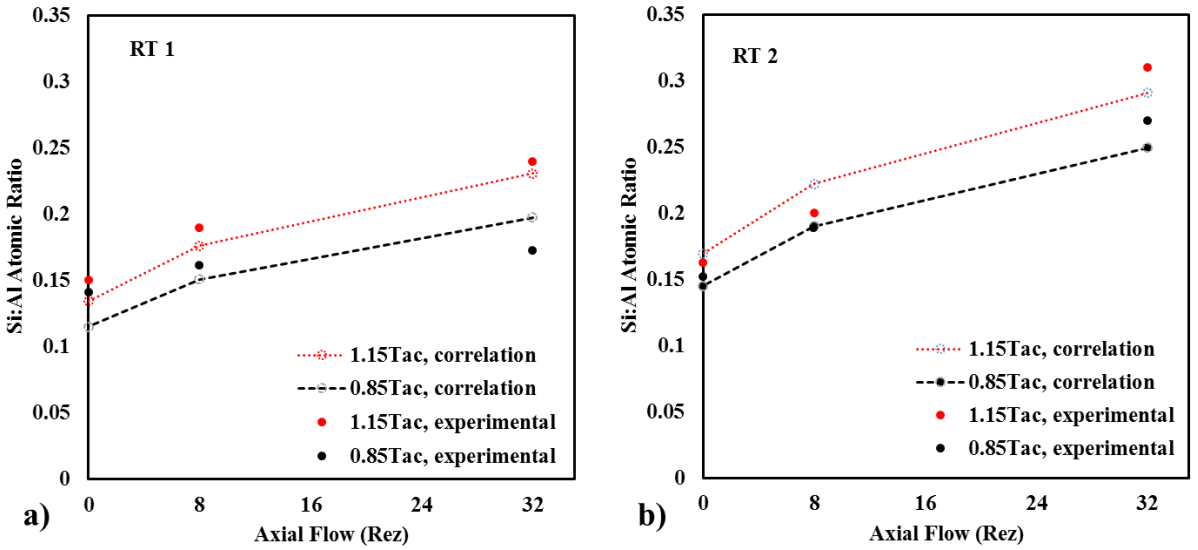

Figure 4.4.3 Comparison of predicted Si:Al atomic ratio compared to measured values.

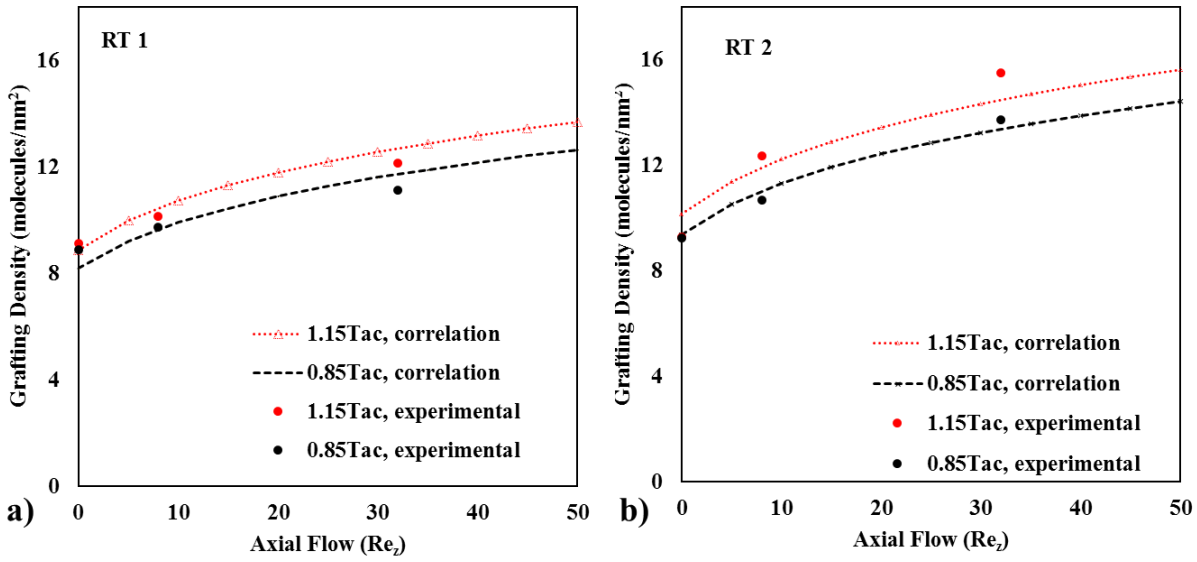

Figure 4.4.4 Comparison of predicted MPS grafting density compared to measured values.

4.5 Conclusion

Conventionally, organosilane coatings have been known to be primarily influenced by reaction conditions such as pH, catalysis and filler surface topology [102]. The current study

on functionalization of aluminum with MPS below and above the onset of instability in Taylor Couette flow provides empirical evidence on the influence of changing hydrodynamic conditions on the degree of organosilane self-assembly and in fine-tuning the overall coating properties. In general, the increase in mixing due to increased shear associated with growing axial flow was found to be critical in enhancing coating efficiency, providing particles with superior properties. At the same time, the onset of vortex instability provided more uniform surface coverage and narrower variation in coating pattern, as evidenced rom SEM and DLS particle size measurements. As evident in our study, MPS functionalization of aluminum improves the anticorrosive performance of aluminum pigments, which could be applied in water-borne paint, a more environmentally benign alternative to organic solvent based paints. As such, aluminum pigments can retain their silvery appearance and minimize deterioration of their metallic glare [134].

CHAPTER 5

DEVELOPMENT OF CONTINUOUS SCALABLE PROCESS FOR PRODUCTION OF FUNCTIONALIZED METAL FILLERS VIA TAYLOR COUETTE REACTORS

5.1 Introduction

Development of high performance hybrid materials that involve the incorporation of inorganic building blocks into an organic matrix is a promising approach to enhance properties of materials through synergistic interaction between their various components [149]. The processes for making such materials require the uniform dispersion and placement of metallic fillers within polymeric matrix. This is particularly important when it comes to developing metallic particles with enhanced optical properties, which requires a high degree of homogeneity and optical transparency. The dispersion of metal particles into liquids or polymers is required for the fabrication of optoelectronic devices, nonlinear optical devices [149], and color filters [100]. In such systems, metal fillers act as the active optical component, while the host polymer matrix stabilizes and disperses the particles in ways that enhance optical clarity [100]. Poly-methyl methacrylate (PMMA) has been identified as one of the suitable versatile polymeric materials for preserving the metallic appearance of for polymer-metal composites due to its high transparency and durability, even at high particle contents [103].

Optimizing such a metallo-organic framework remains challenging, as the macroscopic properties of the resulting composite is dependent not only on the individual fillers and/or polymer, but is also significantly affected by the polymer-metal interface [100]. Metallic fillers and polymer matrix in general have very poor affinity, which gives rise to inhomogeneous structures as well as poor material properties [118]. For the creation of such high potential polymer/metal composites, it is critical to control the phase-mixing of the filler inorganic

particles within the organic polymer matrix to prevent misalignment and aggregation [102]. Increasing affinity between metal filler and matrix by modifying fillers' surface is crucial to attain compatibility of the nanoparticles with the polymer matrix and the prevention of poor alignment [149].

As a method that preserves the bulk properties of filler material, surface modification of metal fillers is a common approach to achieve a desired surface functionality that enhances the interface between metallic aluminum particles and polymer matrix [100]. Such wet-chemistry functionalization approach is usually done through the assembly of organosilanes over filler surface through covalent bonding with the hydroxyl-terminated surface of the thin oxide layer that protectively encompass metals such as aluminum [150]. Organotrialkoxysilane monomers, such as methacryloxypropyltrimethoxysilane, provide organic functional radicals that can be readily co-polymerized. As a monofunctional unsaturated monomer, MPS provides light absorption/emission in the desired region due to its index of refraction (1.42) being close and almost matching to that of PMMA (1.49), thus offering high light transmittance [103]. MPS has been shown to alter the surface energy of metallic particles, and Silane coatings on aluminum, as low as 2wt%, have been reported to allow for more than a two-fold increase of combustion front velocity [151].

Silanization of inorganic surfaces with organofunctional alkoxysilanes is typically done in either dry aprotic solvents, both polar [103] [104] [105] and non-polar [106] [107] [108] [119], protic aqueous environment [110] [111] [112] [101] [113] [114] [115] [116] [117] [118], and is occasionally done in pure water [119], [120]. MPS silanization under dry environment is sometimes carried out in polar-aprotic solvents, such as DMF [103], but is most commonly applied via non-polar aprotic solvents such as Toluene, with inert environment and reaction

times that vary from 16 hours [119] all the way to 24 hours [106] [107]. Under such conditions, high temperatures that range from 55C to 70C are usually needed to promote condensation, as well as a catalyst, such as maleic anhydride [104] [105] or 2,6-dimethylpyridine [107], and an anti-polymerization radical scavenger agent, such as hydroquinone [109] [108]. Such temperatures have also been used in aqueous environments that include methanol [118], ethylene glycol [121], boiling acetone [104] [105] and water-ethanol [117] mixtures, with reaction times that vary from 2hours [104] [105] to 24hours [118]. MPS silanization under aqueous alcohol environment of either ethanol or propanol has been done under milder conditions that require no heating, and shorter residence time (varying from 3minutes [111] to 90 minutes [110]). An acidic environment of pH~4.5 is maintained to act as both a reaction catalyst, and anti-polymerization radical scavenger [102] [122]. To avoid inconvenient complex processing steps associated with silanization under aprotic environment, the grafting in this study was done by preparing separate mixtures of coupling agent (MPS) and aluminum particle suspensions in the midst of 90% 2-Propanol (IPA), with a pH of 4.5, then mixing the separate solutions within the reaction vessel. Prior to that, the MPS is first hydrolyzed by the trace quantities of water present in the solution followed by reaction with surface silanols forming covalent bonds with the surface. Water content is minimized to avoid the formation of extensive polysiloxane bonds that can lead to the formation of silsesquioxane structures [150] [123].

Process arrangements suggested for the production of nano-composites should have the capacity for scaling up the process to be at least in the kg-range, coupled with transforming the production approach from batch-type to a continuous mode of production [152]. In comparison with reactions carried out in batch reactors, continuous flow configuration offers great benefits that include miniaturization, better control over reaction parameters, improved process safety,

simpler product recovery, and enhanced productivity through transport intensification [153]. In addition to producing reproducible coating layers, functionalization of metallic fillers and nano-composite production via continuous flow methodology offers the ability to provide more efficient and predictable reaction scale up [154]. In this regard, Taylor-Couette reactors offer a well-characterized mixing environment that can be conveniently operated in a continuous-flow fashion with high-throughput [93], [94].

Understanding mixing characteristics and influence of flow behavior on mass-transport during such functionalization reaction is critical for the development of polymer-metal hybrid fillers with uniform and well-characterized coating layer. As a model reactor system where flow takes place in the annulus between two concentric cylinders, Taylor-Couette flow allows for examining hydrodynamic instabilities while stimulating vortex motion, offering a highly active interface for mass transfer and phase mixing [17]. Although the flow is steady and purely azimuthal for low angular cylindrical velocities, a series of hydrodynamic instabilities emerge during the gradual increase of inertial forces against viscous forces [13]. Emerging vortices act to increase the surface area of the interface between different and partially unmixed materials, offering a high surface-to-volume ratio [55].

The present work involves both the development of a scalable continuous flow surface modification process for the functionalization of disk-shaped micron-sized aluminum fillers with MPS monomer surface functionality, designed for industrial applications that aim at overcoming misalignment of disk shape fillers in polymer composites. Due to the effect of flow and filler shape, the disk fillers tend to align along the thickness direction of the mold. Providing resistance to orientation via controlling interaction between filler and matrix can reduce misalignment.

In most silanization processes, the functionalization reaction is done under variable mixing environment that utilizes magnetic stirring to induce agitation and increase particle dispersion within the solvent [107] [108] [109] [110]. Though stirring speeds are rarely reported, intense stirring conditions are often desired [124]. However, no studies so far have examined the effect of rate of mixing on the degree of functionalization. This study focuses on examining the favorable aspects induced by the functionalization in Taylor-Couette flow relative to conventional tank-vessel reactors. Then we focus on delineating the effect of reaction time and the introduction of axial flow on enhancing the surface functionality of aluminum fillers. The resulting surface-modified fillers were applied to injection/compression molding, and evaluated for metal-like appearance. This study aims to provide a guide towards the continuous high throughput production of aluminum particles with uniform surface functionality.

5.2 Materials & Experimental Methods:

5.2.1 Materials

Disk-shaped aluminum powder (3 to 20 microns) was obtained from Samsung. γ-methacryloxypropyltrimethoxysilane (MPS) was purchased from Momentive under commercial name Silquest A-174®. 2-Propanol (IPA), Glacial Acetic Acid was purchased from Fisher. Deionized water was used throughout the study.

5.2.2 MPS Solution Preparation and Reaction

Acetic Acid was used to adjust pH to 4.5, chosen specifically to minimize the rate of condensation between silanol groups of monomeric silane molecules to larger oligomers, promoting to more stable silane solutions [112]. Higher pH values were found to produce weaker bond strengths than those obtained with silane solutions at pH = 4.5 [155]. 90% Isopropanol (IPA) was particularly chosen as a solvent because hydrolysis of MPS occurs more

readily in Iso-propanol relative to ethanol [155]. Even in coupling experiments done in the medium of ethanol, 2-propanol was used to improve the solubility of the homocondensates [126]. Previous studies that involved the preparation of stable dispersions of nano-sized silica modified by MPS demonstrated the ability to control the degree of grafting of MPS on silica in 2-propanol as needed [127]. Solutions hydrolyzed at different times (up to two hours) were subject to FTIR analysis which indicated no change in the absorption spectrum, confirming that MPS hydrolyzes rapidly in 90% Iso-propanol with pH=4.5. Although traces of water have been reported to be essential for the formation of well-packed monolayers [128], water content was limited to 10vol% to help in hydrolyzing the MPS and avoid the formation of complex networks of poly-siloxane bonds that can lead to the formation of silsesquioxane structures [101].

Low silane concentrations ranging between 2 to 3.24 wt% were selected because they are known to produce thin siloxane films (with a thickness of ca. 10–50 nm) enough to promote the resin-to-metal bond [155]. Maintaining a relatively low silane concentration, such as below 5 vol.%, preserves the silane–solvent system in such a balance that the silane monomers do not autopolymerize. Commercial dental silanes are typically of the relatively same concentration level which is ca. 1–5 vol.% and their shelf-life is typically a couple of years [111]. Although grafting density increases with higher silane content, lower MPS concentration is reported to give higher the grafting yield [101]. The silane solutions were allowed to hydrolyze for at least 1h at room temperature. Such hydrolysis time of the silane/IPA solution was selected because it was found to result in optimum coupling of MPS on the aluminum flakes. Shorter hydrolysis times were found to result in poorer MPS coupling.

The methoxy groups react in the acid catalyzed aqueous alcohol solution undergoing hydrolysis resulting, intermediate silanol groups (–Si–OH). Silanols can condense to form stable

condensation products, initially dimeric cross-linked siloxane bonds, –Si –O– Si. Chemically suitable hydroxyl groups are found on the outermost surface of most metal surfaces, which form a thin, passive oxide layer. Once mixed with the filler substrate, the silanol groups will react with the hydroxylated surface of the aluminum fillers initially forming stable hydrogen bonds, which undergo condensation to form stable metallo-siloxane –Si –O– M– covalent bonds at the metal-solvent interface.

Once the reaction is terminated, samples are collected in centrifuge tubes, and centrifuged for 30minutes under 6500RPM. Bressy et al, indicated that the centrifugation step was able to remove unreacted MPS molecules effective in preventing additional MPS-homocondensed layers from bonding to the functionalized surface [1]. For more certainty, samples are washed once with IPA to remove excess silane and then filtered. Once separated, the functionalized particles are dried at 110C for 1 hour to ensure solvent/water removal and to induce further condensation for the formation of strong covalent bonds across the filler surface. Heating for longer time (6 hours) was observed to slightly compromise the MPS coating layer.

5.2.3 Characterization Methods

Detail FTIR analysis of bonding mechanism during salinization reaction was done through Magna Nicolet FTIR spectrometer with a miracle ATR sampling accessory from Pike Technologies (Madison, WI), operating at $4\ cm^{-1}$ resolution. . The spectral subtraction capability of FTIR spectroscopy enables the selective monitoring of the structure of the coupling agent. External pressure was applied on ATR measurement to ensure good contact of the samples with the diamond ATR crystal. Single-beam spectra of the disk-shaped samples were obtained and ratioed against the background spectrum of air to present the spectra in absorbance units. To emphasize the chemical modifications produced by the MPS grafting

treatment, the spectral subtraction method was used, consisting of the subtraction of a reference spectrum from the sample spectrum [156]. Specifically, subtracting the spectrum of the untreated filler from the spectra of the MPS-treated fillers helped eliminate absorbance other than that contributed by silane C=C. The spectra are mathematically processed (including smoothing, baseline correction), in order to minimize noise, and to make the spectra comparable [112].

Quantitative elemental analysis as well as chemical bonding information were possible through X-ray photoelectron spectroscopy (XPS). CasaXPS was used for curve fitting and signal interpretation. Initial confirmation of MPS bonding on Aluminum disk fillers was detected via solid-state NMR (INOVA 500). Automated atomic force microscopy (AFM) (Veeco Dimension 3100) was performed for disk-shaped fillers to assess surface morphology, measure roughness and depth profiles. Surface imaging of particle morphology and aggregation was assessed through Tescan Mira3 Field Emission Scanning Electron Microscopy (FESEM). Energy dispersive X-ray (EDX) spectroscopy enabled elemental mapping of MPS distribution on aluminum surface.

5.2.4 Taylor Couette Reactor Setup:

The experimental setup of the TC reactor, illustrated in Figure 5.2.1, consisted of two coaxial cylinders, with the aluminum inner cylinder rotating while the Plexiglas outer cylinder is fixed. The inner cylinder rotation rate is controlled by a phase inverter, connected to a motor drive that provides rotation rates in the range of 30-1750 RPM.

Table 1 includes the physical specifications of the TC crystallizer used in the current study. The primary hydrodynamic instability marks the transition from Taylor Couette Flow (TCF) to Taylor Vortex Flow (TVF), as determined by the critical Taylor number (Ta_c). Uniformly

spaced counter-rotating cellular vortices, with each pair forming an axial wave, is characterized by critical wavenumber (a_c) and wavelength (λ_c).

As specified by the Taylor number (Ta), the onset of Taylor vortex flow by the centrifugal instability depends on reactor geometry and fluid properties including the gap width and the radii of inner and outer cylinders. As the inner cylinder rotation increases further beyond the critical speed, higher order harmonics become important, leading to a second instability that is marked by non-axisymmetric periodic flow, known as wavy vortex flow (WVF). Flow transitions towards turbulence occur through a progression of flow instabilities, each of which represents a flow regime transition, such as modulated wavy vortex flow (MWVF) and turbulent Taylor flow (TTF).

The dynamic viscosity of the MPS solutions was measured via Ostwald capillary viscometer using water as the reference liquid. Temperature was assumed to be constant in the range of 20°C. The density of the mixtures was derived from the mass balance and the corresponding volume of the solutions. Correlations that describe the properties of slurry mixtures were used to account for the change in viscosity and density due to the addition of aluminum. Given the small volume fraction occupied by the aluminum disks in the solution, the Einstein correlation (Equation 5.2.2) was most appropriate to estimate the dynamic viscosities of the slurry solutions. Meanwhile, Equation 5.2.1 was used to estimate the density of the slurry solutions. As displayed in the reactor schematic in Figure 5.2.1, the kinematic viscosity estimated for all cases was within $\nu = 2.941 \times 10^{-6} \pm 0.007 \times 10^{-6}\, m^2/s$, resulting in negligible variations when it comes to estimating Tar values ($Ta_r \pm 0.005 Ta_r$). The estimated kinematic viscosity was consistent with that obtained from the flow visualization experiment for the onset of instability, as presented in Figure 4.2.3 in chapter 4.

Equation 5.2.1 Estimating density of aluminum slurry solution

$$\phi_{sl} = \frac{\rho_s(\rho_{sl} - \rho_l)}{\rho_{sl}(\rho_s - \rho_l)}$$

Where ϕ_{sl} is the solids fraction of the slurry (state by mass), ρ_s is the solids density, ρ_{sl} is the slurry density and ρ_l is the liquid density.

Equation 5.2.2 Estimating dynamic viscosity of aluminum slurry via Einstein correlation

$$\mu_s = \mu_r \mu_l$$

Where μ_s and μ_l are respectively the dynamic viscosity of the slurry and liquid (Pa·s) and μ_r is the relative viscosity (dimensionless), which is estimated as$\mu_r = 1 + 2.5\varphi$.

5.2.5 Experimental Methodology

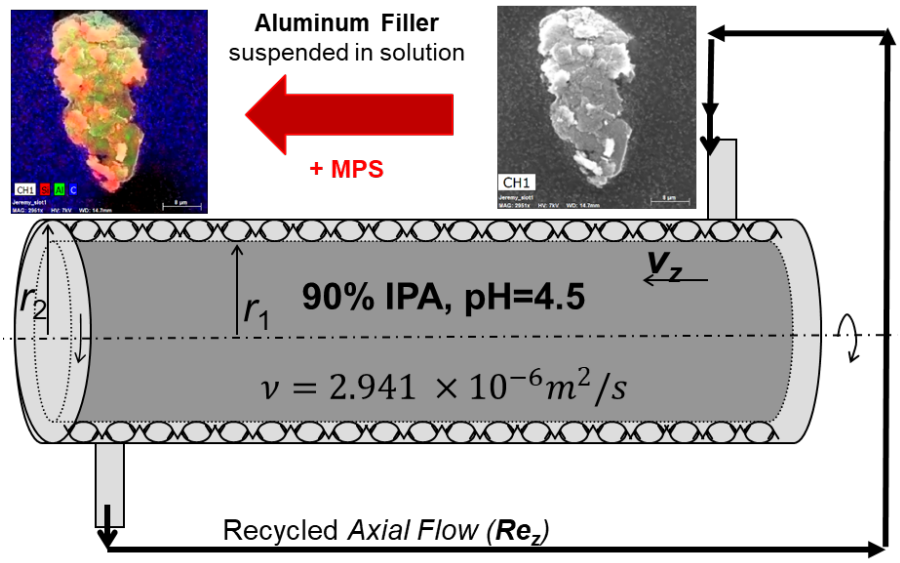

Figure 5.2.1 Schematic of functionalization of Aluminum in Taylor Couette reactor

Table 5.2.1 Dimensions of Taylor Couette Reactor

r_1 (cm)	r_2 (cm)	$d\,(r_2\text{-}r_1)$ (cm)	L_r (cm)	d/r_1	r_1/r_2	L_r/d
2.28	**2.53**	**0.258**	**30**	**0.11**	**0.90**	**116**

5.2.5.1 Performance of Taylor Couette (TC) reactor with Tank Reactor (TR) in Batch Mode

As summarized in Table 5.2.2, 10g of MPS was added to 300ml solutions of 90% IPA solution with pH=4.5, mixed and hydrolyzed for 1 hour under room temperature. The hydrolyzed MPS solution was added to the tank reactor, and mixing was triggered under a stirring speed of 125RPM. 5g of disk-shaped aluminum powder was added rapidly while stirring. The reaction was allowed to go for 60 minutes. A separate sample was done in Taylor-Couette flow (see Figure 5.2.1 for schematic) under rotation rates of 60, 72 and 125 RPM, corresponding to Ta_r = 0.85, 1.2 and 3.6, respectively. Operating at 125 RPM, and with an estimated kinematic viscosity of 3.06×10^{-6} m^2/s, the CSTR solution is subject to $Re = \frac{(RPM) \times D^2}{60 \times \nu} = 272$, where D=20mm is the impeller diameter. The TCR solution exhibited a Re_θ= 251 ($Re_\theta/Re_{\theta c}$ = 1.9), providing close values to that of the tank reactor. The samples were then analyzed with XPS, FTIR, NMR and SEM.

Table 5.2.2 MPS Functionalization conditions and corresponding hydrodynamic parameters for experiments assessing reactor configuration and flow structure.

Al (g)	MPS (g)	Al wt%	MPS wt%	MPS/Al Weight Ratio	Solvent Volume (ml)	RPM range	Ta/Ta_c	Residence Time
5	**10**	**1.9**	**3.87**	**2.0**	**300**	**58 - 125**	**0.85 - 3.9**	**60 minutes**

5.2.5.2 Influence of Reaction Time

With the same preparation approach, additional experiments were carried out under batch mode to examine the influence of long residence time on the degree of functionalization with the conditions shown in Table 5.2.3.

Table 5.2.3 MPS Functionalization conditions and corresponding hydrodynamic parameters for experiments assessing the influence of reaction time.

Al (g)	MPS (g)	Al wt%	MPS wt%	MPS/Al Weight Ratio	Solvent Volume (ml)	RPM range	Ta/Ta_c	Residence Time
5	**2.5**	**1.9**	**0.98**	**0.5**	**300**	**600**	**91**	**0.16 to 22 hours**

5.2.5.3 Influence of Continuous Axial flow in Taylor-Couette (TC) Reactor

2.8 wt% MPS solutions of 90% IPA solution with pH=4.5 (2.05 vol% MPS), was mixed and hydrolyzed for 1 hour under room temperature, as displayed in Table 5.2.4.. Directly following the addition of the MPS solution to the TC reactor, aluminum disk fillers were seeded into the reactor, resulting in a 5.5wt% aluminum suspension, with an MPS:Al weight ratio of 0.5. The mixtures were recycled under variable axial flow rates: Re_z = 4.5, Re_z = 14 and Re_z = 26 with short and long residence time: 1 and 2 minutes, while the rotational speeds varied from 100 RPM, 200 RPM, to 600 RPM, at each flowrate. For the largest axial flow rate, additional experiments at rotation rates of 400, 800, 1000 and 1200 RPM were performed. Under the range of axial flow rates used, the solutions were subject to variable shear flow with Taylor numbers ranging from Ta/Tac~1.6 (laminar Taylor vortex flow regime) to Ta/Tac~226 (weakly turbulent flow regime). The samples were then analyzed with XPS, FTIR, TGA and AFM.

Table 5.2.4 MPS Functionalization conditions and corresponding hydrodynamic parameters for experiments assessing the influence of axial flow.

Al (g)	MPS (g)	Al wt%	MPS wt%	MPS/Al Weight Ratio	Solvent Volume (ml)	RPM range	Ta/Ta_c	Flow Rate (ml/s)	Rez	Residence Time
15	**7.6**	**5.5**	**2.8**	**0.5**	**300**	**100 - 1200**	**1.6 - 226**	**2, 6.1 , 11.7**	**4.5, 14, 26**	**1min, 2min**

5.3 Results

5.3.1 Performance of TCR and Tank Reactor (TR) in Batch Mode

5.3.1.1 Bond Characterization

FTIR analysis of the functionalized aluminum powder was performed to confirm the addition of the proper addition of the MPS surface functionality to the disk-shaped fillers and to confirm specific bonding interactions. Figure 5.3.1 shows the FTIR spectra that was obtained for the neat aluminum (unfunctionalized) and the MPS-functionalized samples for both the tank reactor and Taylor Couette reactors in batch mode under 100RPM stirring speeds. While the spectrum for the neat aluminum had limited features, the functionalized samples exhibited clearly distinctive features associated with MPS coupling. The peaks associated with the spectrum for the Taylor Couette functionalization are clearly more prominent than those observed in the case of the tank reactor.

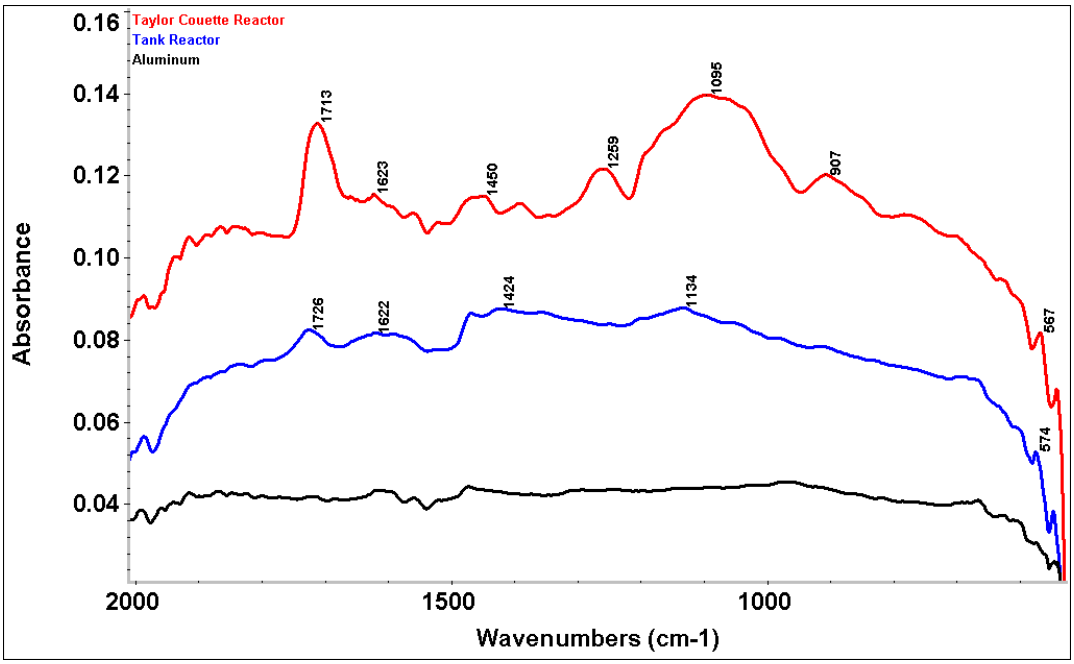

Figure 5.3.1 FTIR spectrum of neat aluminum, and functionalized disk-shaped filler under batch mode in Tank reactor and Taylor Couette reactor

5.3.1.2 XPS Surface Analysis

Surface atomic composition of the samples was acquired via high resolution XPS in parallel with FTIR data collection. All three samples were probed to binding energies from 0 to 1000eV, displaying peaks corresponding to O1s (532eV), C1s (282) and Al2p (70eV). The functionalization of the disk-shaped fillers is confirmed by the reduction in the Aluminum binding energy peak and a corresponding increase in the peak for silicon, Si2p (99eV). The reduction in aluminum and increase in Si was observed to be more significant for the sample functionalized in Taylor Couette reactor. A shift in the Si2p peak towards higher binding energies could be attributed to additional Si-O-Al covalent coupling. While C1s signal peaks were also observed in the neat aluminum (from surface contamination due to adsorbed organics), the carbon peaks of the functionalized samples were shifted to the right. The larger area in the range of 287-290eV is attributed to C=O binding energy. The Si:Al atomic ratio derived from XPS data for the sample functionalized in Tank reactor was 1.2, while that of the Taylor-Couette was Si:Al = 3.2.

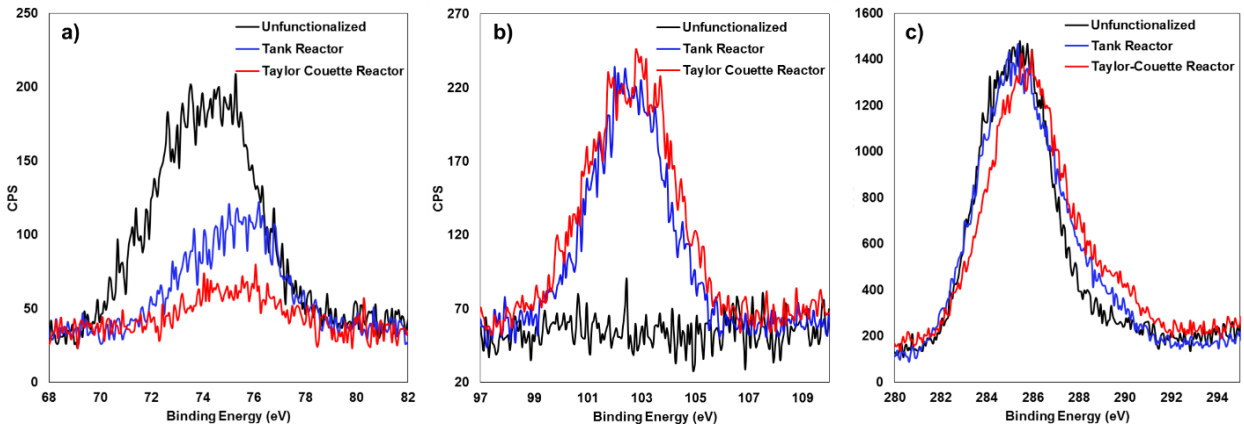

Figure 5.3.2 High resolution XPS analysis of Aluminum (a), Silicon (b) and Carbon (c)

5.3.1.3 Thermal Analysis

To monitor the reaction efficiency, the mass loss due to the thermal decomposition of the organic component under nitrogen atmosphere was measured via TGA for each functionalization condition, as displayed in Figure 5.3.3. These curves represent the degradation of the MPS monomer, either physisorbed, bound, or in polymer form, on the particle surface. While the loss between 100 and 200 °C is attributed to physisorbed monomer, the drastic mass loss beyond 200°C indicates the significant decomposition of any MPS that was either covalently bound to the aluminum surface or polymerized into strongly adhered MPS layer [109]. Based on the surface area of the filler particles (6.6 m^2/g, measured via BET), the MPS molecular density on the surface was estimated from the TGA decomposition pattern, as described by Bressy et al [157]. The corresponding grafting densities, coupling efficiency (% of MPS grafted) along with the Si:Al atomic ratio from xps analysis for each reactor configuration are summarized in Table 5.3.1.

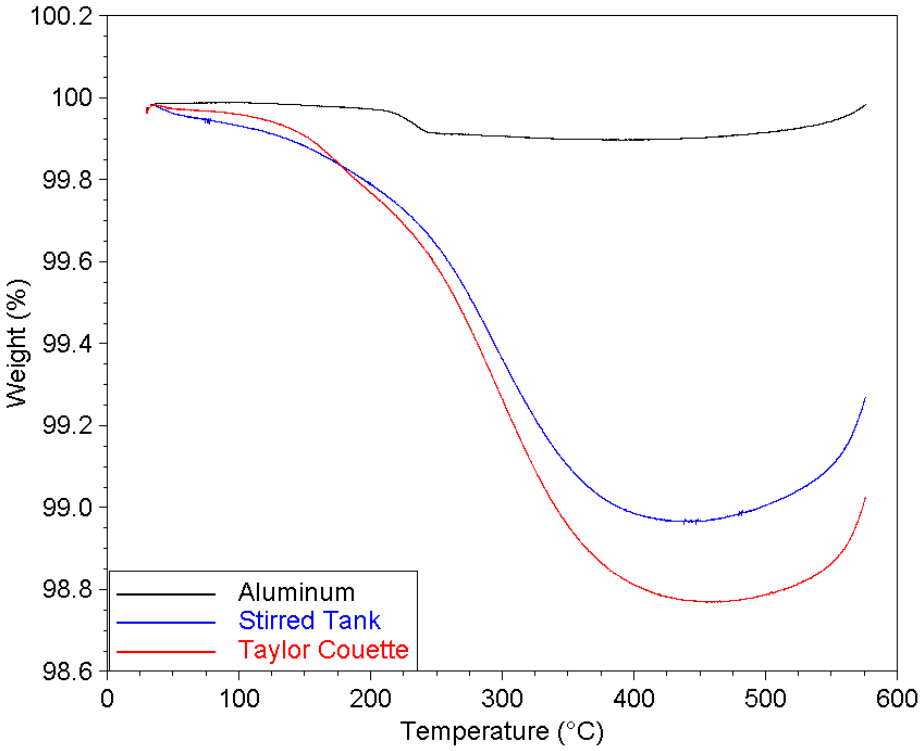

Figure 5.3.3 TGA analysis for reference aluminum disk particles and the particles functionalized under tank and TC reactors.

Table 5.3.1 Comparing the degree of functionalization in TC reactor compared to CSTR

Mixing Configuration	**Grafting Density (molecules/nm^2)**	**Coupling Efficiency %**	**Si:Al atomic Ratio**
CSTR	**3.7**	**1.4**	**1.2**
Taylor Couette	**4.5**	**1.7**	**3.2**

5.3.1.4 **Surface Coverage**

The surface coverage and uniformity of MPS grafting on the surface of aluminum fillers was assessed via Chemical characterization in the scanning electron microscope (SEM). A meaningful image of the elemental composition and distribution for each sample was enabled

using energy dispersive X-ray analysis (EDX). Elemental maps of functionalized fillers in Tank reactor and Taylor Couette reactor are displayed in Figure 5.3.4. The functionalization in the tank reactor resulted in less uniform distribution of MPS molecules over the surface, resulting in an uneven surface coverage of MPS, compared to that observed in Taylor Couette Reactor.

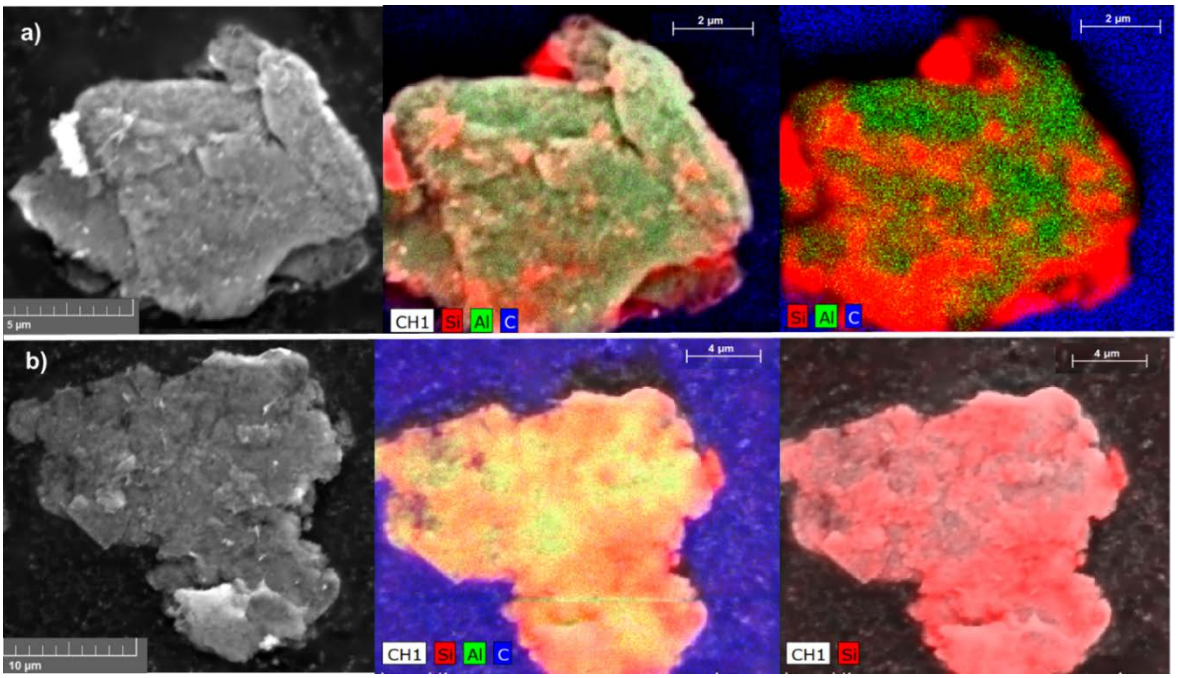

Figure 5.3.4 Elemental maps of functionalized aluminum disk-fillers under 100RPM in batch mode in Tank reactor (a) and Taylor Couette reactor (b)

5.3.1.5 **Influence of the Onset of Instability on Particle Dispersion**

As concluded in chapter 4, greater particle agglomeration observed in SEM morphological studies under laminar Taylor Couette flow ($<Ta_c$) than in Taylor vortex flow (see Figure 5.3.5). The particle agglomerates observed by the latter flow regime were relatively smaller and more uniform in size than those observed for particles functionalized in a tank reactor.

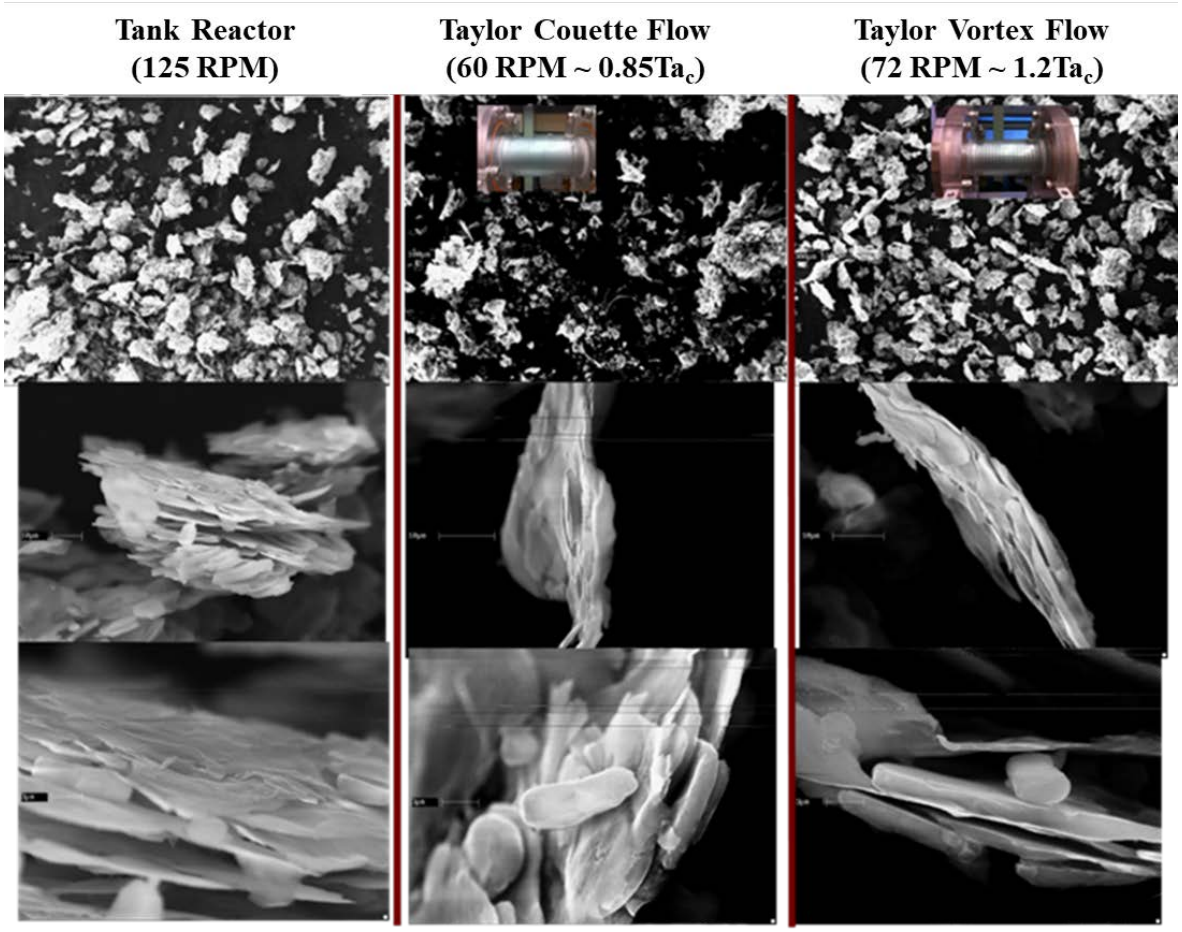

Figure 5.3.5 dispersion of functionalized particles under different reactor configurations.

5.3.1.6 **Surface coverage elemental analysis**

To further confirm the uniform distribution of MPS over the filler surface, a line profile of the elemental composition along the length of the filler was taken to assess the lateral distribution and homogeneity of the grafted MPS molecular layer as displayed in Figure 5.3.6. The silicon binding energy is evenly distributed along the length of the filler with stable peaks. The enhanced functionalization in Taylor Couette reactor is also confirmed by the EDX elemental composition displayed in Figure 5.3.6 and the individual elemental maps of carbon, oxygen, silicon and aluminum displayed in Figure 5.3.7.

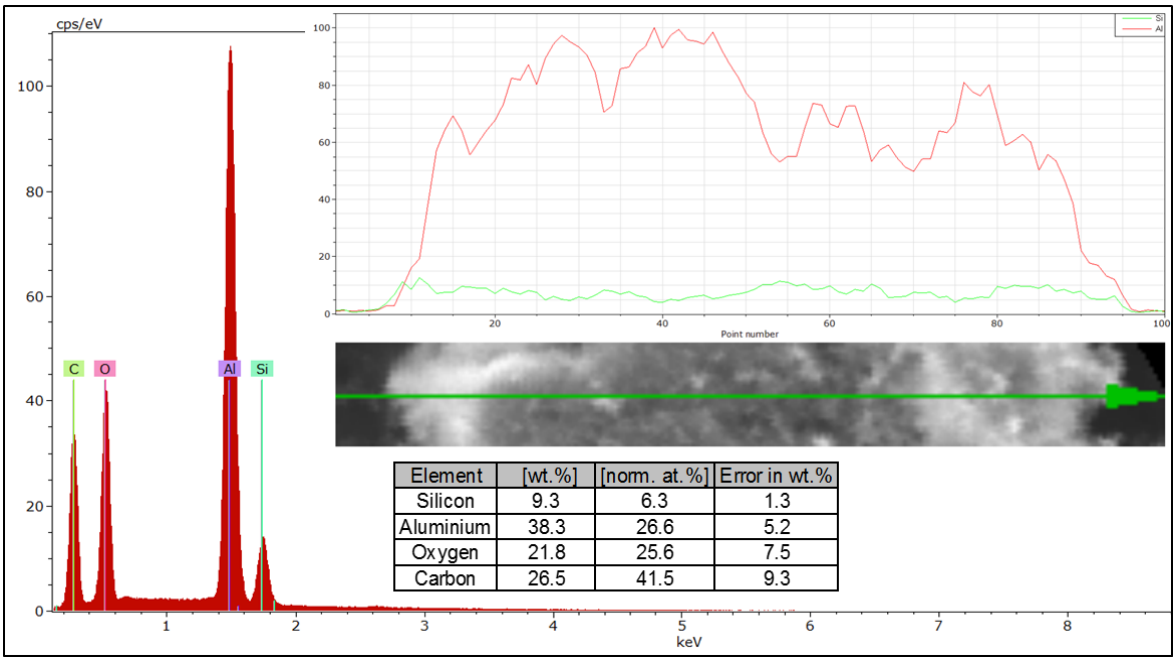

Figure 5.3.6 EDX elemental composition for fillers functionalized in Taylor-Couette Reactor at 100RPM. The specific elemental composition along the length of the filler is displayed in the top corner

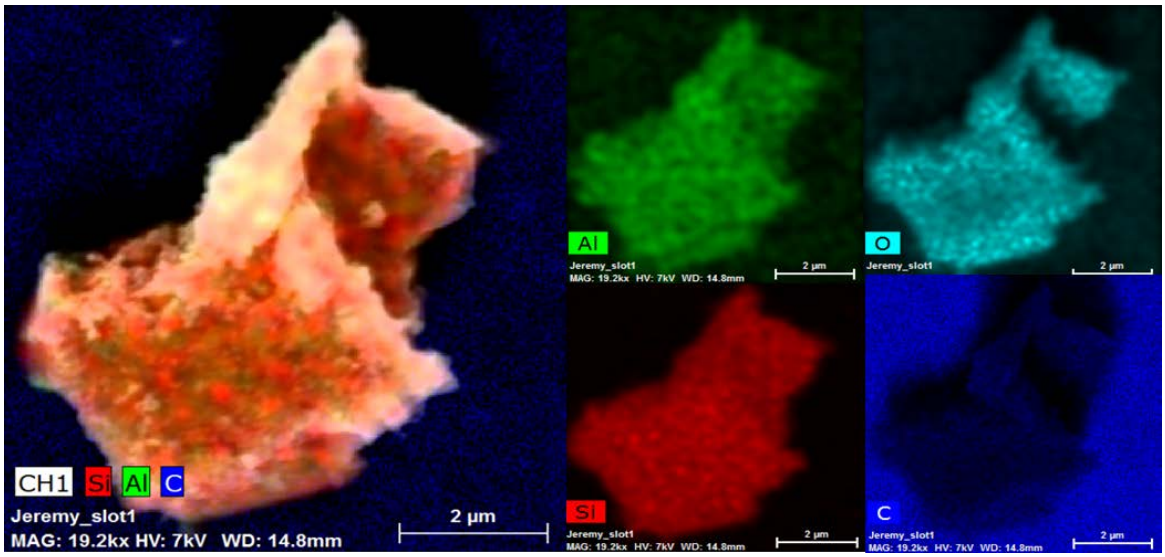

Figure 5.3.7 Elemental maps for aluminum disk-shaped fillers functionalized under Taylor Couette flow of 100RPM.

5.3.1.7 FTIR Analysis of MPS layer on Aluminum

To examine the functionalized layer on the disk-shaped fillers, the FTIR spectrum for the sample functionalized in Taylor Couette reactor were subtracted arithmetically from the spectrum for the neat aluminum. By comparing the resulting spectrum with the MPS spectrum, Figure 5.3.8 displays the peaks and confirm their association with MPS. The MPS monomeric ligand react with the surface hydroxyls present on the amorphous oxide passivated layer on the aluminum fillers, thereby covalently anchoring the monomers to the filler surface. Peaks from 900 to 1000 cm^{-1} are attributed to the formation of metallo-siloxane (Al-O-Si) bonds anchored on the surface. Formation of siloxane networks Si-O-Si is indicated by peaks between 1000 and 1200 cm^{-1}. Absorption bands in the range of 1400 to 1500 are attributed to the CH_2, CH_3 bending and scissor vibration Peaks at 1720 cm^{-1} (C=O) and 1639 ($C=CH_2$) confirm the preservation of the desired MPS surface functionality. Upholding the acrylic portion of the MPS ligand ensures the opportunity to directly incorporate the particles into methacrylate composite systems.

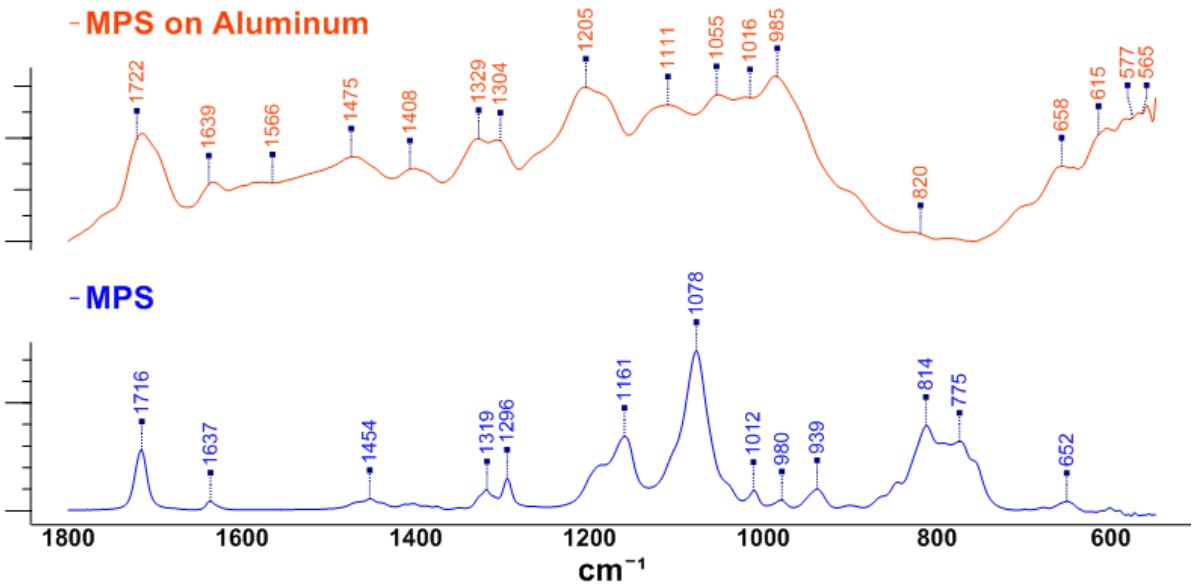

Figure 5.3.8 FTIR spectrum of MPS surface functionality on aluminum (top) and MPS reference spectrum (bottom).

5.3.1.8 NMR Analysis to Confirm MPS Coupling

NMR analysis of the disk-shaped filler functionalized in Taylor Couette reactor displayed in Figure 5.3.9 confirms the presence of the MPS with all its characteristic bonds. The band observed at 128 ppm is ascribed to the nonpolymerized double bonds of the methylene carbons [158] [121] [159].

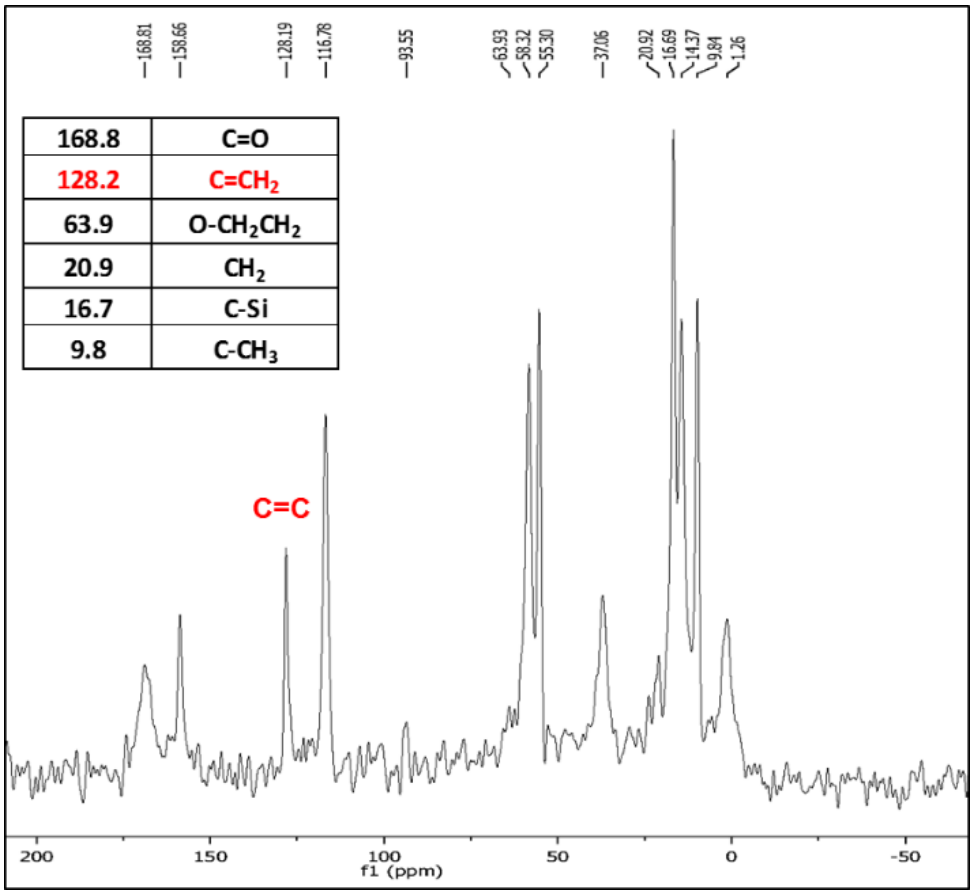

Figure 5.3.9 NMR analysis of the perseveration of monoacrylic surface functionality via the characterization of the Acryloyl group, where the C=C and C=O bonds are conjugated

5.3.1.9 Angle-resolved XPS Analysis of MPS layer on Aluminum

The structure of the MPS layer on aluminum was investigated using angle-resolved XPS, and the resulting depth profiles are summarized in Figure 5.3.10. Overall the peak strengths of all

elements decreased considerably moving from a depth of 27nm to 9nm. While aluminum still registered at the smallest depths, silicon appeared more strongly even at the largest depths. This implies that the coating layer could be larger than 7nm, which is the accepted sensitivity of this technique [160]. The elemental concentration data in Table 5.3.2 shows some differences in the atomic concentration of each element at different depths, indicating preferential functional group-substrate interaction rather than the formation of a lamellar network structure of siloxane chains [160]. This is further confirmed by the increase in Si:Al atomic ratio as you move from within (27nm) towards the outer coating layer (9.2nm). This is further confirmed by the shape of the elemental peaks (Figure 5.3.7) as well as their shift towards higher binding energies at largest depths (27 and 26nm), which correspond to the binding energies of Al-O-Si metalosiloxane bond (O1s (533eV) [132], Si2p (102) [160]. and Al2p (73eV)) [157] and methacrylate carbonyl carbon (–COO–) (C1s (288eV)) [157].

Table 5.3.2 Functionalization conditions and corresponding hydrodynamic parameters

angle	depth (nm)	Si	Al	C	O	Si: Al Atomic Ratio
0	**27**	4.4	8.6	52.2	34.8	0.77
15	**26.1**	5.0	10.4	50.2	34.5	0.72
30	**23.4**	5.0	8.2	52.8	34.0	0.90
45	**19.1**	5.0	8.2	52.6	34.2	0.92
55	**15.5**	5.8	7.3	53.3	33.6	1.19
70	**9.2**	5.0	6.8	54.0	34.2	1.11

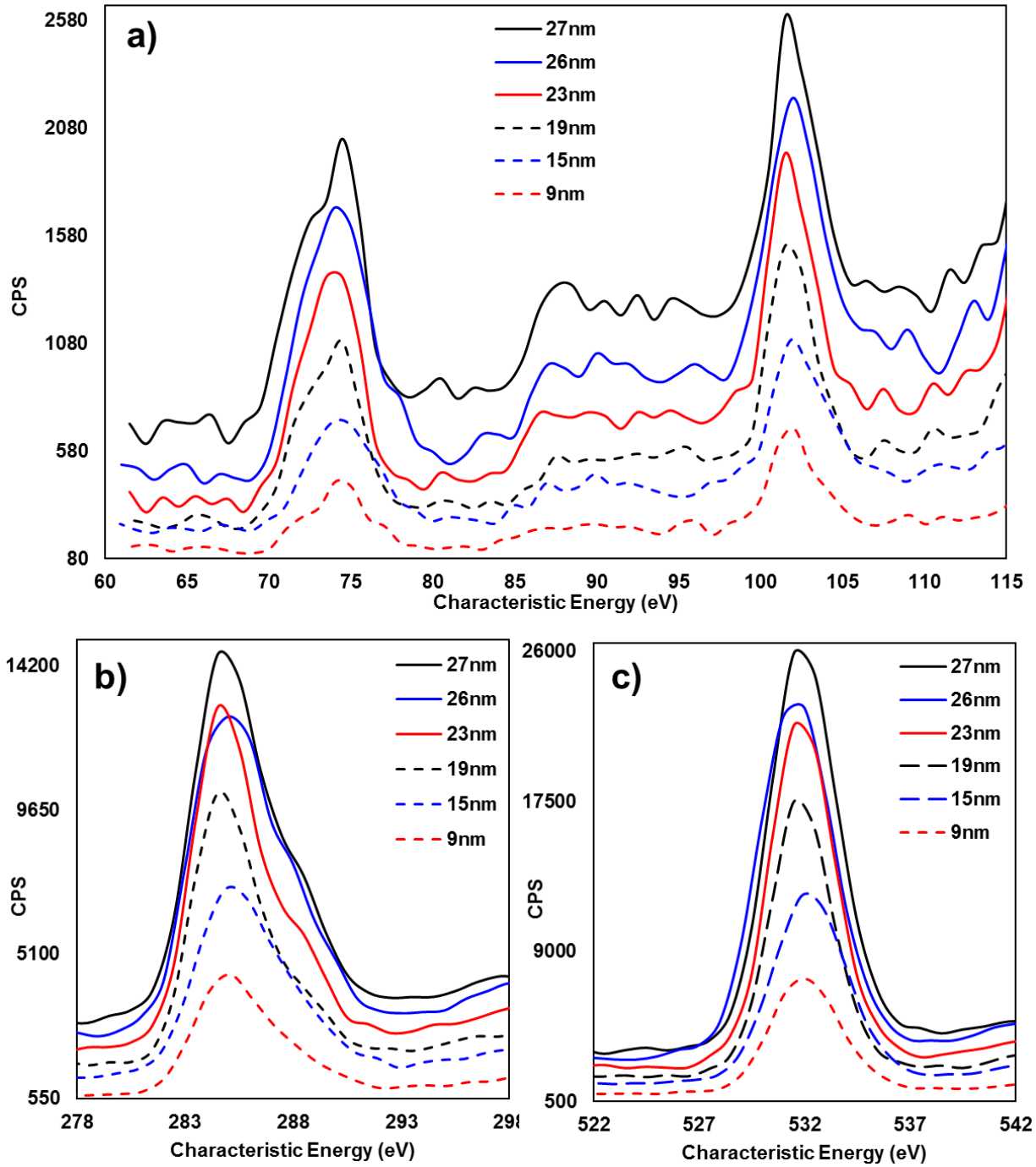

Figure 5.3.10 Angle Resolved XPS analysis of Aluminum (a), Silicon (b) and Carbon (c) and Oxygen (d).

5.3.2 Influence of Reaction Time

5.3.2.1 XPS Analysis

Surface atomic composition of the samples functionalized at different residence times is displayed in Figure 5.3.11 for peaks corresponding to Al2p (70eV) and Si2p (99eV). The higher degree of functionalization of the disk-shaped fillers with increasing residence time is confirmed by the reduction in the Aluminum binding energy peak and a corresponding increase in the peak for silicon. Studies of XPS surface spectroscopy of silane coupling suggested that the center of Si $2p_{3/2}$ ionization in silane compounds ranges between 100.5 and 102.92 eV, depending on the nature of coupling [157]. Increasing the residence time resulted in shifting the center of the Si2p binding energy to slightly higher values. Such higher binding energies are attributed to more bonding of the MPS monomer to the aluminum surface via the formation of covalent metallo-siloxane bonds (Si–O–Al). J.B. Bajat et al. examined the Si2p on Al substrate functionalized with vinyltriethoxysilane and attributed the peak at 103.5 eV for silicon bonded to aluminum [157]. They also indicated that the shift in aluminum Al2p to higher binding energies corresponds to more covalent bond formation between the silane and the aluminum surface, particularly peaks at 73.3 and 74.1 eV (Al–O–Si) [157]. As observed in Figure 5.3.11 of the supporting materials, the peaks for carbon C1s exhibited a similar shift in binding energy towards higher values, particularly in the range of 287.1 to 289.5 eV, which is associated with carbonyl carbon (–COO–) in the silane [157]. The presence of the covalent metallo-siloxane bond (Si–O–Al) was also confirmed by examining the shape of the O 1s (532 eV) spectra. Such trends were quantitatively assessed by estimating the Si:Al atomic ratio, displayed in Figure 5.3.12, obtained from the XPS surface elemental composition.

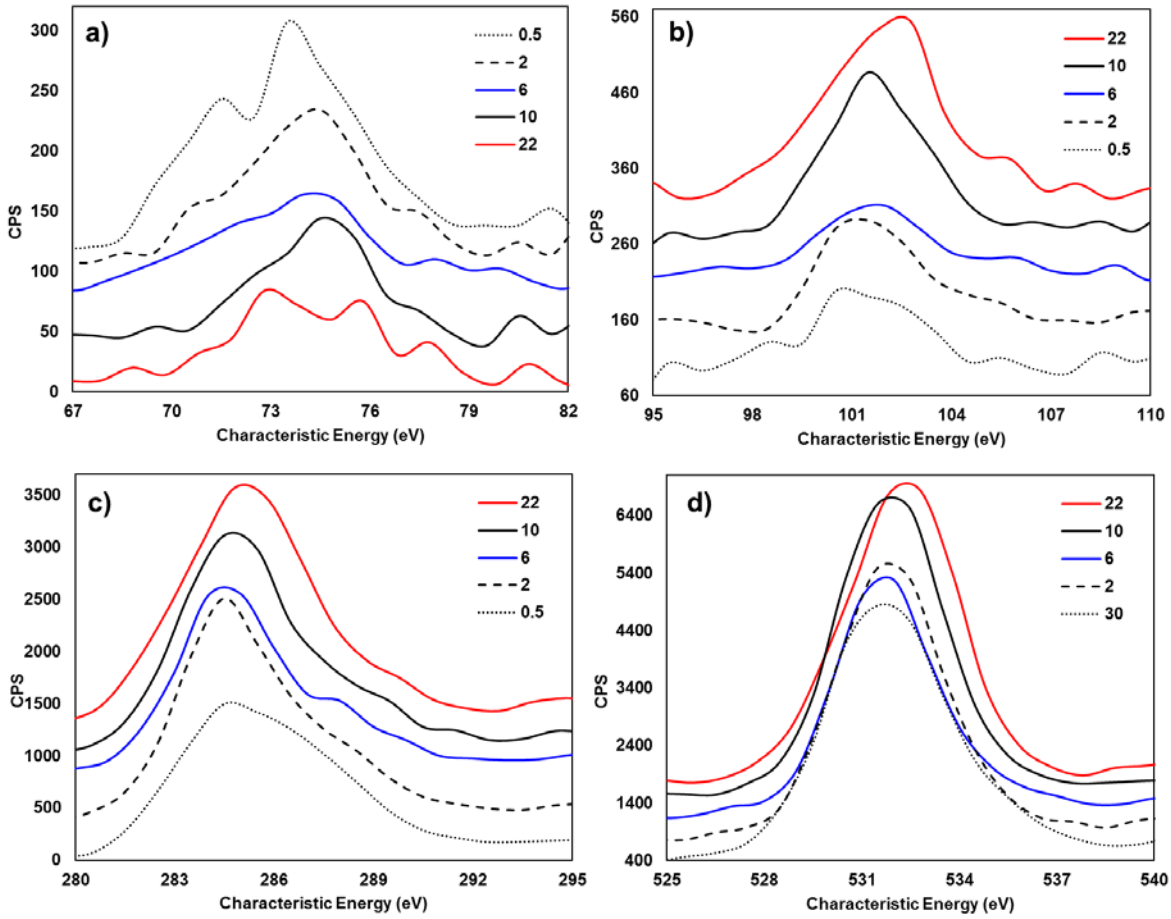

Figure 5.3.11 Influence of changing reaction time in hours on XPS analysis of Aluminum (a), Silicon (b) and Carbon (c) and Oxygen (d).

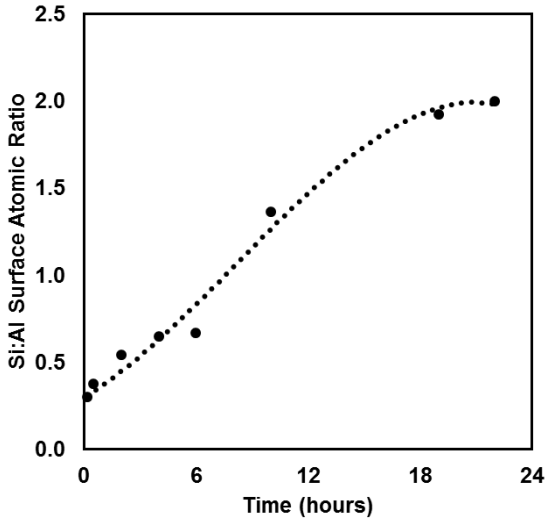

Figure 5.3.12 Change of Si:Al atomic ratio with reaction time.

5.3.2.2 **Thermal Analysis**

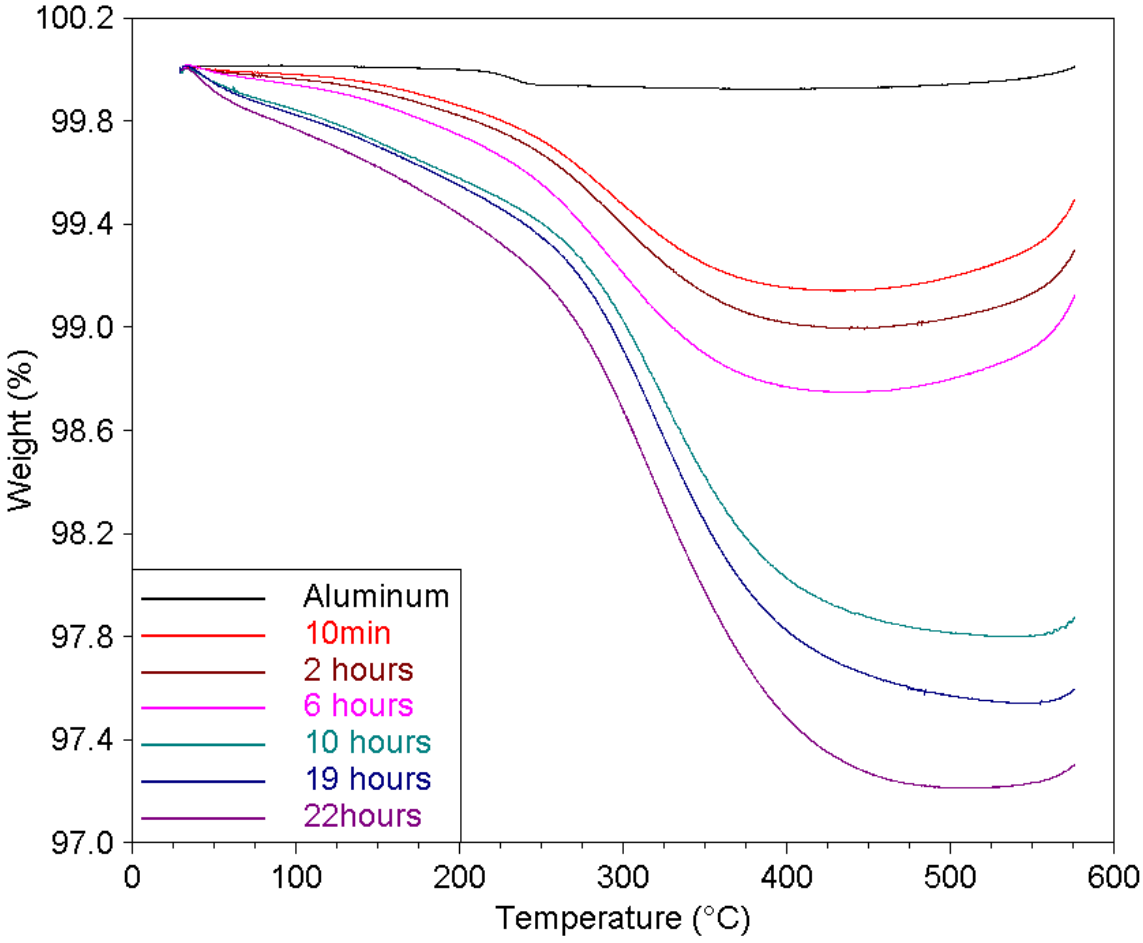

Figure 5.3.13 Influence of changing reaction time on TGA analysis.

To further quantify the change in the degree of functionalization with increasing residence time, the mass loss due to the thermal decomposition of the organic component under nitrogen atmosphere was measured via TGA, as displayed in Figure 5.3.13. These curves display greater degradation of MPS monomers with increasing residence times, indicating an increase in the amount of grafted MPS on the surface of the metallic disks, as quantified by the increase in grafting densities and coupling efficiencies displayed in Figure 5.3.14.

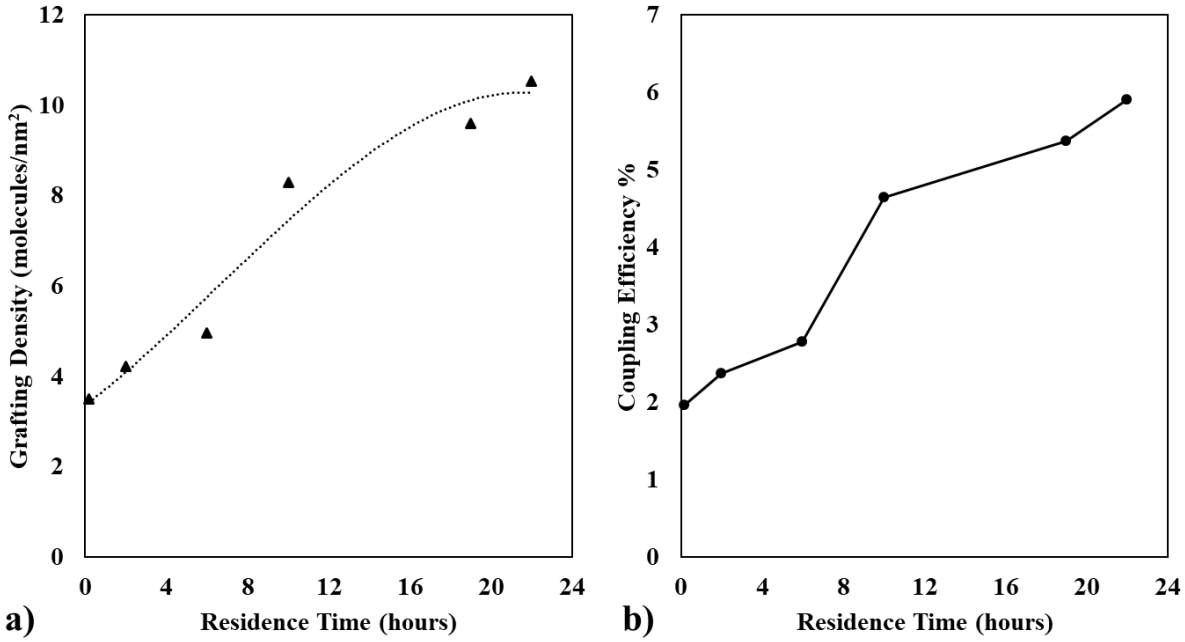

Figure 5.3.14 Influence of changing reaction time on a) MPS grafting density and b) MPS coupling efficiency.

5.3.2.3 FTIR Analysis

To quantify the change in spectral peaks corresponding to the preservation of the methylene functional groups after grafting, FTIR spectral peaks in the range between 1635 cm-1 and 1665cm-1 were mathematically processed with peak area integrals displayed in Figure 5.3.15. Similar to the trends observed via XPS and TGA analysis, stronger concentrations of C=C bonds were observed with increasing functionalization residence time. However, it seems that the degree of C=C functionality changes only a little beyond a residence time of 6hours. This suggests that there may be a threshold residence time after which the polymerization of the methacrylate functional groups, dominates the process of multilayer growth rather than proceeding through the typical orderly growth process through self-assembly [143].

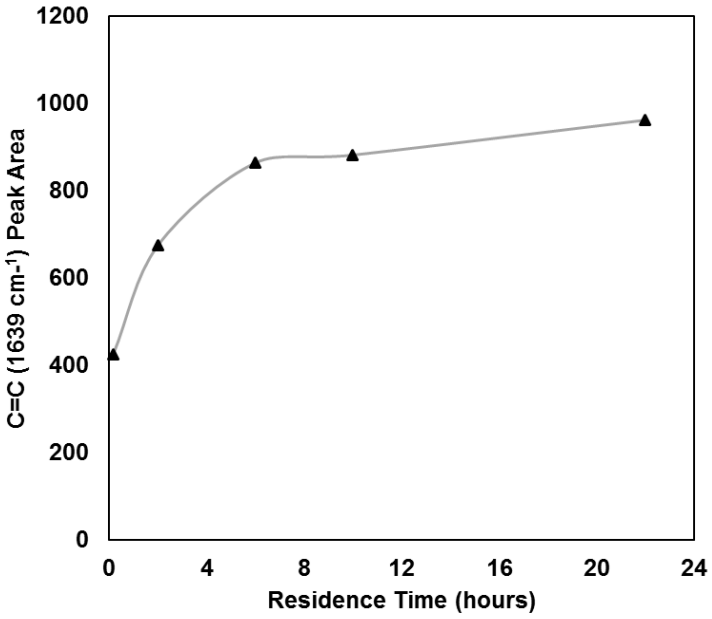

Figure 5.3.15 Influence of changing reaction time on the peak area of the C=C bond characterized via FTIR analysis.

5.3.3 Influence of Continuous Axial flow in Taylor-Couette (TC) Reactor

5.3.3.1 XPS Analysis

XPS analysis showing the surface atomic composition of samples functionalized at different flowrates, rotation rates and residence times are displayed in Figure 5.3.16, Figure 5.3.17 and Figure 5.3.19, respectively. The higher degree of functionalization of the disk-shaped fillers with increasing flowrate, rotation rate and residence times is confirmed by the consistent reduction in the Aluminum binding energy peak, Al2p (70eV), and a corresponding increase in the peak for silicon, Si2p (99eV).

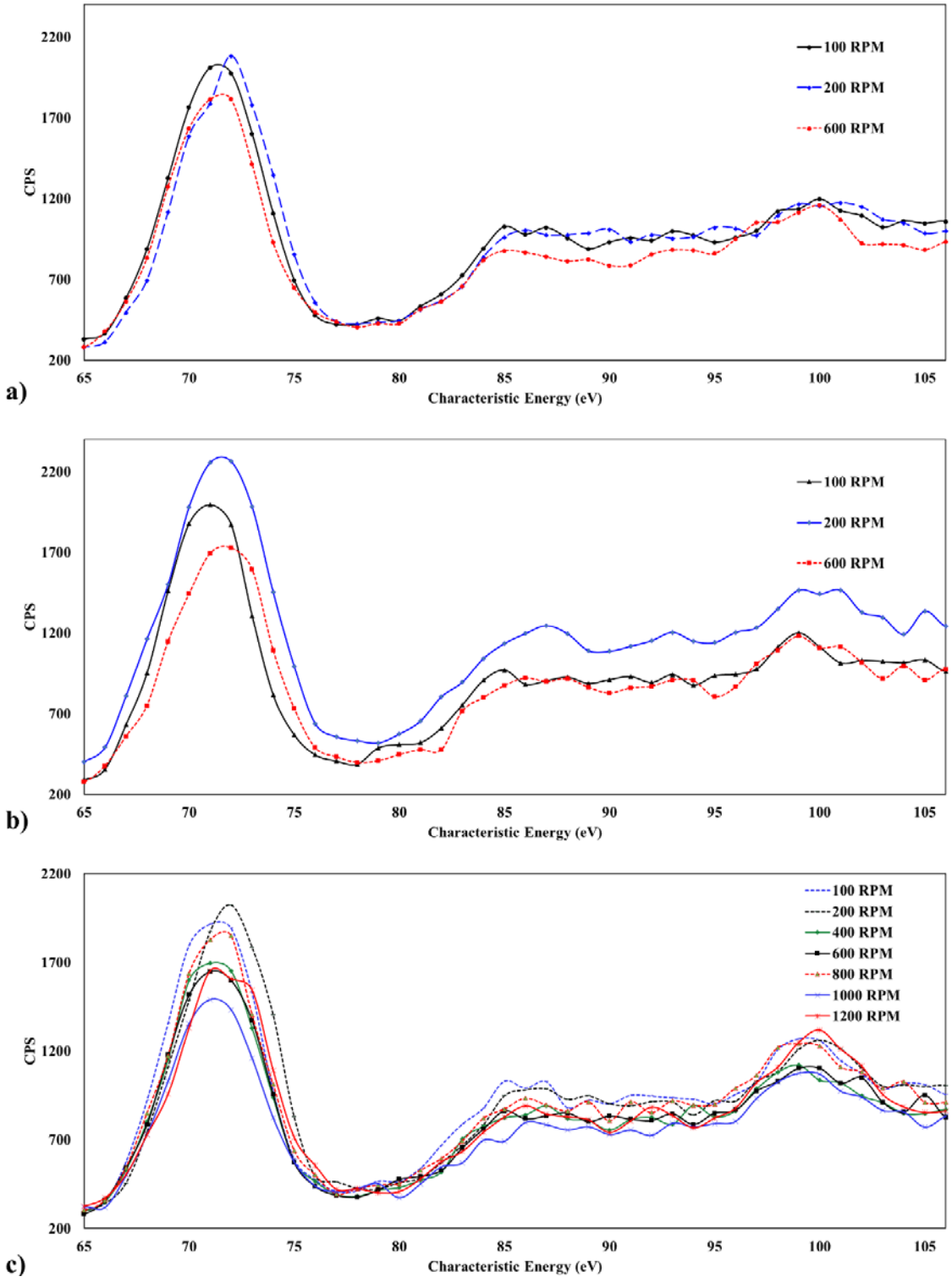

Figure 5.3.16 XPS analysis of Al2p (70eV), and, Si2p (99eV) for samples functionalized under axial flowrates of a) Re_z =4.5, b) Re_z =14 and c) Re_z =26.

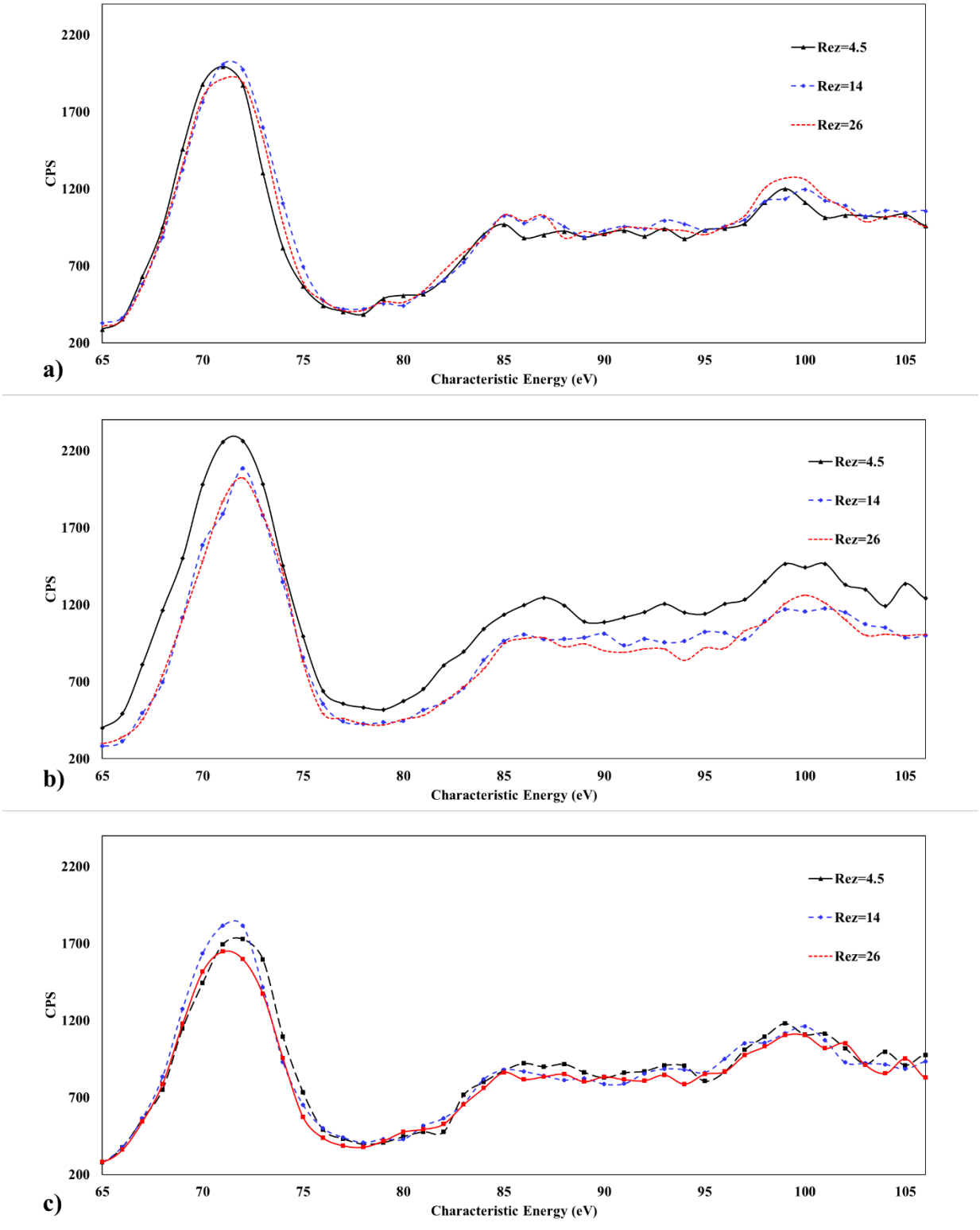

Figure 5.3.17 XPS analysis of Al2p (70eV), and, Si2p (99eV) for samples functionalized under rotation rates of a) 100 RPM, b) 200 RPM and c) 600 RPM.

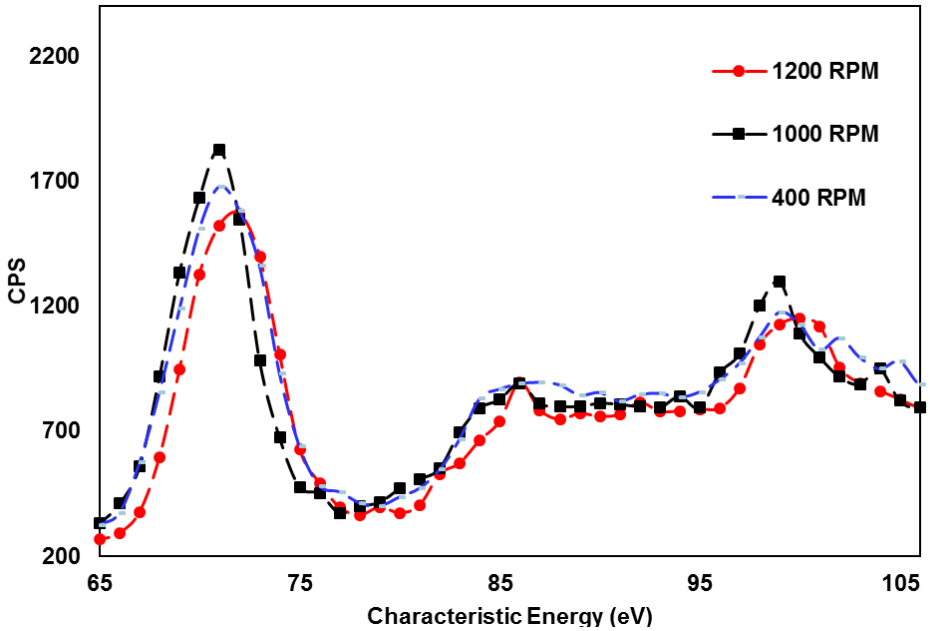

Figure 5.3.18 Comparing the influence of RPM at longer residence time (RT2=10s).

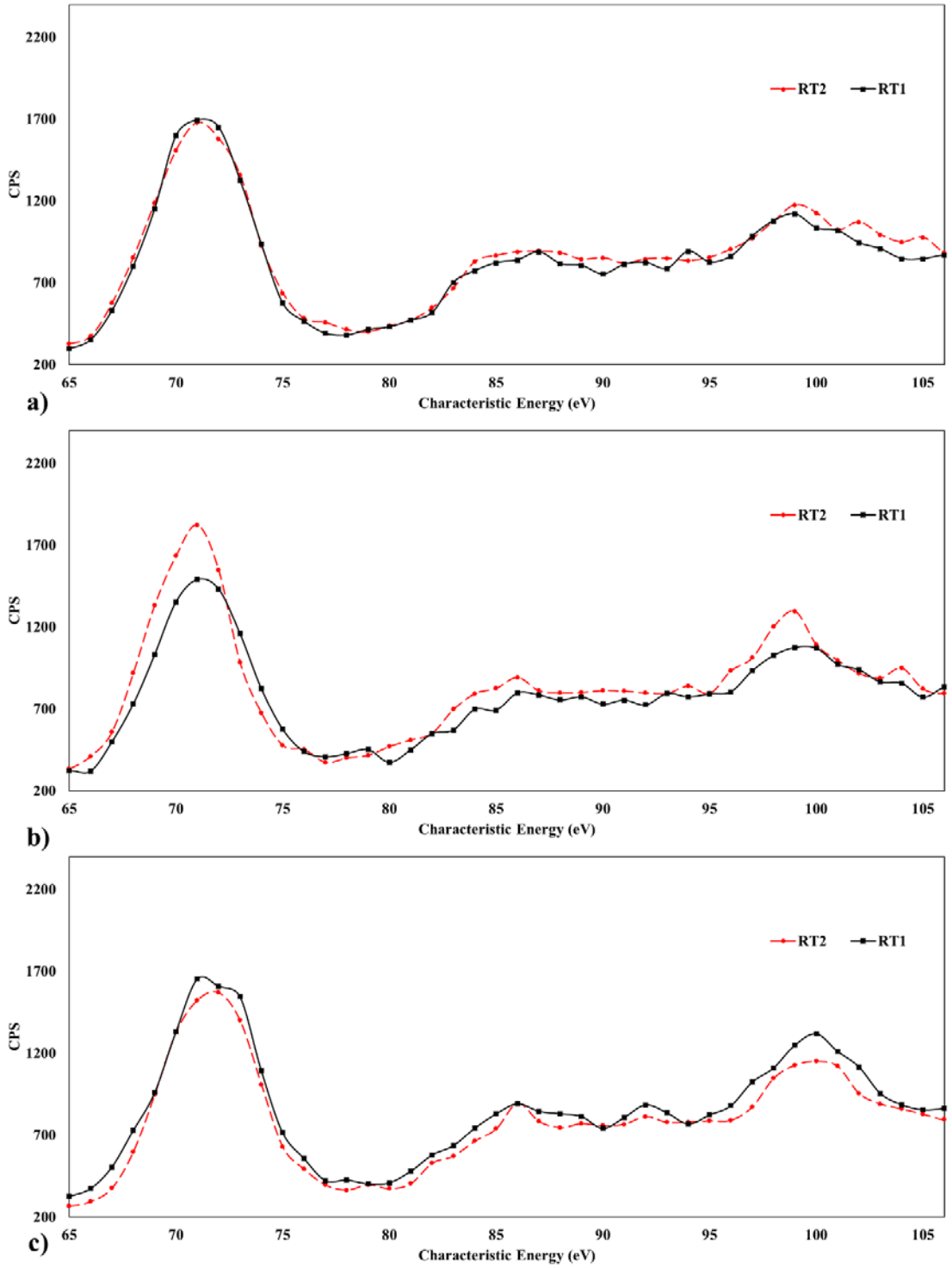

Figure 5.3.19 Comparing the influence of changing residence time on XPS analysis of Al2p (70eV), and, Si2p (99eV) for samples functionalized under rotation rates of a) 400 RPM, b) 1000 RPM and c) 1200 RPM.

To further quantify the impact of axial flow and rotational speed on the functionalization of disk-shaped aluminum fillers with MPS , Si:Al atomic ratio obtained from the XPS surface elemental composition were assessed. As displayed in Figure 5.3.20, the MPS content increases with increasing axial flow and increasing rotational speed of the inner cylinder, marked by the reduced Taylor number (Ta/Tac). It is important to note that a slight increase in the rotational speed, from 100RPM to 200RPM, resulted in great increase in Si:Al ratio. This is marked by the transition in flow structure from laminar Taylor vortex flow to wavy Taylor Vortex flow. Further increase in rotation results in major increase in Si:Al ratio, reaching a maximum around Ta~ 226Ta_c, as displayed in Figure 5.3.20. This indicates that the grandest contribution to the enhanced functionalization occurs within after the onset of modulated wavy vortex flow (MWVF) regime (Ta_r>40), due to the rapid increase in azimuthal nonaxisymmetric vortex oscillations in such flow structure.

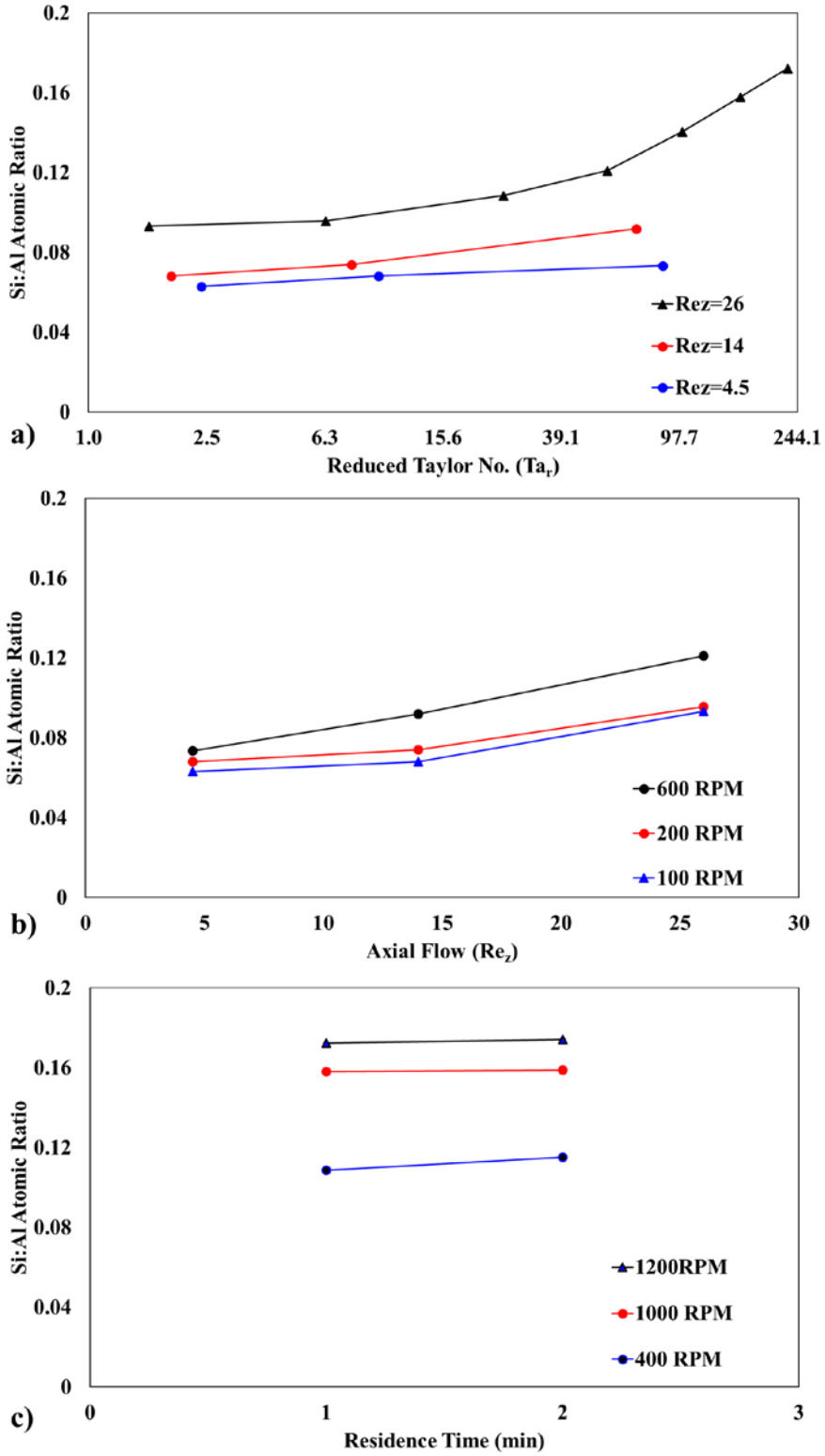

Figure 5.3.20 Change in Si:Al atomic ratio derived from XPS as a function of a) rotational motion, b) axial flowrate and c) residence time.

5.3.3.2 **FTIR Analysis**

The FTIR spectral absorptions observed for these samples were much less intense (see Figure 5.3.21) than those observed in the batch experiments due to the low organic content present on the filler surface, as the residence times involved in these experiments were on the scale of seconds, i.e. 100 times shorter than reaction time for the batch experiment (barely sufficient to obtain an observable IR spectrum). This was confirmed by the low Si:Al atomic ratio observed to be lower than 0.2 compared to 3.2 for the case of 1-hour surface treatment.

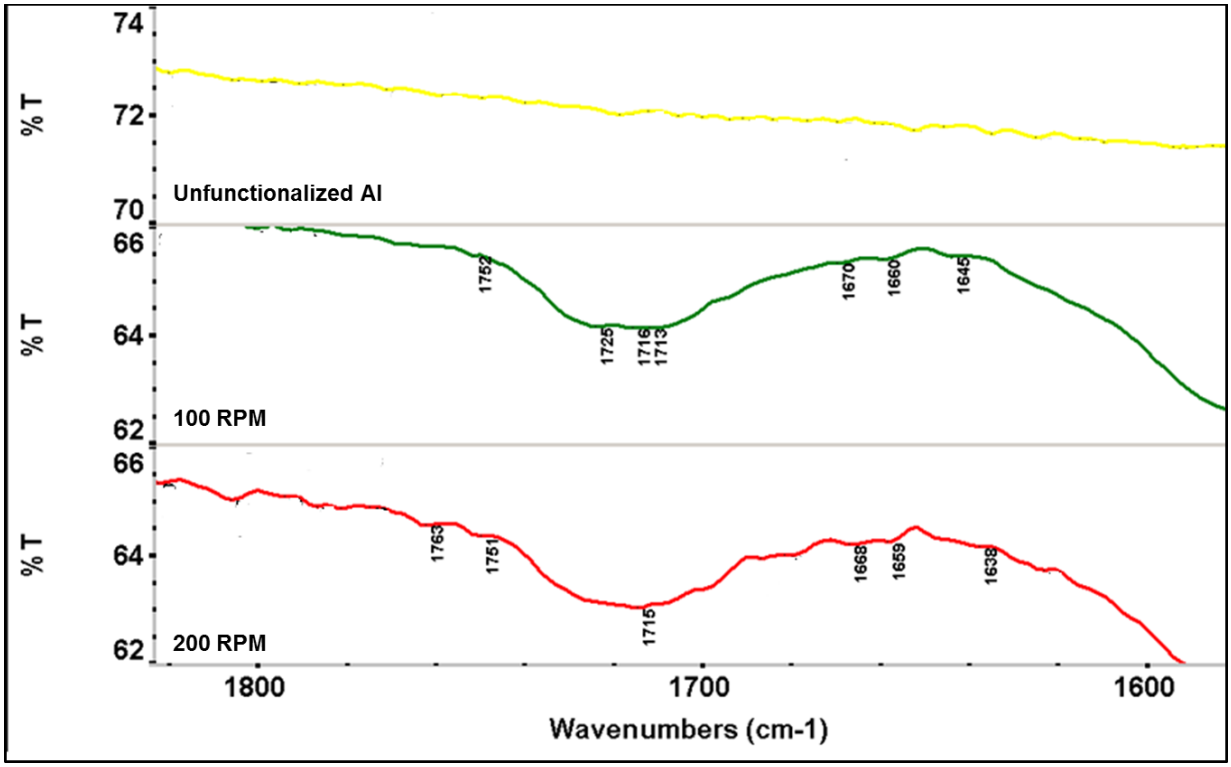

Figure 5.3.21 Sample FTIR characterization of C=C bond.

To quantify the change in spectral peaks corresponding to the preservation of the methylene functional groups after grafting, FTIR spectral peaks in the range between 1635 cm-1 and 1665cm-1 were mathematically processed with peak area integrals displayed in Figure 5.3.22.

We can observe that the C=C functionality increases gradually with the increase in axial flow and with the increase in rotation rates, an indication of the increase in the growth of self-assembled multilayers. The growth, which typically occurs at slow rates [143], was significantly accelerated with the increase in toroidal mixing.

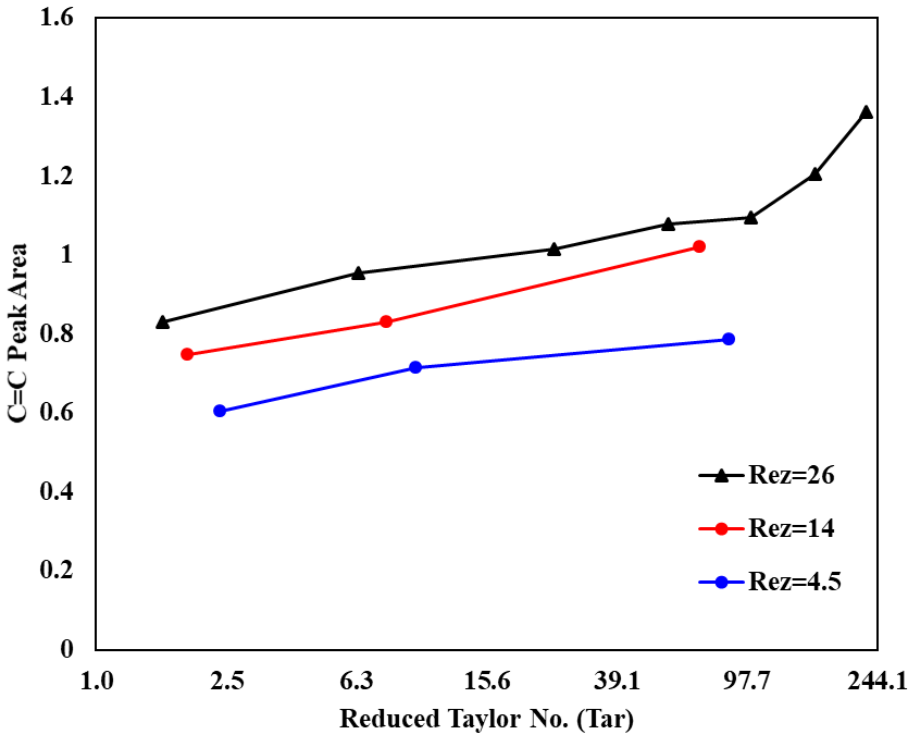

Figure 5.3.22 The change in C=C bond peak area as a function of rotational motion for different flow rates.

5.3.3.3 **Thermal Analysis**

To monitor the reaction efficiency, the mass loss due to the thermal decomposition of the MPS for each functionalization condition, as displayed in Figure 5.3.23 and Figure 5.3.24. The grafting densities estimated from these curves, displayed in Figure 5.3.25, resulted in coupling efficiencies ranging from 1.57% up to 3.75%, with trends proportional to those observed for the graphing densities.

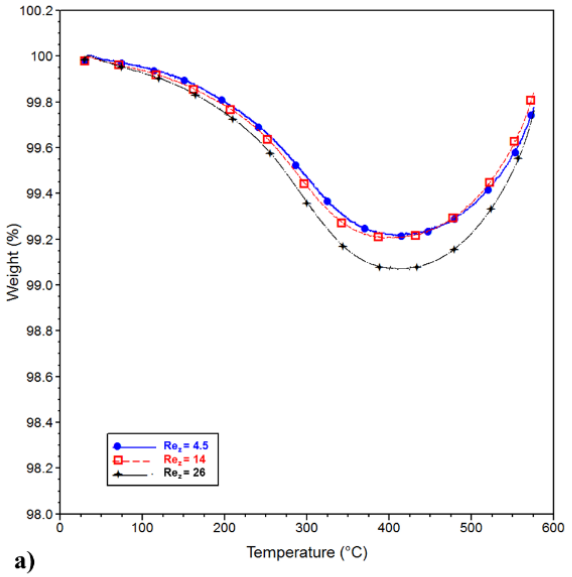
Weight (%)
Temperature (°C)
Re$_z$ = 4.5
Re$_z$ = 14
Re$_z$ = 26

a)

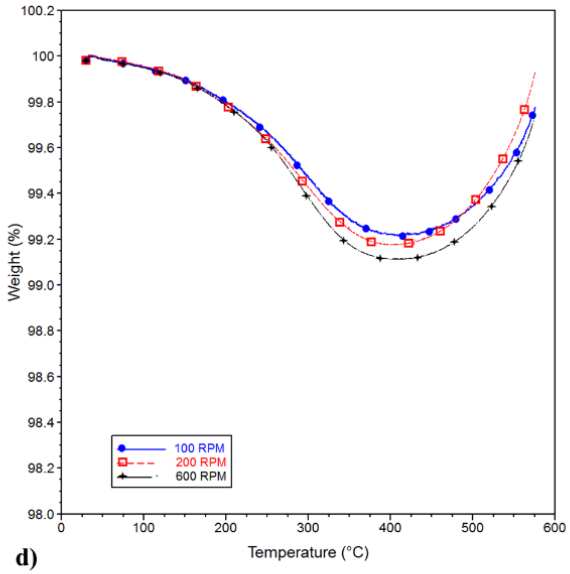
Weight (%)
Temperature (°C)
100 RPM
200 RPM
600 RPM

d)

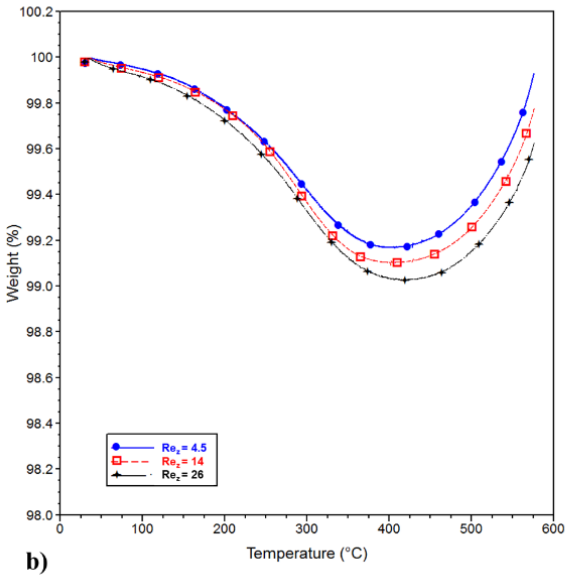
Weight (%)
Temperature (°C)
Re$_z$ = 4.5
Re$_z$ = 14
Re$_z$ = 26

b)

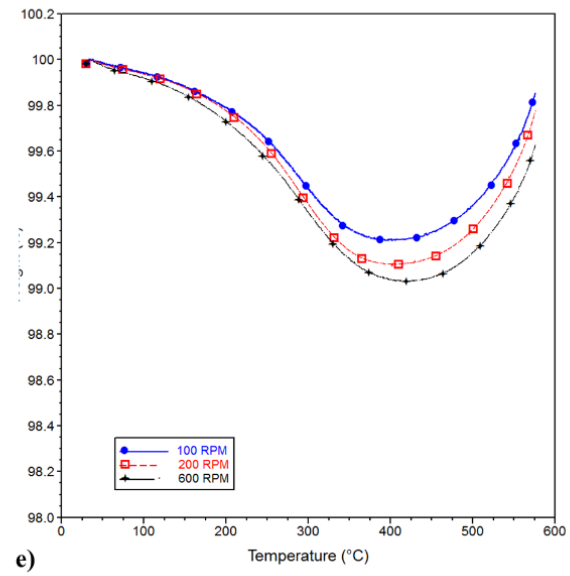
Weight (%)
Temperature (°C)
100 RPM
200 RPM
600 RPM

e)

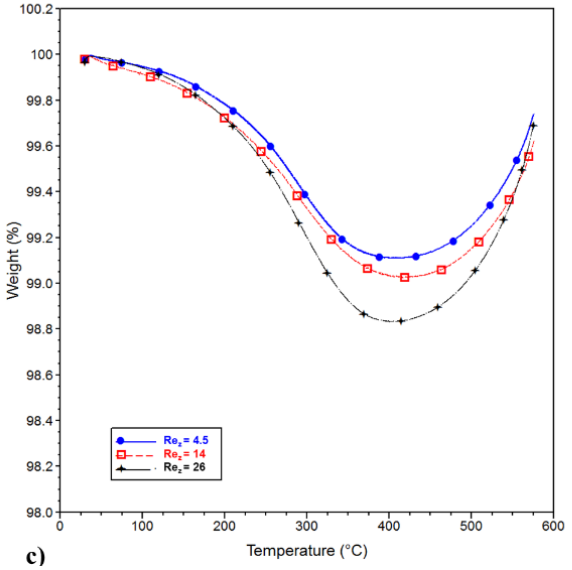
Weight (%)
Temperature (°C)
Re$_z$ = 4.5
Re$_z$ = 14
Re$_z$ = 26

c)

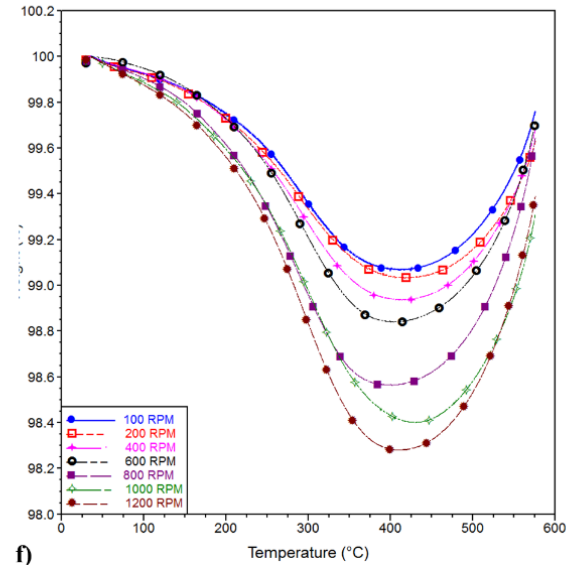
Weight (%)
Temperature (°C)
100 RPM
200 RPM
400 RPM
600 RPM
800 RPM
1000 RPM
1200 RPM

f)

Figure 5.3.23 TGA analysis for the influence of changing axial flow rates at a) 100 RPM, b) 200 RPM, and c) 600 RPM; And for the change in rotational motion at a) Re_z =4.5, b) Re_z =14, and Re_z =26.

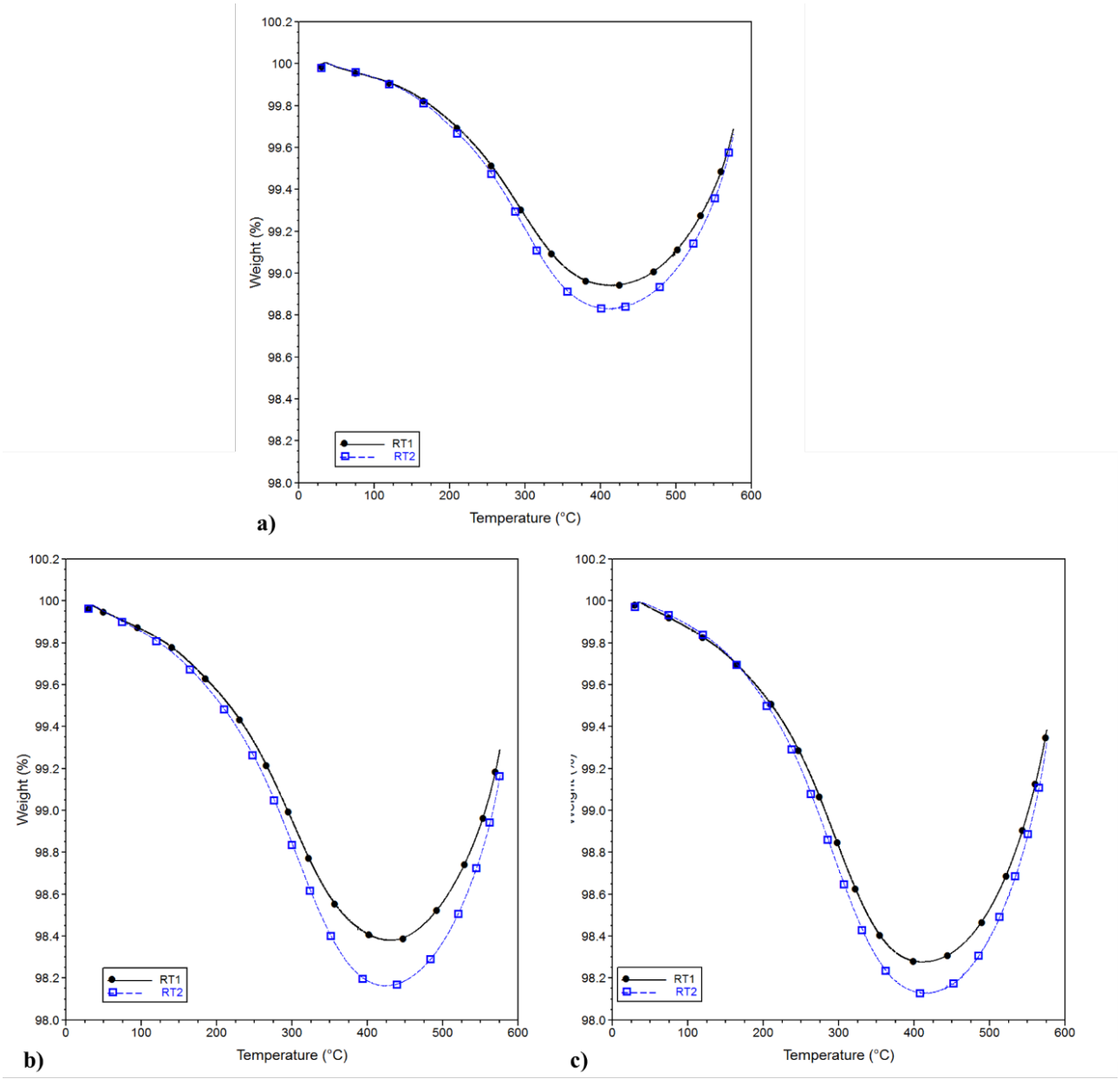

Figure 5.3.24 Influence of changing residence time on the TGA profiles for a) 400 RPM, b) 1000 RPM, and c) 1200 RPM.

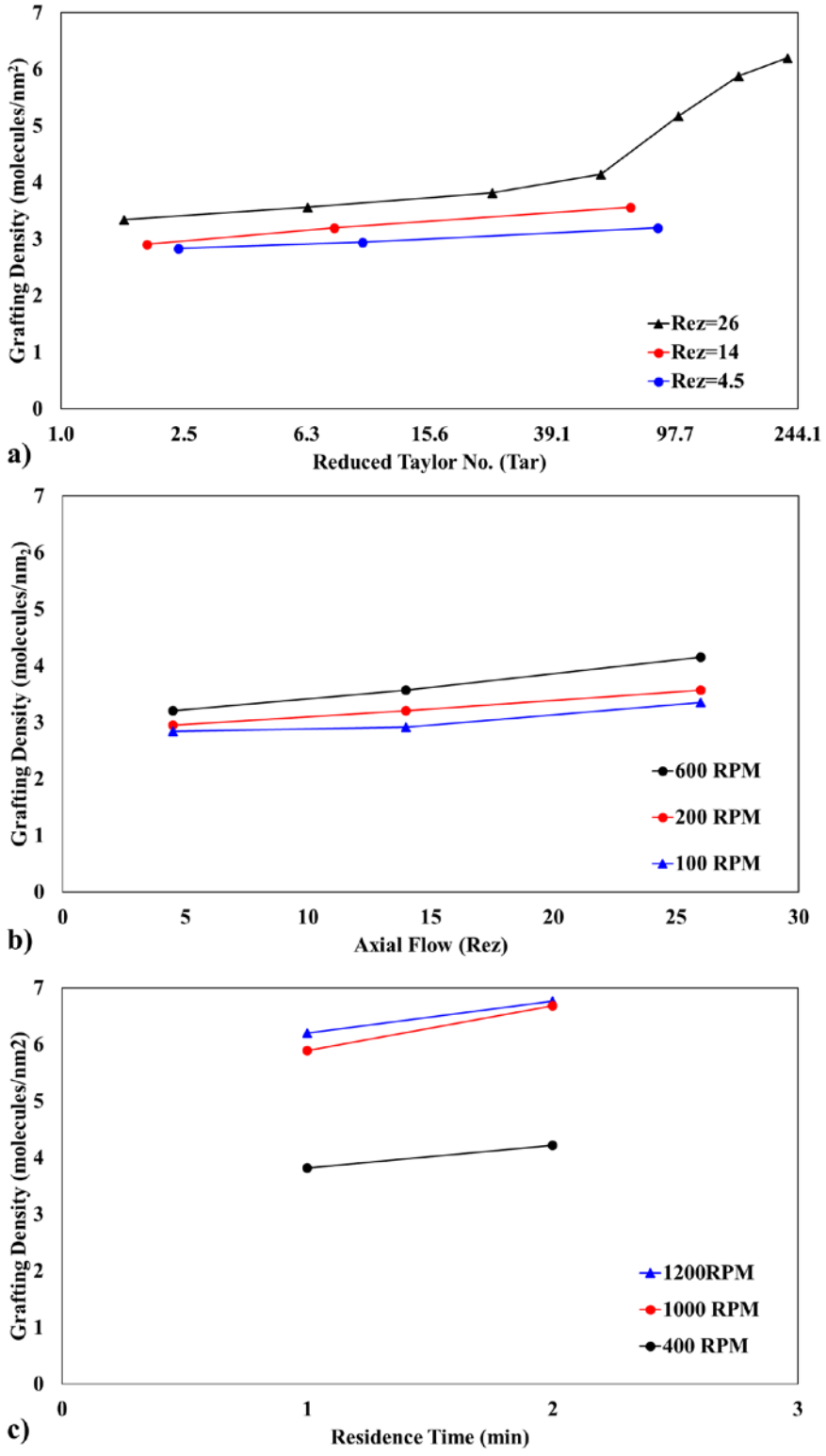

Figure 5.3.25 Change in MPS grafting density derived from TGA as a function of a) rotational motion, b) axial flowrate and c) residence time.

5.3.3.4 AFM Analysis

Pristine unfunctionalized aluminum particles had a roughness of less than 2nm, while all functionalized particles exhibited roughness values beyond 5nm.

AFM analysis was performed to assess the surface morphology of functionalized fillers and quantify the nano-level dispersion of the grafted MPS. The height and phase contrast AFM images of the room-temperature sample show formation of islands with diameters in the range of 40-100nm and with a height varying from 5 to 20 nm (Figure 5.3.26). Given height of a γ-MPS monolayer is about 0.7 nm, the larger height of the islands observed in AFM imaging confirm the formation of multilayer structures [119].The arithmetic mean value of the surface roughness exhibited by each flow condition is displayed in Figure 5.3.27. The quality of the topography of the grafted surface improved greatly with increased cylinder rotation. A drastically smoother surface was obtained by just slightly increasing the rotational speed enough to generate the onset of Taylor vortices. The surface roughness observed at higher Taylor numbers are within the range observed for steel plates functionalized with γ-aminopropyltriethoxysilane [119]. The change in topography and depth profiles of the functionalized surface at axial flow of Re_z =26 before the onset of wavy secondary instability (Ta~) and after the emergence of wavy flow regime is displayed in Figure 5.3.26(b) and (c), respectively.

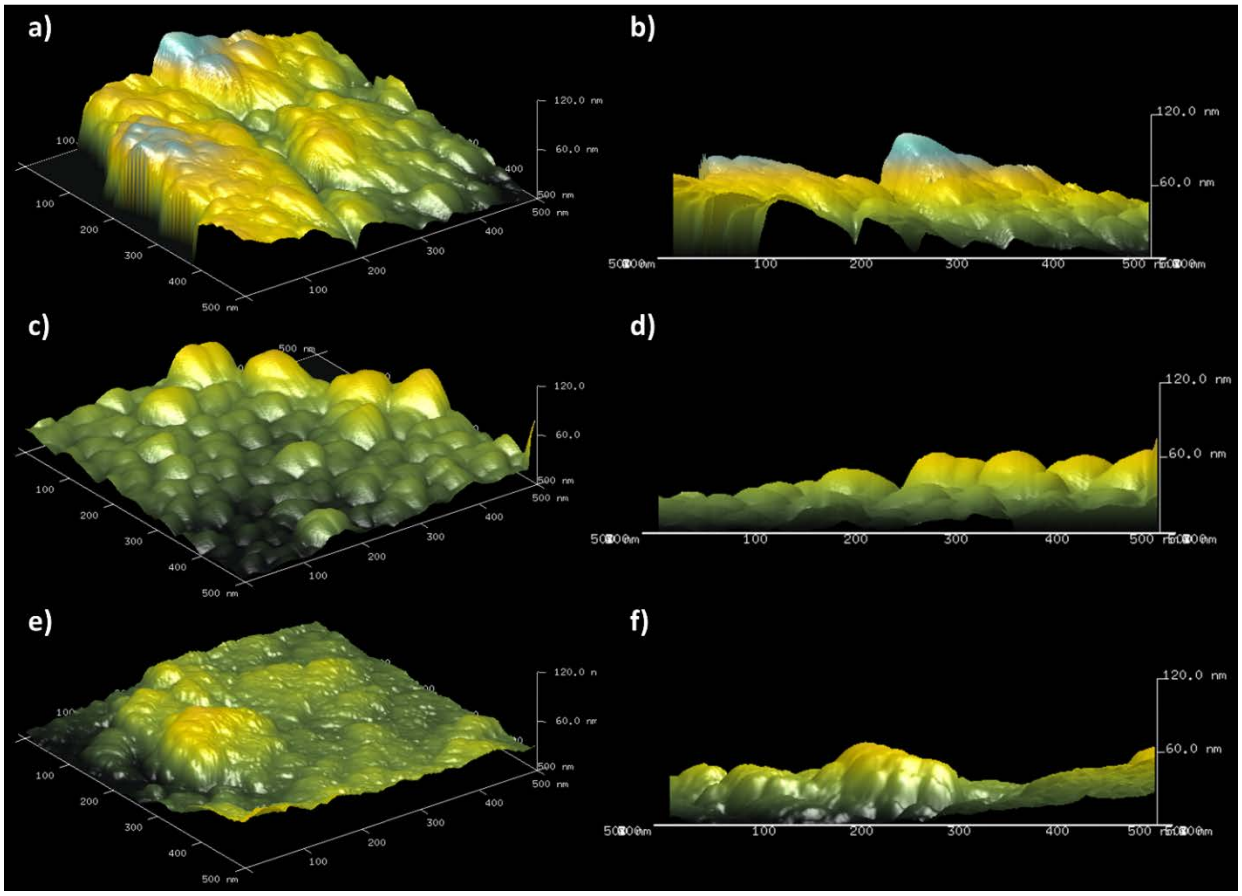

Figure 5.3.26 AFM analysis of Surface morphology Roughness (a), Surface morphology and depth profile at 2.38Ta_c (b) and 9.5Ta_c for Re_z= 4.5 and (c) 6.3Ta_c for axial flow at Re_z =26.

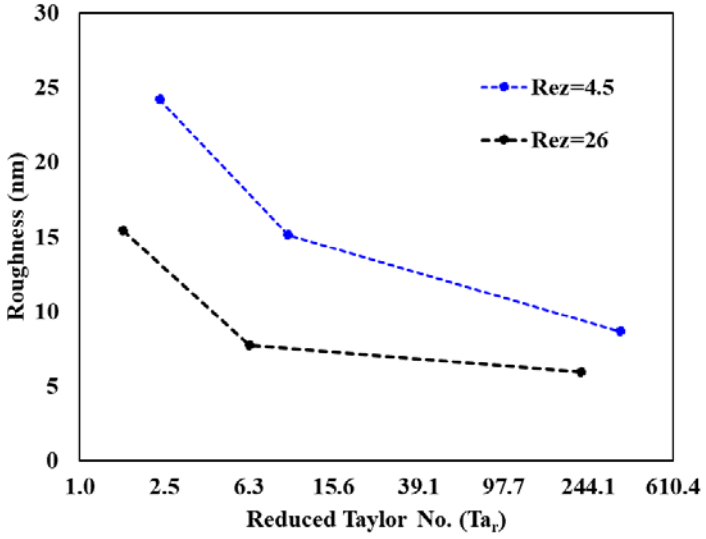

Figure 5.3.27 Average surface roughness of functionalized particles.

5.3.3.5 **Particle Luminescence**

Starting with island type growth configuration [142], the grafted MPS molecules assemble forming a patchy-like morphology [143] that is visible beyond the AFM molecular scale, as can be seen from the TEM image in Figure 5.3.28. Control of such coating morphology is critical to preserving the metallic appearance of the disk-shaped particles. Indeed, although there is negligible change in Metal look after MPS functionalization, the luminescence of the particles is slightly reduced, as observed by microscopic imaging displayed in Figure 5.3.29

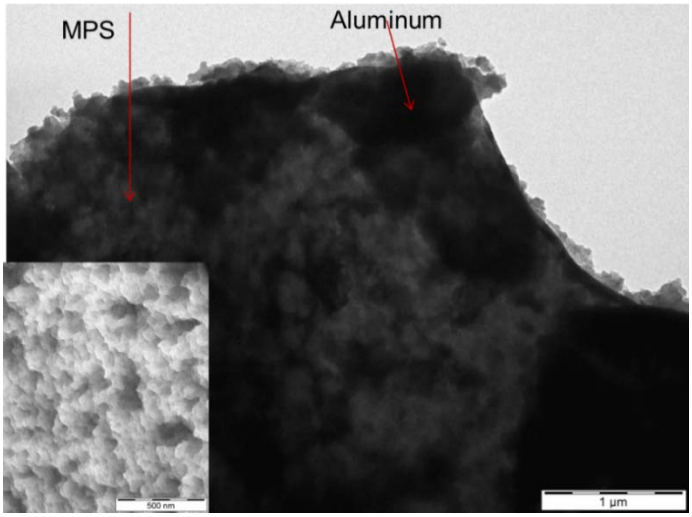

Figure 5.3.28 TEM showing the island-like morphology of MPS on the surface of functionalized aluminum particles.

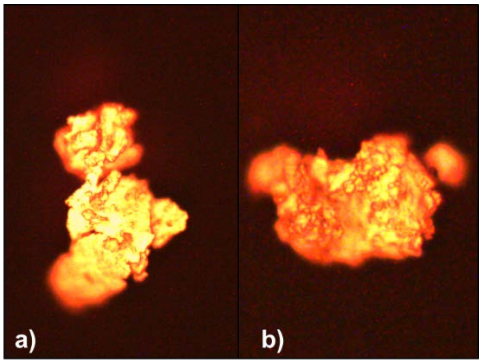

Figure 5.3.29 Reduction in luminescence of functionalized particles (b) compared to the pristine aluminum (a), as observed via microscope.

5.3.3.6 **Injection Molding Test**

Although showing improved alignment due to successful surface modifications of the metal-disk fillers, Injection molding tests performed by Samsung also confirm the reduction in luminescence.

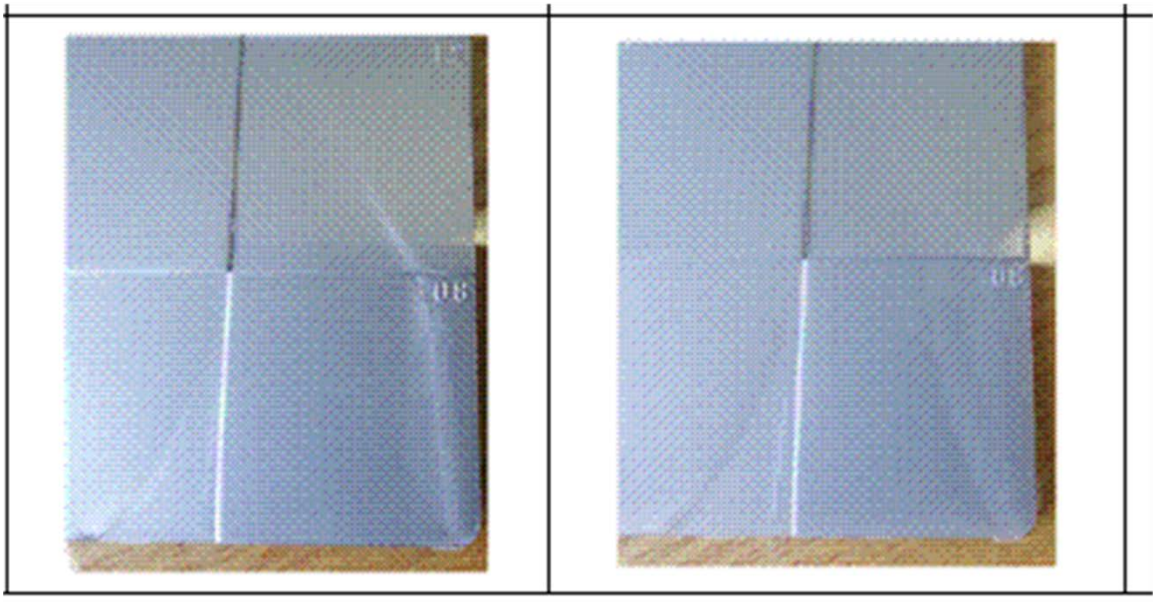

Figure 5.3.30 Improved alignment of functionalized aluminum particles during injection molding test.

5.3.3.7 **Particle Dispersion**

The improvement in alignment is also associated with the reduction in the formation of aggregates during the functionalization process. Examining images obtained via SEM analysis in Figure 5.3.31, for particles functionalized at different conditions, it can be easily noticed that greater particle agglomeration is observed at lower mixing rates (Figure 5.3.31 a and b), with the combination of lower flowrates producing the most aggregates. Increasing the mixing energy of dissipations helps in dispersing the particles during the functionalization, so that the metal-disk shaped particles exhibit less agglomeration and more uniform secondary particle sizes, as observed in Figure 5.3.31 (e and f).

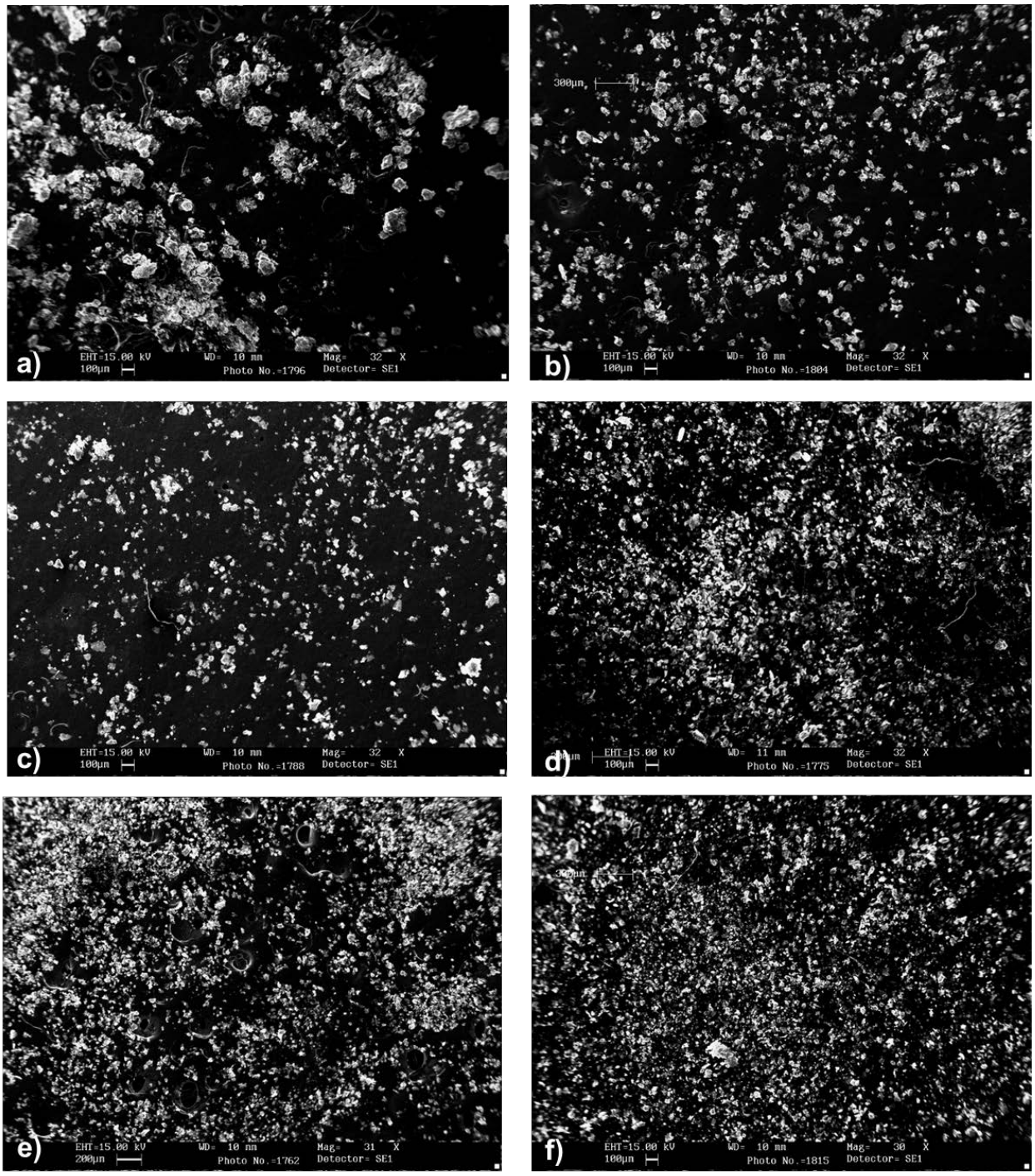

Figure 5.3.31 Influence of functionalization condition on particle dispersion. Low axial flowrate of Re_z = 4.5 with RPM=100, 200 and 600 a, c, and e, respectively. High axial flow rate of Re_z = 26 with RPM=100, 200 and 600 a, c, and e, respectively

5.3.3.8 **Zeta Potential**

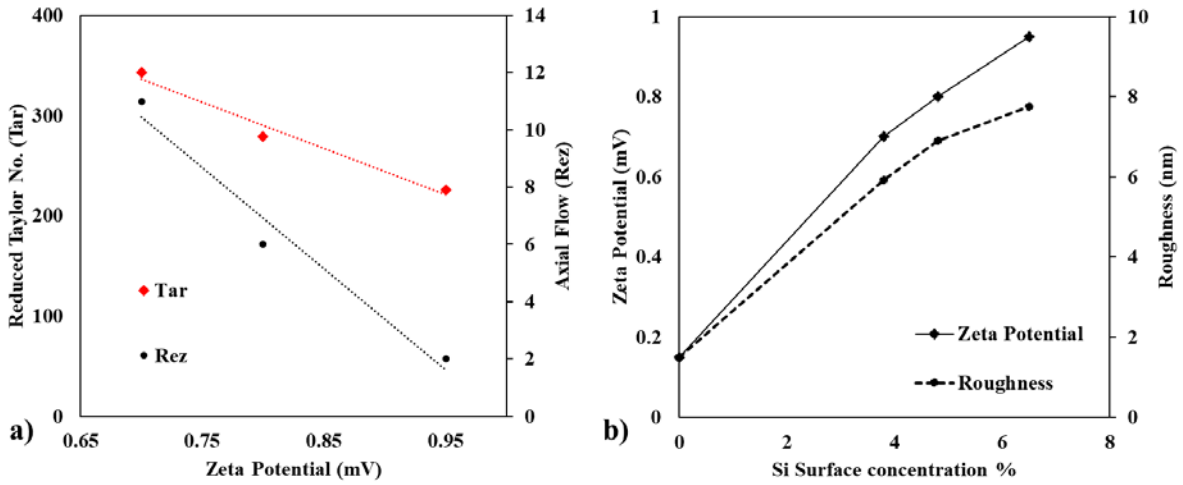

Figure 5.3.32 a) The measured zeta potential is lower for particles functionalized under stronger axial flow and stronger azimuthal motion , b) the measured increase in zeta potential and surface roughness correlates with the increase of Si surface concentration, as derived via xps analysis.

The hydrodynamic diameter of the dispersions is controlled primarily by the ionic strength of the dispersion media, which is a function of the electro-kinetic surface potential, known as the zeta-potential. As displayed in Figure 5.3.32, pristine aluminum disk particles had a zeta potential of less than 0.2 mV. The electro-kinetic potential surface charge was observed to increase with enhanced MPS concentration on the surface, as represented by Si atomic concentration obtained via xps. Thus, as displayed in Figure 5.3.32, the increase in axial flow (Re_z) and in rotational motion (Ta_r) resulted in reduced surface potential, reflecting the drop in roughness due to enhanced coating uniformity under these flow conditions.

5.4 Discussion

5.4.1 General

The collection of experimental data in this study strongly suggests that the effectiveness of MPS coupling on the aluminum surface is markedly influenced by the flow structure, mixing conditions and residence time during the silanization reaction.

5.4.2 Performance of Taylor Couette (TC) reactor and Tank Reactor (TR) in Batch Mode

In comparison with conventional tank reactor, the estimated MPS grafting densities in TCR were 1.2 times higher than that of CSTR, while the Si:Al atomic ratio was more than 2.6 times larger. This indicates that although the degree of functionalization is slightly increased with the TCR, the unique hydrodynamics of TC flow allow for more uniform deposition of MPS over the surface, where it is more likely to have a uniform monolayer of MPS, resulting in more surface coverage for the same grafting densities, just as was demonstrated by elemental color maps obtained via the EDX-SEM. This is also confirmed by the bond characterization from FTIR analysis which showed that the peaks associated with metallo-siloxane (Al-O-Si) bonds, between 900 to 1000 cm^{-1}, were rather weak in the case of the tank reactor. Detailed characterization of the coating layer for particles functionalized under Taylor Couette flow confirmed the uniform deposition of MPS molecules over the surface of the aluminum disks, while still retaining their methylene/methacrylate functionality. Even though the Taylor vortex flow structure doesn't necessarily offer nano-scale control, perhaps even down to molecular level like in a homogenizer, the vortex structure formed offers enhanced homogeneity for the self-assembly of organosilanes over the inorganic substrate. Indeed, the flow structure helped in making particles functionalized in the Taylor-Couette reactor exhibit better dispersions and more uniform agglomerates when compared to the tank reactor. The dispersions appeared to be less uniform when operating the TCR at lower rpm in the laminar flow regime, below the onset of the instability, as confirmed by dispersion results from chapter 4.

5.4.3 Influence of Reaction Time

Experiments assessing the residence time were operated at 600RPM (Tar ~92), which is within the onset of chaotic vortex flow as determined from flow visualization experiments in chapter 2 and in the literature [69]. The residence time of the salinization process was found to have a strong impact on the increase in MPS grafting densities and surface coverage, especially when extended to long reaction times, beyond 6 hours. As reported in former studies, long reaction times that vary from 2hours [104] [105] to 24hours [118] are typical for organosilane deposition and chemisorption unto surfaces. In particular, reaction times on the order of 24 hours were cited as most suitable for achieving complete functionalization at room temperature [109]. Nevertheless, bond characterization via FTIR revealed that the degree of C=C functionality changes only a little beyond a residence time of 6hours, suggesting that at longer reaction times, the polymerization of the methacrylate functional groups dominates the process of multilayer growth rather than proceeding through the typical orderly growth process through self-assembly [143], which is more likely to produce monolayers that can better retain the methylene/methacrylate functionality.

5.4.4 Influence of Higher rotation rates

The other major part of the study was dedicated to examining the influence of introducing axial flow while operating at flow regimes with high energy of dissipation, and at excessive rotational speeds, in ranges that are certainly beyond the onset of primary instability and rather within flow regimes corresponding to secondary instabilities. Under the mixing conditions used, flow regimes between Ta_r =1.6 to Ta_r = 226 were applied, going through laminar Taylor vortex flow (LTVF: 1< Ta_r <2.2~2.4), wavy vortex flow (WVF: 2.4< Ta_r <40), modulated wavy vortex flow (MWVF: Ta_r >40), chaotic vortex flow (Ta_r >92) and weakly turbulent vortex flow (WTVF: Ta_r > 178).

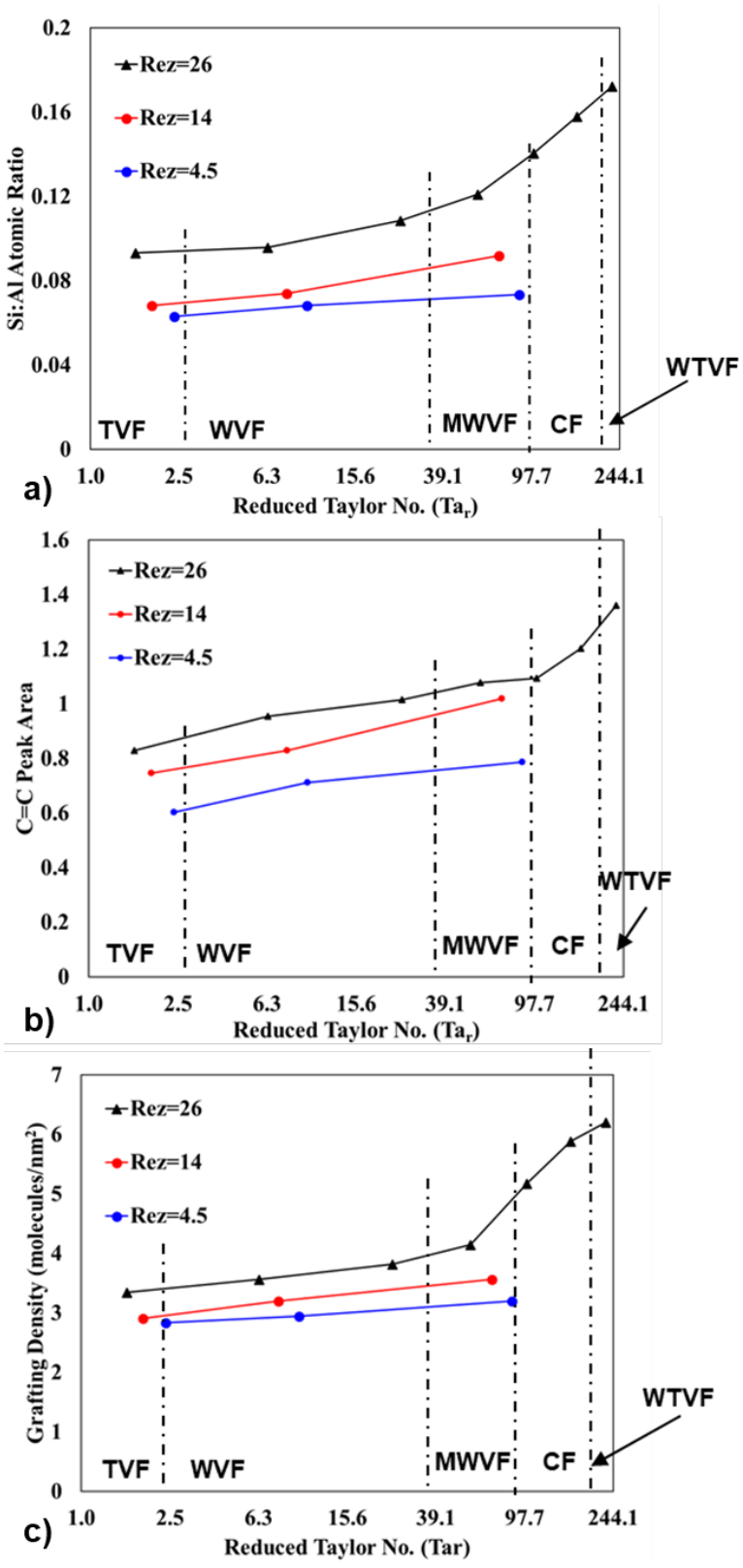

Figure 5.4.1 Mapping the onset of secondary instabilities and transitions of flow regimes.

Flow regimes within the WVF range can exhibit more complicated flow structures with progressive increase in rotational motion, usually with oscillating spiral vortices, as suggested by linear stability analysis [57]. The first signs of turbulence emerge in the wavy vortex flow regime with higher rotations while preserving the vortex structure even with the transition to turbulence [25]. Though it can exhibit significant changes, oscillations and reductions, the vortex structure continues to persist with no major discontinuity [161] up until after the onset of fully developed turbulent Taylor vortex flow (TTVF).

The flow dynamics impacting the functionalization process are predominantly governed on the molecular level through controlling the micro-fluid motion. Inhomogeneities in the flow can be grouped into three stages: macro-, meso- and micromixing, according to the characteristic length scale of mixing [55]. Macromixing, which occurs on length scales in the range of reactor geometry, mainly affects the inertial-convective dispersion [55]. Enhancing the macromixing increases material exchange between different mixing zones, helping to achieve a more uniform average composition [2]. Macromixing time is mainly a function of the mixing kinetics within the axial direction, and thus can be characterized in terms of the axial dispersion coefficient as stated in [55]:

Equation 5.4.1 Estimation of macromixing time via axial dispersion correlation

$t_{macro} = \frac{2d^2}{D_{ax}}$, where D_{ax} can be estimated from correlations derived as:

$$D_{ax} = \frac{2.4\times10^{-1}[v][Re_{z-L}]^{0.25}[Re_{\emptyset}]^{0.57}}{\left[\frac{r_1}{r_2}\right]} \text{ for the turbulent flow regime}$$

$$\text{And } D_{ax} = \frac{2.\times10^{-3}[v][Re_{\emptyset}]^{1.25}}{\left[\frac{r_1}{r_2}\right]^{1.75}} \text{ for wavy flow regime.}$$

To quantify the change in axial dispersion with increasing rotational motion, the Peclet number, as expressed in , was plotted in Figure 5.4.2. The estimated exponent correlating the dependence of the peclet number on rotational motion, $Pe \propto [Ta_r]^{0.7}$ and $Pe \propto [Ta_r]^{0.63}$, for Rez= 26 and Rez=14 and 4.5, respectively.At high rotational rates, the peclet number drops an order of magnitude from its value at the lowest rotation rate, confirming that the mixing performance of the TCR reaces that of a CSTR.

Equation 5.4.2 Peclet Number

$$Pe = \frac{2V_z \mathrm{d}}{D_{ax}}$$

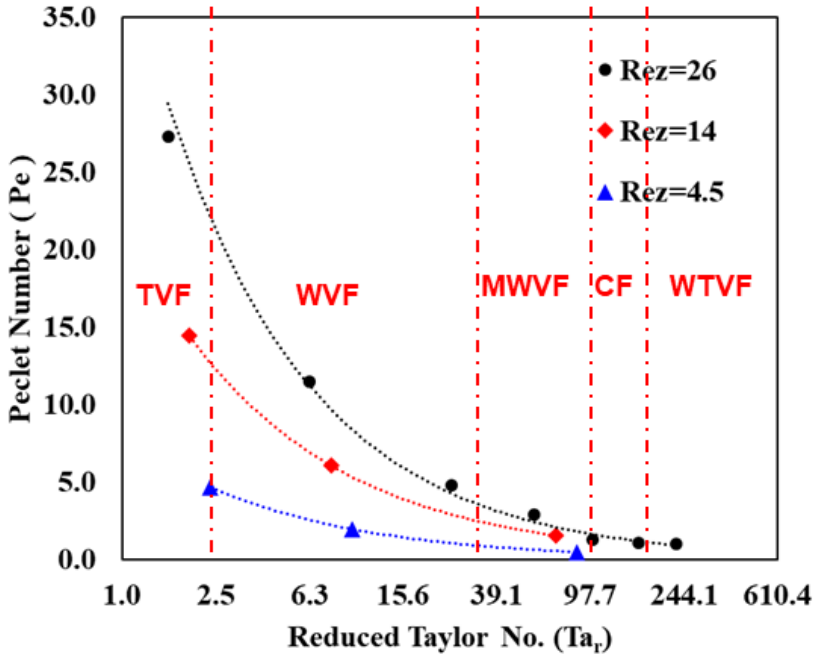

Figure 5.4.2 Effect of rotational motion on axial dispersion, as expressed by the Peclet number (Pe).

Because the macroscopic exchange among the vortices in the flow structure are not perfectly mixed, a mesomixing time scale is introduced to characterize the mixing process which leads

to the homogenization of the vortex composition. Such time scale can be estimated from correlations derived by Racina et al. [55] as follows

Equation 5.4.3 estimation of Meso-mixing timescales.

$$t_{meso} = \frac{2.5\times10^{5}\left[1-\frac{r_1}{r_2}\right]}{\left[\frac{r_1}{r_2}\right]^{1.6}\left[Re_{\emptyset}\right]^{1.48}\left[\frac{2\pi(RPM)}{60}\right]}\text{, for turbulent flow}$$

$$\text{and } t_{meso} = \frac{1.4\times10^{4}\left[1-\frac{r_1}{r_2}\right]}{\left[\frac{r_1}{r_2}\right]^{1.6}\left[Re_{\emptyset}\right]^{0.8}\left[\frac{2\pi(RPM)}{60}\right]}\text{, for wavy flow regime.}$$

Given that the flow is within the onset of turbulence within the higher rotation rates used in this study, the local characteristics of the flow accounting for the micromixing on a molecular level can be estimated via Equation 5.4.4.

Equation 5.4.4 Kolmogorov microscale equations

$$t_{micro} = \sqrt{\frac{\nu}{\varepsilon}} \text{ and } L_{micro} = \sqrt[4]{\frac{\nu^3}{\varepsilon}} \text{ [162].}$$

As displayed in Figure 5.4.3, the reactor exhibits significant macromixing for all rotation rates, with macromixing time scale dropping an order of magnitude as the flow regime is changed from Taylor vortex flow to the onset of modulated wavy vortex flow (MWVF). With the onset of chaotic flow (Ta_r>92), the macromixing time scale becomes steady and experiences no further drop. Meanwhile, the mesomixing time-scale exhibits a drastic drop in its mean-value, decreasing an order of magnitude when progressively increasing rotation in the wavy flow regime and another drop in magnitude while transitioning towards the onset of MWVF. A more dramatic change in the mesomixing time scale occurs when transitioning towards chaotic flow, after which the mixing in the meso-scale drops slightly but steadily. In contrast, the change in the mixing scale on a microscopic level is monotonic and only drops an order of magnitude when moving from the lowest to the highest rotations used in this study.

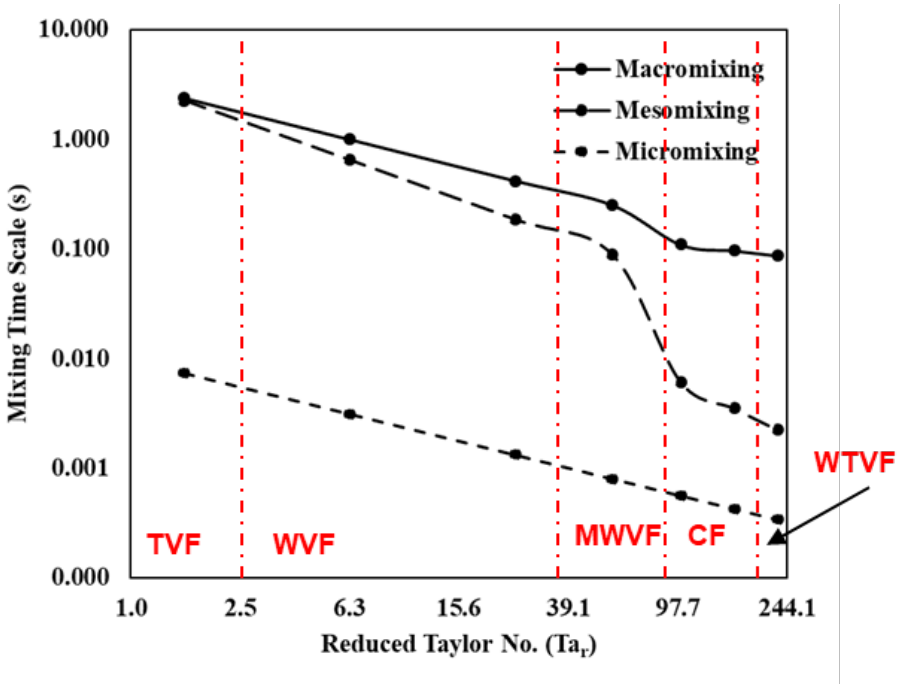

Figure 5.4.3 Mapping flow regime transitions on the Kolmogorov mixing timescales.

Close to the onset of turbulence, the Kolmogorov equations can be applied to show that the micromixing time (intra-vortex mixing) is close to 0.5 milliseconds, while the macromixing (inter-vortex) is less than 0.1 seconds, as shown in Figure 5.4.4. Under the onset of turbulence, mesomixing timescales drop to less than 5 milliseconds, indicating a high degree of homogenization inside the vortex cells [55]. In mixing conditions within the wavy vortex flow ($2.2< Ta_r <40$), the wavy motion directs the fluid from the vortex boundaries into the core, producing regions of upward and downward vortex deformation [56]. This contributes to an increase in intra-vortex axial mixing and enhances the mixing taking place radially through the rotational motion in the azimuthal direction, so that nearly half of the vortex volume is transported into and out of a vortex in one azimuthal wave period [56].

Enhanced surface functionalization beyond this rotational motion, show that upon the transition to wavy, modulated wavy vortex flow regimes and evolving to the onset of turbulence, the

mixing intensity of the flow is dramatically increased, transforming the flow in the reactor from nearly plug-flow behavior with a possible bypass into a well-mixed vessel [163]. Given that mixing on the macro-scale is most dominant limiting stage for the whole mixing process in a Taylor-Couette reactor [55], it is expected that the increase of axial flow can significantly enhance the whole mixing process.

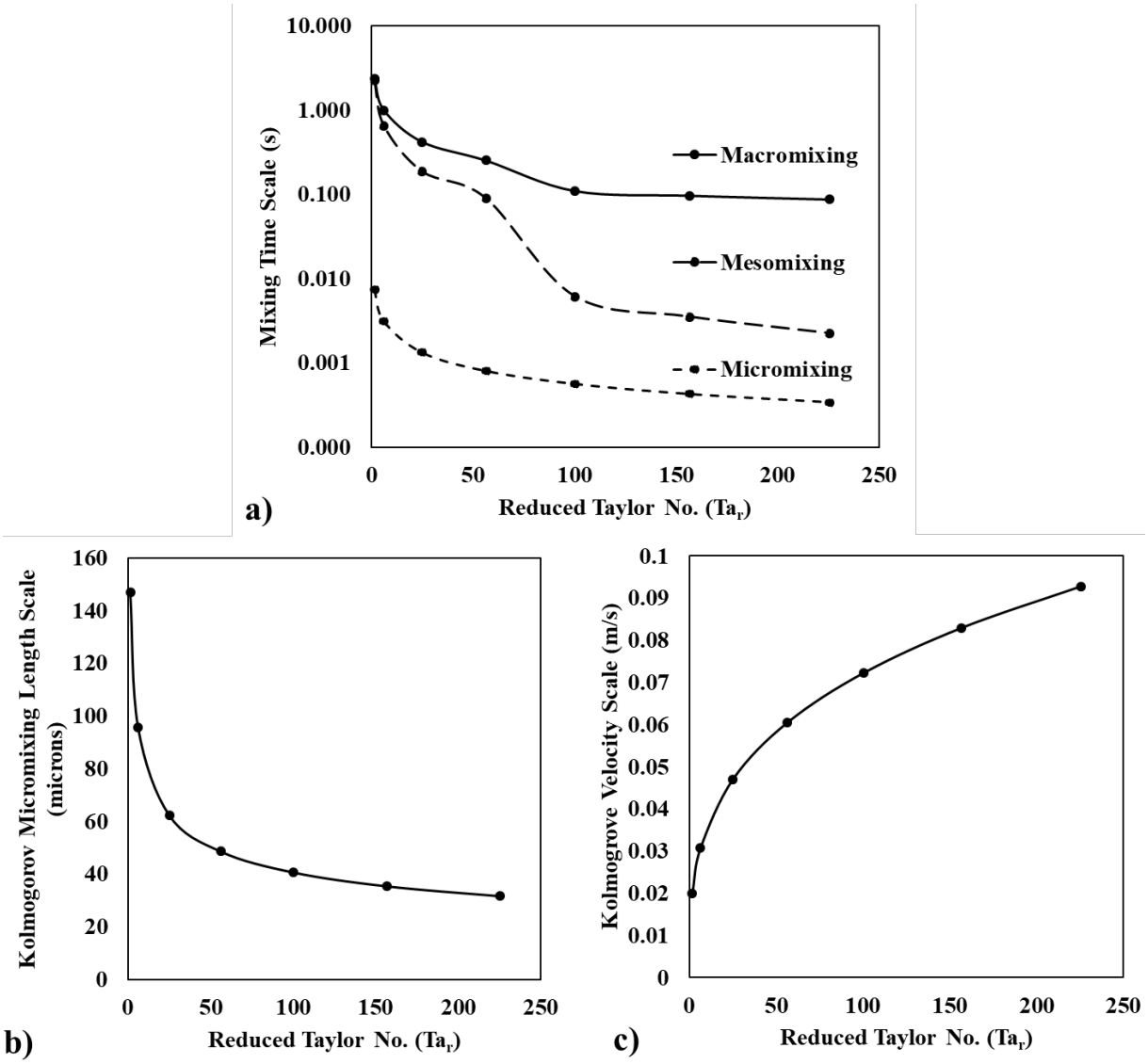

Figure 5.4.4 Mixing on the Kolmogorov scales a) time, b) length and c) velocity.

5.4.5 Influence of Continuous Axial flow

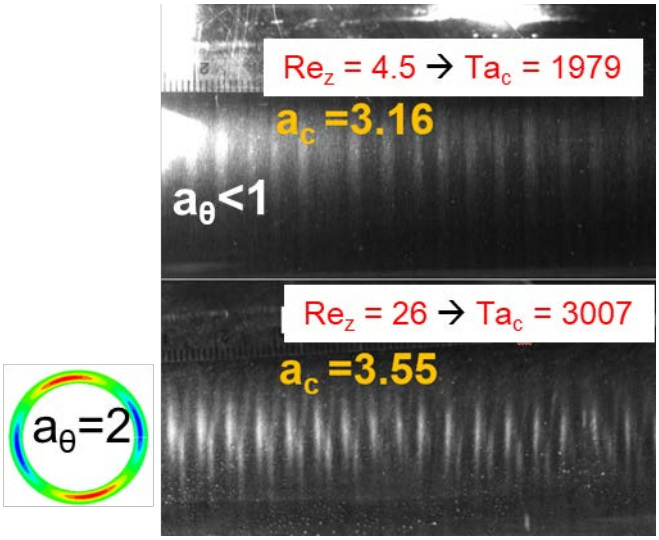

Figure 5.4.5 Change in number of vortices and evolution of spiral topology with increasing axial flow.

As for the influence of axial flow, from detailed flow visualization imaging done in an earlier study [57], and given the reactor length of 30 cm, we can estimate the number of vortices present at Re_z =0 to be around 116 (58 pairs). With the increase of axial flow to Re_z =4.5, the number of vortices barely increases. With Re_z = 14, the number of vortices available becomes close to 120, resulting in two additional unitary vortex cells, each consisting of a pair of counter-rotating vortices. And with the maximum flowrate used in this study, Re_z =26, six additional pair of vortices emerge, corresponding to a total of 132 vortices (66pairs). In addition, the increase in axial flow introduces significant enhancement in circumferential mixing due to the emergence of stronger non-axisymmetry.

5.4.6 Predictive Correlations

Although predicting the degree of functionalization in Taylor Couette flow is challenging due to the multiple parameters affecting the silanization process, empirical correlations can be developed based on experimental results presented in this study to quantify the changes in the

properties of functionalized particles based on the range of axial flowrates and cylinder rotation rates used in this system. To relate the changes in functionalization to changes in the fluid flow structure, two correlations for Si:Al atomic ratio and MPS grafting density, based on XPS and TGA data, respectively, were developed via nonlinear least squares regression:

Equation 5.4.5 Correlation for predicted Si:Al atomic ratio from XPS analysis

$$Si{:}\,Al\ Atomic\ Ratio = 3.6 \times 10^{-5}(Ta_r + 307.3)^{1.2}(Re_z + 0.635)^{0.305};\ R^2 = 0.96$$

Equation 5.4.6 Correlation for predicted in C=C bond peak area from FTIR analysis

$$C = C\ bond\ peak\ area = 0.57(Ta_r)^{0.085}(Re_z)^{0.194};\ R^2 = 0.96$$

Equation 5.4.7 Correlation of zeta potential of functionalized particles

$$Grafting\ Density\ \left(\frac{molecules}{nm^2}\right) = 0.0011(Ta_r + 357.5)^{1.25}(Re_z + 2.74)^{0.2};\ R^2 = 0.97$$

$$Roughness\ (nm) = \frac{41.7}{(Ta_r)^{0.353}(Re_z)^{0.176}}$$

Equation 5.4.8 Correlation of zeta potential of functionalized particles

$$Zeta\ Potential = \frac{10.84}{(Ta_r)^{0.6}(Re_z)^{0.11}};\ R^2 = 1$$

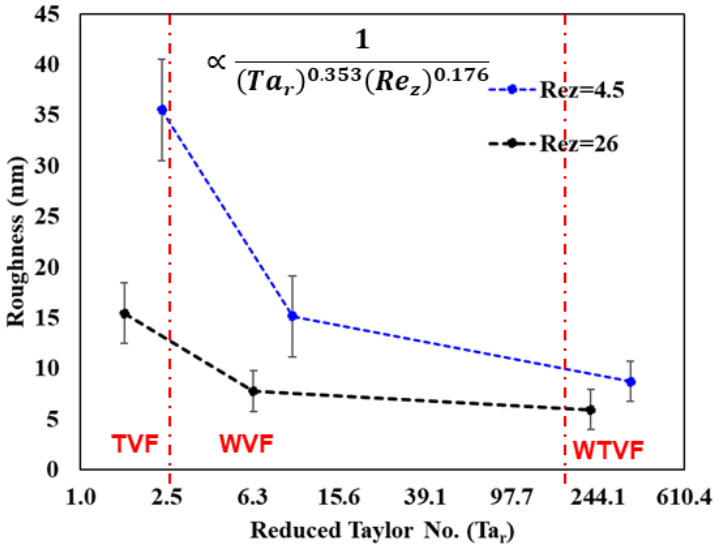

Figure 5.4.6 Mapping flow regime transitions on the change in average surface roughness of functionalized particles.

The equations demonstrate that the change in rotational motion is the dominant factor for improving the degree of functionalization. Although the influence of reaction time was important, the change in axial flow has a stronger impact on MPS deposition on the surface of aluminum particles.

5.4.7 Properties of MPS-aluminum disk fillers

Island-type growth has been attributed to the formation of silane aggregates previously formed in the solution [119]. Thus, the decrease in roughness, which suggests reduced island-like MPS grafting, can be attributed to the significant mixing within the bulk aqueous suspension which results in fewer silane aggregation and minimal siloxane bond formation before reaching the solid-liquid interface near the metal surface. Indeed, the onset of instability helps in increasing the uniformity of the coating, as expressed in terms of a reduction in surface roughness [141], and the increase in surface coverage. As observed via SEM, starting with island type growth configuration [142], the grafted MPS molecules assemble forming a patchy-like morphology [143]. If the MPS molecules are oriented vertically as rods aligned perpendicularly to the aluminum surface, then an estimated grafting density of 4 molecules/nm^2 is enough to form a monolayer [118]. Actual grafting densities usually diverge from such values due to the formation of multilayers. This is also confirmed by the minimum surface roughness observed in this study which was at least 4nm higher than that of the pristine particles. Given height of a γ-MPS monolayer is about 0.7 nm [119] a minimum of 5 to 6 multilayers is formed at the highest mixing intensity conditions (Re_z =26 and Ta_r=226), while up to 32 MPS multilayers could be anticipated when functionalization takes place in laminar Taylor vortex flow. Flow regimes beyond WVF (Ta_r <40) offer significantly lower probabilities for particle collision

and flocculation [164], offering a more evenly suspended slurry with rather more uniform MPS coupling to the surface of the aluminum flakes.

5.5 Conclusion

Beyond the onset of primary instabilities, this study examined the role of secondary instabilities in controlling the mass-transfer among the aqueous organosilane solution and the suspended aluminum disk particles. It was found that the flow regimes within WVF and after the onset of MWVF induced mixing conditions that favored the preferentially condensation of MPS molecules to form hydrogen bonds with the hydroxyl groups on the aluminum substrate rather than larger oligomeric siloxanes, which lead to the formation of Silsesquioxane structures, at laminar Taylor-Couette flow conditions [113]. Close to turbulent conditions, the Taylor Couette reactor proved to be particularly advantageous in the coating of large particles where the Kolmogorov micromixing length scale can be of the same magnitude as the smallest predicted eddy. On such a scale, greater control over the self-assembly of organosilanes can be achieved while allowing only minimal dimeric homocondensation. As such, the surface roughness of the functionalized particles can be reduced, helping aluminum pigments to retain their silvery appearance and minimize deterioration of their metallic glare [7].

In summary, this study attempted to explore the tailoring of mixing conditions in the Taylor-Couette reactor to promote the production a well-defined reproducible organosilane monolayer, which are very challenging to produce under currently available technologies [128]. Due to its uniform and dynamically comparable flow conditions [130], functionalization in Taylor vortex flow regime allowed for more accurate control. As such, the Taylor Couette reactor provides a scalable [130] functionalization process with a predictable coating performance.

CHAPTER 6

EFFECT OF FLOW MIXING PATTERNS ON CARBON DIOXIDE-CALCIUM HYDROXIDE INTERFACIAL INTERACTION DURING CALCIUM CARBONATE PRECIPITATION IN TAYLOR COUETTE CRYSTALLIZERS

6.1 Introduction

Interfacial precipitation via gas-liquid phase reaction is a critical step in the production of calcium carbonate with fine-tuned surface properties while eliminating the formation of soluble ionic byproducts that are typically associated with liquid-liquid reactions [78]. Ultrafine precipitated calcium carbonate (PCC) crystals with uniform morphology have found favorable use in a variety of applications that extend from fillers in composites such as plastics [165], paper [166], textile, rubber [167] , pigments [168] to acidic gas removal technologies, for both CO_2 [169] and H_2S [170] [171], as well as in wastewater treatment [172]. In addition to being extensively used as nanosorbents [165] and catalyst support [173], porous nano- $CaCO_3$ particles are particularly popular as novel biomimetic scaffolds for target drug delivery and tissue engineering [173]. As opposed to micro- $CaCO_3$, the decreasing particle size of nano-$CaCO_3$ along with the increase in specific surface area accelerates the overall reaction rate [174]. Calcium carbonates with open pore structure can enhance reactivity and exhibit higher conversion [175], especially if the pores were optimized for the mesoporous region so as to allow access to molecules while still being immune to pore shrinkage, blockage and thermal sintering [170]. Although some studies [170] [175] observed that $CaCO_3$ derived via carbonation route exhibits lesser loss of structural properties after calcination than hydrate-derived particles, conventional bubble column carbonation approach typically produces spindle-shaped particles with sizes beyond 2 μm [176].

Aspects of interfacial transport, including gas absorption and molecular transport, associated with the two phase nature of the precipitation introduce difficulties in controlling the degree of crystallization [78] and analyzing crystal formation processes [167]. A number of studies in recent years have focused on the intensification of the gas-liquid absorption- crystallization reaction by focusing mainly on expanding the interfacial area between the gas-liquid phases [177]. As attempts to obtain PCC with finer morphologies, several studies have focused on adjusting sparger shape and size [176] as well as resorting to alternative carbonation generation approaches such as microbubble generator (MBG) [171], [178], [179] [180], membrane dispersion minireactor [181], rotating disc reactors [182] [7] [183, 184], sonochemical carbonization [185] [186] , narrow channel reactors [187] [2] and microporous tube-in-tube microchannel reactor [188]. Such approaches are based on the production of smaller bubbles, which can provide high gas holdup values while increasing the gas-liquid interfacial area, leading to an increase in the overall yield and conversion efficiency of the multiphase precipitation process [177]. In the case of PCC, dispersion of CO_2 is believed to be a critical factor in determining the degree of nucleation, growth and particle morphology [176]. Experiments comparing PCC formation using porous frits of different pore sizes observed that the carbonation reaction rate became faster when using frits with smaller pore sizes [189]. Still, predictions of crystal size and morphology of PCC remain challenging due to the overlap between multiple factors including the mixing, reactant concentration, mean residence time, pH of the solution, and reactor configuration [78]. Utilizing a novel high shear mixer placed in the CO_2 feeding zone in a stirred tank precipitation apparatus enabled for enhanced control on the PCC aggregate structure [190]. In addition to interfacial transport, the energy dissipation rate and mixing chamber configuration greatly influence the degree of crystal aggregation [191],

particularly for the production of nano-$CaCO_3$. Geometrical characteristics of the gas/liquid contact device to carry out the precipitation is critical in enhancing interfacial mass-transfer [192]. Lack of intense and thorough mixing in the case of $CaCO_3$ precipitation via MBG resulted in disorderly aggregation of particles, challenging the prospect of obtaining reproducible results [171]. Even when an agitator is used, as in the case of MSMPR (Mixture Suspension Mixed Product Removal) [193], non-homogeneities still persist due to the differential hydrodynamic intensity that is much stronger near the agitator and gets rather weaker moving away from the mixer [194].

To improve the PCC formation and ensure homogeneous crystallization, the robust radial vortex flow offered by the Taylor-Couette reactor configuration has been applied for the production of PCC [47] [78] [167] [195] [196]. As a model reactor system where flow takes place in the annulus between two concentric cylinders, Taylor-Couette flow allows for examining hydrodynamic instabilities [13] while stimulating vortex motion, offering a highly active interface for mass transfer and phase mixing. Although the flow is steady and purely azimuthal for low angular cylindrical velocities, a series of hydrodynamic instabilities emerge during the gradual increase of inertial forces against viscous forces [14]. Emerging vortices act to increase the surface area of the interface between different and partially unmixed materials, offering a high surface-to-volume ratio. Distinct flow patterns emerge when a second disperse immiscible fluid phase is introduced to the Taylor-Couette flow system [59]. Higher shear rates in Taylor Couette flow may be utilized to significantly reduce the bubble size of carbon dioxide as opposed to the random turbulent eddy flow associated with conventional crystallizers [194]. Specific gas-liquid interfacial area obtained in Taylor Couette reactors is typically reported as being an order of magnitude higher than those obtained for a stirred tank reactor [197]. In

addition to influencing the degree of interfacial transport between the gas-liquid phases, the Taylor Couette reactor offers macro and micro fluid motion that further enhances the degree of mixing intensity, effecting the crystallization process and PCC properties, such as particle size distribution [78], surface area and pore volume as demonstrated in this study. In addition, vigorous and efficient mixing in Taylor Couette flow allows for the handling of highly viscous suspensions with high concentration of $Ca(OH)_2$ compared to precipitation done in bubble column configuration [171].

The objective of this study is to investigate the variety of flow patterns in a three-phase system, reacting gaseous carbon dioxide (CO_2) with aqueous calcium hydroxide ($Ca(OH)_2$) to precipitate solid calcium carbonate crystals ($CaCO_3$) in a Taylor-Couette reactor (TCR), and to examine the influence of the corresponding flow dynamics, CO_2 gas bubble size and interfacial area on calcium carbonate crystal properties. Recent studies [58] [6] [59] [60] revealed that the interfacial area in a gas–liquid system in a Taylor-Couette reactor varies substantially depending on the flow regime, since a variety of flow states can be observed due to the interaction between centrifugal and buoyancy forces. These studies have investigated the change in the degree of physical and chemical absorption by measuring the volumetric mass transfer and correlating it to the dissipation energy [198] [199] [197] [200]. While previous studies on Taylor-Couette reactors in horizontal configuration only focused on the influence of dissipated energy, in this study we extend our understanding of changes in two phase interfacial transport with variation in flow regime behavior, by assessing vortex dynamics using flow visualization tools. The first part of this study includes an experimental characterization of flow patterns by assessing gas bubble dispersion and bubble size, while identifying flow-patterns with highest interfacial area. In the second part, the ideal mixing flow regimes identified from

flow-visualization experiments were used as conditions for PCC production. It was found that the evolution of certain flow-patterns, particularly “ring flow”, can compromise the interfacial transport despite higher energy of dissipation. Such observations confirmed that crystal properties, such as internal crystal structure, particle microstructure and morphology, are more dependent on the interfacial area than on the intensity of mixing or degree of turbulence.

6.2 Experimental Section

6.2.1 Reactor Setup and Characteristic Parameters

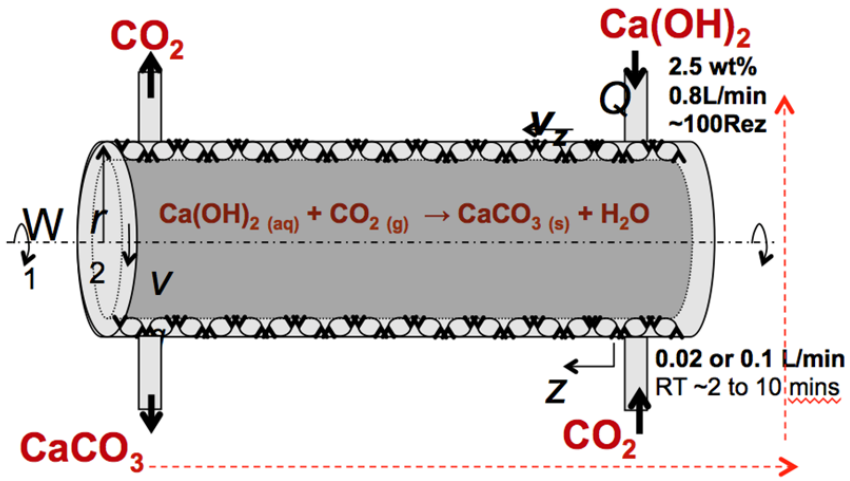

Figure 6.2.1 Schematic of calcium carbonate precipitation in Taylor Couette Crystallizer.

The experimental setup of the TC crystallizer, illustrated in Figure 6.2.1, consisted of two coaxial cylinders, with the aluminum inner cylinder rotating while the Plexiglas outer cylinder is fixed. The inner cylinder rotation rate is controlled by a phase inverter, connected to a motor drive that provides rotation rates in the range of 30-1800 RPM. The horizontal configuration of Taylor-Couette flow was selected for this study because it has been suggested that the change in interfacial area with increasing rotational speeds is rather insignificant for the case of vertically oriented TC reactors when compared to the horizontal orientation [59]. The primary hydrodynamic instability marks the transition from Laminar Taylor Couette Flow (LTCF) to

the Laminar Taylor Vortex Flow (LTVF), as determined by the critical Taylor number (Ta_c). Uniformly spaced counter-rotating cellular vortices, with each pair forming an axial wave, is characterized by critical wavenumber (a_c) and wavelength (λ_c).

Given that the influence of the reactor annulus width becomes most significant when operating within narrow gaps [6], the annulus of the reactor was fixed to the narrow range of r_1/r_2=0.9. Table 6.2.1 includes the physical specifications of the TC crystallizer and Table 6.2.2 the properties of the fluids used in the current study.

Table 6.2.1 Operating Variables for the TC crystallizer

Property (unit)	**value**
Inner Cylinder radius r_1 (m)	**0.0227**
Outer cylinder radius, r_2 (m)	**0.0253**
Annulus gap width, d(r_2-r_1) (m)	**0.0026**
Reactor Length, L_r (m)	**0.3**
Reactor volume, V_r (ml)	**117**
Gap aspect ratio, d/ r_1	**0.114**
Radius ratio , r_1/ r_2	**0.9**
Length aspect ratio, L_r/ d	**116**
$Re_{\theta c}$	**131.5**
Ta_c (no axial flow)	**1860**
Ta_c (with axial flow, Re_z=93)	**11200**

Table 6.2.2 Flow Parameters of Gas-Liquid flow

Property (unit)	value
Liquid Flow Rate, Q_L (L/min)	**0.896**
Gas Flow Rate, Q_G (L/min)	**0.02 , 0.1**
Gas Flow Rate, Q_G (vvm)	**0.17 , 0.85**
Axial Reynolds number for Liquid Flow, $Re_{z\text{-}L}$	**93**
Axial Reynolds number for Liquid Flow, $Re_{z\text{-}G}$	**4.1, 20.7**
Liquid Mass Flux (kg/m^2s)	**41**
Liquid space velocity, V_L (mm/s)	**38.25**
Gas space velocity, V_G (mm/s)	**0.85mm/s , 4.27mm/s**
Gas/liquid flow ratio ($\beta=u_G/u_L$)	**0.022 , 0.11**
Calcium hydroxide ($Ca(OH)_2$) Concentration	**2.5wt% , 0.34M**
Liquid Phase density, ρ_L	**1.016 g/ml**
Gas Phase density, ρ_G	**1.8 kg/L**
Liquid Phase viscosity, μ_L	**0.001085 N s/m^2**
Gas Phase viscosity, μ_G	**$1.47x10^{-5}$ N s/m^2**
Liquid Phase Kinematic Viscosity, ν_L	**$1.068x10^{-6}$ m^2/s**

The energy dissipation in the Taylor Couette reactor has been suggested as the most optimum way of correlating experimental data of two-phase flow systems [6], and the value of dissipated energy per unit mass of the mixture was derived as suggested in [47] :

Equation 6.2.1 Estimation of dissipated energy due to cylinder rotation

$$\varepsilon = \frac{\pi L_r {r_1}^4 \omega^3 f}{V_R} \text{ , where } f = 0.8 \left(\frac{d}{r_1}\right)^{0.35} Re^{-0.53} \text{ for } Re \geq Re_c$$

Equation 6.2.2 Estimation of critical azimuthal Reynolds number without axial flow.

$$Re_c = 41.2 \left(\frac{d}{r_1}\right)^{-0.5} + 27.2 \left(\frac{d}{r_1}\right)^{0.5} + 2.8 \left(\frac{d}{r_1}\right)^{1.5}$$

To better quantify the hydrodynamics of each flow regime, the shear stress, $\tau_{wi} = \frac{f\rho {r_1}^2 \omega^2}{2}$ [47], and shear rate, $\sqrt{\frac{\varepsilon}{\nu}}$ [201] , were estimated based on the following equations. The characteristic parameters of each rotational flow rate used in the study is summarize in Table 6.2.3.

Table 6.2.3 Rotational conditions used in this study.

RPM	Re_θ	Ta	$Re_\theta / Re_{\theta c}$	$T_r = Ta/Ta_c$	ε (W/kg)	Shear stress	Shear Rate (1/s)
200	1151	142349	8.8	12	0.2	1.0	406
400	2301	569398	17.5	48	1.0	2.8	956
800	4603	2277591	35.0	191	5.4	7.9	2250
1200	6904	5124579	52.6	431	14.7	14.3	3712
1750	10068	10898628	76.6	916	37.4	24.9	5916

A semi-batch gas–liquid Taylor–Couette reactor configuration was used for the experiments, where the liquid phase is fully recycled back in to the reactor while the gas phase passes through without recirculation, as shown in Figure 6.2.1. Given that the interfacial area in a gas-liquid two phase Taylor Couette flow is minimally influenced by liquid axial flow [6], a fixed flowrate of 0.896L/min (u_L=38.25 mm/s) was used for the aqueous calcium hydroxide solution.

The superimposed axial flow is characterized by the axial Reynolds number (Re_z) which was fixed at $Re_{z\text{-}L}$~ 93, as estimated by

Equation 6.2.3 Axial Reynolds number for aqueous phase

$$\mathrm{Re}_{Z-L} = \frac{u_L d}{\nu_L} = \frac{Q_L(r_2 - r_1)}{A\nu_L} = \frac{Q_L}{\pi(r_2 + r_1)\nu_L},$$

where u_L is the mean axial velocity, Q_L is the flow rate and A is the cross-sectional area of the channel. The axial flow rate corresponded to a mass flux of G=41 kg/m^{2}s, which was estimated based on this equation, as suggested by Hubacz [58]:

Equation 6.2.4 Axial flow mass flux (kg/m^{2}s)

$$G = \frac{Q_L \rho_L}{\pi(r_2^{\,2} - r_1^{\,2})}\left(\frac{\rho_{H_2O}}{\rho_L}\right)^2\left(\frac{\mu_L}{\mu_{H_2O}}\right),$$

The critical Taylor number (Ta_c=11200) corresponding to this axial flow rate was estimated based on flow visualization experiments published in a former study [57]. Following that, the reduced Taylor number (Ta_r) was estimated as the ratio of the Taylor number at each rotation rate relative to the fixed critical Taylor number, as follows $Ta_r = Ta/Ta_c$. Both the Taylor and Axial Reynolds numbers were estimated for the fluid phase of the 2.5wt% calcium hydroxide ($Ca(OH)_2$) slurry aqueous solution, which has an approximate kinematic viscosity of 1.068×10^{-6} m^2/s, based on a solution density of 1.016g/ml and an estimated viscosity of 0.001085 N s/m^2. This concentration of calcium hydroxide was selected because it was reported to precipitate high surface area $CaCO_3$ particles [175] and that higher concentrations did not necessarily improve the qualities of the produced PCC [174] [169], and could instead result in the formation of larger particles due to the formation of excess $CaCO_3$ primary nuclei [181].

Three kinds of forces influence the motion of the gas bubbles in this experimental apparatus, namely: gravitation, centrifugal and interaction between the phases (e.g. drag force) [58].Taylor Couette reactors are most effectively applied in two-phase gas-liquid mixing applications when the ratio of the volumetric gas to liquid flow rates is extremely small [202]. Studies examining the effect of gas flow rate on the flow stream function found that the vortex wavelength becomes increasingly elongated with increasing gas-flowrates to the extent that the Taylor vortices can vanish altogether [203]. As a result, relatively low gas flow rates were employed to minimize the impact on the vortex structure. Given the reactor geometry and fluid properties, it was found that larger flowrates induce significantly higher superficial gas velocities that could partially

compromise the vortices and influence the axial wavelength (the spacing/size of the vortices). Flow visualization analysis of gas phase behavior under flowrate of 0.5L/min, as displayed in Figure 6.2.2, revealed that the toroidal structure became significantly perturbed due to the axial flow of gas–slugs, indicating the transition towards full slug-flow, as suggested by Hubacz et al [58]. They indicated that such disturbance of the ring-flow structure is due to a surplus of the gas phase, which cannot gather in the limited space between the liquid Taylor vortices.

Figure 6.2.2 Flow visualization analysis of gas phase behavior under flowrate of 0.5L/min.

Moreover, the minimum rotation rate used in the experiments differed based on the gas flow rate, which influences the range of gas-holdup values. 200RPM and 400RPM were selected as the minimum rotation conditions at which the centrifugal forces is strong enough to overcome buoyancy effects for the gas flowrates of 0.02L/min (u_G=0.85 mm/s, $Re_{z\text{-}G}$=4.1) and 0.1L/min (u_G=4.27mm/s, $Re_{z\text{-}G}$=20.7), respectively, where the axial Reynolds number for the gas phase is described by

Equation 6.2.5 Axial Reynolds number for gas phase

$$\mathrm{Re}_{Z-G} = \frac{u_g 2d}{\nu_L} = \frac{Q_g(r_2 - r_1)}{A\nu_L} = \frac{Q_g}{\pi(r_2 + r_1)\nu_L},$$

Accordingly, experiments conducted in this study operate beyond the low rotation region, which is defined as the range where gravity dominates the motion of the gas phase [58]. Flow visualization studies examining the influence of varying gas/liquid flow ratio (β=u_G/u_L) and reactor gap-width ($d = r_2 - r_1$) show that changing such parameters has negligible effects on the observed flow patterns when operating within such a relatively high range of rotation rates [58].

6.2.2 Calcium Carbonate Precipitation

4.48 g of $Ca(OH)_2$ (Junsei Chemical, 96%) was added to 175ml of deionized water to provide a loading of 2.5 wt%, which is about 16 times its saturation solubility (0.16 g/100 g of water, which results in a pH of around 12 at the start of the experiment. The remaining $Ca(OH)_2$ stays suspended in the solution, forming a slurry aqueous phase that was placed in a feed tank equipped with a measuring grid and an Orion 3 star pH meter (Thermo Scientific), and kept at an initial temperature of 20ºC. Before each experiment, the reactor wall and inner cylinder were carefully rinsed with dilute acetyl acid solutions and distilled water to minimize the effect of the heterogeneous surface on the precipitation process [78]. A peristaltic pump was used to fill the reactor with the $Ca(OH)_2$ slurry (~117ml), with the remaining suspension measuring up to around 58ml in the feed tank.

As typically done in slurry carbonation apparatus [169] [59], Gaseous CO_2 of 99.9% purity was supplied to the reactor (0.02L/min, 0.1L/min) through a porous sparger stone frit (Water & Wood Muffler Air, pore size 180µm) at the feed entry of the gas to limit the bubble size and

ensure a better distribution of CO_2 in the slurry aqueous phase [176] [171]. Gas flow rate controller (Alicat MFC series) was used to control the CO_2 feed to the reactor, and precipitation conditions were monitored throughout the reaction by recording the time, pH and feed tank volume. As the precipitation reaction proceeds, Ca2+ ions are continuously replenished by the suspended $Ca(OH)_2$, maintaining a stable pH of 12 (theoretical is 12.3, derived from the equilibrium dissolution of calcium hydroxide [204]) throughout most of the precipitation process, until all the suspended $Ca(OH)_2$ dissolves and becomes depleted. The pH of the slurry changed from a basic to an acidic solution, and the reaction was assumed to be fully complete at pH=7 [205] [186] [204], when the $Ca(OH)_2$ phase is completely consumed [186], after which the pH reaches a steady-state of 6 [190], corresponding to the accumulated of H+ ions from the dissolution of CO_2 at its equilibrium solubility in water [169]. The pH measured in the circulation vessel was assumed to be identical to the pH in the reactor, as former studies on $CaCO_3$ precipitation in TC flow have shown that pH exhibits minimal variation across the axial length of the reactor [196]. The pH was measured at 30-seconds measurement interval to ensure accurate detection of the completion time of the precipitation process. At the end of each experiment, 60 ml of the final suspension was collected and centrifuged at 6500rpm for 15minutes [206], as centrifuging is cited as the preferred method relative to filtration due to the possibility of retaining a greater number of finer particles [174]. The samples were washed once with deionized water [207], centrifuged once again at the same conditions and then dried at 110 °C for 1 hour to remove all remaining moisture [208], before characterizing the PCC product properties.

6.2.2.1 **Material Characterization**

Phase structure and crystallite size of $CaCO_3$ was identified using a Scintag Theta-Theta X-ray Diffractometer (XRD) (Cu K_ radiation, λ = 1.5418A°), while the crystal size and morphology were examined using Tescan Mira3 Field Emission Scanning Electron Microscopy (FESEM). Analysis of the particle size of calcium carbonate was possible through size measurements performed in the Malvern Zetasizer instrument (measures between 0.6 nm – 6 μm), which works on Dynamic Light Scattering (DLS) principle. After treatment in ultrasonic bath for 10minutes to ensure crystal redispersion [206] [167] and minimize secondary agglomerates [189], samples were filtered in a 0.5μm filter before performing measurments in the Malvern Zetasizer. The specific surface area (SSA) was measured using Tristar 3000 (Micromeritics, Norcross, GA, USA) analyzer after pre-treatment at 573 K to remove all moisture from the pores. The nitrogen gas was assumed to be adsorbed in multiple layers on the surfaces of $CaCO_3$ particles. The SSA of PCC was calculated using Brunauer–Emmet–Teller (BET) adsorption isotherms, and pore size distribution was calculated using the Barrett–Joyner–Halenda (BJH) method as well as density functional theory (DFT).

6.2.3 Gas-Liquid Flow Characterization

Prior to the crystallization study, experiments examining flow patterns, gas bubble size and dispersion at each precipitation condition were performed. Flow visualization was the primary technique used to assess the variety of flow patterns generated during the mixing of the gas and aqueous phases at different rotation rates. For the purpose of capturing the bubbles more clearly, mixed gas and 2% glycerin solution were chosen as the system to get clear images, avoiding the milkiness of the $Ca(OH)_2$ solution (see Figure 6.2.3) while mimicking its hydrodynamic behavior, by introducing glycerin content that leads to matching kinematic viscosities.

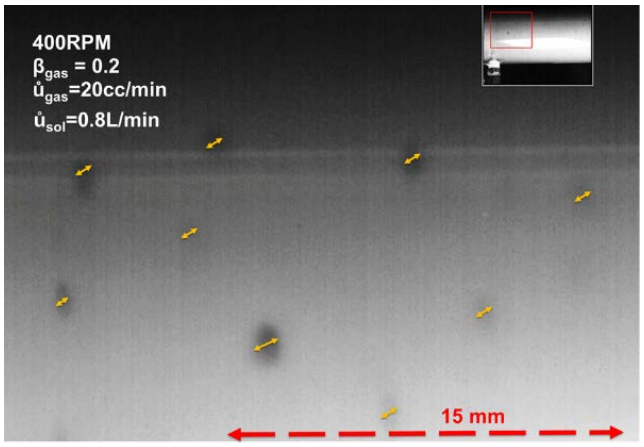

Figure 6.2.3 In-situ flow visualization during precipitation is limited due to milkiness of the $Ca(OH)_2$ solution.

Given that the bubble size is directly related to the pore size of the frit, the anticipated CO_2 bubble size produced by the frit was estimated to be around 2mm, using the following equation, as suggested by Xian et al [204]:

Equation 6.2.6 Estimated gas bubble size produced by sparger frit

$$d_b = \left(\frac{6d_0\sigma}{\Delta\rho g}\right)^{\frac{1}{3}}$$

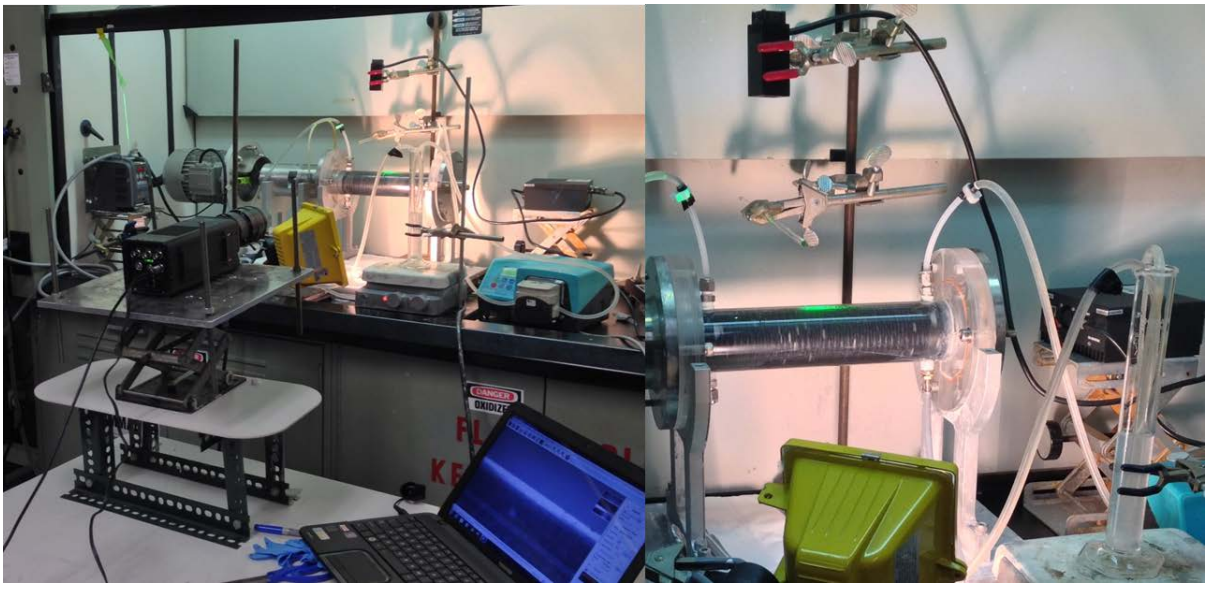

Figure 6.2.4 Gas-Liquid Flow Visualization Experimental Setup

Small superfine reflective anisotropic particles were seeded in the given fluid. The pigmented titanium dioxide coated mica flakes (Kalliroscope: 4x32 microns, 3.1 g/ml) align themselves with the local shear stress direction, and light reflectance off the particles makes the flow field visible. To create an opaque and highly light scattering solution, the flakes were added to the fluids at a volume fraction of 2×10^{-5}, as suggested in other studies [63]. Different flow regimes were identified via flow visualization using a high speed CCD video camera, which acquired and stored the images directly in 256 shades of gray. The on-board memory is sufficient for 3300 images, which can be captured at any rate up to 1000 Hz. To adjust image quality for different operating conditions, parameters, such as, exposure, image capturing rate (Hz), and movie playing speed (frames per second) were modified accordingly.

The high-speed CCD video camera was used to record the images at the outside of the transparent Plexiglas outer cylinder with a minimum frequency of 100 images per second. Similar to former studies [181] , the size distribution of the bubbles at each mixing condition was evaluated via the photographic image processing method by measuring the sizes of at least 150, and 230 well-defined individual minibubbles for gas flowrates of 0.02L/min and 0.1L/min, respectively, taken from a minimum of 15 different images, using an ImageJ analysis software package. To avoid refraction distortions associated with the curvature of the transparent outer cylinder only bubbles appearing in the mid frame region were taken into consideration, as they exhibited distortions. Along with a reference length scale of 5 mm calibration grid attached onto the outer surface reactor provided, the spatial scale for the gas bubbles was adjusted with a pixel aspect ratio of 0.8 to account for potential axis skewness associated with the oblate spheroid shape of some bubbles [209], which is close to the experimentally observed average bubble ellipticity for gas-liquid phase dispersions in vertical reactors [59] [60].

To complement the optical technique, digital photographs of the annulus were acquired via laser-sheet visualization. To provide more qualitative information of the flow field, laser sheet illumination of the flow in the *r-z* plane was used along a cross-section of the annulus [57]. A 50mW Argon-ion laser beam was expanded into a laser sheet by a simple rod-shaped cylindrical lens. When the laser sheet is coplanar with the axis of the cylinders, the interface is clearly visible, and qualitative details about the fluid motion are obtainable. Probed by illuminating the gap, the axial and radial structure of the disturbance flow in the highlighted cross-section can be determined. For flow visualization, the camera is placed orthogonal to the illuminated section. As displayed in Figure 6.2.4, laser-sheet imagery in the annulus provided more insights into the geometric characteristics of the bubbles.

Similar to the apparatus in the crystallization study, the average CO_2 the gas hold-up (ε_g) at each mixing condition, which is necessary to determine the gas–liquid interfacial area [210], was measured by monitoring the change in aqueous liquid fraction of $Ca(OH)_2$ inside the feed tank vessel. The gas volume fraction grew progressively until it reaches its steady-state value in less than 100seconds for the flowrates and gas-holdups applied in this study [211]. From the gas hold-up and bubble diameters, the specific interfacial area of the bubble was obtained by the following equation [212, 59] [7]:

Equation 6.2.7 Specific interfacial area (m^{-1})

$$a = \frac{6\alpha_g}{d_{32G}(1-\alpha_g)}$$

6.3 Results

6.3.1 Bubble Analysis

6.3.1.1 **Bubble size distribution**

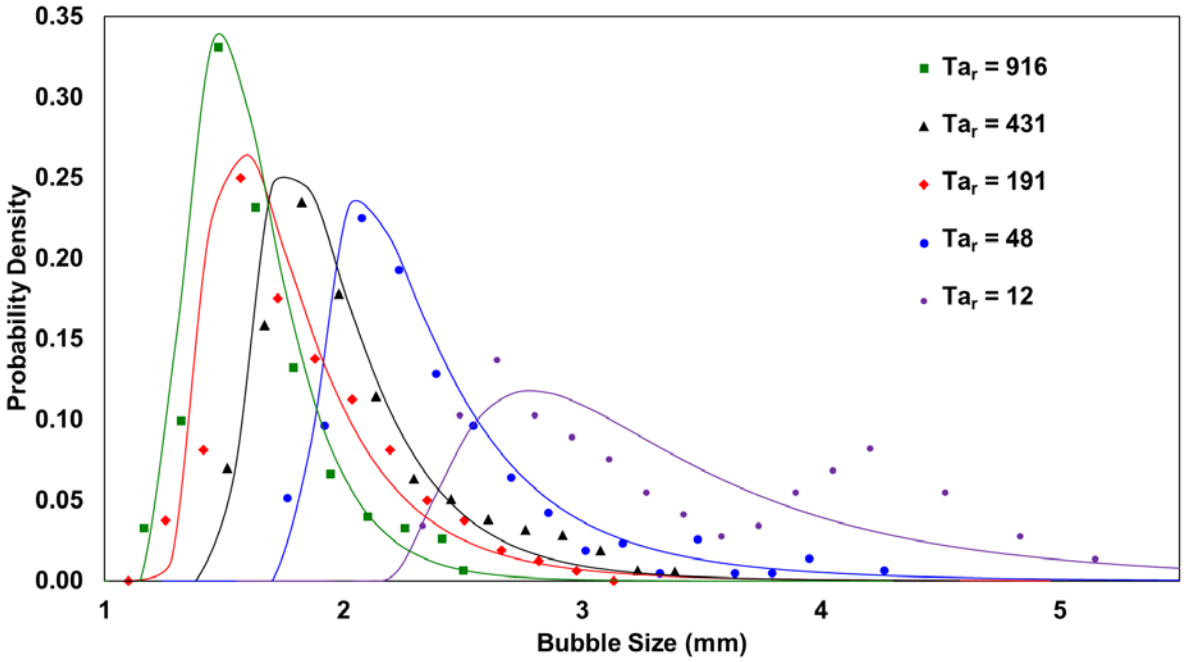

Figure 6.3.1 Bubble size distribution fit to a log-normal probability density for the case of 0.02L/min CO_2 flowrate (Re_{z_G} = 4).

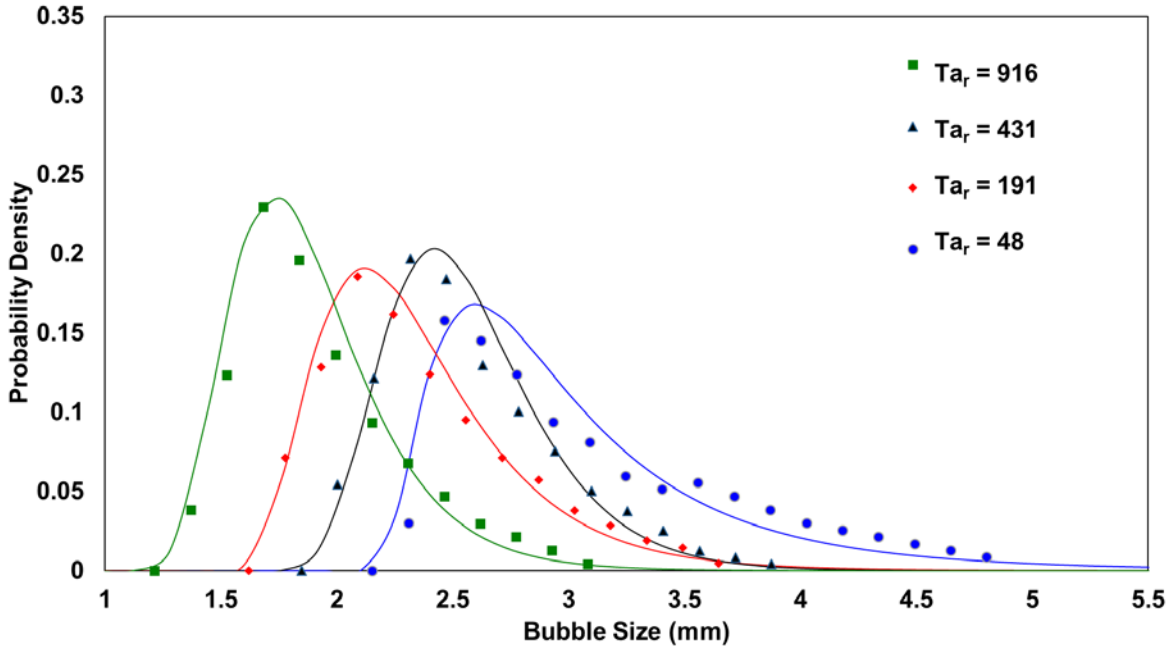

Figure 6.3.2 Bubble size distribution fit to a log-normal probability density for the case of 0.1L/min CO_2 flowrate (Re_{z_G} = 21).

The distributions of bubble sizes measured for a minimum of 150, and 230 well-defined individual minibubbles for gas flowrates of 0.02L/min and 0.1L/min, are shown in Figure 6.3.1 and Figure 6.3.2, respectively. Each probability distributions for the bubble mean diameter is fit to a log-normal probability density function having identical values of the mean and standard deviation as the corresponding experimental distribution. With the exception of 200 RPM, the experimentally determined bubble size distributions were well represented by log-normal functions for all cases. The bubble size distribution are mostly monomodal and exhibited a shift towards smaller ranges with increasing cylinder rotation and decreasing gas flowrate. In general, the BSD followed a distribution pattern that is skewed towards larger bubbles, resembling that of log-normal distribution. At low rotation rates buoyancy forces the curve is broad, indicating bubble coalescence, which can be clearly seen in the bimodal distribution of the bubble size at 200rpm for a gas flowrate of 0.02L/min. An increase in the broadness of the

BSD can be noticed when shifting from 800rpm to 1200rpm for both gas flowrates. With further increase in the rotation rate, the bubble size distribution (BSD) curve appears to narrow the most at the highest rotation rate.

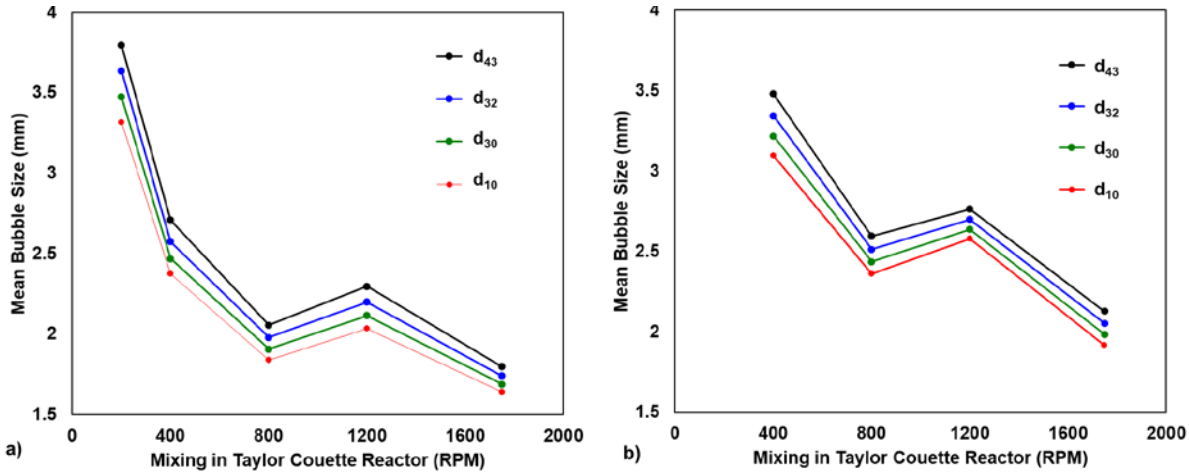

Figure 6.3.3 The different mean bubble diameters derived from the probability distributions for a) 0.02L/min CO_2 flowrate (Re_{z_G} = 4), and b) 0.1L/min CO_2 flowrate (Re_{z_G} = 21).

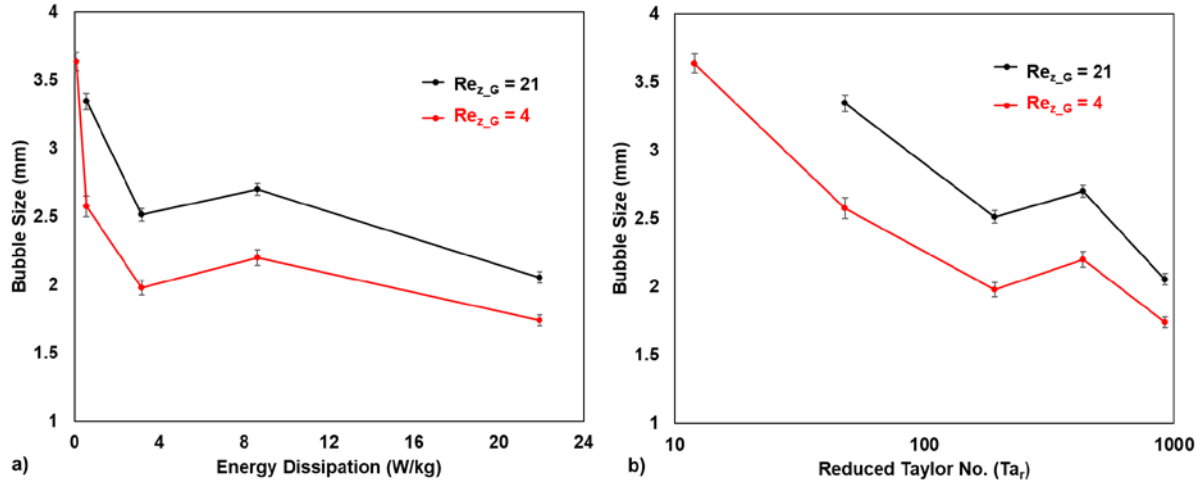

Figure 6.3.4 Sauter bubble diameter (d_{32}) derived from the bubble size probability distributions.

The histograms of the experimentally determined bubble size distributions were used to estimate the mean bubble diameter used multiple estimates, as plotted in Figure 6.3.3, including the arithmetic diameter (d_{10}), volume-mean diameter (d_{30}), Sauter diameter (d_{32}) and DeBroukere diameter (d_{43}). The bubble arithmetic mean diameter varied between

approximately 1.5-3.5 mm for most cases with standard deviations of in the range between 0.5mm and 0.9 mm. Given that the estimated mean bubble diameter produced by the frit is around 2mm, conditions that produce smaller bubbles facilitate more bubble breakage while conditions that produce larger bubble sizes indicate that bubble coalescence dominates bubble breakage. Since it is the most common measure in fluid dynamics as a way of estimating active surface area, particularly when it comes to efficiency studies and quantifying mass transfer [213], the Sauter diameter (d_{32}), displayed in Figure 6.3.4, was selected as the most suitable bubble diameter to be used in the quantifications of the interphase mass transfer [60].

6.3.1.2 Flow Structure visual analysis

Samples of the flow patterns captured using the photographic technique to obtain gas bubble size distribution in the reactor are displayed in Figure 6.3.5 and Figure 6.3.6 for gas flowrates of 0.02L/min and 0.1L/min, respectively. As observed in a study examining bubble behavior in the highly turbulent vortex flow regime [214] and in a study exploring mass-transfer in gas-liquid flow in vertical Taylor vortex reactors [212], the bubbles tended to lean towards the inner cylinder at higher rotation rates of 1200RPM and 1750 RPM, particularly in the case of the lower gas flow rate of 0.02L/min, as can be seen from the laser sheet visualization in Figure 6.3.5 (i and j), but also in Figure 6.3.6 (g) for the case of 1200RPM at 0.1L/min CO2 flowrate. Although bubble clustering was still significant in the case of 1750rpm, bubble coalescence was observed to be lower than in the case of 1200rpm, a feature that has been observed in the case of bubble clusters in highly turbulent flow regimes in horizontal turbulent channel flow [215] .

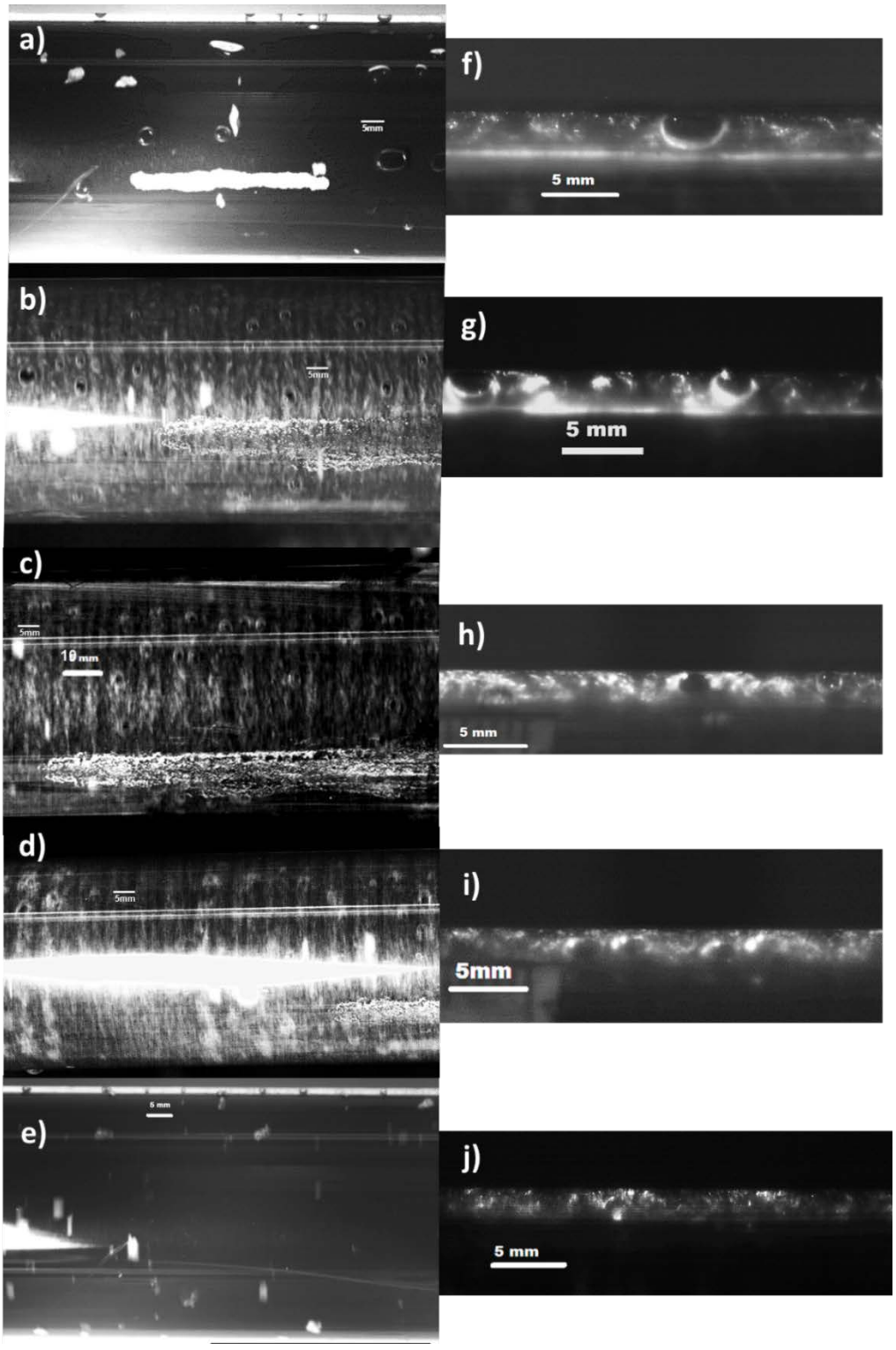

Figure 6.3.5 At condition of 0.02L/min CO_2 flowrate, samples of the flow patterns captured using the photographic technique to obtain gas bubble size distribution in the reactor (a-e), and samples of laser sheet visualization (f-j), for Ta_r= 12, 48, 191, 431 and 916, respectively.

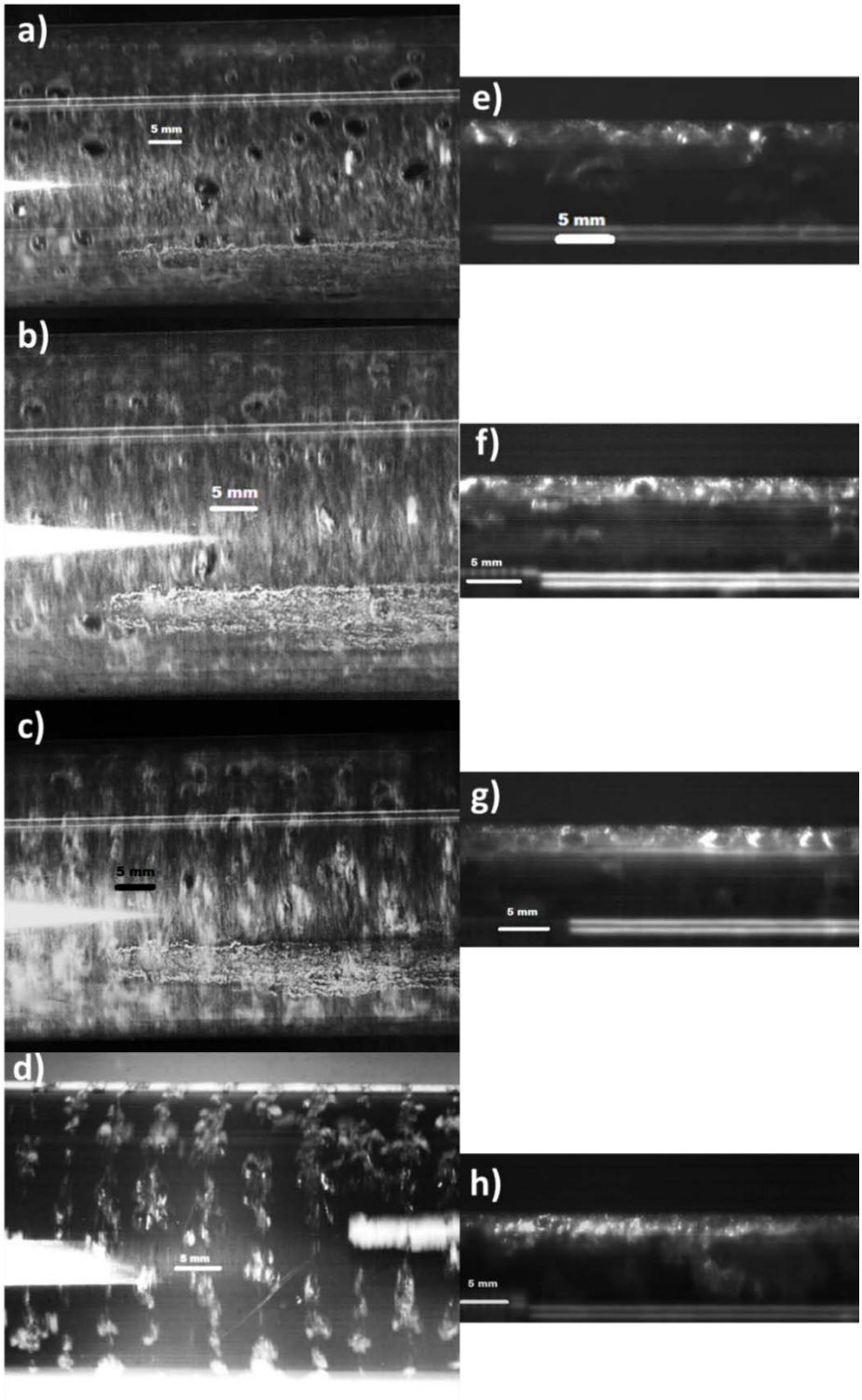

Figure 6.3.6 At condition of 0.1L/min CO_2 flowrate, samples of the flow patterns captured using the photographic technique to obtain gas bubble size distribution in the reactor (a-d), and samples of laser sheet visualization (f-h), for Ta_r = 48, 191, 431 and 916, respectively

Similarly, increasing the cylinder rotation speed has been also observed to lead the bubbles to migrate radially towards the inner cylinder in the case of a vertical Taylor Couette reactor [59], pushing the bubbles in between the Taylor vortices, causing them to coalesce, and thereby increasing the bubble size. Such gas-rich spots form intermittently in the case of lower gas flowrate as a result of the coalescence of a smaller number of bubbles than in the uniformly distributed alternating gas-rich rings that can be clearly observed at higher gas flowrates. As show in Figure 6.3.5, the bubbles at such conditions tend to gather at the outflow boundaries of the Taylor vortices [58]. With higher rotation rates (i.e. 1750rpm) the bubbles are coerced to follow flow contour lines rather reducing buoyancy effects to a minimum, as smaller bubbles proceed with lower slip velocities [177]. Hubacz et al observed that such bubbly ring flow structure started to emerge at high rotation rates (above 4.03W/kg, which correspond to $Ta \geq 2.9x10^6$; $Ta_r=Ta/Ta_c$= 236 or 900 rpm in this study) only for the smallest gap width (η=0.92), with a gas–liquid flow rate ratio (β=1/8) [58]. Early studies on gas-liquid mixing in Taylor-Couette flow identified that uniform toroidal ring-form spiral patterns of bubble dispersion predominate at higher rotation rates, while dispersed bubbly flow patterns dominate the flow field at low rotation rates, due to weaker vortex motion [216]. Under such spiral patterns, the bubbles are thought to accumulate in the outflow regions located between two counter-rotating vortices [217]. Ring flow patterns, where liquid Taylor vortices were separated by the rings of bubbles, for the case of vertical Taylor Couette flow have been identified to occur at specific range of large Taylor numbers [218] that correspond to values matching a mixing rate of 1100rpm (Ta_r=363) in our study.

6.3.1.3 **Gas phase parameters**

In addition to bubble size, the gas volume fraction during the experiment was continuously monitored throughout each experiment, as summarized in Figure 6.3.7 (a). The CO_2 average residence time in the reactor was estimated as shown in Figure 6.3.7 (b).

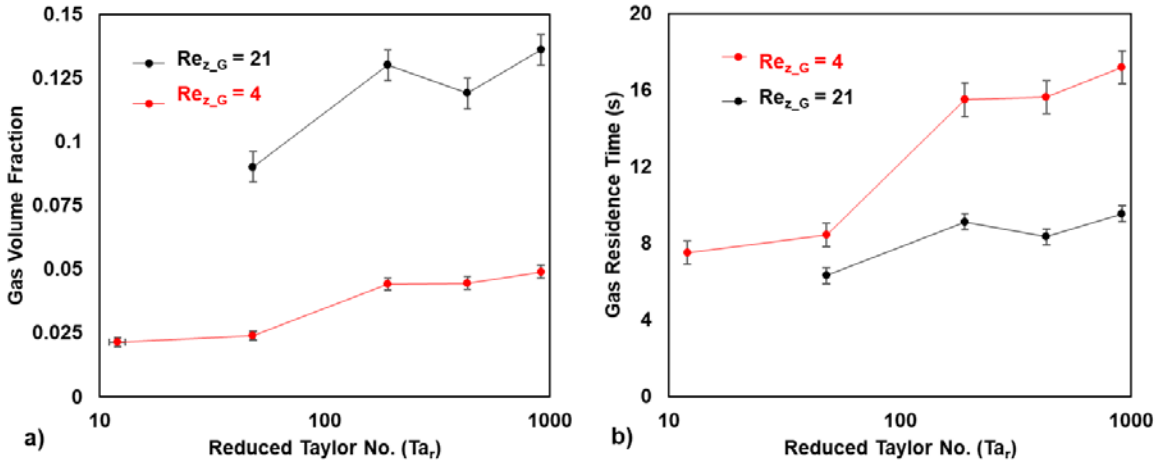

Figure 6.3.7 The measured gas volume fraction (a) and the estimated gas residence time (b) plotted against Ta_r.

Since the residence time distribution is mainly controlled by the macro-fluid motion [78] , the gas volume fractions and the corresponding gas residence times were observed to exhibit minimal change once the reduced Taylor number surpasses 200, which corresponds to the transition to weakly turbulent vortex flow (WTVF), typically observed at $Ta_r = Ta/Ta_c \sim 178$ [75]. The increase in residence time when transitioning to 1750RPM, which corresponds to 980Tac, is more prominent in the case of the lower gas flowrates, as the average bubble size is smaller under such conditions, allowing the bubbles to conform to the streamlines associated with fully turbulent Taylor vortex flow (TTVF), which is expected to emerge at $Ta_r=Ta/Ta_c$ ~1000 [75], and can be reached at lower Taylor number values as the gap becomes increasingly smaller [12]. Interestingly, the CO_2 residence time was observed to be similar at the rotation of 400RPM (Ta_r = 51) for both CO_2 flow rates. The gas volume fraction and gas-residence times were observed to increase dramatically beyond Ta_r= 207 (800rpm) for both large and low

gas flowrates, while remaining within a similar range under higher rotation conditions. Such dramatic increase is due to the shift towards the HR (high rotation) flow regime behavior, which is estimated to be around 580rpm (Ta_r=101), according to the dimensionless correlation developed by Hubacz to predict the transition to HR flow behavior [219]. The development of helical ring flow increases the contour-lengths of the flow streamlines leading to an increase in the travel-distance of gas bubbles passing through the reactor [200].

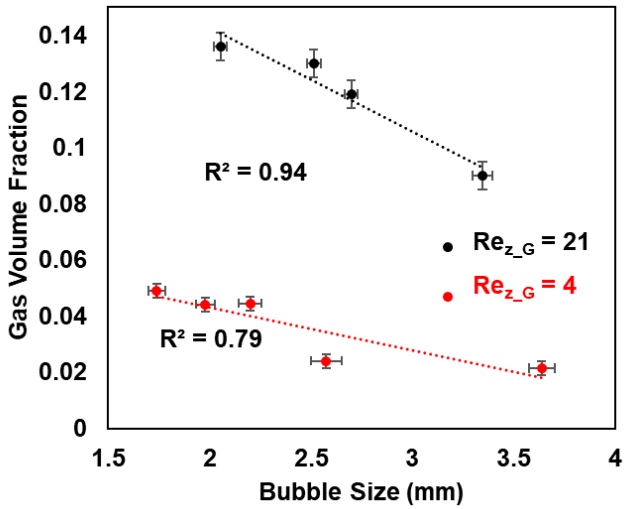

Figure 6.3.8 Smaller bubbles were produced with rotational conditions that accommodated larger gas volume fractions.

As observed in previous studies [177], Figure 6.3.8 shows that smaller bubbles yield higher gas holdup rates. Such phenomena has been attributed to smaller bubbles become trapped within the vortices as the flow becomes increasingly turbulent, which in turn, results in an increased bubble residence time [200]. As in a bubble column [210], increasing the gas flow-rate led to a proportional increase in the mean bubble diameter and the gas volume fraction in the reactor. Taylor toroidal flow tends to be disturbed by random bubble flow at low rotational rates due to weak centrifugal forces compared with buoyancy forces acting on bubbles, leading to lower gas hold-up values [7].

6.3.1.4 Interfacial Area Analysis

Sauter Mean diameter (SMD), d_{32}, is the most common measure in fluid dynamics as a way of estimating active surface area, particularly when it comes to efficiency studies and quantifying mass transfer [213], thus, the Sauter mean diameter of all the bubbles was used was used to quantify the interphase mass transfer [60]. Since the ratio of the ratio of area to volume of a gas bubble is inversely proportional to its diameter, smaller bubbles hold higher interfacial area [177]. The measured gas average bubble sizes (d_{32G}) in these experiments were assumed to be identical to those that exist during the precipitation reaction since the reaction regime is not instantaneous [210]. The specific gas–liquid interfacial area per unit reactor for each condition was estimated using the gas hold-up and Sauter mean bubble diameter as per Equation 6.2.7, and the absolute interfacial area *A* (m^2) was estimated as suggested in [181] by:

Equation 6.3.1 Absolute interfacial area *A* (m^2)

$$A = \frac{6V\alpha_g}{d_{32G}}$$

Figure 6.3.9 demonstrates how the reactor hydrodynamic mixing conditions influence the gas–liquid interfacial area. As with the bubble size measurements, the interfacial area does not experience a monotonic increase with higher rotation rates, and a local extrema is observed at around 1200RPM [6]. The aggregation of dispersed bubbles and resulting coalescence has been observed to reduce the interfacial area [200]. Indeed, such reduction in interfacial area is due to the emergence of the transition structure which results in ordered flow structure that enhances phase segregation, until the rotation rate is increased to ranges where vortices diminish and the flow becomes turbulent, leading to a further enhancement in the surface area [6]. Unlike in a bubble column where the gas volume fraction is primarily controlled by the gas-flowrate, it was

found that reducing the bubble size via rotational energy has more impact on the interfacial area per unit volume than the volume fraction, which is mainly controlled by the gas-flowrate in bubble column configuration [210].

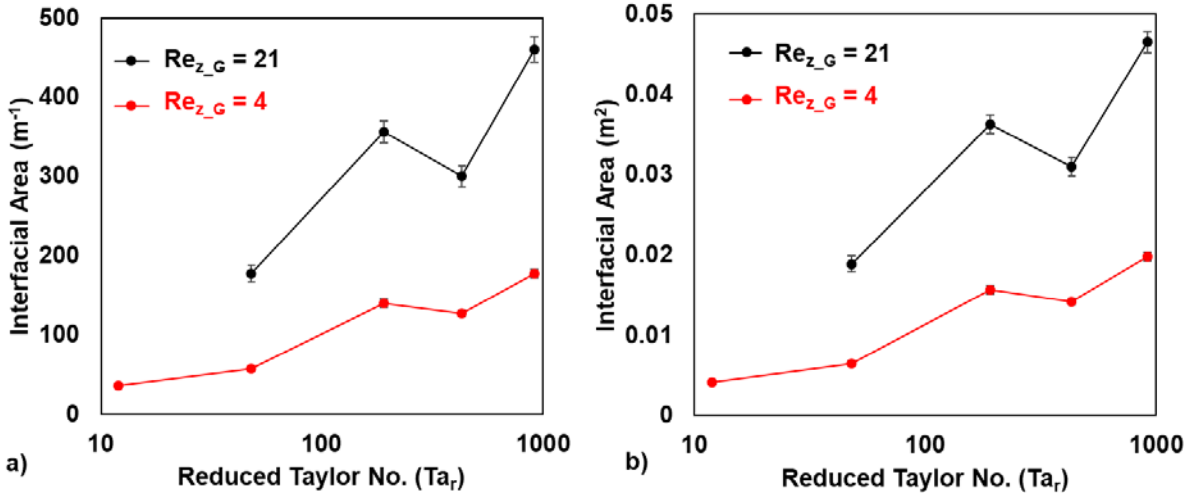

Figure 6.3.9 a) The relative interfacial area, *a* (m^{-1}), and b) the absolute interfacial area *A* (m^2).

6.3.2 Calcium Carbonate Precipitation

6.3.2.1 Yield and Acquisition Time

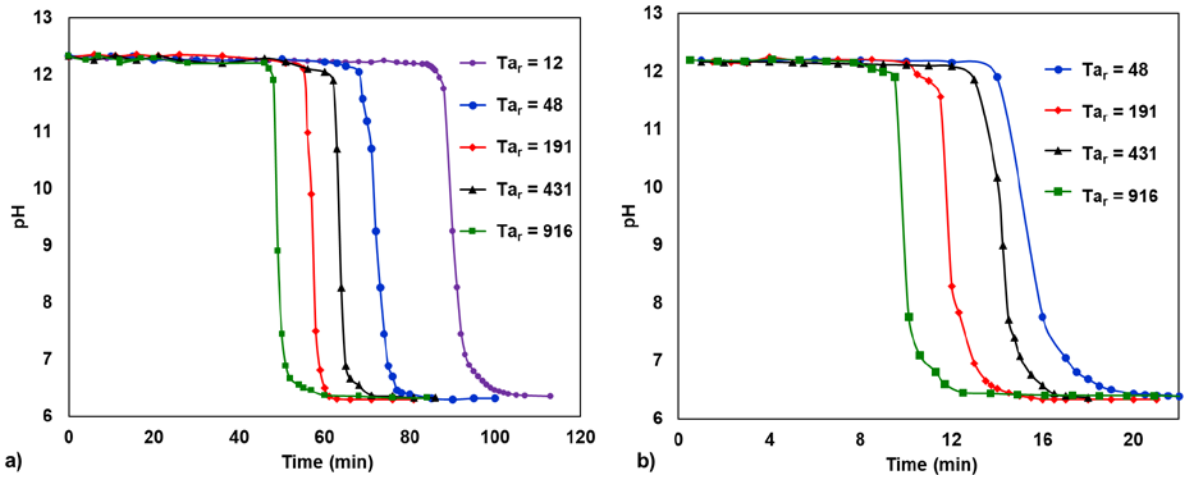

Figure 6.3.10 Change of pH values with acquisition time for different rotation rates at a) 0.02L/min CO_2 flowrate, and b) 0.1L/min CO_2 flowrate.

The progress of the precipitation reactions at each condition was controlled by monitoring the change in pH with the acquisition time, as the hydroxyl ions from the calcium hydroxide

dissociation are consumed to for the production of calcium carbonate [192] [24]. The rate of $CaCO_3$ can be estimated from the depletion rate of the calcium hydroxide during the carbonation, since both proceed with almost identical rates [220]. As can be seen in Figure 6.3.10, most of $CaCO_3$ precipitation occurs at a steady-state pH around, 12.3, which corresponds to the saturation solubility of $Ca(OH)_2$ in water [205]. At such high pH conditions, where CO_2 dominates in the form of carbonate ion [178] [14], precipitation of $CaCO_3$ is known to take place instantaneously [189][21]. As the hydroxyl ions become depleted, the variation of pH as a function of time exhibited a steep decrease in the pH of the suspension, entering the neutralization stage, which is marked by the Hatched region of the time-pH curve, and moving towards an acidic steady-state of pH=6.23, which marks the presence of dissolved gaseous carbon dioxide, in the form of H_2CO_3 [178] [14]. The reaction was assumed to be fully complete at pH=7, within the hatched region of the neutralization state [205] [186] [204].

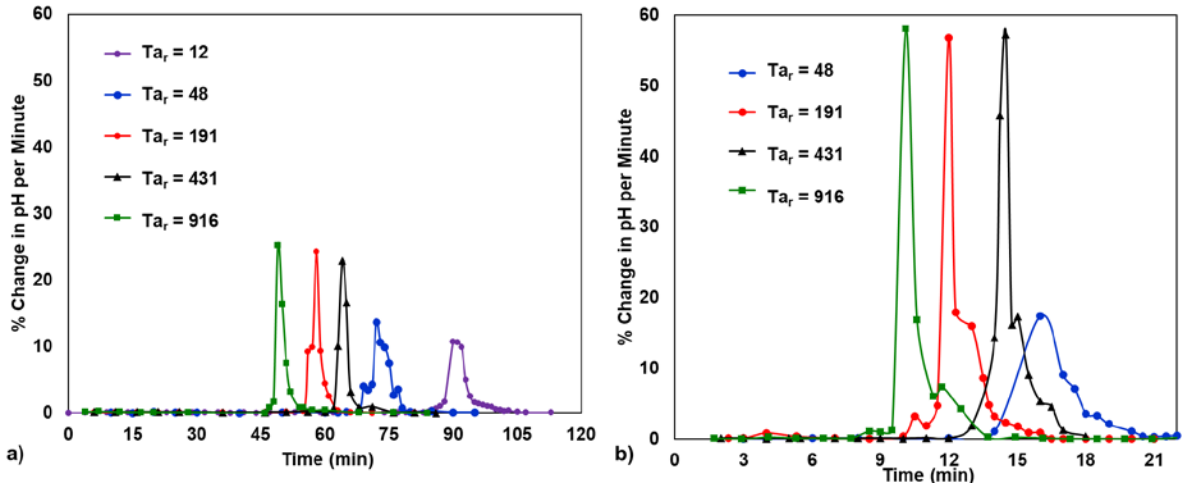

Figure 6.3.11 The rate of pH change per minute values with acquisition time for different rotation rates at a) 0.02L/min CO_2 flowrate, and b) 0.1L/min CO_2 flowrate.

The deviations in pH were quantified by taking the slope of the pH curve, i.e. the difference between two subsequent pH values per time interval, and the negative time derivative of pH is plotted in Figure 6.3.11. The negative of the pH time derivative steeply rises at a certain point,

signifying the rapid completion of the reaction reaching a pH minimum value of. The precipitation reaction rate was estimated from monitoring the variation in pH.

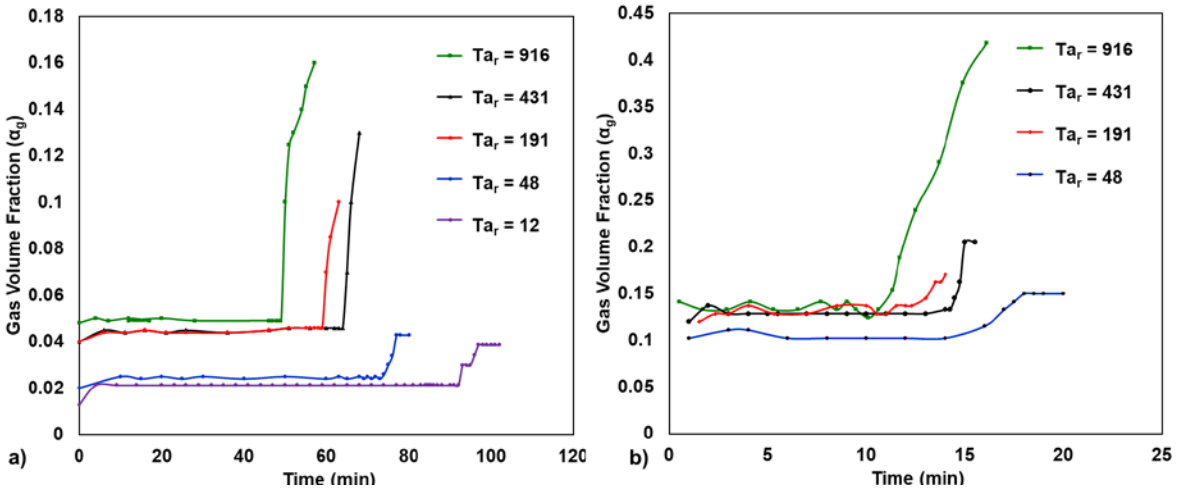

Figure 6.3.12 The change in measured gas volume fraction during precipitation reaction for a) 0.02L/min CO_2 flowrate, and b) 0.1L/min CO_2 flowrate.

The gas volume fraction during the experiment was continuously monitored throughout each experiment, as summarized in Figure 6.3.12. The values observed during the precipitation nearly equivalent to those observed without reaction as displayed in Figure 6.3.7 (a).

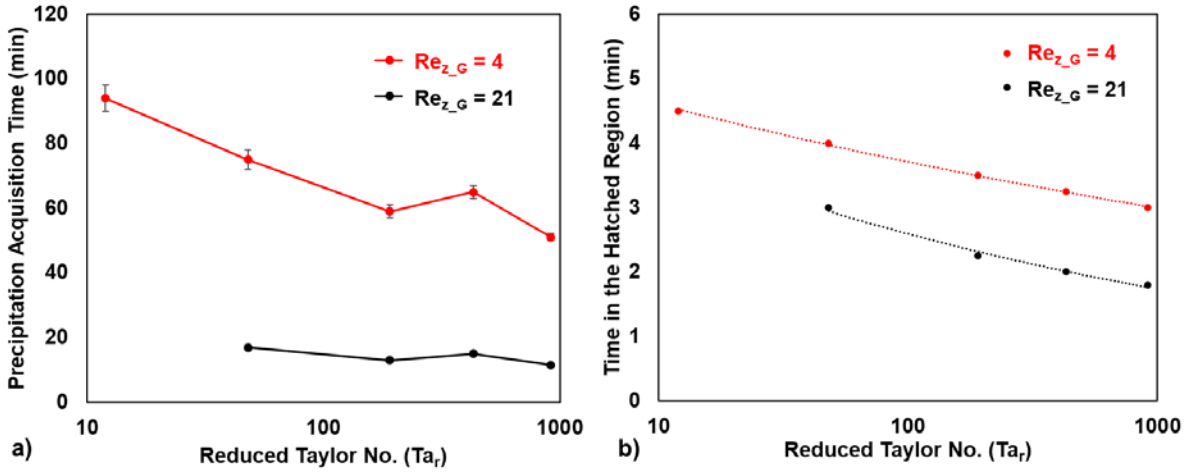

Figure 6.3.13 a) Precipitation acquisition time, and b) time spent in the hatched region, as derived from the change in pH data.

The acquisition time was observed to be significantly shorter as the injection flow rate of carbon dioxide increased from 0.02L/min to 0.1L/min, as can be seen in Figure 6.3.13 (a) and (b), respectively. The dependence of the precipitation acquisition time upon the CO_2 flow rate was close to linear [190], but tended to deviate more as the interfacial area increased, indicating more efficient CO_2 uptake. As observed in former studies that assessed the influence of rpm on reaction rate [190], the carbonation reaction generally proceeded at faster rates with higher cylinder rotation rates. Steeper decline and a narrower hatched region with reduced width (duration) was observed with increasing RPM, as summarized in Figure 6.3.13 (b). It was found that precipitating $CaCO_3$ through the carbonation route by bubbling carbon dioxide at 800rpm, as opposed to 1200rpm, reduced the precipitation acquisition time.

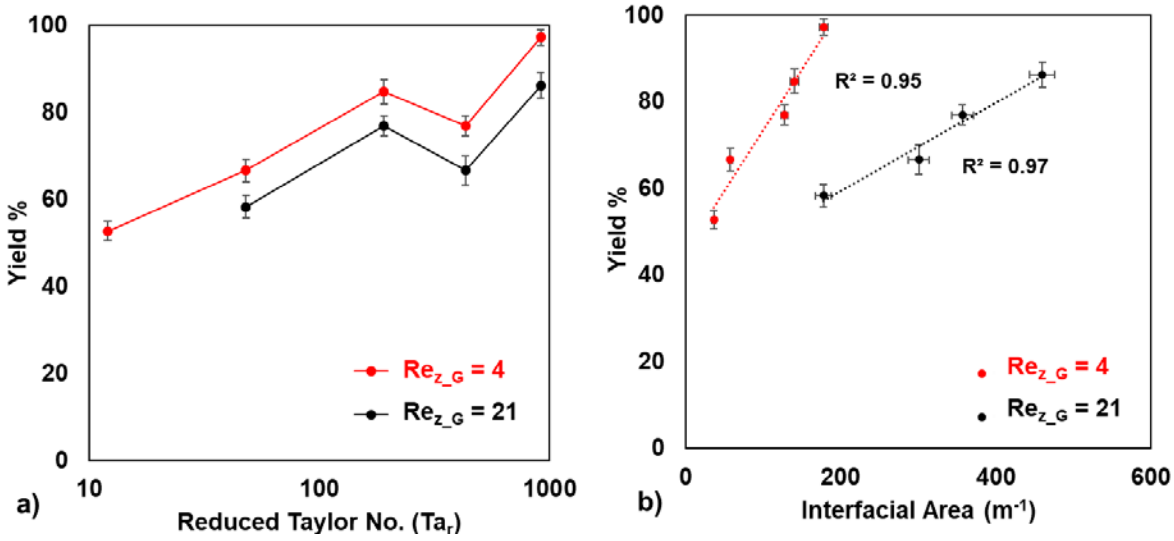

Figure 6.3.14 The increase in precipitation yield % (actual/theoretical) as a function of a) rotational motion and b) interfacial area.

Figure 6.3.14 displays the yield or the conversion efficiency of carbon dioxide reacting to form carbonate minerals. The estimated yield of the reaction was observed to be lower for the case of higher gas flowrate due to the in the incomplete dissolution and partial leak of the gas, resulting in lower CO_2 uptake [190]. As anticipated, the rate of production of PCC crystals,

displayed in Figure 6.3.15, was much more significant for the samples precipitating with higher CO_2 flowrates. The change in mixing intensity and the corresponding increase in the interfacial area had more impact on the rate of production for PPC formed under higher CO_2 flowrates.

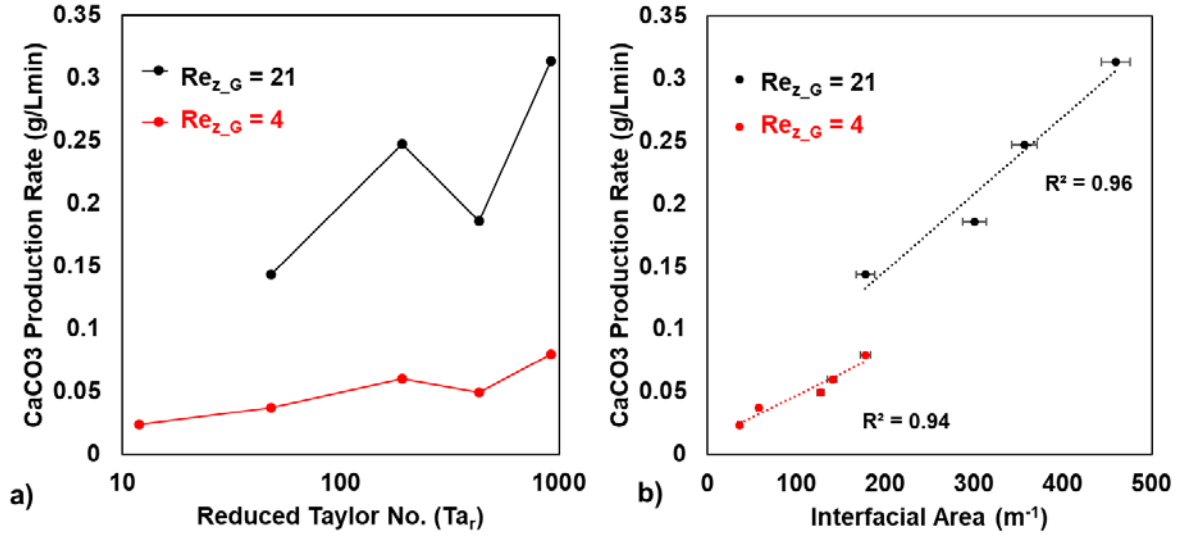

Figure 6.3.15 The change in the rate of CaCO3 production in g/Lmin as a function of a) rotational motion and b) interfacial area.

6.3.2.2 **XRD Analysis**

XRD analysis revealed that PCC samples at all conditions produced similar diffracted patterns that displayed peaks which matched typical rhombic calcite polymorph peaks, as can be seen in Figure 6.3.16 and Figure 6.3.17, for PCC formed under 0.02L/min and 0.1L/min CO_2 flowrates, respectively. By referring to the prominent 104 peak on the calcite surface, observed at $2\theta = 29.35 \pm 0.1$, the crystallite sizes for the PCC samples were estimated using the Debye Scherrer Equation and are plotted in Figure 6.3.18 . The reduction in crystallite size was found to linearly correlate to the increase in interfacial area, especially in the case of higher CO_2 flowrate. The range of crystallite sizes found in this study were similar to the ones observed

for $CaCO_3$ precipitated under the influence of ultrasound [185] and nanostructured PCC using rotating disc reactor unit [182], and close to the found here (30nm) [182].

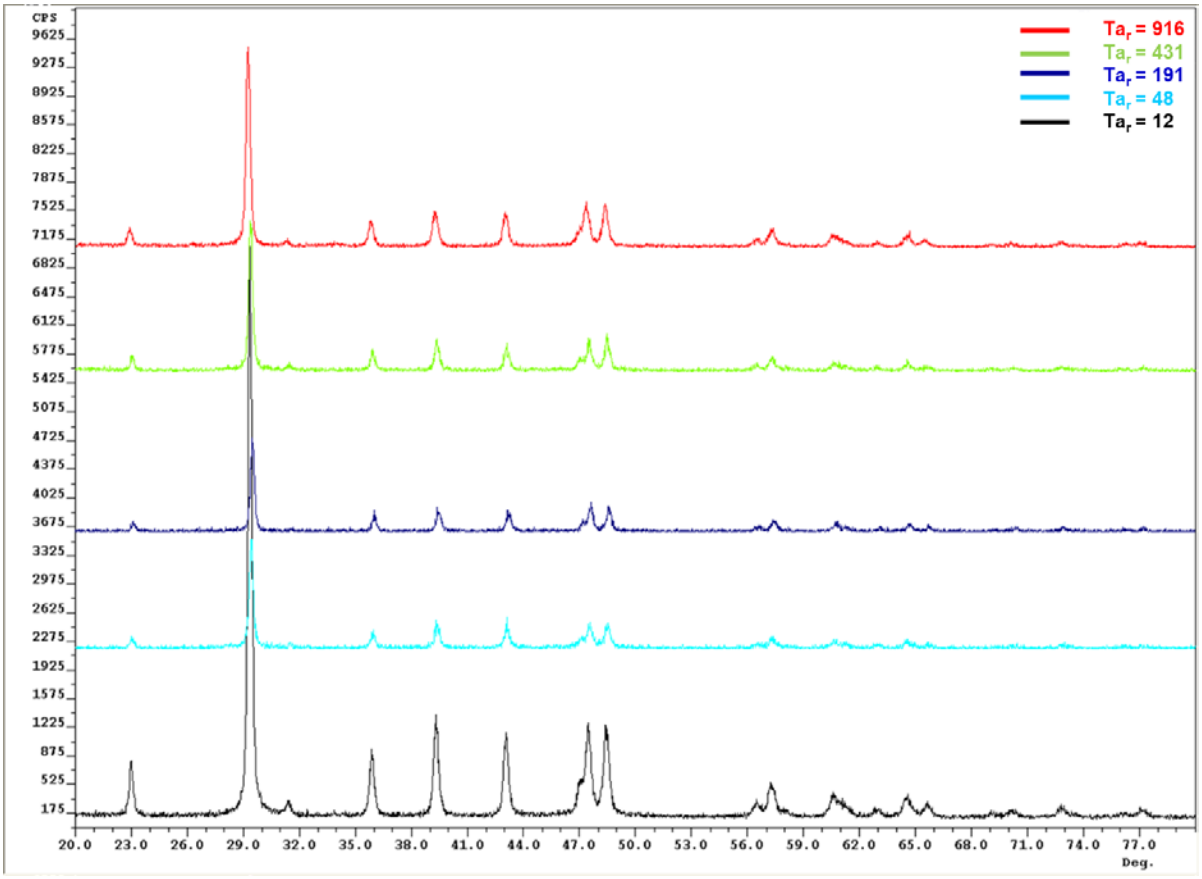

Figure 6.3.16 XRD analysis for PCC formed under 0.02L/min CO_2 flowrate.

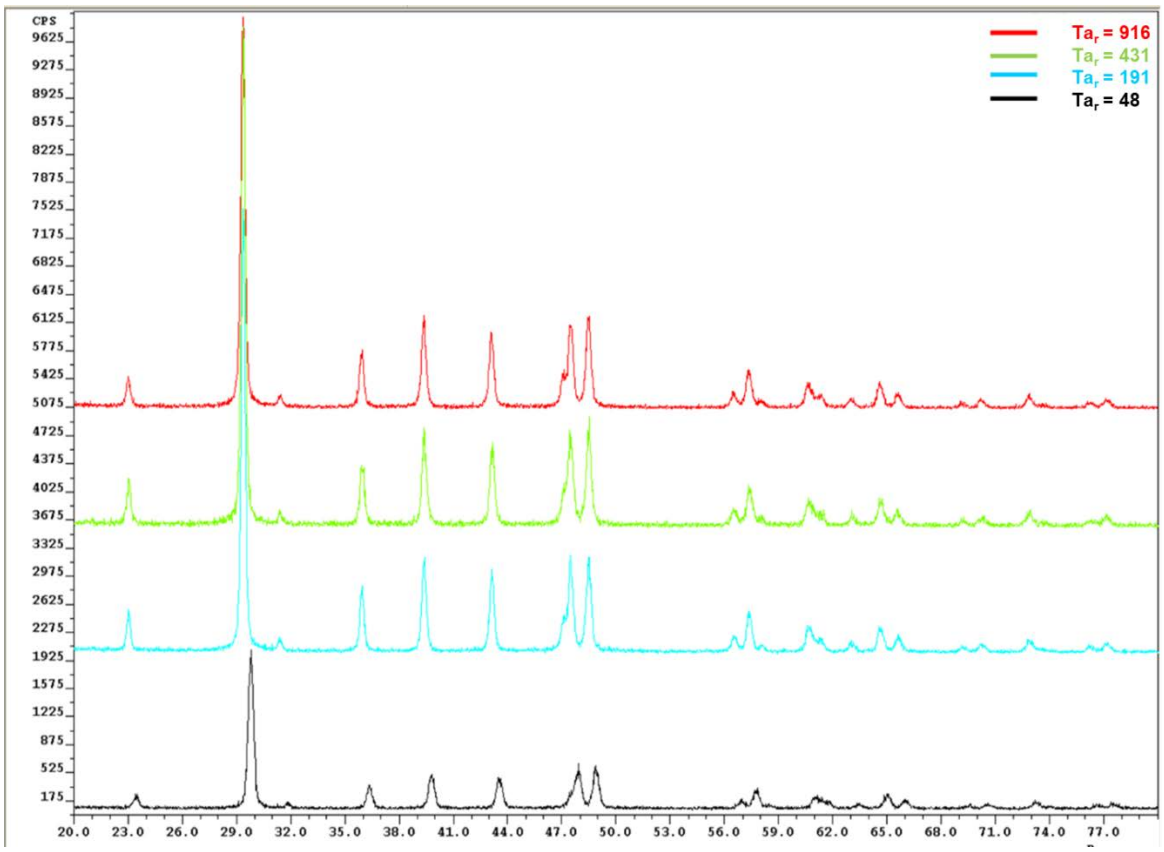

Figure 6.3.17 XRD analysis for PCC formed under 0.1 L/min CO_2 flowrate.

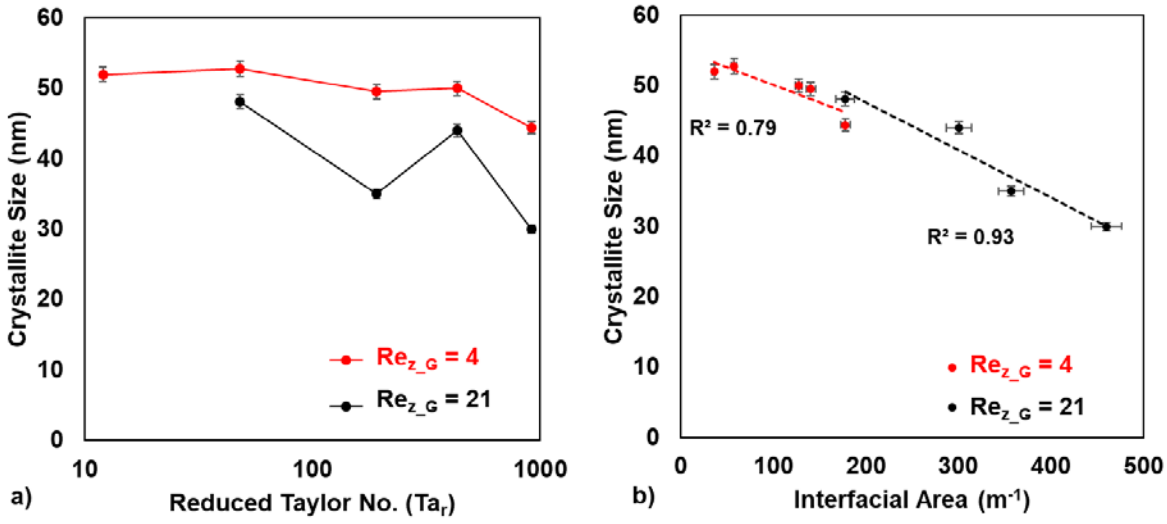

Figure 6.3.18 Change in crystallite size as estimated from XRD analysis as a function of a) rotational motion and b) interfacial area.

6.3.2.3 **Morphology**

The morphology of PCC formed under different rotational speeds for CO_2 flowrates of 0.1 L/min and 0.02 L/min can be viewed in Figure 6.3.19 and Figure 6.3.20, respectively. Under lower CO_2 flowrates, PCC morphology changed from random scalenohedral shape at 200rpm to more uniform and well-defined shapes at 400rpm, with significantly reduced size and narrower aspect ratio at 800rpm. Increasing the rotation rates further to 1200rpm resulted in an increase in particle size with larger aspect ratio. The size and shape of the PCC formed was drastically changed when reaching a rotation rate of 1750rpm, as the crystals appear much smaller with spherical morphology. A similar trend is observed when examining the crystal size in the SEM images for PCC formed under higher CO_2 flowrate (0.1L/min), but in this case no scalenohedral crystals are observed, rather spherical morphology dominates under all rotation conditions. This is consistent with previous studies which observed that changing the calcium-to-carbonate ratio greatly affects the morphology of PCC particles [190], and that lower CO_2 flowrates lead to the domination of spindle-shaped needle-like morphologies [78].

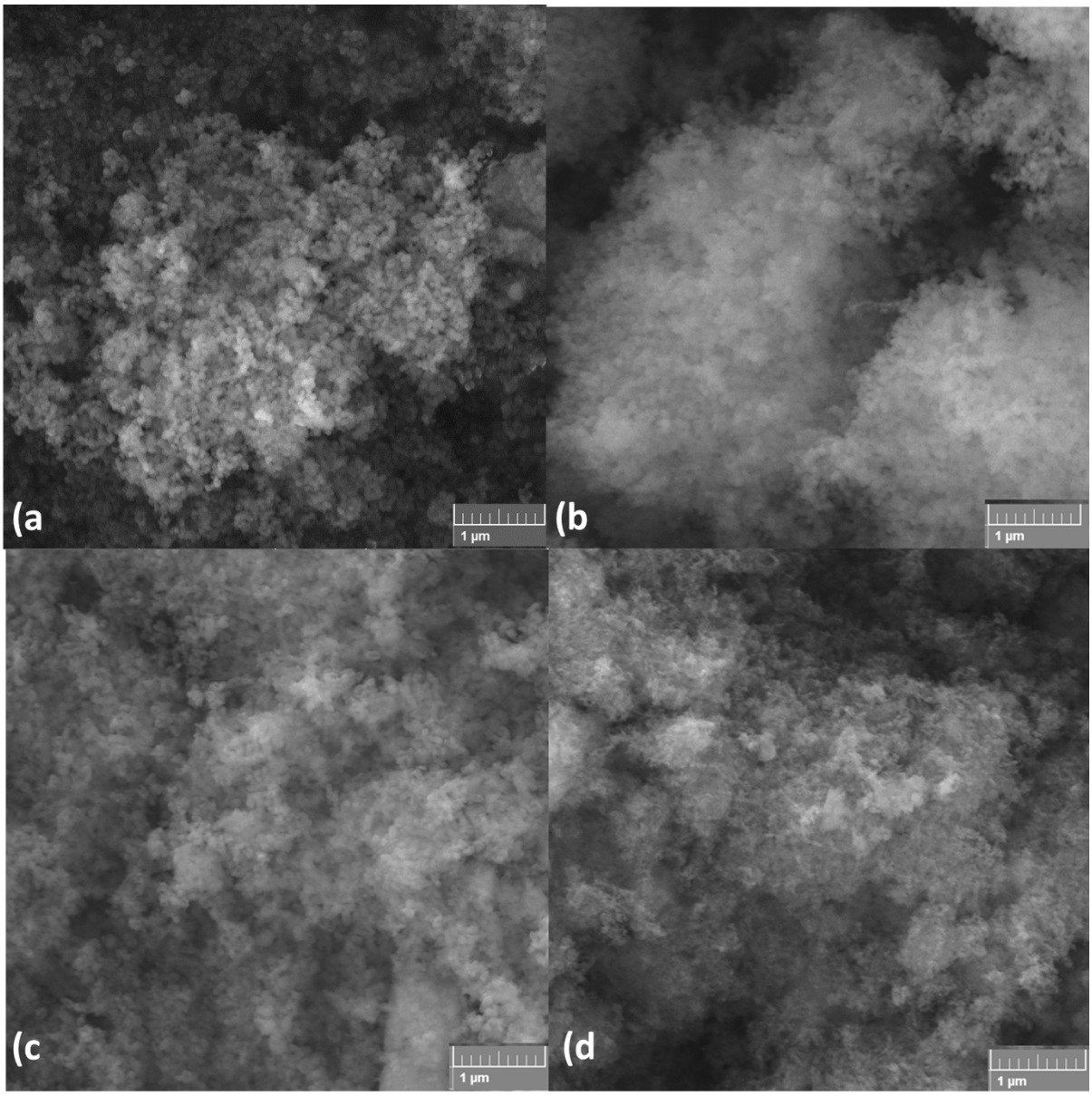

Figure 6.3.19 Impact of increasing cylinder rotation on particle size and morphology formed under 0.1 L/min CO_2 flowrate: Ta_r = 48(a), Ta_r = 191 (b), Ta_r = 431 (c), Ta_r = 916 (d).

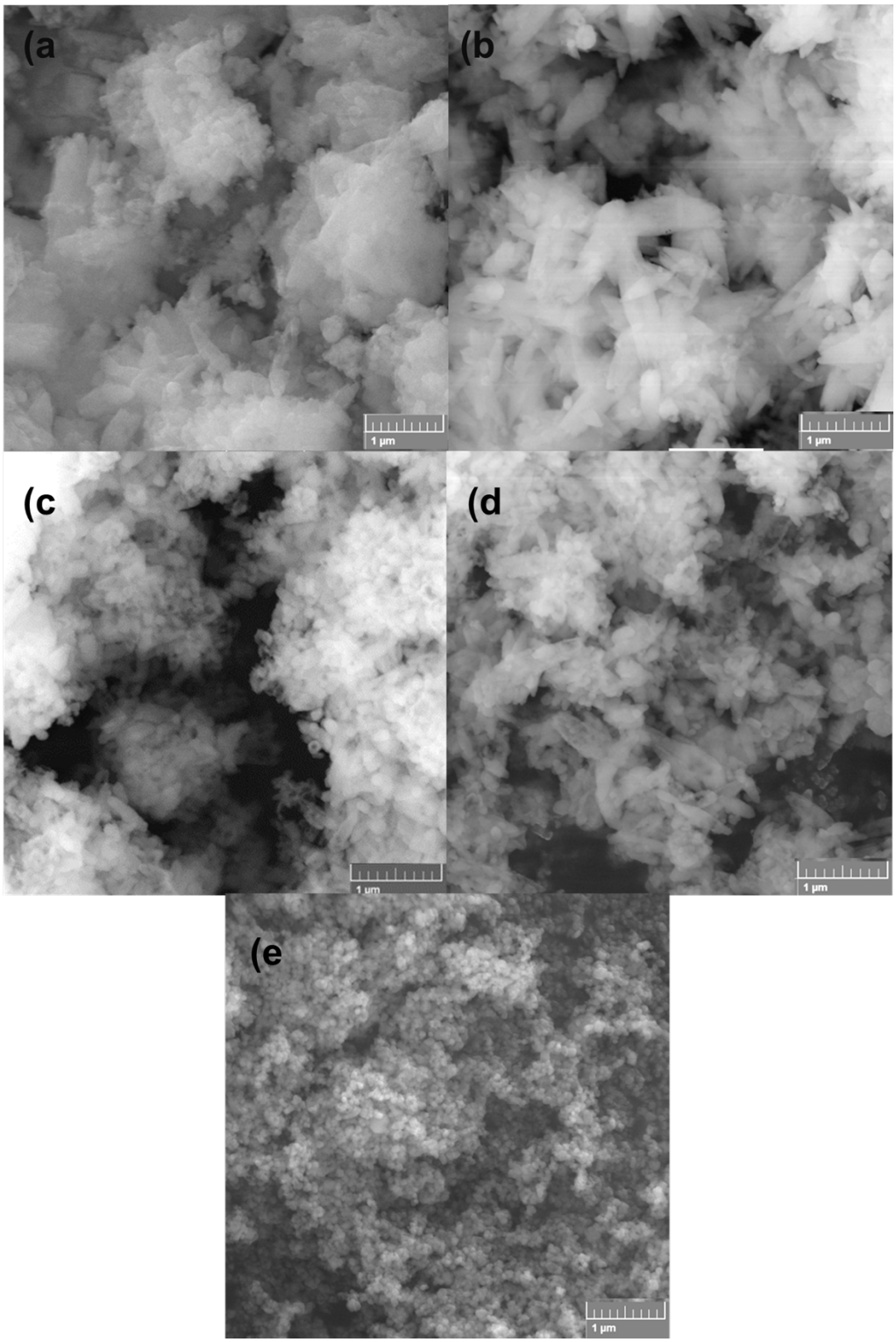

Figure 6.3.20 Impact of increasing cylinder rotation on particle size and morphology formed under0.02L/min CO_2 flowrate: Ta_r = 12 (a), Ta_r = 48 (b), Ta_r = 191 (c), Ta_r = 431 (d), Ta_r = 916 (e).

6.3.2.4 **Particle Size Analysis**

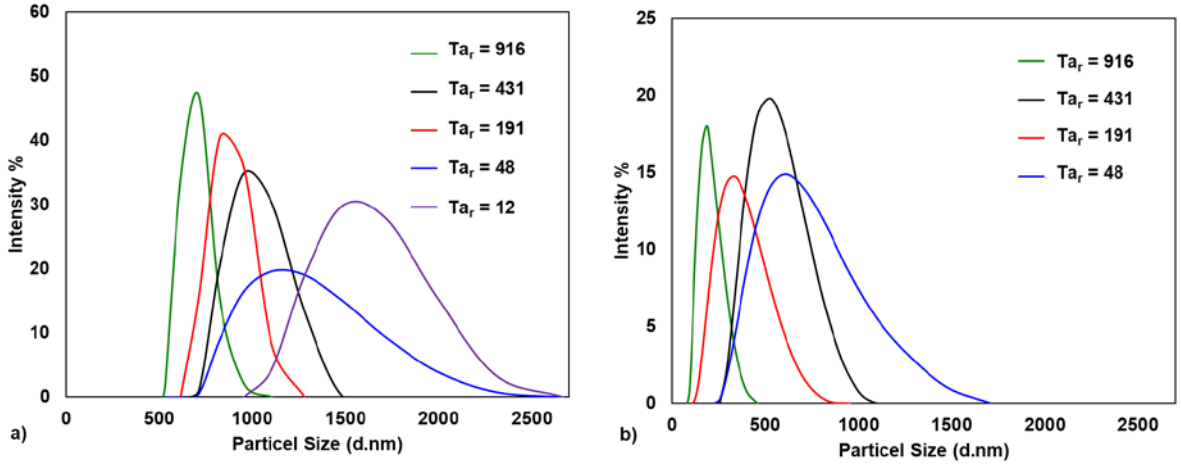

Figure 6.3.21 Change in the particle size distributions (PSD) measured via DLS of PCC formed under a) 0.02L/min CO_2 flowrate, and b) 0.1L/min CO_2 flowrate.

To better quantify the trends in particle size, dynamic light scattering (DLS) measurements of the particle size distribution of obtained PCC was done for CO_2 flowrates of 0.02 and 0.1 L/min, as displayed in Figure 6.3.21 (a) and (b), respectively. As observed on the SEM micrographs, primary particles tended to exhibit monomodal secondary aggregation [184] to varying degrees depending on the agitation condition, with a smaller portion of free stable primary particles [191]. The fraction of monodispersed particles, however, was observed to increase with higher rotation rates, especially when reaching fully developed turbulent Taylor vortex flow (TTVF). The ultrasonic treatment of the crystals minimized the potential for bimodality associated with tertiary agglomeration [78], which can take place during the centrifuging and drying steps of the preparation of PCC particles for analysis. Similar to the SEM observations, the increase in CO_2 flowrates resulted in the reduction of PCC particle size, due to the enhanced mass transfer flux density of CO_2 [181] [171]. Likewise, with the exception of the 1200RPM condition, where the “ring-flow” gas-liquid mixing pattern dominates, the increase in RPM provided fluid dynamic conditions that resulted in smaller particles. These flow mixing conditions offered

higher interfacial area, narrower variation of CO_2 bubble size, which resulted in more uniform particle distributions, increased particle mono-dispersity and enhanced the potential of breaking the formation of secondary aggregates, due to higher mixing intensity and energy dissipation [78].

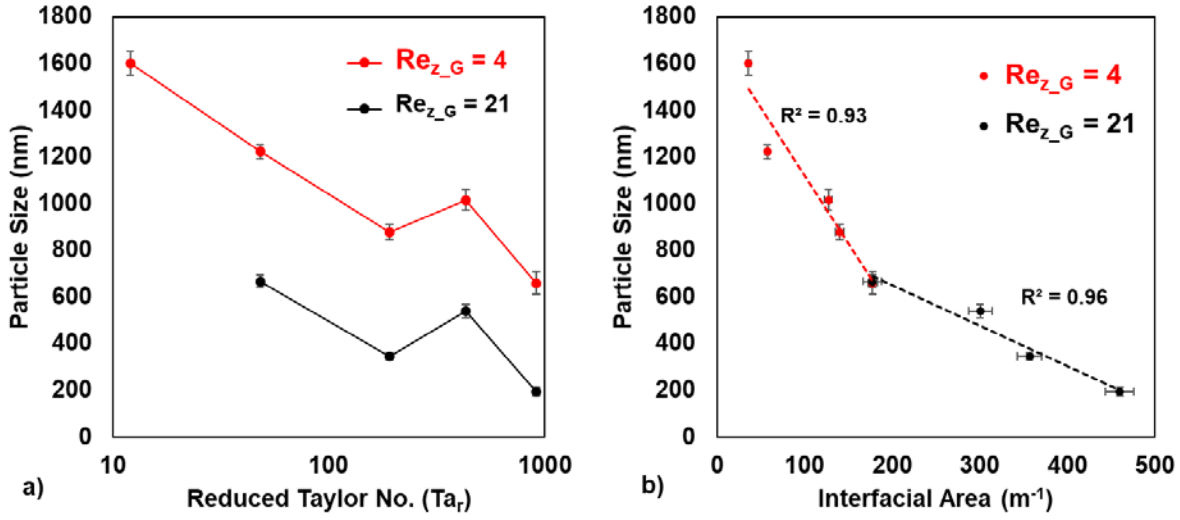

Figure 6.3.22 Change in particle size as measured via DLS analysis as a function of a) rotational motion and b) interfacial area.

Figure 6.3.22 (b), shows the reduction in average particle size with increasing interfacial area for PCC formed under 0.02 and 0.1 L/min CO_2 flowrates, respectively. Overall, the reduction in particle size was linearly proportional to the interfacial area. Despite differences in CO_2 flowrate and rotational conditions, PCC of nearly identical particle size was formed when conditions facilitated similar absolute interfacial area. This suggests that secondary particle size can be controlled by selecting operating conditions that result in similar contact area between the gas and liquid phases, rather than just focusing on varying one factor apart from the other (i.e. CO_2 flowrate vs cylinder rotation rate). Examining the influence of rotational energy on particle size reveals that the increase in RPM influences the particle size in similar fashion,

despite the change in CO_2 flowrate. However, the influence of rotational energy on reducing particle size is slightly more significant at lower CO_2 flowrate.

6.3.2.5 Surface Area and Pore Volume Analysis

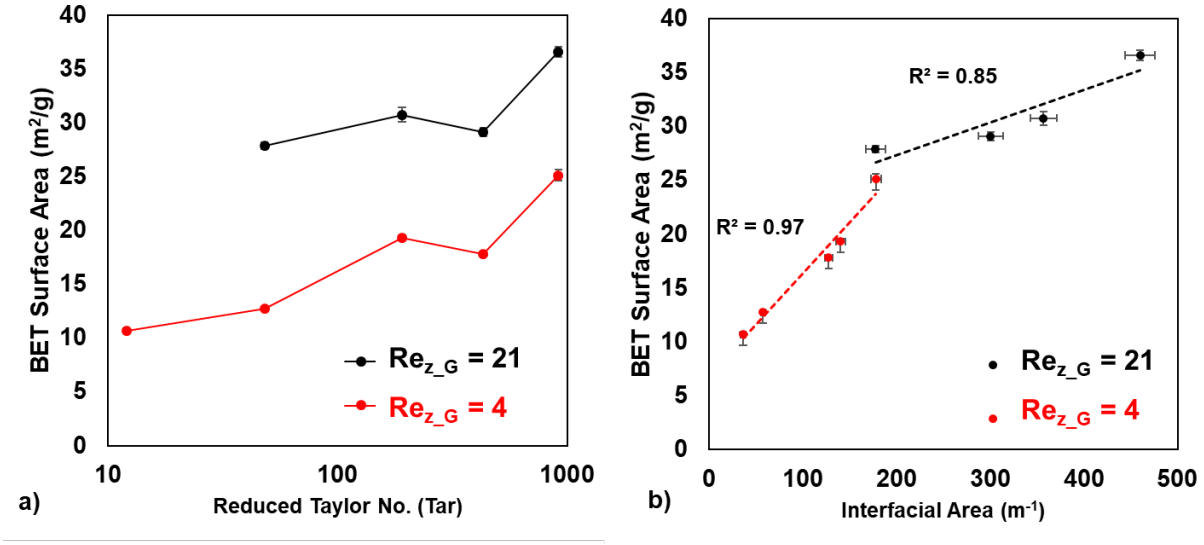

Figure 6.3.23 Change in BET surface area as a function of a) rotational motion and b) interfacial area.

The specific surface area of the produced calcite exhibited similar trends to the particle size, as can be viewed in Figure 6.3.23. The BET surface area was varied from 10.7 m^2/g to 25.1 m^2/g by changing the cylinder rotation from 200rpm to 1750rpm, under a CO_2 flowrate of 0.02 L/min. The change in BET surface area was less significant when moving from 400rpm to 1750rpm for the case of 0.1 L/min CO_2 flowrate, as the surface area changed from 27.8 to 36.6 m^2/g, respectively. BJH pore structural analysis revealed the change in average pore volume, which is plotted in Figure 6.3.24 against the change in interfacial area. The overall pore volume generally increased with the increase in interfacial area, with the change in pore volume being the largest when increasing the rpm from 400 to 800, where the pore volume increased 250% and 139% for the case of 0.02 L/min and 0.1 L/min CO_2 flowrates, respectively. A similar

observation can be deduced from Figure 6.3.25 and Figure 6.3.26, depicting the BJH cumulative pore volume and cumulative pore surface area, respectively.

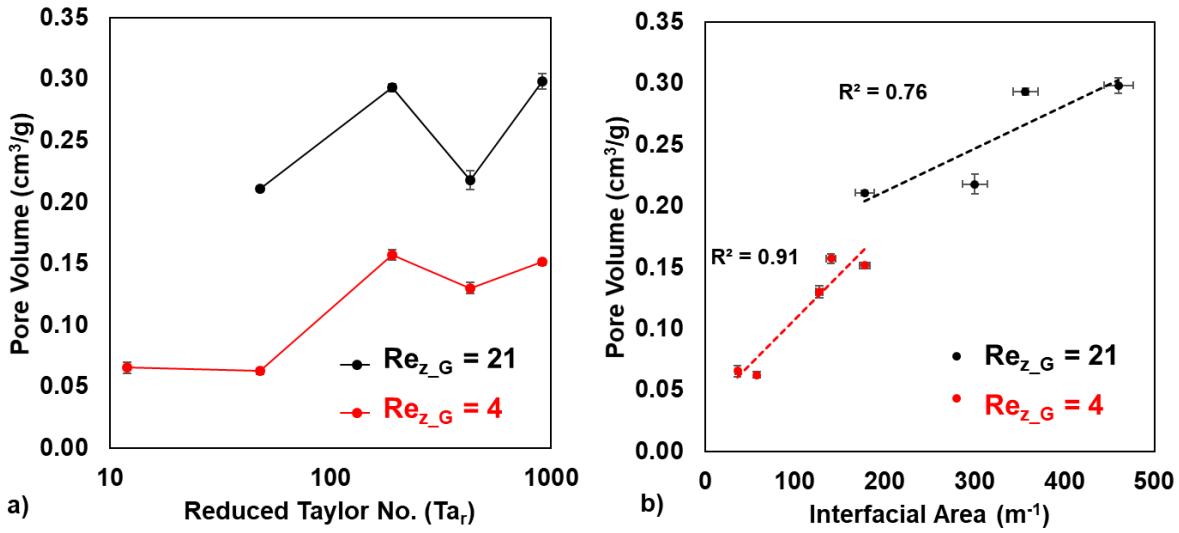

Figure 6.3.24 Change in measured pore volume as a function of a) rotational motion and b) interfacial area.

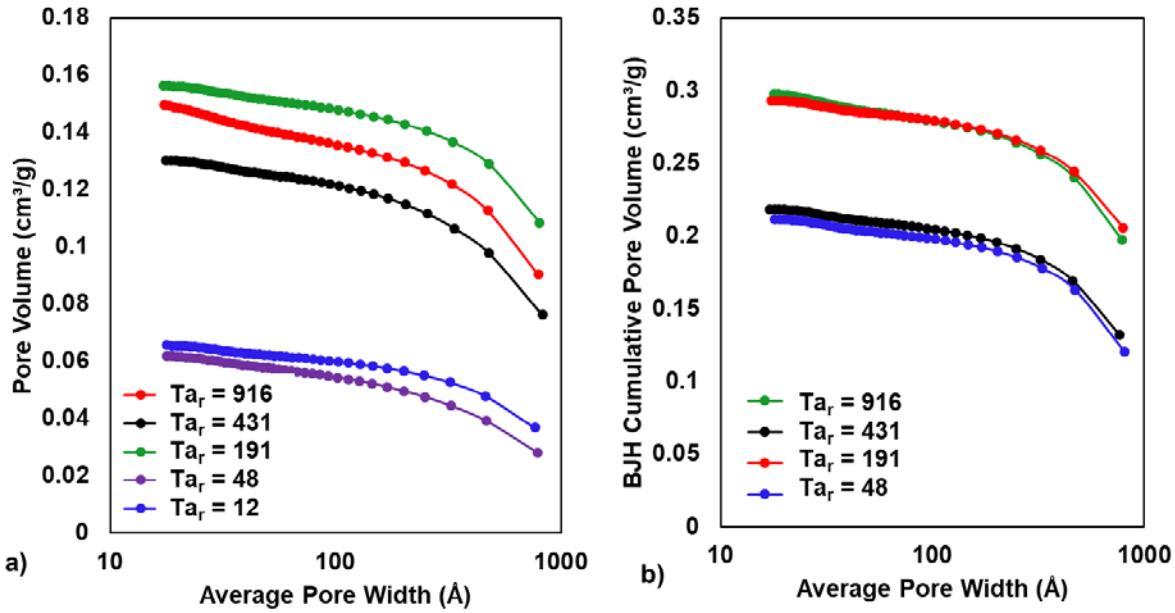

Figure 6.3.25 Cumulative pore volume distribution obtained via BJH analysis of PCC formed under a) 0.02L/min CO_2 flowrate, and b) 0.1L/min CO_2 flowrate.

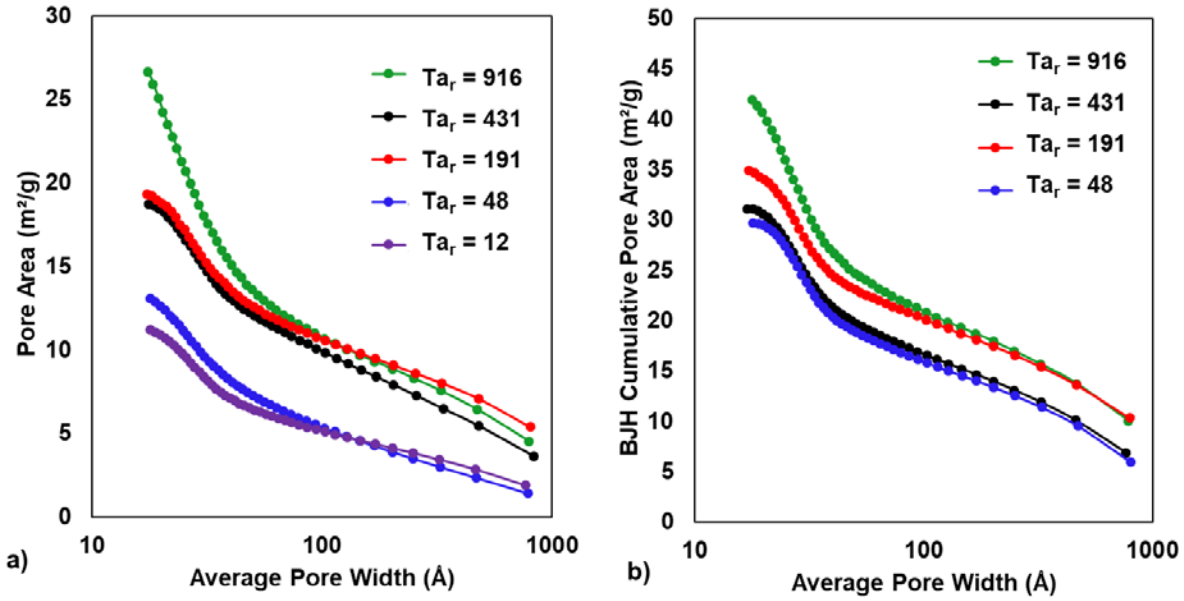

Figure 6.3.26 Cumulative pore surface area distribution obtained via BJH analysis of PCC formed under a) 0.02L/min CO_2 flowrate, and b) 0.1L/min CO_2 flowrate.

The BJH pore volume distribution and pore surface area distribution (per unit pore radius [221]), as displayed in Figure 6.3.27 and Figure 6.3.28 , respectively, show a sharp increase in the proportion of smaller pores for PCC formed under 1750rpm, when compared with lower rotation rates for both high and low CO_2 flowrates. The biggest change in pore surface area and pore volume per unit pore radius occurs in the range from 1.78nm to 5nm at lower rotation rates and can extend up to 7nm in the case of the highest rotation rate (i.e. 1750rpm). This suggests that the main contribution to pore surface area and pore volume is from small pores (<10nm), and that the contribution decreases with increasing pore radius [222]. Figure 6.3.27, reveals that the pore volume per unit pore radius peaks in the range of pore widths less than 3nm, with most of its pore volume originating from mesopores in the 2-10nm range, as observed in previous studies [222].

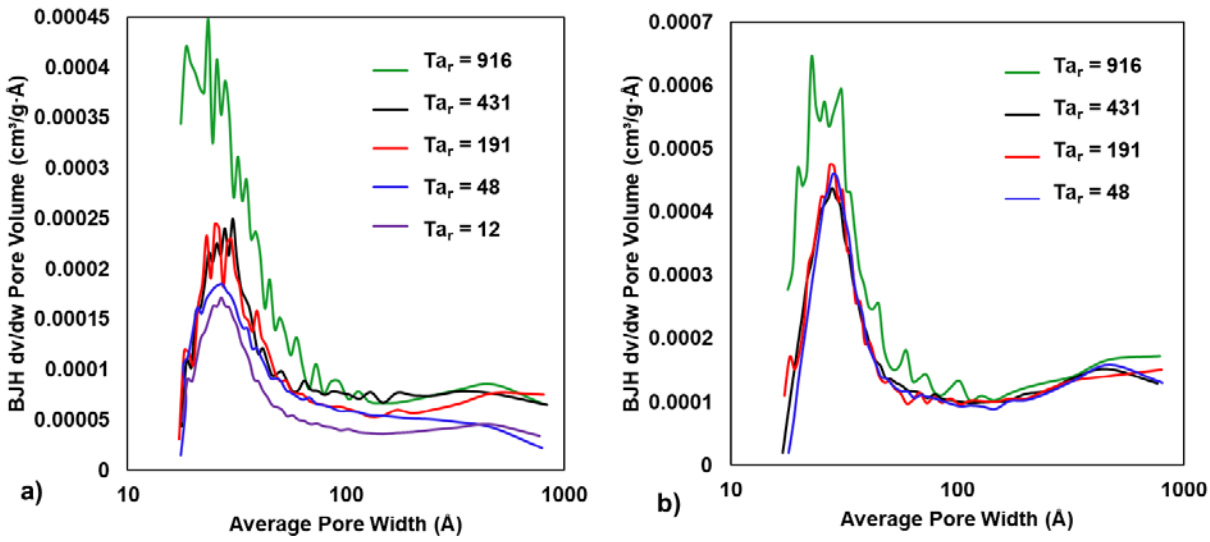

Figure 6.3.27 Change in BJH pore volume distribution per unit pore radius of PCC formed under a) 0.02L/min CO_2 flowrate, and b) 0.1L/min CO_2 flowrate.

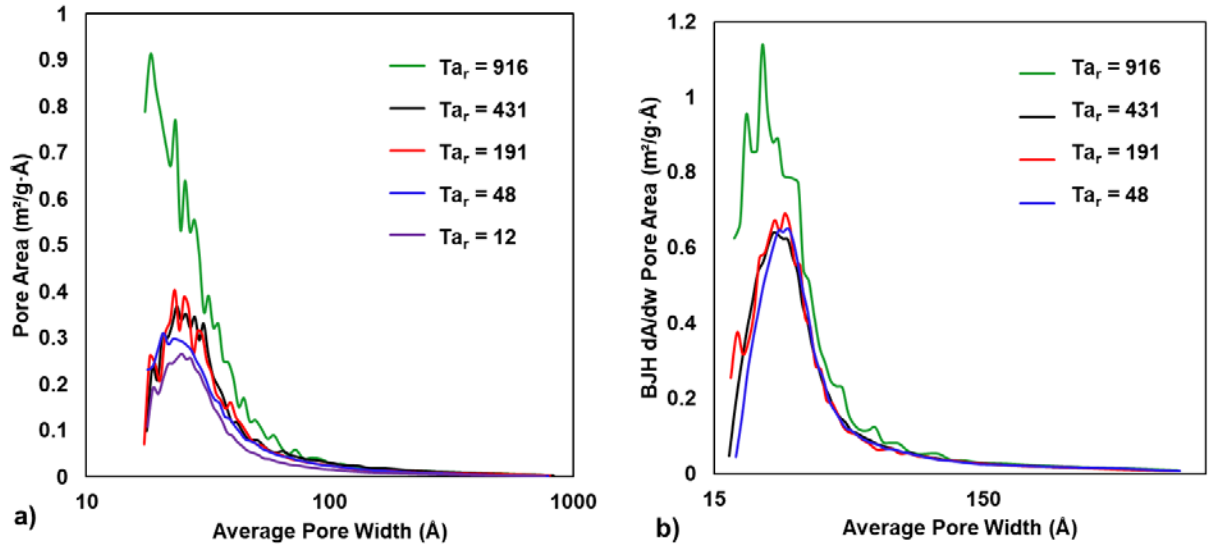

Figure 6.3.28 Change in BJH pore surface area distribution per unit pore radius of PCC formed under a) 0.02L/min CO_2 flowrate, and b) 0.1L/min CO_2 flowrate.

As depicted in Table 6.3.1, analysis of the BJH data revealed that the percent of micropores (<2nm) contributing to the pore volume and pore surface area increased from 0.3% to 0.7% and from 4% to 9%, respectively, when increasing the rotation rate from 200rpm to 1750rpm, for PCC formed under 0.02 L/min. Similarly, as shown in Table 6.3.2, the pore volume and pore

surface area in the microporous region increased from 0.1% to 0.5% and from 1.5% to 7%, respectively, when increasing the rotation rate from 400rpm to 1750rpm, for PCC formed under 0.1 L/min. Meanwhile the proportion of mesopores (2nm< pore width <50nm) contributing to the pore volume and pore surface area decreased from 44% to 39% and from 79% to 74%, respectively, when increasing the rotation rate from 200rpm to 1750rpm, for PCC formed under 0.02 L/min. Similarly, the proportion of mesopores contributing to the pore volume and pore surface area decreased from 43% to 33% and from 78% to 69%, respectively, when increasing the rotation rate from 400rpm to 1750rpm, for PCC formed under 0.1 L/min. Such observations agree with the previous observations from SEM and DLS, which indicated smaller particles being precipitated at higher rotation rates, which results in a higher contribution of the external surface area to the overall surface area, thus reducing the proportional contribution of the mesoporous structure to the overall surface area. The overall BJH surface area was increased from 29.7 m^2/g to 42 m^2/g when transitioning from 400rpm to 1750rpm, under 0.1 L/min and from 11.2 m^2/g to 26.7 m^2/g when transitioning from 200rpm to 1750rpm under 0.02 L/min.

Table 6.3.1 BJH mesoporous pore volume and mesoporous pore surface area for PCC formed under 0.02L/min CO_2 flowrate.

Mixing (RPM)	Pore Volume (cm^3/g)	Macropores	Mesopores	Micropores	Pore Area (m^2/g)	Macropores	Mesopores	Micropores
1750	0.150	60%	39%	0.7%	26.65	17%	74%	9%
1200	0.130	59%	41%	0.1%	18.74	20%	78%	3%
800	0.156	69%	30%	0.2%	19.31	28%	68%	4%
400	0.062	45%	54%	0.5%	13.09	11%	84%	5%
200	0.066	56%	44%	0.3%	11.20	17%	79%	4%

Table 6.3.2 BJH mesoporous pore volume and mesoporous pore surface area for PCC formed under 0.1L/min CO_2 flowrate.

Mixing (RPM)	Pore Volume (cm^3/g)	Macropores	Mesopores	Micropores	Pore Area (m^2/g)	Macropores	Mesopores	Micropores
1750	0.298	66%	33%	0.5%	41.9	24%	69%	7.1%
1200	0.218	60%	39%	0.2%	31.1	22%	75%	2.8%
800	0.293	70%	30%	0.2%	34.9	30%	67%	3.5%
400	0.211	57%	43%	0.1%	29.7	20%	78%	1.5%

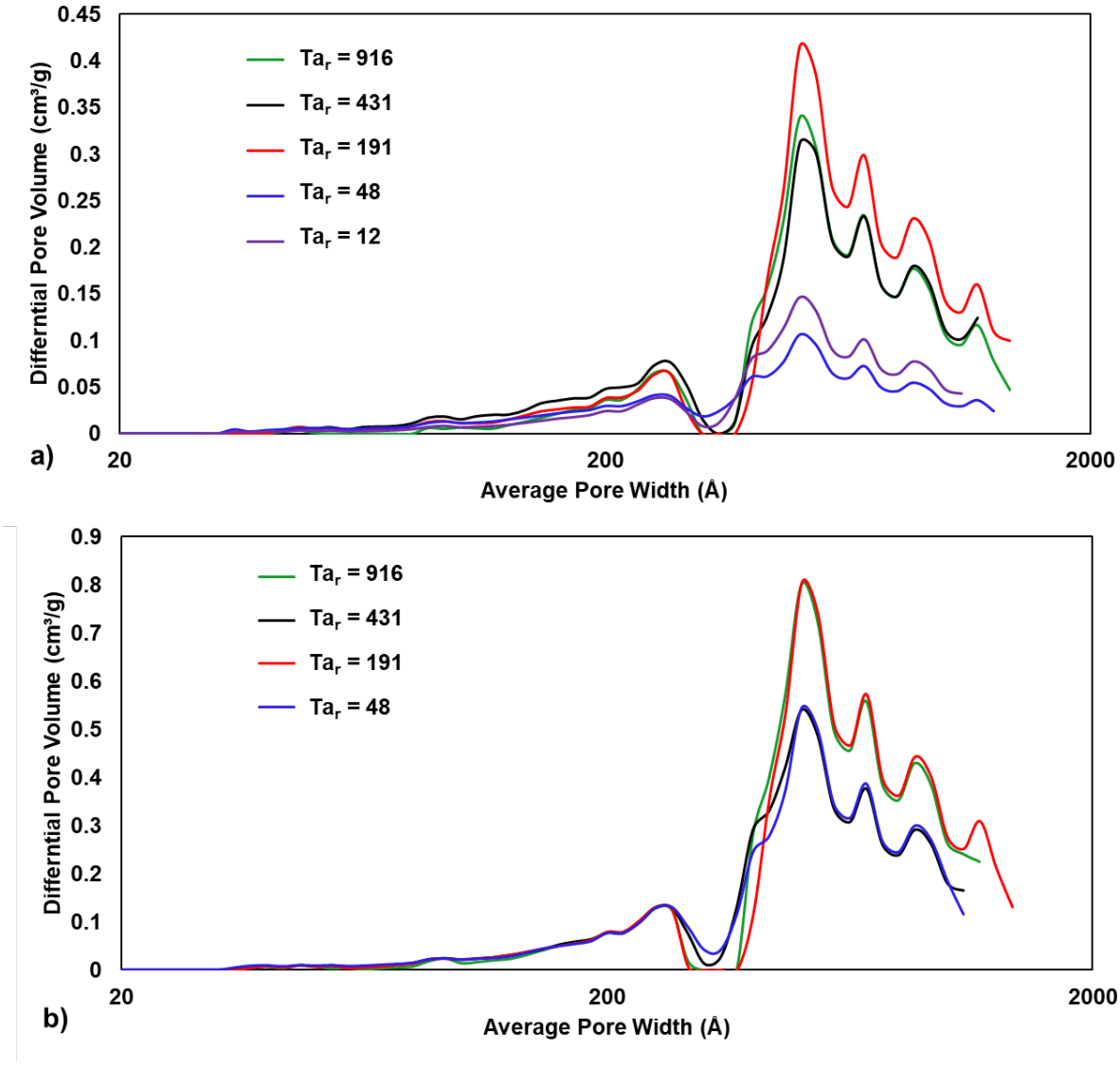

Figure 6.3.29 Change in log-differential pore volume distribution obtained via DFT analysis of PCC formed under a) 0.02L/min CO_2 flowrate, and b) 0.1L/min CO_2 flowrate.

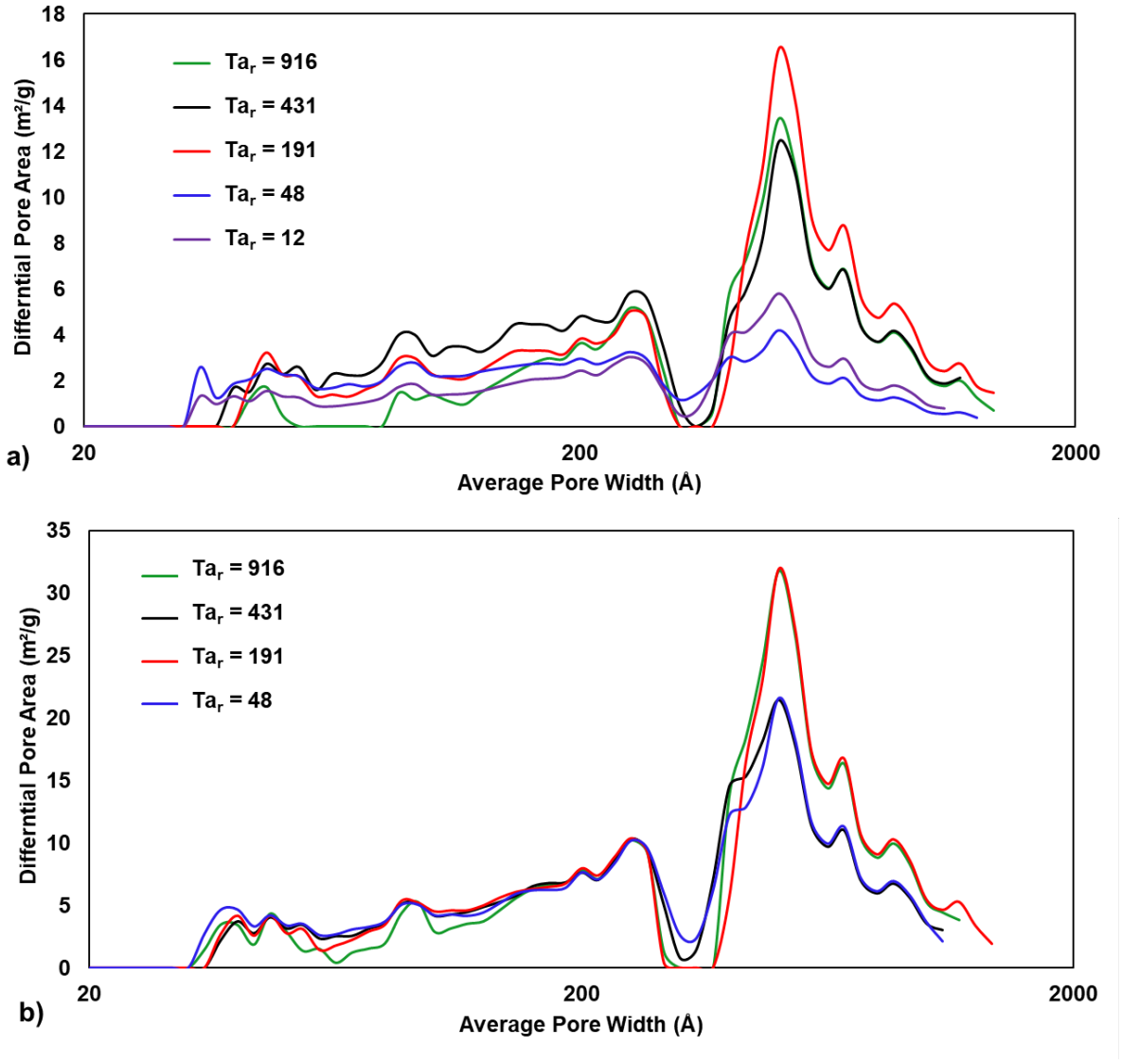

Figure 6.3.30 Change in log-differential pore surface area distribution obtained via DFT analysis of PCC formed under a) 0.02L/min CO_2 flowrate, and b) 0.1L/min CO_2 flowrate.

To complement the BJH analysis, density functional theory (DFT) was applied to the surface adsorption data, from which the log-differential pore volume and pore surface area distributions in Figure 6.3.29 and Figure 6.3.30, respectively were obtained. Overall, the proportion of the mesopores contributing to the total DFT pore volume and DFT pore surface area ranged from 48% to 40% and from 73% to 63%, respectively, when increasing the rotation rate from 400rpm

to 1750rpm, for PCC formed under 0.1 L/min, as summarized in Table 6.3.4. Similarly, the proportion of the mesopores contributing to the total DFT pore volume and DFT pore surface area ranged from 52% to 39% and from 76% to 61%, respectively, when increasing the rotation rate from 200rpm to 1750rpm for PCC formed under 0.02 L/min, as displayed in Table 6.3.3. Although they exhibited similar trends, the pore volume estimated via BJH was slightly larger than that estimated via the DFT method. Overall, DFT analysis revealed that the contribution of mesopores to the distribution of the internal pore surface area and internal pore volume decreases as the PCC average particle size is reduced, owing to the increasing contribution of the large external pores associated with smaller crystals [223].

Table 6.3.3 DFT mesoporous pore volume and mesoporous pore surface area for PCC formed under 0.02L/min CO_2 flowrate.

Mixing (RPM)	Pore Volume (cm^3/g)	Macropores	Mesopores	Pore Area (m^2/g)	Macropores	Mesopores
1750	0.111	61%	39%	4.63	39%	61%
1200	0.112	57%	43%	5.96	30%	70%
800	0.140	57%	43%	6.26	42%	58%
400	0.048	42%	58%	3.43	16%	84%
200	0.054	48%	52%	3.07	24%	76%

Table 6.3.4 DFT mesoporous pore volume and mesoporous pore surface area for PCC formed under 0.1L/min CO_2 flowrate.

Mixing (RPM)	Pore Volume (cm^3/g)	Macropores	Mesopores	Pore Area (m^2/g)	Macropores	Mesopores
1750	0.251	60%	40%	11.24	37%	63%
1200	0.191	51%	49%	10.07	27%	73%
800	0.263	55%	45%	11.62	39%	61%
400	0.189	52%	48%	10.17	27%	73%

6.4 Discussion

6.4.1 General

The overall precipitation process occurs through a combination of parallel and successive mechanisms that involve nucleation, growth, and secondary processes such as agglomeration, attrition, breakage and ripening. The collection of experimental data presented above strongly suggests that the interfacial area between the gaseous CO_2 phase and the aqueous phase of dissolved and suspended $Ca(OH)_2$ phase is markedly influenced by the flow structure and mixing conditions during the precipitation reaction, which in turn has a strong impact on modifying the final properties of PCC.

6.4.2 Precipitation Mechanism

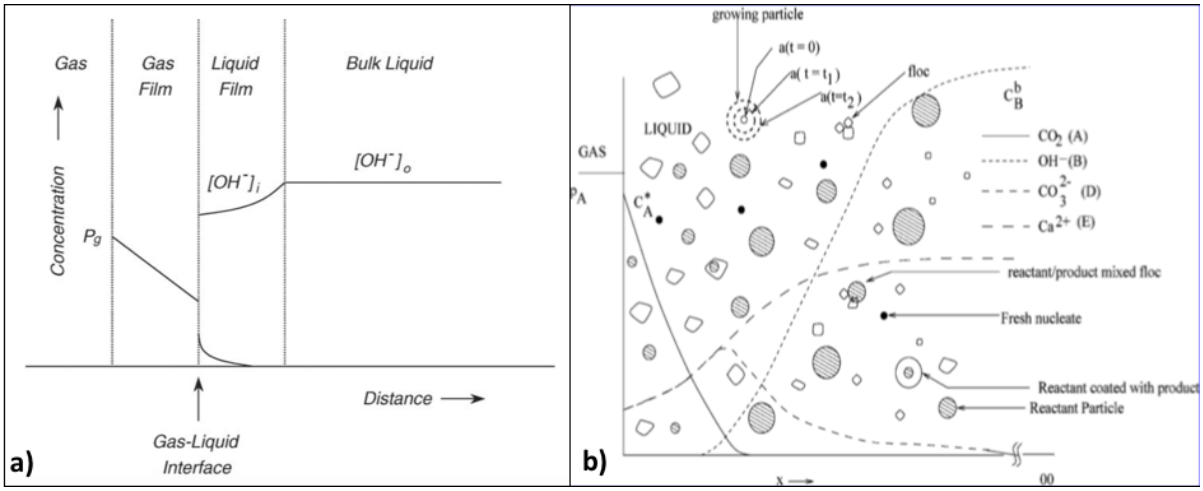

Figure 6.4.1 a) general concentration profile for gas/liquid absorption with precipitation reaction [192], b) concentration profiles and product/reactant mix near the gas/liquid interface [224].

Properties of PCC are shaped by the interaction of several rapid steps involved, such as interfacial mass-transfer, mixing, nucleation, growth, self-assembled and arbitrary aggregation. Due to the nature of their kinetics, studying each step individually presents a challenge as they don't necessarily take place sequentially. Rather, some steps could occur simultaneously,

resulting in competition between the corresponding sub-processes. In this study, it was found that primary steps, such as mixing of the educts on macro, micro and molecular scale, as well as the reaction, nucleation and growth of the particles can be partially paralleled by secondary arbitrary aggregation and ripening [99]. As displayed in Figure 6.4.1 (a), the precipitation process is driven by the degree of supersaturation taking place across the CO_2-aqueous film interface [184], which is the major driving force for both the rate-limiting step of nucleation, which occurs initially, and the following steps leading to crystal growth [225]. Larger quantities of absorbed CO_2 lead to increased local supersaturation which, in turn, results in the formation of finer primary particles due to higher nucleation rate [175]. Across the gas-liquid interface, as displayed in Figure 6.4.1 (b), the CO_2 is absorbed into the liquid thin-film, whose thickness is in the range of 10nm [226], in the form of bicarbonate and carbonate ions. These ions are consumed rapidly near the gas–liquid interface, rendering the amount of CO_2 in the bulk of the liquid to be negligible [47]. At the same time, the slurry $Ca(OH)_2$ suspension dissolution occurs predominantly in the bulk region, so that close to the interface, most $Ca(OH)_2$ particles are assumed to have dissolved [224]. Since the hydroxide concentration at the gas/liquid interface is nearly equivalent to that in the liquid bulk [171], as displayed in Figure 6.4.1 (a), the reaction can be assumed to occur completely at the interface. The relative magnitudes of the maximum reaction rate of CO_2 in the film to that of the maximum rate of physical mass transfer per unit interfacial area can be quantified in terms of Hatta number via Equation 6.4.1 [227]. If the Hatta number is above the criteria defined by Equation 6.4.2 then the reaction is considered to be instantaneous [226]. Given the CO_2 solubility ~37.5 mol/m^3 and $D_{Ca(OH)2}$ ~7.2x10^{-10} m^2/s [228], the criteria defined by Equation 6.4.2 is estimated to be around 0.22. As plotted in Figure 6.4.2,

the range of values for the Hatta number show that CO_2 and hydroxyl ions are reacting predominantly and instantaneously within the interfacial film.

Equation 6.4.1 Estimation of Hatta Number [227]:

$$Ha^2 = \frac{\left(2k\, C_{Ca(OH)_2}^{bulk} D_{co_2}\right)}{{k_L}^2},$$

Where $k = 7.1 \times 10^3 m^3 \cdot kmol^{-1} \cdot s^{-1} at\ 22℃$, is the kinetic constant of the chemical reaction between hydroxyl ions and CO_2, $C_{Ca(OH)_2}^{bulk} = 21.8\, mol \cdot m^{-1} at\ 22℃$ is the solubility of calcium hydroxide and $D_{co_2} = 1.9 \times 10^{-9} m^2 \cdot s^{-1} at\ 22℃$ is the diffusivity of carbon dioxide [227].

Equation 6.4.2 Criteria for Hatta Number [226]:

$$\frac{C_{Ca(OH)_2}^{bulk} D_{Ca(OH)_2}}{C_{CO_2}^{int} D_{co_2}}$$

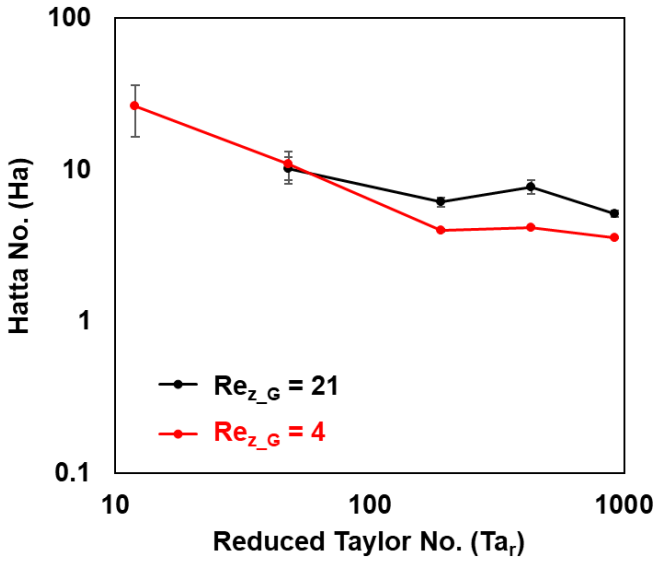

Figure 6.4.2 Hatta Number

Still, the dissolution of the reactant particles occurs simultaneously with the formation of $CaCO_3$. Therefore, the particle growth of the PCC can be modeled according to “shrinking

core" mechanism for the reaction among the CO_2 and $Ca(OH)_2$ phases, where the former diffuses into the $Ca(OH)_2$ particle, reacting to form carbonate, which, gets deposited on the hydroxide particle as soon as it is precipitated due to its poor solubility [224]. Such nuclei act as a convergence point for solute molecules touching the newly formed crystal whose dimension grows in successive layers [225]. Although the initially formed $CaCO_3$ precipitates on the suspended $Ca(OH)_2$ particles in the amorphous phase, it quickly transforms into stable calcite crystal structure, as the precursor is extremely unstable [207]. The nuclei stabilize after reaching a critical size beyond which they are likely to grow into crystals with visible size [220]. The formed $CaCO_3$ particles remain within the interface for some time until they are sent to the bulk of the liquid phase under the influence of rotational motion. Such presence of $CaCO_3$ particles at the interface reduces the effective mass transport area [192]. Therefore, the increase in the energy of dissipation should help in minimizing the presence of solid particles at the interface, and the period of time that the formed solid spends at the interface is reduced in a proportional manner to the increase in Taylor no.

6.4.3 Particle Morphology

In a similar manner, the significant degree of mixing associated with the increase in the dissipation energy minimizes the probability of crystallite collisions that can lead to the aggregation of the $CaCO_3$ crystals [192]. Such reductions in collisions affect the range of secondary particle growth taking place right after nucleation, leading to different ripening rates, which in turn, affect the overall morphologies of the PCC, especially as the formed particles migrate out of the thin-film region at faster rates when operating at higher rotations. Changes in PCC morphology due to variations in the mixing rotation speed has been confirmed in experiments studying $CaCO_3$ precipitation in a high-shear circulation reactor [190]. At the same

time, reduction in the CO_2 flow rate results in the over-dosage of $Ca(OH)_2$ during crystallization, which introduces an excess of Ca^{2+} ions, thereby increasing the pH under which significant changes in the crystal morphology can take place [47] [78].

6.4.4 Particle Size

With narrower bubble size distributions for the gas phase, diffusion of carbon dioxide gas into the surface of the calcium hydroxide solution occurred more homogeneously, resulting in more uniform particles that tended to be more monodispersed at certain conditions. In addition to having the secondary particle size be impacted by the high rotational speeds that can break up larger particles into very small pieces [190], the primary crystal size is dependent on the efficiency of the reaction and the crystal growth steps, which are predominantly controlled by the micro-fluid motion [78]. Both the primary particle size revealed from the SEM and secondary particle size, as measured by the DLS technique, were observed to be significantly larger than the crystallite size estimated from the XRD pattern, which confirms that the calcite crystals arrange, ripen and form larger aggregates with a porous structure [9]. As displayed in Figure 6.4.3, the increase in the surface area of the PCC correlated with the reduction in secondary and primary particle size, [190] both of which were directly influenced by the increase in interfacial area as a result of bubble size reduction due to variation in the flow regime. For a similar particle size of around 660nm, PCC formed under 0.1L/min flow of CO_2 exhibited higher surface area, which can be attributed to the increase in the mesoporous structure associated with the higher mass-transfer taking place under the higher CO_2 flowrate, despite the significantly lower mixing rate of 400rpm, relative to the 1750rpm for the 0.02L/min gas flow rate. It is suggested that lower energies of dissipation promote crystal collisions which contribute to secondary agglomeration, while the breakage of crystal agglomerates has been

observed to exceed chances of crystal-collision induced agglomeration at higher rotational energies [78].

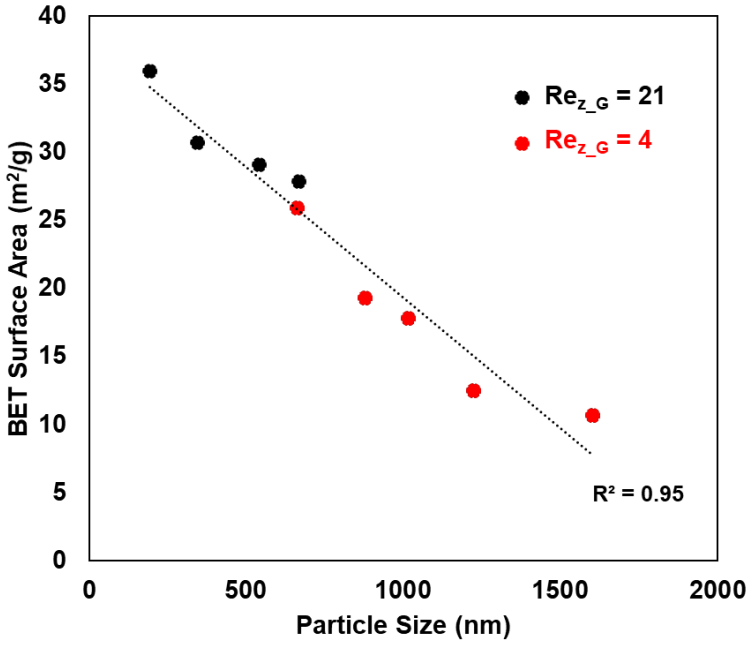

Figure 6.4.3 Increase in BET surface area is proportional to the reduction in average particle size.

6.4.5 Pore Structure

The basic porous structure of the PCC is attributed to factors influencing the transformation of the amorphous precursor PCC, formed on the on the surface of suspended $Ca(OH)_2$ particles, which undergoes dissolution according to the "shrinking core" model, into nano-sized crystallites that ripen and aggregate forming nano-structural mesoporous calcite [207]. As observed in previous studies [229], the contribution of narrow to medium-size mesopores was found to be most crucial to increasing the porosity (pore surface area and volume), while micropores remained negligible [229]. PCC with a mesoporous structure that maximizes the porosity in the 5−20-nm pore size range has proven to be less susceptible to pore blockage and plugging, with fewer structural limitations than microporous $CaCO_3$. Such constraints has

previously limited calcium-based sorbents from attaining theoretical conversions in reactions such as sulfation, or CO_2 capture [7]. Indeed, the particles formed in this study exhibited significant pore volume, which suggest, as confirmed by the BJH and DFT models, that a substantial proportion of the overall PCC surface area resides in the interior of the particle. In contrast, most studies that involve PCC formation in the absence of a surfactant found that most of the pore volume is limited to the exterior of the particles [170].

Since controlling the growth of nanocrystals has been attributed to the limited access of crystalline growth sites, it can be suggested that the increase in mixing (with higher cylinder rotation rates) helps in rendering the growth unit integration into the crystal lattice to be minimal compared to their transfer from the bulk to the liquid-crystal interface [220]. The higher CO_2 flowrate results in an increase in the overall interfacial mass-transfer, which allows a larger number of available nuclei to assemble at the early stage of crystal growth. As observed in our experiments, such early aggregation of nuclei has been associated with an open pore structure with a high pore volume and surface area [170].

6.4.6 Mass Transfer

To better quantify the impact of the observed change in interfacial area on controlling the properties of PCC, the mass-transfer of the CO_2 into the liquid-film interface, which is the rate-determining step [181], should be assessed in an approach similar to that of characterizing mass transfer coefficients of turbulent flow in stirred tanks and conventional bubble columns [197]. To do this, the average bubble slip velocity was estimated as the difference in superficial velocities of the liquid and gas phases, using the measured volume fraction, represented by:

Equation 6.4.3 Average bubble slip velocity

$$u_{Slip} = \left(\frac{V_G}{\alpha_g}\right) - \left(\frac{V_L}{\alpha_L}\right)$$

Danckwerts' modifications on Higbie's penetration theory to accommodate for surface renewal were used to estimate the individual mass transfer coefficient, as expressed here [230] [212]:

Equation 6.4.4 Individual mass transfer coefficient based on penetration theory

$$k_L = F\sqrt{\frac{4D_L u_{slip}}{\pi d_b}}$$

Meanwhile, penetration theory (recommended for small gas flowrates) was used to estimate the mass transfer coefficient, as displayed in Figure 6.4.4 and Figure 6.4.5. The values of the mass transfer coefficients derived in this study were found to be in ranges close to the ones found in previous studies [212] [59], and were also within those obtained from correlations developed by Wronski [202] to quantify the physical mass-transfer among CO_2-H2O phases in a Taylor Couette reactor. Gao et al. also confirmed that the penetration theory model presents more accurate predictions of mass transfer at high rotation rates and low gas flow rates, while the eddy cell model overestimates the mass transfer coefficient when operating at low gas flow rates and a range of high rotation rates [212]. According to the Kolmogorov's inertial range hypothesis, the overall mass transfer coefficient depends on the power consumption per unit volume, which for aerated stirred vessels scales with the energy of dissipation as $k_L a \sim \varepsilon^{0.65}$ [230]. In the case for this study, the estimated mass transfer coefficient via penetration theory scaled in a similar range, with $k_L a \sim \varepsilon^{0.69}$, $k_L a \sim \varepsilon^{0.67}$ for CO_2 flowrates of 0.02L/min and 0.1 L/min, respectively.

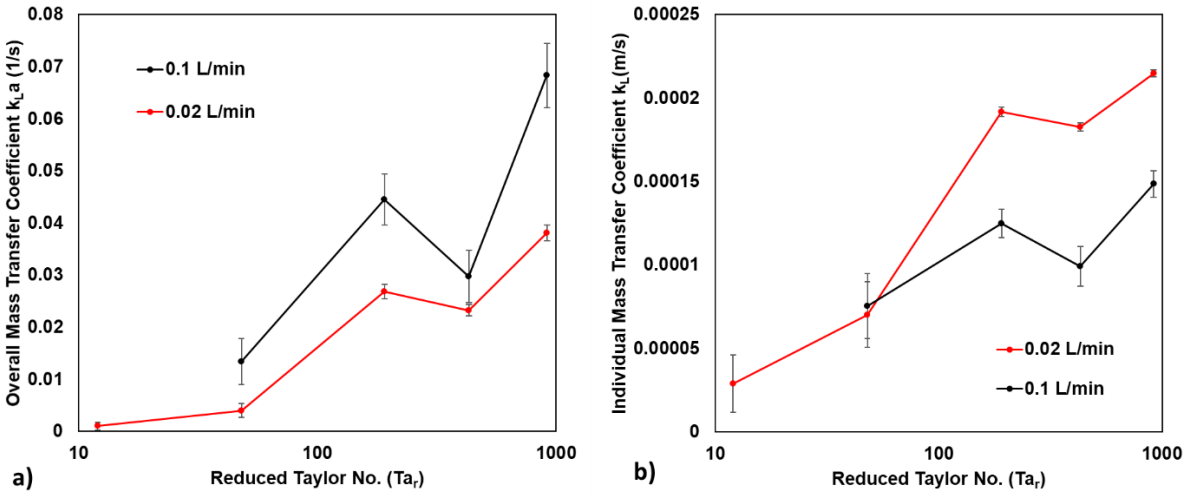

Figure 6.4.4 The influence of increasing energy of dissipation on the a) Overall mass transfer coefficient and b) specific individual mass transfer coefficient.

As suggested in studies exploring the influence of changing the geometry during $CaCO_3$ precipitation in TC reactor, the small gap geometry of the reactor in this study reduces the sensitivity of the mass transfer coefficient to the increase in the energy of dissipation [78], especially beyond $Ta_r = 200$. The further increase in the individual mass transfer coefficient in regions close to turbulence has been attributed to the presence of a threshold of rotational speed at which large gas bubbles breakup into smaller discrete bubbles [59]. The relatively small changes in k_La values in regions below the onset of MWVF, $10<Ta_r<50$, for the case of 0.02 L/min CO_2 flowrate, have also been noted in studies examining CO_2 transport time scales for biomass growth, where they cited that mass transfer is relatively insensitive to the increase in rotational in flow regimes corresponding to $24<Ta_r<100$ [231].

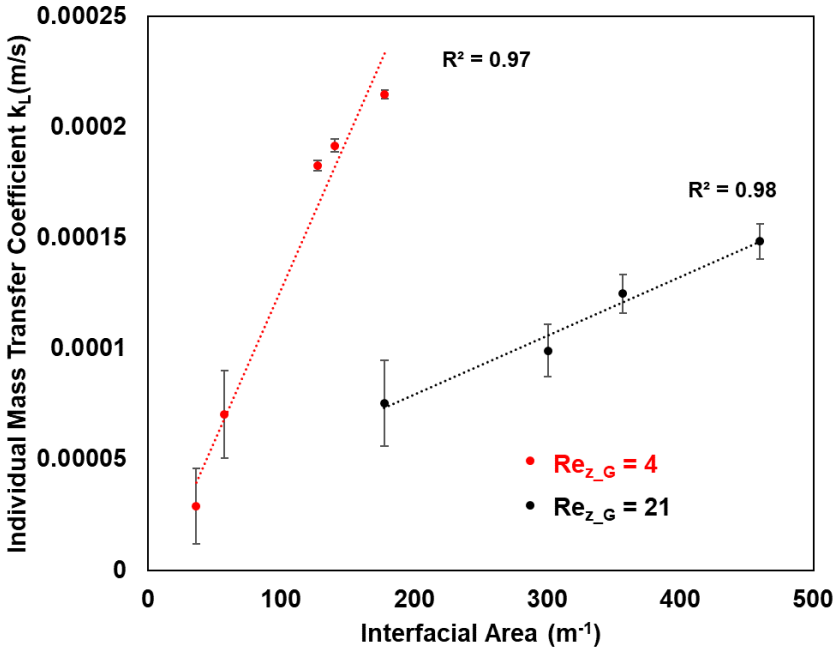

Figure 6.4.5 Mass transfer coefficient estimated via penetration theory increases linearly with the increase in interfacial area.

As shown in Figure 6.4.5, the individual mass transfer coefficient estimated from penetration theory increases proportionally with the increase in interfacial area. And given that the estimated interfacial area for the conditions in these experiments are considerably higher than those observed for CSTR [197], it is expected that the mass transfer coefficient will also be larger than that of a stirred tank reactor. The effect of reducing bubble size on the increase in the overall mass transfer coefficient K_La and the reduction in the mean $CaCO_3$ particle size has also been observed in studies attempting to control the dispersion of CO_2 via changing the sparger micropore size [188]. Spargers with smaller micropore size were associated with stronger micromixing effects and larger formation of primary nuclei, whereas the precipitation acquisition time and crystal growth time decreased, resulting in smaller PCC [188].

6.4.7 Predictive Correlations

Although predicting PCC properties, such as particle size, surface area and pore volume, remains a challenge due to the multiple parameters affecting the crystallization process [78], a series of empirical correlations can be developed based on the results presented in this study to quantify the changes in particle properties based on the range of CO_2 flowrates and cylinder rotation rates used in this system. In terms of dimensionless numbers, the mass transport can be approximated through a single force convective transfer correlation, characterized by the Sherwood number, which for the gas-liquid TC system, can be expressed as ratio of the actual mass transfer coefficient to the purely diffusive value [56] as described in [212] [59], by:

Equation 6.4.5 Sherwood number for gas-liquid interfacial mass transport

$$Sh = \frac{[k_L a][d_B]^2}{D_{CO_2}}$$

To relate the CO_2 mass transport in this system to changes in the fluid flow regime, a mass transport correlation resulting from nonlinear least squares regression can be expressed in terms of the reduced Taylor number (Ta_r) and the axial reynolds number of the CO_2 phase (Re_{z-g}), and was found to be:

Equation 6.4.6 Correlation for Sherwood number with α_g, (Ta_r) and (Re_{z-g})

$$Sh = \frac{1094554\left[\alpha_g\right]^{2.63}}{\left[Re_{z-g}\right]^{1.1}[Ta_r]^{0.04}}$$

This correlation provided predictive values that demonstrated an excellent fit, with $R^2 = 0.98$.

Equation 6.4.7 Correlation for change in gas volume fraction with (Ta_r) and (Re_{z-g})

$$\alpha_g = 0.0051[Ta_r]^{0.191}\left[Re_{z-g}\right]^{0.685}$$

Although attempting to approximate the gas volume fraction in terms of Ta_r and Re_{z-g}, as expressed in Equation 6.4.7, resulted in a good overall fit, with $R^2 = 0.96$, it still fails to account for the nuance changes in the volume fraction that takes place with the emergence of ring flow pattern. The shortcomings of such correlation are due to the multiple factors that influence gas-holdup values which include change in phase velocities and bubble diameter [177]. Therefore, in order to have a correlation that effectively describes the overall transport process over a wide range of operating conditions merged into a single global transport correlation [130], while accounting for changes in the flow structure, the actual gas volume fraction must be taken into consideration. Still the correlation developed for the gas volume fraction confirms that the gas flow rate has a greater impact on the gas volume fraction than the increase in cylinder rotation, in agreement with conclusions from former studies [212]. And if the two correlations are combined, then we get

Equation 6.4.8 Correlation for Sherwood number with (Ta_r) and (Re_{z-g}) only.

$$Sh = 1.02[Ta_r]^{0.46}\left[Re_{z-g}\right]^{0.71}$$

Although such correlation provides an inadequate fit to the data in this study, with $R^2 = 0.78$, it still reflects how the gas flow rate is expected to be more effective in increasing interphase mass transport than the increase in rotational energy [203].

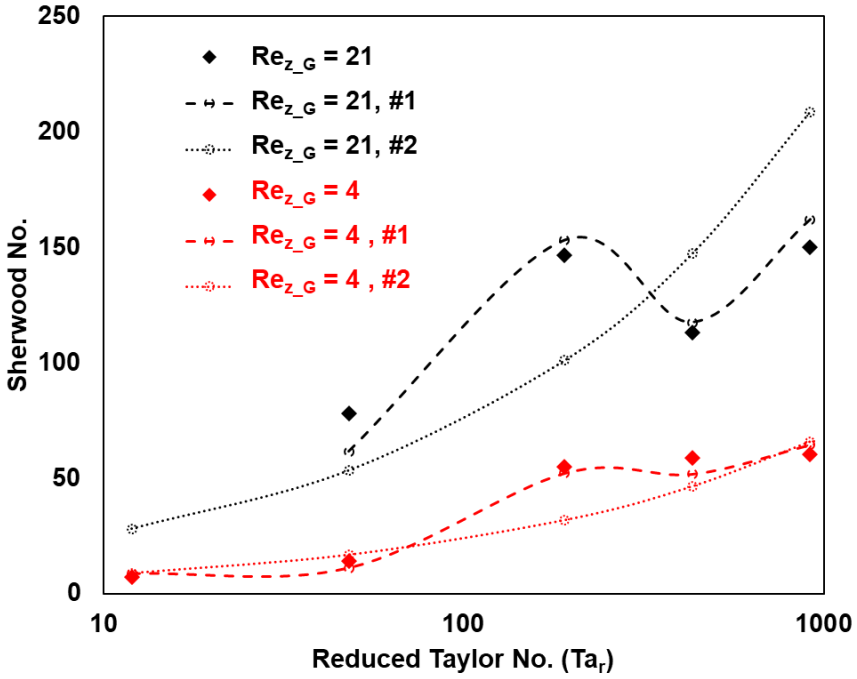

Figure 6.4.6 Change in Sherwood number with increasing rotational motion (Ta_r), theoretical (solid points) and estimated from Equation 6.4.6 (dashed line) and Equation 6.4.8 (dotted line).

Figure 6.4.6 shows the theoretical Sherwood values and those found using the two correlations in Equation 6.4.6 and Equation 6.4.8. As with studies examining the change in Sherwood number with increasing Taylor number for a single liquid phase [44], the interphase mass transfer is more sensitive to the increase in energy of dissipation at lower Taylor numbers than at higher Taylor numbers closer to the fully turbulent Taylor vortex flow (TTVF). The dependence of mass transfer on rotational motion estimated from this relation $Sh \propto [Ta_r]^{0.46}$ is close to that observed in the literature $Sh \propto [Ta_r]^{0.5}$ [43], while its relation to the gas flow rate, $Sh \propto \left[Re_{z-g}\right]^{0.7}$ is slightly lower than that estimated by Ramezani et al. for an oxygen-water interfacial system, $Sh \propto \left[Re_{z-g}\right]^{0.8}$ [59]. The lower diffusivity of CO_2 than oxygen

contributes to the slightly higher dependence of the mass transport on the flowrate of the gas phase.

In as similar manner, applying a multiple non-linear least squares regression to different parameters that describe the precipitation process and the final $CaCO_3$ properties, a number of correlations are developed:

Equation 6.4.9 Correlation for individual mass-transfer coefficient

$$k_L(\frac{m}{s}) = \frac{0.77[\alpha_g]^{2.05}[Ta_r]^{0.0346}}{[Re_{z-g}]^{1.55}}\,;\, R^2 = 0.96$$

Equation 6.4.10 Correlation for overall mass-transfer coefficient

$$k_L a(\frac{1}{s}) = \frac{19208.6[\alpha_g]^{0.093}[Ta_r]^{0.1}}{[Re_{z-g}]^{2}}\,;\, R^2 = 0.97$$

Equation 6.4.11 Correlation for precipitation acquisition time for PCC

$$Acquisition\ Time\ (minutes) = \frac{17.62}{[\alpha_g]^{0.611}[Ta_r]^{0.0028}[Re_{z-g}]^{0.51}}\,;\, R^2 = 0.98$$

Equation 6.4.12 Correlation for yield of PCC

$$Yield\ (\%) = \frac{232.41[\alpha_g]^{0.314}[Ta_r]^{0.62}}{[Re_{z-g}]^{0.283}}\,;\, R^2 = 0.85$$

Equation 6.4.13 Correlation for production rate of PCC

$$Production\ Rate\ (\frac{g}{L\ min}) = 0.4[\alpha_g]^{0.87}[Ta_r]^{0.071}[Re_{z-g}]^{0.27};\, R^2 = 0.95$$

Equation 6.4.14 Correlation for interfacial area

$$Interfacial\ Area\ (\frac{m^2}{m^3}) = \frac{4155[\alpha_g]^{1.217}[Ta_r]^{0.1186}}{[Re_{z-g}]^{0.22}};\, R^2 = 0.98$$

Equation 6.4.15 Correlation for pore volume of PCC

$$Pore\ Volume\ (cm^3) = \frac{197.4[\alpha_g]^{1.73}}{[Ta_r]^{0.14}[Re_{z-g}]^{0.72}};\, R^2 = 0.97$$

Equation 6.4.16 Correlation for PCC particle size

$$Particle\ Size\ (nm) = \frac{17504.5[\alpha_g]^{0.166}}{[Ta_r]^{0.27}[Re_{z-g}]^{0.69}};\ R^2 = 0.92$$

Equation 6.4.17 Correlation for PCC BET surface area

$$BET\ Surface\ Area\ (m^2) = \frac{71.18[\alpha_g]^{0.515}}{[Ta_r]^{0.056}[Re_{z-g}]^{0.018}};\ R^2 = 0.94$$

Equation 6.4.18 Correlation for PCC crystallite size

$$Crystallite\ Size\ (nm) = \frac{97.6[\alpha_g]^{0.175}}{[Ta_r]^{0.064}[Re_{z-g}]^{0.175}};\ R^2 = 0.66$$

And if we simplify the above correlations by substituting the gas volume fraction by Equation 6.4.7, we get:

Equation 6.4.19 Correlation for individual mass-transfer coefficient without volume fraction

$$k_L(\frac{m}{s}) = \frac{1.5\times10^{-5}[Ta_r]^{0.43}}{[Re_{z-g}]^{0.14}};\ R^2 = 0.73$$

Equation 6.4.20 Correlation for overall mass-transfer coefficient without volume fraction

$$k_L a(\frac{1}{s}) = 9.29\times10^{-5}[Ta_r]^{0.79}[Re_{z-g}]^{0.49};\ R^2 = 0.8$$

Equation 6.4.21 Correlation for precipitation acquisition time for PCC without volume fraction

$$Acquistion\ Time\ (minutes) = \frac{442.3}{[Ta_r]^{0.12}[Re_{z-g}]^{0.92}};\ R^2 = 0.99$$

Equation 6.4.22 Correlation for yield of PCC without volume fraction

$$Yield\ (\%) = \frac{44.4[Ta_r]^{0.121}}{[Re_{z-g}]^{0.068}};\ R^2 = 0.82$$

Equation 6.4.23 Correlation for production rate of PCC without volume fraction

$$Production\ Rate\ (\frac{g}{L\ min}) = 0.041[Ta_r]^{0.237}[Re_{z-g}]^{0.86};\ R^2 = 0.93$$

Equation 6.4.24 Correlation for interfacial area without volume fraction

$$Interfacial\ Area\ (\frac{m^2}{m^3}) = 6.73[Re_{z-g}]^{0.616}[Ta_r]^{0.35};\ R^2 = 0.93$$

Equation 6.4.25 Correlation for pore volume of PCC without volume fraction

$$Pore\ Volume\ (cm^3) = 0.0211[Ta_r]^{0.188}\left[Re_{z-g}\right]^{0.47};\ R^2 = 0.84$$

Equation 6.4.26 Correlation for PCC particle size without volume fraction

$$Particle\ Size\ (nm) = \frac{7257.3}{[Ta_r]^{0.24}\left[Re_{z-g}\right]^{0.58}};\ R^2 = 0.92$$

Equation 6.4.27 Correlation for PCC BET surface area without volume fraction

$$BET\ Surface\ Area\ (m^2) = 4.71[Ta_r]^{0.155}\left[Re_{z-g}\right]^{0.33};\ R^2 = 0.91$$

Equation 6.4.28 Correlation for PCC crystallite size

$$Crystallite\ Size\ (nm) = \frac{81.1}{[Ta_r]^{0.058}\left[Re_{z-g}\right]^{0.15}};\ R^2 = 0.67$$

The correlations developed above help us not only to dissect the impact of increasing the cylinder rotation and adjusting the CO_2 flow rate on the precipitation process and the final properties of the PCC, but it also enables us to predict the progress of the precipitation process and the resulting particle properties given only the measurements of the CO_2 volume fraction within the reactor during the precipitation. This quantitative approach of using empirical correlations evades the need to perform elaborate flow visualization experiments separate from the precipitation experiments.

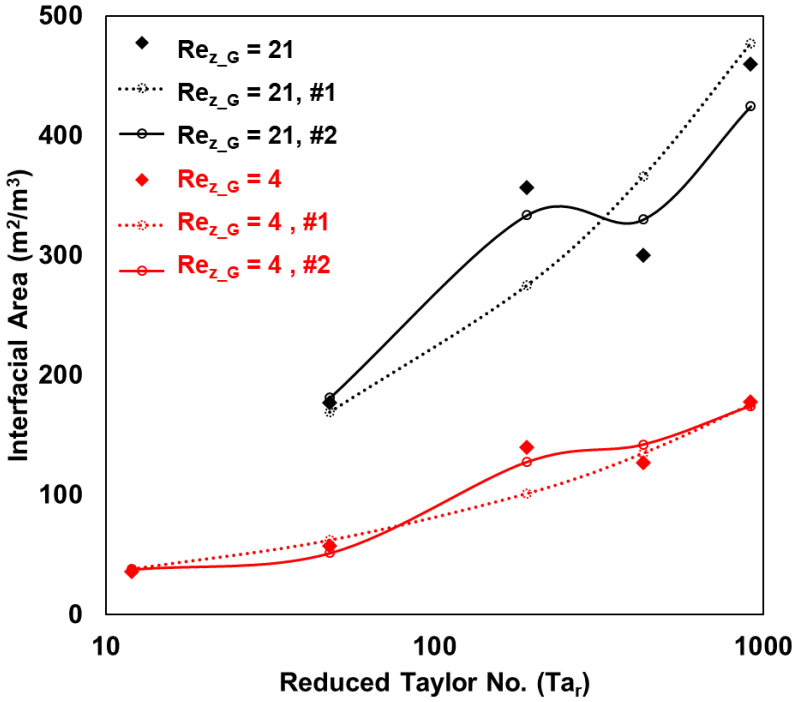

Figure 6.4.7 Change in interfacial area (m^{-1}) with increasing rotational motion (Ta_r), measured (solid points) and estimated from Equation 6.4.14 (solid line) and Equation 6.4.24 (dotted line).

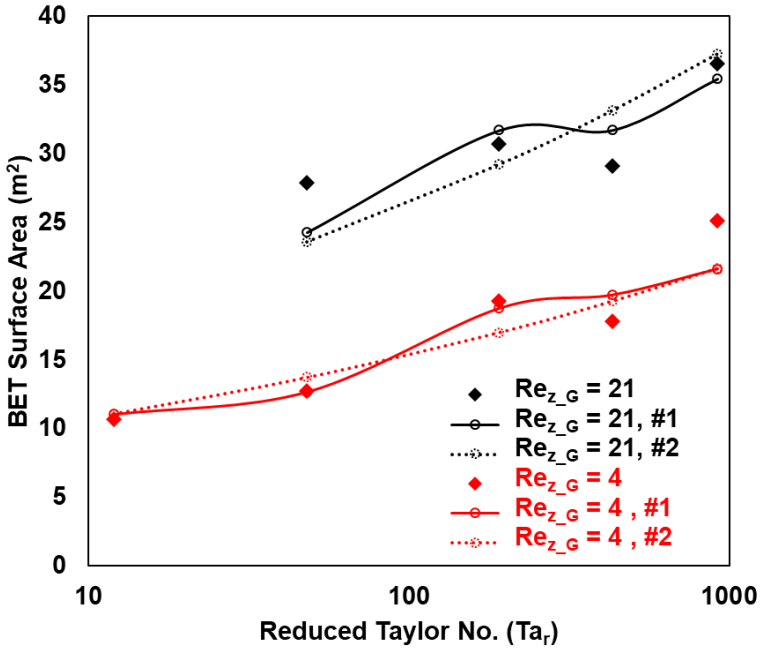

Figure 6.4.8 Change in PCC BET surface area with increasing rotational motion (Ta_r), experimental (solid points) and estimated from Equation 6.4.17 (solid line) and Equation 6.4.27 (dotted line).

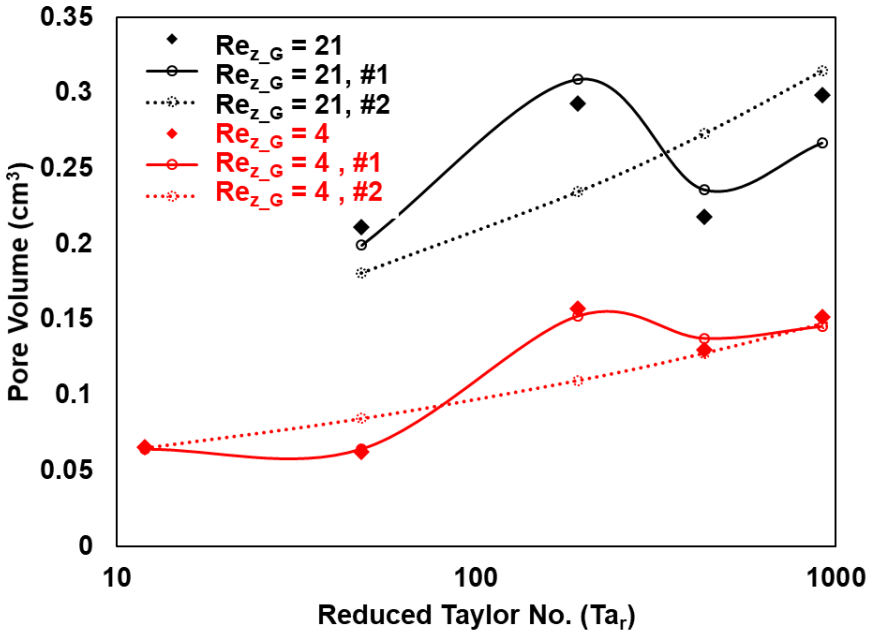

Figure 6.4.9 Change in PCC pore volume with increasing rotational motion (Ta_r), experimental (solid points) and estimated from Equation 6.4.15 (solid line) and Equation 6.4.25 (dotted line).

6.4.8 Flow Aspects

It has been suggested that axial mixing in two-phase Taylor vortex flow can lead to significant axial dispersion relative to radial dispersion [232], so that the assumption of plug-flow like mixing characteristics may not be most apt for the multiphase precipitation of $CaCO_3$. The presence of slip velocities between the two phases, as estimated from Equation 6.4.3, confirms that the mixing follows a regime that is more complex than simple plug-flow behavior [6]. Due to the strong relative contribution of buoyancy, in flow regimes with lower cylinder rotation speeds (Tar<200), the CO_2 bubbles will not be uniformly distributed azimuthally. Rather, they will accumulate closer to the inner cylinder, which is the azimuthal location corresponding to the highest vertical location in the gravity field [59]. At such conditions, the interphase mass transfer is predominantly limited to regions near the inner cylinder [212]. In contrast, higher

cylinder rotation rates (Tar>200) diminish the influence of buoyancy, resulting in a more uniform distribution of CO_2 bubbles within the reactor annulus, allowing for the interphase mass transfer to take place beyond the limited region near the inner cylinder, which makes a more efficient use of the reactor volume.

Under the mixing conditions used, flow regimes between Ta_r =12 to Ta_r~ 1000 were applied, going through laminar Taylor Couette flow (Ta_r <1), Taylor vortex flow (1< Ta_r <2.2), wavy vortex flow (2.2< Ta_r <40) chaotic Taylor vortex flow (93< Ta_r < 200), weakly turbulent Taylor vortex flow (Ta_r >200) and fully developed turbulent Taylor vortex flow (Ta_r ~1000).

Mass-transfer correlations described by Equation 6.4.19 and Equation 6.4.20, which do not account for the gas volume fraction, show that the rate of interphase mass transfer in general depends more strongly on the azimuthal mixing rather than the increase in the gas flow rate, as observed in earlier studies [212].

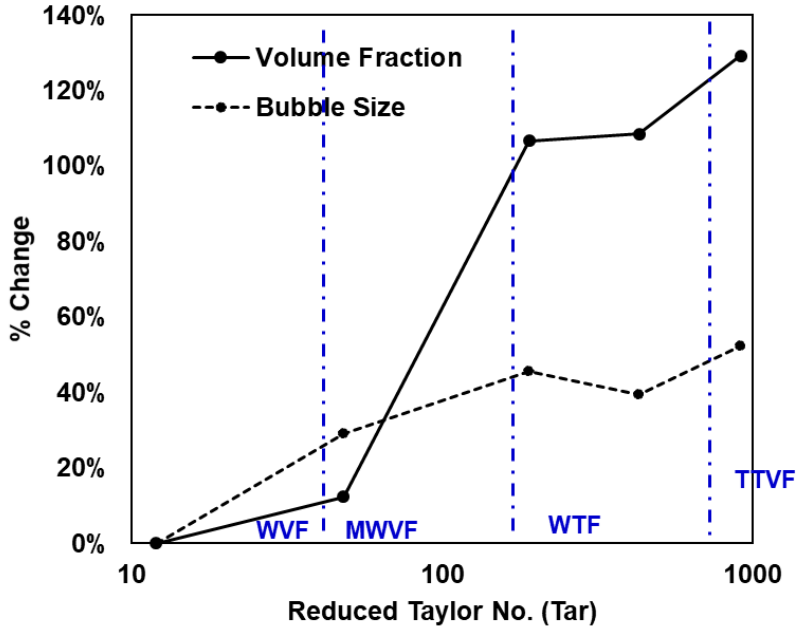

Figure 6.4.10 change in the gas-holdup values and average bubble size.

The change in the gas-holdup values, as indicated by the volume fraction, is greatest when transitioning from MWVF to WTF, and has a greater impact on the change in interfacial area than bubble size reduction during this transition.

6.4.9 Mixing influence on $CaCO_3$

Although the residence time distribution within the reactor is mostly determined by the scale of macro-fluid motion, the flow dynamics impacting the precipitation process are predominantly governed through controlling the micro-fluid motion, [78]. Just as the inhomogeneities in the flow can be grouped into three stages (macro-, meso- and micromixing) according to the characteristic length scale of mixing [55], the process of crystal growth can also be occur on three different size levels: molecular, microscopic and macroscopic [233]. Macromixing, which occurs on length scales in the range of reactor geometry, mainly affects the inertial-convective dispersion [55]. Enhancing the macromixing increases material exchange between different mixing zones, helping to achieve a more uniform average composition [2]. Macromixing time is mainly a function of the mixing kinetics within the axial direction, and thus can be characterized in terms of the axial dispersion coefficient as expressed in Equation 6.4.29.

To quantify the change in axial dispersion with increasing rotational motion, the Peclet number, as expressed in, Equation 6.4.30, was plotted in Figure 6.4.11. The estimated exponent correlating the dependence of the peclet number on rotational motion, $Pe \propto [Re_\theta]^{1.09}$ is similar to that derived in [25], $Pe \propto [Re_\theta]^{1.05}$. At high rotational rates, the peclet number drops an order of magnitude from its value at the lowest rotation rate, confirming that the mixing performance of the TCR reaches that of a CSTR.

Equation 6.4.29 Estimation of macromixing time via axial dispersion correlation

$$t_{macro} = \frac{2d^2}{D_{ax}}$$, where:

$$D_{ax} = \frac{2.\times10^{-3}[v]\left[Re_{\emptyset}\right]^{1.25}}{\left[\frac{r_1}{r_2}\right]^{1.75}}$$ for wavy flow regime.

$$D_{ax} = \frac{2.4\times10^{-1}[v][Re_{Z-L}]^{0.25}\left[Re_{\emptyset}\right]^{0.57}}{\left[\frac{r_1}{r_2}\right]}$$ for turbulent flow regime.

Equation 6.4.30 Peclet Number

$$Pe = \frac{2V_z\mathrm{d}}{D_{ax}}$$

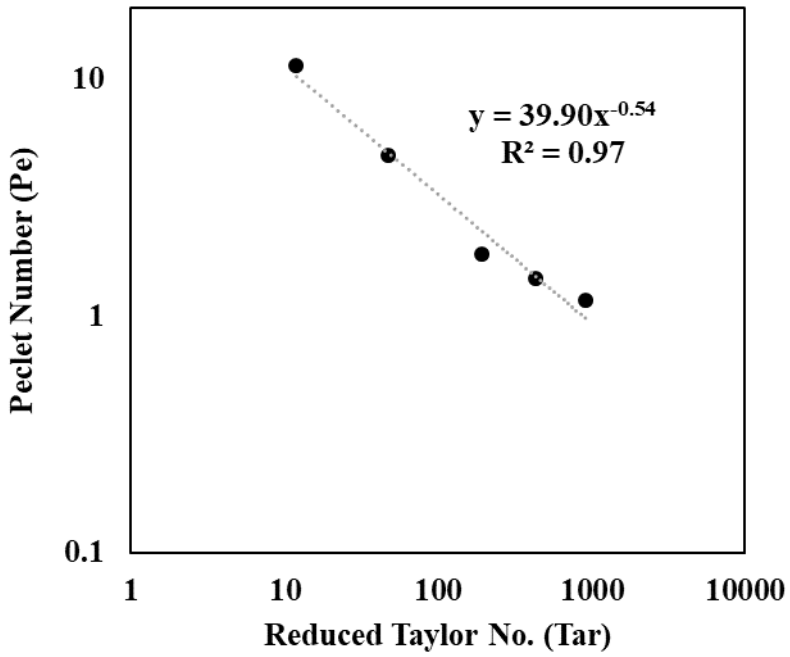

Figure 6.4.11 Effect of rotational motion on axial dispersion, as expressed by the Peclet number (Pe).

Because the macroscopic exchange among the vortices in the flow structure is not perfectly mixed, a mesomixing time scale is introduced to characterize the mixing process which leads to the homogenization of the vortex composition. Such time scale can be estimated from correlations derived by Racina et al. [55] as follows

Equation 6.4.31 estimation of Meso-mixing timescales.

$$t_{meso} = \frac{2.5\times10^5\left[1-\frac{r_1}{r_2}\right]}{\left[\frac{r_1}{r_2}\right]^{1.6}\left[Re_{\emptyset}\right]^{1.48}\left[\frac{2\pi(RPM)}{60}\right]}$$, for Tar>61 and $$t_{meso} = \frac{1.4\times10^4\left[1-\frac{r_1}{r_2}\right]}{\left[\frac{r_1}{r_2}\right]^{1.6}\left[Re_{\emptyset}\right]^{0.8}\left[\frac{2\pi(RPM)}{60}\right]}$$, for Tar<61

Given that the flow is mostly turbulent within the rotation rates used in this study, the local characteristics of the flow accounting for the micromixing on a molecular level can be estimated via :

Equation 6.4.32 Kolmogorov microscale equations

$$t_{micro} = \sqrt{\frac{\nu}{\varepsilon}} \text{ and } L_{micro} = \sqrt[4]{\frac{\nu^3}{\varepsilon}}$$ [162].

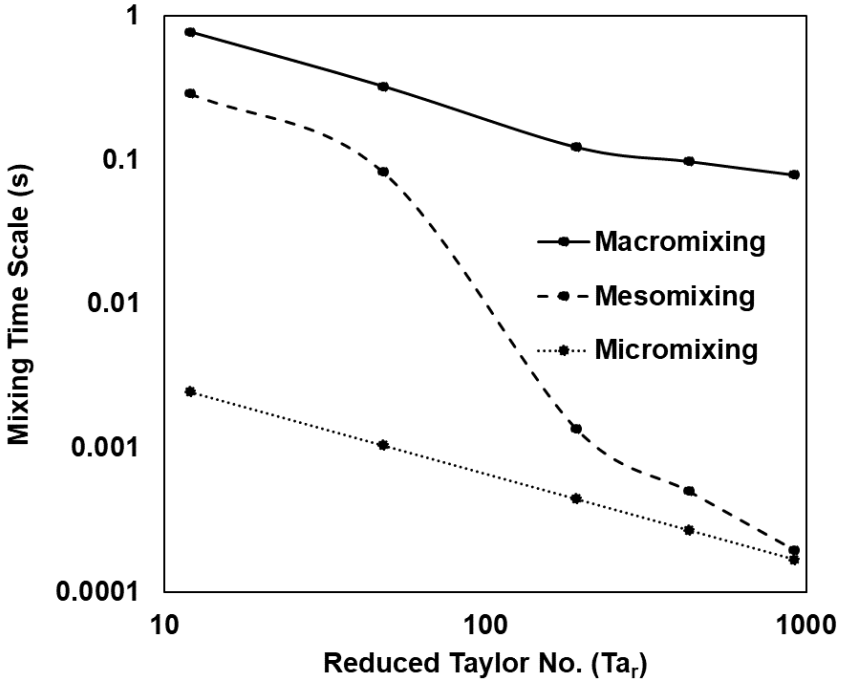

Figure 6.4.12 The three different mixing timescales in the Taylor vortex crystallizer: macromixing, meso-mixing and micromixing.

As displayed in Figure 6.4.12, the reactor exhibits significant macromixing for all rotation rates, with macromixing time scale decreasing but remaining within the same range. Meanwhile, the mesomixing time-scale exhibits a drastic drop in its mean-value, decreasing in nearly two orders of magnitude as the cylinder rotation is increased from 400RPM (Ta_r=48) to 800RPM (Ta_r

=191). In contrast, the change in the mixing scale on a microscopic level is monotonic and only drops an order of magnitude when moving from the lowest to the highest rotations used in this study. As we approach the fully turbulent Taylor vortex flow (TTVF) at rotation rates close to Ta_r = 1000, mesomixing time-scales approach that of micromixing, indicating that vortex composition at high rotations becomes uniform on a microscopic scale, since the small vortices stretch within range of Kolmogorov microscale [55].

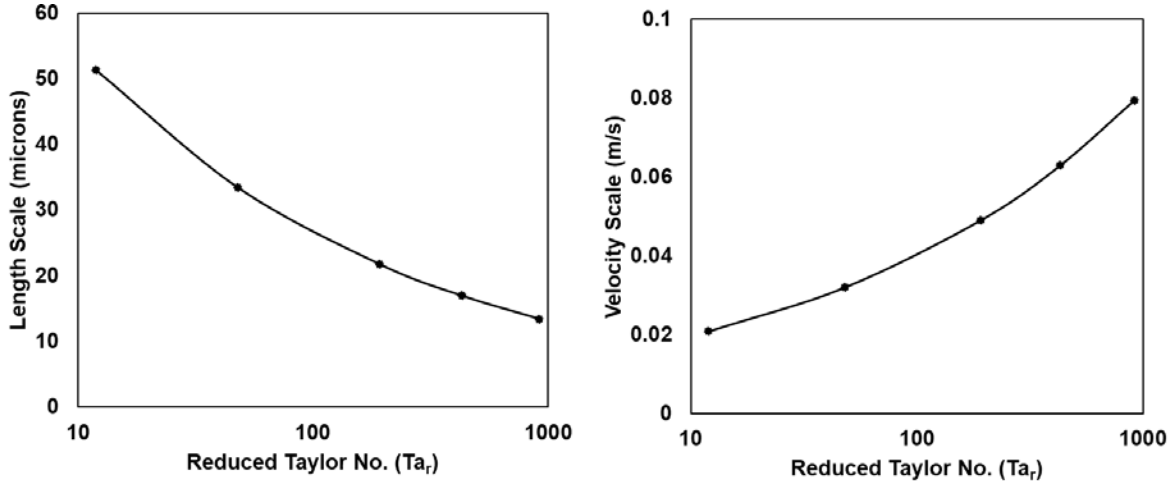

Figure 6.4.13 Change in micromixing length scale and velocity on the Kolmogorov scale with increasing rotational motion.

In the precipitation of $CaCO_3$, good macromixing conditions enhance the uniform spatial concentration distributions within the bulk of the slurry aqueous suspension, a factor that is important in producing super-fine $CaCO_3$ particles [182]. In particular, with enhanced macromixing, both the suspended undissolved $Ca(OH)_2$ particles and PCC closely follow fluid streamlines generated by the main convective toroidal flow pattern imposed by the cylinder rotation. The Kolmogorov micromixing length scale plotted in Figure 6.4.13 (a), exhibit values which suggest that the smallest predicted eddies within such turbulent flow regimes vary between 50 and 10 microns. Such small eddies ensure that the particles in the slurry are very well-mixed. The velocity of the smallest eddies, displayed in Figure 6.4.13(b), become higher

than the liquid space velocity (0.038m/s), with Tar>50, confirming that mixing on the microscopic scale is the main factor contributing in dramatically enhancing the interphase transfer observed at Ta_r>50.

Considering that micromixing describes the diffusive transfer of species on length scales close to the molecular scale [55], it becomes critical in controlling the nucleation in the premixing region [47]. The higher nucleation rates at such mixing conditions result in the generation of a larger number of smaller crystallites that are more likely to exhibit growth by aggregation. Such aggregation is associated with the coalescence of small crystals that grow together and form larger particles. As observed in this study, although such growth leads to the formation of random aggregates of spherical particles that lack preferential direction of growth, the produced particles still retain an enhanced porous internal crystal structure [84]. Due to significant mixing within the bulk liquid, "growth by aggregation" becomes a more likely crystal growth mechanism, thereby competing with primary processes, such as nucleation, crystallite growth and the self-assembled aggregation of crystals into ordered regular geometric structures such as cubes or ellipsoids. In fact, such morphologies were observed for crystals formed with lower CO_2 flowrates (0.02L/min) and flow regimes below fully turbulent Taylor vortex flow (TTVF).

6.4.10 Comparative Performance

Relative to conventional bubble columns or stirred tanks, precipitation in the TC reactor was carried out with higher efficiency evident from the higher conversion ratio and the reaction rate [171] due to the greater interphase mass transfer, indicated by kLa values that were as high as 0.068 s^{-1}, closer to that of CO_2 membrane contactors (.075 s^{-1}) [234] , and significantly higher than the values observed for stirred tanks (0.04 s^{-1}), bubble column (0.004 s^{-1}), packed beds (0.002 s^{-1}) [197], microbubble columns (0.00153 s^{-1}) [235]. Such high transport rates confirm

the TC reactor as a suitable mixing medium to provide the process intensification that is critical to controlling the precipitation process [2].

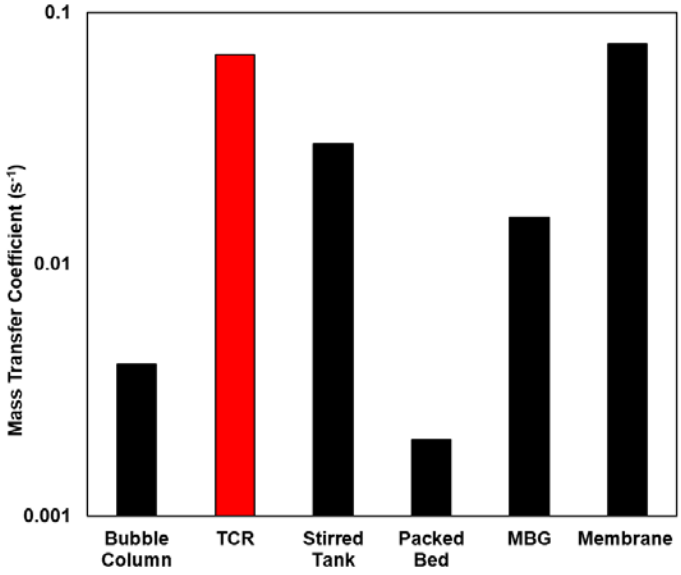

Figure 6.4.14 Comparing individual mass transfer coefficients of various precipitation arrangements.

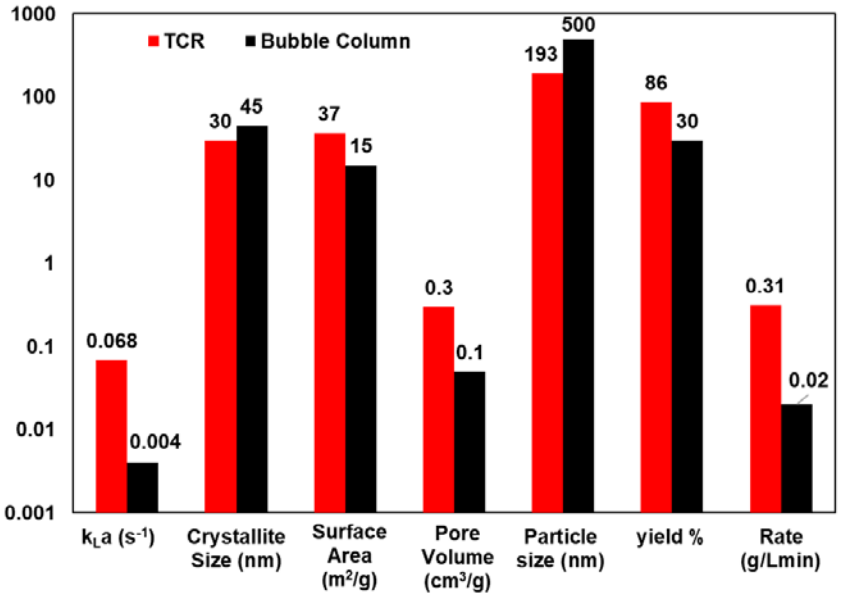

Figure 6.4.15 Comparing PCC properties and precipitation efficiency of TCR vs Bubble Column.

6.4.11 Energy of Dissipation

Although examining the influence of rotation flow in terms of Taylor number allows for the identification of transitions in flow-regime, it is important to quantify the results in terms of the total energy of dissipation per unit mass, as displayed in Figure 6.4.16. While power dissipation may not be the most critical criterion for the understanding and prediction of mass transfer and mixing efficiency in the Taylor Couette reactor, it becomes important when it comes to evaluating the performance of the TCR technology and predicting operating costs. Specifically, as marked in Figure 6.4.16, operating at the highest shear mixing rate only enhances the mass-transfer by 50%, with more than 7 times higher dissipation energy. Mass transfer coefficients of 0.0.45 s^{-1} and 0.028 s^{-1} can be achieved with a dissipation energy of only 5.4 W/kg, for 0.02L/min (Re_{z_G} = 4), and b) 0.1L/min (Re_{z_G} = 21) CO_2 flowrates, respectively. As such, operating at very high rotational rates close to turbulence, may not be a cost effective approach towards PCC particles production.

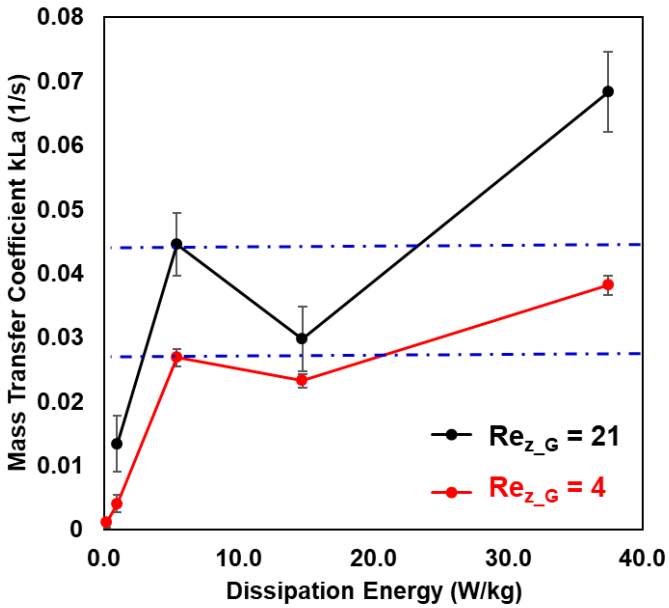

Figure 6.4.16 Influence of dissipation energy on the overall mass transfer coefficient.

6.5 Conclusion

Fluid dynamic conditions play a critical role in determining the crystal size, morphology, surface area and porous structure. The precipitation approach in this study mimics the carbonation method commonly practiced on industrial scales [236] , but with a unique mixing approach that aims at producing submicron calcite particles with a nanoporous internal structure, having a surface area as high as 36 m^2/g, pore volume of 0.3 cm^3, particle size of less than 200nm and a crystallite size of 30nm, produced under a CO_2 flowrate of 0.1 L/min at a yield of over 86 % and a production rate of 0.31 g/min per liter of CO_2. While fixing the size and configuration of the mixing chamber, modifying the mixing energy dissipation rate enabled us to better control the production of nanoparticles without the need for stabilizers or additives. The degree of toroidal mixing was critical in increasing the reaction rates and inhibiting crystal agglomeration, both of which contributed to the formation of smaller particles [78] [236]. High concentration of $Ca(OH)_2$, which are typically assumed to be unsuitable for obtaining reproducible results for PCC in the case of bubble columns [171] , were easily accommodated in the case of TC reactor configuration, due to improved mixing within such highly viscous suspensions.

Relative to conventional bubble columns or stirred tanks, precipitation in the TC reactor was carried out with higher efficiency evident from the higher conversion ratio and reaction rate [171] due to the greater interphase mass transfer, indicated by kLa values that were as high as $0.068s^{-1}$, within the same range observed in experiments operating at much higher CO_2 flowrates [199]. Such high transport rates confirm the TC reactor as a suitable mixing medium to provide the process intensification that is critical to controlling the precipitation process [2]. The mass transfer across the gas-liquid film is renewed at higher rates with increased mixing intensity. However, the evolution of the “ring-flow” structure compromises the high mixing

intensities, and results in a reduction in the interfacial mass transfer among the gas and liquid phases. This leads to the overall observation that enhancement of the submicrometric properties of PCC particles is non-monotonically proportional to the increase in mixing rate or Taylor number. Rather, it is the flow-structure that was found to govern the increase in interfacial mass transfer.

Under the highest mixing rate, the cumulative pore surface area and the cumulative pore volume of macropores accounted for only 17% and 60% for the highest surface area submicron PCC formed under a CO_2 flowrate of 0.02L/min, with similar proportions (24%, 66%) for PCC formed under a CO_2 flowrate of 0.1 L/min. The resulting mesoporous calcite particles have a nanoporous internal structure that provides sufficient surface area to ensure rapid kinetics when producing highly reactive CaO sorbents [7], which can be used for applications related to carbon capture and utilization, offering superior CO_2 consumption and a more economically profitable production approach [171]. Although process costs and energy requirements can be significant, producing commercially valuable high purity PCC via TCR technology may still be economically competitive especially if flue gases are used as CO_2 source. In this regard, Fagerlund suggested that PCC production through flue gas carbonation can be a suitable candidate for being among the first commercially viable carbon sequestration/storage via mineralization routes [237].

The empirical correlations developed for correlating interphase mass-transfer, process performance parameters and particle properties to the azimuthal rotation and CO_2 flowrate provide valuable predictive values that evade the need to quantify the interfacial area experimentally via flow visualization. Although the developed correlations accommodate a wide range of azimuthal rotation rates that can be industrially relevant, additional studies

examining flow behavior and the change in interfacial area under higher gas flow rates may be needed. Using a micron sparger to supply CO_2 bubbles restricted the range of gas flowrates used in this study, as higher flowrates could result in the elongation of vortices and could lead to the complete disruption of the toroidal structure that characterizes the TC reactor [203]. Future studies exploring the influence of higher CO_2 flowrates on the PCC formed in a TC crystallizer should consider adjusting the reactor geometry and using better spargers that ensure the generation of smaller bubbles while supplying the gas into the reactor.

CHAPTER 7

CONCLUSION

7.1 General

This work described fundamental studies related to assessing the influence of changing mixing hydrodynamics and flow structure in a Taylor Couette reactor on the mass transport in multiphase reactions. Since the performance of continuous Taylor-Couette reactors can be significantly improved by the presence of vortex structure, understanding the general stability characteristics and characterizing the transport phenomena and flow transitions in TCR flow was a necessary task. The onset of Taylor vortices by the centrifugal instability depended on fluid properties and reactor geometry, including the gap width and the radii of inner and outer cylinders. As the inner cylinder rotation increased further beyond the critical speed, higher order harmonics became important, leading to a progression of secondary instabilities, passing through a variety of flow regimes all the way to the onset of full turbulence. As demonstrated in this thesis, while the TCR may be used for any solid-liquid-gas reaction, the reactor is particularly useful for difficult feed streams such as those containing high viscosity feeds, heterogeneously catalyzed reactions, as well as suspended solids (with applications relating to precipitation, catalyst synthesis, coating and surface functionalization).

7.2 Influence of Flow Structure on Multiple Reactions

By studying the precipitation of barium sulfate below and above the onset of Taylor primary instability we were able to elucidate the influence of vortex motion on crystal growth and self-assembled aggregation. In general, crystal size decreased with increasing flow rate and decreasing residence time. More importantly, the crystal size distribution was found to be much broader in the case of laminar Taylor Couette flow when compared to the narrow range

observed for Taylor-vortex flow under different conditions of axial flow. The predicted difference in particle residence time/contour length below and above the instability served as a confirmation of the observed crystal size trends.

To extend this understanding on the influence of the onset of vortex flow to a model heterogeneous solid-liquid phase reaction, aluminum metal fillers were coated with Methacryloxypropyltrimethoxysilane (MPS) to functionalize the filler's surface with specific (H_2C=C) functionality, which would increase the affinity of the fillers to polymer matrices, such as PMMA. The reaction between the metal particles and the MPS solution proceeded successfully in the TCR, and was performed under different flow conditions. It was observed that the degree of functionalization was significantly enhanced when increasing rotation rates beyond the onset of Taylor vortices. The increase in mixing due to increased shear associated with growing axial flow was found to be critical in enhancing the coating efficiency, providing particles with superior properties. At the same time, the onset of vortex instability provided more uniform surface coverage and narrower variation in coating pattern, as evidenced from SEM and DLS particle size measurements. In addition, the roughness of the coated surface was found to decrease with increasing RPM. As a result, the coating reaction in TCR enabled us to effectively functionalize the aluminum surface while reducing the roughness of the coated layer.

When applied to multiphase gas-liquid-solid precipitation of $CaCO_3$, the higher shear rates in Taylor Couette flow were utilized to significantly reduce the bubble size of carbon dioxide as opposed to the random turbulent eddy flow associated with conventional crystallizers [194]. Specific gas-liquid interfacial areas obtained in Taylor Couette reactors were found to be an order of magnitude higher than those obtained for a stirred tank reactor [197]. In addition to

influencing the degree of interfacial transport between the gas-liquid phases, the Taylor Couette reactor offered macro and micro fluid motion that further enhanced the degree of mixing intensity, affecting the crystallization process and PCC properties, such as particle size distribution, surface area and pore volume as demonstrated in this study.

Relative to conventional bubble columns or stirred tanks, precipitation in the TC reactor was carried out with higher efficiency evident from the higher conversion ratio and the reaction rate [171] due to the greater interphase mass transfer, indicated by kLa values that were as high as 0.068 s^{-1}, closer to that of CO_2 membrane contactors (.075 s^{-1}) [234] , and significantly higher than the values observed for stirred tanks (0.04 s^{-1}), bubble column (0.004 s^{-1}), packed beds (0.002 s^{-1}) [197], microbubble columns (0.00153 s^{-1}) [235]. Such high transport rates confirm the TC reactor as a suitable mixing medium to provide the process intensification that is critical to controlling the precipitation process [2]. The empirical correlations developed for correlating interphase mass-transfer, process performance parameters and particle properties to the azimuthal rotation and CO_2 flowrate provided valuable predictive tools that evade the need to quantify the interfacial area experimentally via flow visualization.

Evidently, Taylor Couette flow was demonstrated to be an integrative technology when it comes to multiphase precipitation, combining the performance of a bubble column with that of a microbubble generator, through the utilization of a small frit to feed the gas in the TCR. Such integrative approach operated at continuous-flow mode is one of the key features that highlight Taylor Couette flow configuration as a competitive technology in the field of process intensification [1].

7.3 Impact of this Work

This research focused on elucidating the impact of flow structure and the corresponding changes in the shape of the fluid streamlines on reactions ranging from single-phase (homogenous), two-phase (heterogeneous solid-liquid) to multiple phases (solid-liquid-gas). Overall, it can be concluded that it is not just the increase of energy of dissipation (turbulence) that is critical towards enhancing the mixing but rather the structure of the flow regimes, which if elaborately understood and characterized, enables us to exercise more effective control over the mass transfer in a reaction. By discerning the different flow patterns in any reactor configuration, we can apply changes in the flow structure to model chemical reactions in homogeneous single phase, heterogeneous and multiple phase environments. This emphasis on flow-structure was quantified by developing empirical mass transport correlations to relate the advective mass transfer to changes in the fluid flow regime.

7.4 Extensions of this study (recommended future work):

Comparing the performance of TCR with other competitive rotating reactors would provide new insights for reactor selection. To make a more rigorous assessment of TCR, future studies can pursue combining this reactor configuration with multistage spinning disk reactor [238] in the form of Taylor-Couette Disc Contactor [239]. Such hybrid reactor could be developed by modifying the conventional design of the Taylor-Couette Reactor into a TCR with ribbed inner and outer cylinders. Studies have investigated the introduction of ribs in attempts to enhance mixing intensity and reduce the degree of macromixing [163]. Such features allow for the decoupling of micromixing from axial dispersion [163], providing greater intensification of micromixing and larger surface to volume ratio. This is supported by studies that showed that the utilization of ribs also helped in enhancing gas hold-up values [7].

The flow visualization techniques presented in chapter 2 for two-phase flow and the multiphase flow in chapter 6 provided important insights into characterizing the general flow structure at each flow regime. However, assessment of flow-structures via conventional optical techniques and laser-based visualization become particularly challenging when operating in multiphase flow close to the turbulent flow regime. The mixing region under such conditions is rather opaque and visual access is limited to regions near the outer wall of the reactor [240]. The simple optical techniques used in this study was sufficient for understanding the general characteristics of the flow, but it could be complemented by more elaborate techniques such as Particle Image Velocimetry (PIV) [241], Laser Doppler Anemometry (LDA) [75] , magnetic resonance imaging velocimetry (MRIV) [61] or planar laser induced fluorescence (PLIF) [33].

REFERENCES

[1] D. Reay, C. Ramshaw and A. Harvey, Process Intensification: Engineering for efficiency, sustainability and flexibility, Oxford, UK: Butterworth-Heinemann, 2013.

[2] G. Trippa, "Process Intensification of liquid phase and gas-liquid precipitation of calcium carbonate in narrow channel reactors," PhD Dissertation, School of Chemical Engineering and Advanced Materials, University of Newcastle upon Tyne, January 2006.

[3] K. Boodhoo and A. Harvey, "Process Intensification: An Overview of Principles and Practice," in *Process Intensification for Green Chemistry: Engineering Solutions for Sustainable Chemical Processing*, Chichester, UK., John Wiley & Sons, Ltd, 2013.

[4] T. Letcher, . Scott and . A. Patterson, Chemical Processes for a Sustainable Future, Cambridge, UK: Royal Society of Chemistry, 2014.

[5] H. Wang, A. Mustaffar, A. N. Phan, V. Zivkovic, D. R. R. Law and K. Boodhoo, "A review of process intensification applied to solids handling," *Chemical Engineering & Processing: Process Intensification,* vol. 118 , p. 78–107, 2017.

[6] S. Wroński, R. Hubacz and T. Ryszczuk, "Interfacial area in a reactor with helicoidal flow for the two-phase gas–liquid system," *Chemical Engineering Journal,* vol. 105, no. 3, p. 71–79, January 2005.

[7] H. Masuda, W. Zheng, T. Horie and N. Ohmura, "Enhancement of Gas Hold-up with a Taylor Vortex Flow System Equipped with Ribs," *Journal of Chemical Engineering of Japan,* vol. 46, no. 1, pp. 27-32, 2013.

[8] G. L. Taylor, "Fluid friction between rotating cylinders, I Torque measurements," *Proc. Roy. Soc.,* vol. 157, no. 892, p. 546, 1936.

[9] G. I. Taylor, "Stability of a Viscous Liquid Contained between Two Rotatting Cylinders," *Phil. Trans. R. Soc. Lond. ,* vol. 223, pp. 289-343, 1923.

[10] G. Baier, *Liquid-Liquid Extraction based on a New Flow Pattern: Two-Fluid Taylor-Couette Flow,* Universityof Wisconsin-Madison - Doctoral Thesis, 1999.

[11] R. C. D. Prima and H. L. Swinney, "Instabilities and transition in flow between concentric rotating cylinders," in *Topics in Applied Physics vol 45.*, vol. 45, Berlin, Heidelberg , Springer, 1981, pp. 139-180.

[12] W. M. J. Batten, N. W. Bressloff and S. R. Turnock, "Transition from vortex to wall driven turbulence production in the Taylor Couette system with a rotating inner cylinder," *International Journal for Numerical Methods in Fluids,* vol. 38, pp. 207-226, 2002.

[13] T. R. Mizushina, R. Ito, K. Kataoka, S. Yokoyama, Y. Nakashima and A. Fukuda, "Transition of flow in the annulus of concentric cylinders," *Chemical Engineering, Japan,* vol. 32, pp. 795-800, 1968.

[14] C. D. Andereck, S. S. Liu and H. L. Swinney, "Flow Regimes in a Circular Couette System with Independently Rotating Cylinders," *J. Fluid Mech,* vol. 164, pp. 155-163, 1986.

[15] K. Kataoka and T. Takigawa, "Intermixing over Cell Boundary between Taylor Vortices," *AIChE Journal,* vol. 27, pp. 504-508, 1981.

[16] R. C. Giordano, D. M. F. Prazeres and C. L. Cooney, "Analysis of a Taylor Poiseuille Vortex Flow Reactor II: Reacotr Modeling and Performance Assessment Using Glucose-Fructose Isomerization as Test Reaction," *Chemical Engineering Science,* pp. 3611-3626, 2000.

[17] J. Legrand and F. Coeuret, "Circumferential Mixing in one-phase and Two Phase Taylor vortex flows," *Chemical Engineering Science,* pp. 47-53, 1986.

[18] S. Chandrasekhar, Hydrodynamic and Hydromagnetic Stability., New York: Dover Publications, 1981.

[19] R. C. Di Prima, "The Stability of a Viscous Fluid between Rotating Cylinders with an Axial Flow," *Journal of Fluid Mechanics,* no. 9, pp. 621-631, 1960.

[20] E. R. Krueger and R. C. Di Prima, "The Stability of a Viscous Fluid between Rotating Cylinders with an Axial Flow," *Journal of Fluid Mechanics,* vol. 19, pp. 528-538, 1964.

[21] R. J. Donnelly and D. Fultz, "Experiments on the Stability of Spiral Flow between Rotating Cylinders. Pages 1150-1154," in *Proceedings of the National Academy of Sciences, vol. 46,* USA, 1960.

[22] H. A. Snyder, "Experiments on the Stability of Spiral Flow with Low Axial Reynolds numbers," in *Proc. Roy. Soc. A. 265. 198-214. (1962)*, 1962.

[23] K. Kataoka, H. Doi, T. Komai and M. Firgarva, "Ideal Plug Flow Properties of Taylor Vortex Flow," *J. Chem Eng Japan*, vol. 8, pp. 472-476, 1975.

[24] G. Desmet, H. Verelst and G. V. Baron, "Local and Global Dispersion Effects in Couette-Taylor Flow-II Quantiative Measurments and Discussion of the Reactor Performance," *Chemical Engineering Science*, pp. 1299-1309, 1996.

[25] C. L. Cooney and C. M. Moore, "Axial Dispersion in Taylor-Couette Flow.," *AICHE Journal* , vol. 41, no. 3, pp. 723-727, March 1995.

[26] W. Y. Tam and H. L. Swinney, "Mass Transport in Turbulent Couette-Taylor Flow," *Phys. Rev. A*, vol. 36, pp. 1374-1381, 1987.

[27] N. Ohmura, K. Kataoka, Y. Shibata and T. Makino, "Effective Mass Diffusion Over Cell Boundaries in a Taylor-Couette Flow System," *Chemical Engineering Science*, vol. 52, pp. 1757-1765, 1997.

[28] A. Syed and W. G. Fruh, "Modeling of Mixing in A Taylor-Couette Reactor with Axial Flow," *Journal of Chemical Technology and Biotechnology*, vol. 78, pp. 227-235, 2003.

[29] X. Zhu and R. D. Vigil, "Banded Liquid–Liquid Taylor-Couette-Poiseuille Flow," *AIChE Journal*, vol. 47, no. 9, pp. 1932-1940, 2001.

[30] D. D. Joseph, K. Nguyen and G. S. Beavers, "Non-uniqueness and stability of the configuration of flow of immiscible fluids with different viscosities," *Journal of Fluid Mechanics*, vol. 141, pp. 319-345, 1984.

[31] R. J. Campero and R. D. Vigil, "Flow Patterns in Liquid_Liquid Taylor-Couette-Poiseuille Flow," *, Ind. Eng. Chem. Res.*, vol. 38, p. 1094 , 1999.

[32] X. Zhu and R. Vigil, "Axial Mass Transport in Liquid-Liquid Taylor-Couette Poiseuille Flow," *Chemical Engineering Science*, vol. 55, no. 21, pp. 5079-5087, 2000.

[33] M. J. Sathe, S. S. Deshmukh, J. B. Joshi and S. B. Koganti, "Computational Fluid Dynamics Simulation and Experimental Investigation: Study of Two-Phase Liquid−Liquid Flow in a Vertical Taylor−Couette Contactor," *Ind. Eng. Chem. Res.*, vol. 49 , no. 1, p. 14–28, 2010.

[34] L. J. Forney, A. H. P. Skelland, J. F. Morris and R. A. Holl, "Taylor Vortex Column: Large Shear For Liquid–Liquid Extraction," *Separation Science and Technology,* vol. 37, no. 13, p. 2967–298, 2002.

[35] E. Dluska and A. Markowska, "One-step preparation method of multiple emulsions entrappingreactive agent in the liquid–liquid Couette–Taylor flow," *Chemical Engineering and Processing,* vol. 48 , p. 438–445, 2009.

[36] K. Kataoka, N. Ohmura, M. Kouzu, Y. Simamura and M. Okubo, "Emulsion Polymerization of Styrene in a Continuous Taylor Vortex Flow Reactor," *Chemical Engineering Science,* vol. 50, pp. 1409--1416., 1995.

[37] E. Dluska and A. markowska-Radomska, "Regimes of Multiple Emulsions of W1/O/W2 and O1/W/O2 in the Continuous Couette-Taylor Flow Contactor," *Chemical Engineering Technology,* vol. 33, no. 1, pp. 113-120, 2010.

[38] X. Wei, H. Takahashi, S. Sato and M. Nomura, "Continuous Emulsion Polymerization of Styrene in a Single Couette--Taylor Vortex Flow Reactor," *Journal of Applied Polymer Science,* vol. 80, pp. 1931--1942, 2000.

[39] J. Woliński and S. Wroński, "Interfacial polycondensation of polyarylate in Taylor-Couette-Reactor," *Chemical Engineering and Processing: Process Intensification,* vol. 48, no. 5, pp. 1061-1071, 2009.

[40] M. Cohen and D. Maron, "Analysis of a Rotating Annular Reactor in the Vortex Flow Regime," *Chemical Engineering Science,* vol. 46, pp. 123--134, 1990.

[41] D. Haim and L. Pismen, "Performance of a Photochemical Rreactor in the Taylor--Goertler Vortical Flow," *Chemical Engineering Science ,* vol. 49, pp. 1119--1129, 1994.

[42] F. Coeuret and J. Legrand, "Mass Transfer at the Electrodes of Concentric Cylindrical Reactors Combining Axial Flow and Rotation of the Inner Cylinder," *Electrochimica Acta,* vol. 26, pp. 865--872, 1981.

[43] Z. H. Gu and T. Fahidy, "Mass Transport in the Taylor-Vortex Regime of Rotating Flow," *Chemical Engineering Science,* vol. 40, no. 7, pp. 1145-1153, 1985.

[44] K. Kataoka, H. Doi and T. Komai, "Heat/mass transfer in Taylor vortex flow with constant axial flow rates," *International Journal of Heat and Mass Transfer,* vol. 20, pp. 57-63, 1977.

[45] G. Iosilevskii, H. Brenner, M. C.M.V. and C. Cooney, "Mass Transport and Chemical Reaction in Taylor--Vortex Flows with Entrained Catalytic Particles: Applications to a Novel Class of Immobilized Enzyme Biochemical Reactors," *Philosophical Transactions: Physical Sciences and Engineering,* vol. 345, pp. 259-294, 1993.

[46] R. Giordano, R. Giordano and C. Cooney, "Performance of a Continuous Taylor--Couette--Poiseuille Vortex Flow Enzymatic Reactor with Suspended Particles," *Process Biochemistry,* vol. 35, pp. 1093-1101, 2000.

[47] W. M. Jung, S. H. Kang, W.-S. Kim and C. K. Choi, "Particle morphology of calcium carbonate precipitated by gas–liquid reaction in a Couette–Taylor reactor," *Chemical Engineering Science,* vol. 55, no. 4, p. 733–747, February 2000.

[48] B. Kong, J. V. Shanks and R. D. Vigil, "Enhanced Algal Growth Rate in a Taylor Vortex Reactor," *Biotechnology and Bioengineering,* vol. 110, no. 8, pp. 2140-2149, 2013.

[49] G. A. Ameer, A. G. E., B. Obradovic, C. C. L. and R. Langer, "RTD Analysis of a Novel Taylor-Couette Flow Device for Blood Detoxification," *AIChE Journal,* vol. 45, p. 633, 1999.

[50] A. Grohmann, M. Reiter and U. Wiesmann, "New Flocculation Units with High Energy Efficiency," *Water Science and Technology,* vol. 13, pp. 567-573, 1981.

[51] T. Ogihara, G. Matsuda, T. Yanagawa, N. Ogata, K. Fujita and M. Nomura, "Continuous Synthesis of Monodispersed Silica Particles Using Couette-Taylor Vortex Flow," *J. Ceram. Soc. Jpn., Int.,,* vol. 103, p. 151 , 1995.

[52] S. Lee and R. Lueptow, "Rotating Membrane Filtration and Rotating Reverse Osmosis," *Journal of Chemical Engineering of Japan,* vol. 37, pp. 471--482, 2004.

[53] N. Ohmura, S. T. and Y. Asamura, "Particle Classification in Taylor Vortex Flow with an Axial Flow," *Journal of Physics: Conference Series,* vol. 14, pp. 64-71, 2005.

[54] J. Gradl and W. Peukert, "Characterization of Micro Mixing for Precipitation of Nanoparticles in a T-Mixer," in *Micro and Macro Mixing: Analysis, Simulation and Numerical Calculation,* Kaiserstr, Germany, Springer, 2010, pp. 105-124.

[55] A. Racina, Z. Liu and M. Kind, "Mixing in Taylor-Couette Flow," in *Micro and Macro Mixing: Analysis, Simulation and Numerical Calculation,* Berlin, Springer-Verlag, 2010, pp. 125-139.

[56] R. B. S.J. Curran, "Taylor-Vortex Bioreactors for Enhanced Mass Transport," in *Bioreactors for Tissue Engineering*, Netherlands, Springer , 2005, pp. 47-85.

[57] M. F. Aljishi, A.-C. Ruo, J. H. Park, B. Nasser, W.-S. Kim and Y. L. Joo, "Effect of flow structure at the onset of instability on barium sulfate precipitation in Taylor–Couette crystallizers," *Journal of Crystal Growth,* vol. 373, p. 20–31, 2013.

[58] R. Hubacz and S. Wroński, "Horizontal Couette–Taylor flow in a two-phase gas–liquid system: flow patterns," *Experimental Thermal and Fluid Science,* vol. 28, no. 5, p. 457–466, April 2004.

[59] M. Ramezani, B. Kong, X. Gao, M. G. Olsen and R. D. Vigil, "Experimental measurement of oxygen mass transfer and bubble size distribution in an air–water multiphase Taylor–Couette vortex bioreactor," *Chemical Engineering Journal,* vol. 279, p. 286–296, 1 November 2015.

[60] M. Ramezani, M. J. Legg, A. Haghighat, Z. Li, R. D. Vigil and M. G. Olsen, "Experimental investigation of the effect of ethyl alcohol surfactant on oxygen mass transfer and bubble size distribution in an air-water multiphase Taylor-Couette vortex bioreactor," *Chemical Engineering Journal,* vol. 319, pp. 288-296, July 2017.

[61] K. W. Moser, L. G. Raguin and J. G. Georgiadis, "Tomographic study of helical modes in bifurcating Taylor-Couette-Poiseuille flow using magnetic resonance imaging," *Phys. Rev. E 64, 01631,* vol. 64, no. 1, p. 016319, 2001.

[62] S. Cerimovic, R. Beigelbeck, H. Antlinger, J. Schalko, B. Jakoby and F. Keplinger, "Viscosity and density measurements of glycerol-water mixtures utilizing a novel resonant MEMS sensor," *Proc. of SPIE* , vol. 8066, pp. 80662E-1, 2011.

[63] B. M. Baumert and S. J. Muller, "Flow visualization of the elastic Taylor-Couette instability in Boger fluids," *Rheologica Acta,* vol. 34, no. 2, p. 147–159, March 1995.

[64] A. Weisberg, I. Kevrekidis and A. Smits, "Delaying transition in Taylor–Couette flow with axial motion of the inner cylinder," *Journal of Fluid Mechanics,* vol. 348, pp. 141-151 , 1997.

[65] Y. L. Joo and E. S. Shaqfeh, "Observations of Purely Elastic Instabilities in the Taylor-Dean Flow of a Boger," *Fluid. J. Fluid Mech.,* vol. 262, no. 1, pp. 21-13, 1994.

[66] M. J. Burin, H. Ji, E. Schartman, R. C. Heitzenroeder, W. Liu, L. Morris and S. Raftopolous, "Reduction of Ekman circulation within Taylor-Couette flow," *Experiments in Fluids,* vol. 40, p. 962–966, 2006.

[67] T. T. Lim and K. S. Tan, "A Note on Power-Law Scaling in a Taylor-Couette Flow," *Phys Fluids,* vol. 16, no. 1, pp. 140-144, 2004.

[68] Q. Xiao, T. Lim and Y. Chew, "Effect of acceleration on the wavy Taylor vortex flow," *Experiments in Fluids,* vol. 32, p. 639–644, 2002.

[69] A. Brandstater and H. Swinney, "Strange attractors in weakly turbulent Couette-Taylor flow," *Physical Review A,* vol. 35, no. 5, pp. 2207-2221, 1987.

[70] S. Wereley and R. Lueptow, "Velocity field for Taylor–Couette flow with an axial flow," *Physics of Fluids,* vol. 11, no. 12, pp. 3637-3649, 1999.

[71] A. Tsameret and V. Steinberg, "Competing States in a Couette-Taylor System with an Axial Flow," *Phys Rev.,* vol. 49, pp. 4077-4086, 1994b.

[72] L. G. Raguin and J. G. Georgiadis, "Kinematics of the Stationary Helical Vortex Mode in Taylor-Couette-Poiseuille Flow," *J. Fluid Mech.,* vol. 516, pp. 125-154, 2004.

[73] E. Dumont, F. Fayolle, V. Sobolik and J. Legrand, "Wall Shear Rate in the Taylor-Couette-Poiseuille Flow at Low Axial Reynolds Number," *International Journal of Heat and Mass Transfer,* vol. 45, pp. 679-689, 2002.

[74] A. J. Youd, *Bifurcations in Forced Taylor-Couette Flow,* Thesis, 2005.

[75] S. S. Deshmukh, S. Vedantam and J. B. Joshi, "Computational Flow Modeling and Visualization in the Annular Region of Annular Centrifugal Extractor," *Ind. Eng. Chem. Res.,* vol. 25, no. 46, p. 8343–8354, June 2007.

[76] R. D. Vigil and X. Zhu, "Banded Taylor-Couette-Poiseuille Flow," in *12th Internation Couette-Taylor Workshop,* Evanston, IL, USA, 2001.

[77] H. Bala, W. Fu, Y. Guo, J. Zhao, Y. Jiang, X. Ding, K. Yu, M. Li and Z. Wang, "In Situ Preparation and Surface Modification of Barium Sulfate Nanoparticles," *Colloids and Surfaces A: Physicochem. Eng. Aspects,* vol. 274, pp. 71-76, 2006.

[78] S. H. Kang, S. G. Lee, W. M. Jung, M. C. Kim, W.-S. Kim, C. K. Choi and R. S. Feigelson, "Effect of Taylor vortices on calcium carbonate crystallization by gas–liquid reaction," *Journal of Crystal Growth*, vol. 254, no. 1–2, p. 196–205, June 2003.

[79] J. Baldyga, W. Podgorska and R. Phorecki, "Mixing-Precipitation Model with Application to Double Feed Semibatch Precipitation," *Chem. Eng. Sci.*, vol. 50, pp. 1281-1300, 1995.

[80] D. E. Fitchett and J. M. Tarbell, "Effect of Mixing on the Precipitation of Barium Sulfate in an MSMPR Reactor," *AIChE Journal*, vol. 36, no. 4, April 1990.

[81] W. S. Kim and J. M. Tarbell, "Micromixing Effects on Barium Sulfate Precipitation in a MSMPR Reactor," *Chem Eng. Commun.*, vol. 146, pp. 33-56, 1996.

[82] W. S. Kim and J. M. Tarbell, "Micromixing effects on barium sulfate precipitation in a double-jet semi batch reactor," *Chem. Eng. Commun.*, vol. 176, pp. 89-113, 1999.

[83] A. Petrova, W. Hintz and J. Tomas, "Investigation of the Precipitation of Barium Sulfate Nanoparticles," *Chem. Eng. Technol*, vol. 31, no. 4, pp. 604-608, 2008.

[84] B. Judat and M. Kind, "Morphology and Internal Structure of Barium Sulfate - Derivation of a New Growth Mechanism," *Journal of Colloid and Interface Science*, vol. 269, pp. 341-353, 2004.

[85] J. Gradl, H.-C. Schwarzer, F. Schwertfirm, M. Manhart and W. Peukert, "Precipitation of nanoparticles in a T-mixer: Coupling the particle population dynamics with hydrodynamics through direct numerical simulation," *Chem Eng and Processing*, vol. 45, pp. 908-916, 2006.

[86] G. Wu, H. Zhou and S. Zhu, "Precipitation of Barium Sulfate Nanoparticles via Impinging Streams," *Materials letters*, vol. 61, pp. 168-170, 2007.

[87] B. Pohl, R. Jamshidi, G. Brenner and U. A. Peuker, "Experimental Study of Continuous Ultrasonic Reactors for Mixing and Precipitation of Nanoparticles," *Chemical Eng Sci*, vol. 69, pp. 365-372, 2012.

[88] H.-C. Schwarzer and W. Peukert, "Combined Experimental/Numerical Study on the Precipitation of Nanoparticles," *AICHE Journal*, vol. 50, no. 12, pp. 3234-3247, 2004.

[89] A.-T. Nguyen, Y. L. Joo and W.-S. Kim, "Multiple Feeding Strategy for Phase Transformation of GMP in Continuous Couette-Taylor Cyrstallizer," *Journal of Crystal Growth & Design*, Revised (March 30, 2012).

[90] B. Judat, A. Racina and M. Kind, "Macro-and Micromixing in a Taylor-Couette Reactor with Axial Flow and their Influence on the Precipitation of Barium Sulfate," *Chemical Engineering Technology*, vol. 27, no. 3, pp. 287-292, 2004.

[91] D. L. Marchisio and A. A. Barresi, "Simulatin of Turbulent Precipitation in a Semi-batch Taylor Couette Reactor Using CFD," *AICHE Journal*, vol. 47, no. 3, pp. 664-676, 2001.

[92] F. Scargiali, A. Busciglio, F. Grisafi and A. Brucato, "On the Performance of a Taylor-Couette Reactor for Nanoparticle Precipitation," Università di Palermo, Dipartimento di Ingegneria Chimica, Viale delle Scienze ED.6, 90128 Palermo, Italy.

[93] D. I. Takeuchi and D. F. Jankowski, "A Numberical and Experimental Investigation of the Stability of Spiral Poiseuille Flow," *J. Fluid Mech*, vol. 102, pp. 101-126, 1981.

[94] D. L. Cotrell and A. J. Pearlstein, "Linear Stability of Spiral and Annular Poiseuille Flow for Small Radius Ratio," *J. Fluid Mech*, vol. 547, pp. 1-20, 2006.

[95] B. S. Ng and E. R. Turner, "On the Linear Stability of Spiral Flow between Rotating Cylinders," *Pro. R. Soc. Lond. A*, vol. 382, pp. 83-102, 1982.

[96] R. C. DiPrima and A. Pridor, "The Stability of Viscous Flow between Rotating Concentric Cylinders with Axial Flow," *Pro. R. Soc. Lond. A*, vol. 366, pp. 555-573, 1979.

[97] A.-C. Ruo, M. F. Aljishi, W.-S. Kim and Y. L. Joo, "Stability of Taylor-Couette Flow in the Presence of Axial and Circumferential Pressure Gradient," *in preparation*, 2012.

[98] S. Li, J. Xu and G. Luo, "Control of Crystal Morphology through Supersaturation Ratio and Mixing Conditions," *Journal of Crystal Growth* , vol. 304, pp. 219-224, 2007.

[99] M. Kind, "Colloidal Aspects of Precipitation Processes," *Chem Eng Sci*, vol. 57, pp. 4287-4293, 2002.

[100] L. S. Schadler, "Chapter 2. Polymer-Based and Polymer-Filled Nanocomposites," in *Nanocomposite Science and Technology*, Weinheim, Wiley-VCH Verlag GmbH & Co. KGaA, 2003, pp. 77-145.

[101] Bourgeat-Lami, Elodie, Insulaire, Mickaelle, Reculusa, Stéphane, P. Adeline, S. Ravaine and E. Duguet, "Nucleation of Polystyrene Latex Particles in the Presence of Methacryloxypropyltrimethoxysilane: Functionalized Silica Particles," *Journal of Nanoscience and Nanotechnology*, vol. 6, p. 432–444, 2006.

[102] E. P. Plueddemann, Silane Coupling Agents, New York: Plenum Press, 1991.

[103] O. Parlak and M. M. Demir, "Toward Transparent Nanocomposites Based on Polystyrene Matrix and PMMA-Grafted CeO2 Nanoparticles," *ACS Appl. Mater. Interfaces*, vol. 3, p. 4306–4314, 2011.

[104] N. Amirshaqaqi, M. Salami-Kalajahi and M. Mahdavian, "Corrosion behavior of aluminum/silica/polystyrene nanostructured hybrid flakes," *Iranian Polymer Journal*, vol. 23, no. 9, pp. 699-706, 2014.

[105] F. Bauer, H. Ernst, U. Decker, M. Findeisen, H.-J. Gläsel, H. Langguth, E. Hartmann, R. Mehnert and C. Peuker, "Preparation of scratch and abrasion resistant polymeric nanocomposites by monomer grafting onto nanoparticles, 1 FTIR and multi-nuclear NMR spectroscopy to the characterization of methacryl grafting," *Macromolecular Chemistry and Physics*, vol. 201, no. 18, p. 2654–2659, 2000.

[106] S. Gupta, P. C. Ramamurthy and G. Madras, "Covalent Grafting of Polydimethylsiloxane over Surface-Modified Alumina Nanoparticles," *Ind. Eng. Chem. Res.*, vol. 50, p. 6585–6593, 2011.

[107] H. Liu, H. Ye and Y. Zhang, "Preparation and characterization of PMMA/flaky aluminum composite particle in the presence of MPS," *Colloids and Surfaces A: Physicochemical and Engineering Aspects*, vol. 315, no. 1–3,, p. 1–6, 2008.

[108] E. Bourgeat-Lami and A. G. Ph. Espiard, "Poly(ethyl acrylate) latexes encapsulating nanoparticles of silica: 1. Functionalization and dispersion of silica," *Polymer*, vol. 36, no. 23, p. 4385–4389, 1995.

[109] C. A. Crouse, C. J. Pierce and J. E. Spowart, "Influenceing Solvent Miscibility and Aqueous stability of Aluminum Nanoparticles through Surface Functionalization with Acrylic Monomers," *ACS Appl. Mater. Interfaces*, vol. 2, no. 9, p. 2560–2569, 2010.

[110] J. P. Zhou, K. Q. Qiu and W. L. Fu, "The Surface Modification of ZnO and its Effect on the Mechanical Properties of Filled Polypropylene Composites," *Journal of Composite Materials*, vol. 39, no. 21, pp. 1931-1941, 2005.

[111] J. P. Matinlinna, L. V. Lassila and P. K. Vallittu, "The effect of five silane coupling agents on the bond strength of a luting cement to a silica-coated titanium," *dental materials,* vol. 23, p. 1173–1180, 2007.

[112] J. P. Matinlinna, M. O. zcan and L. V. Lassila, "The effect of a 3-methacryloxypropyltrimethoxysilane and vinyltriisopropoxysilane blend and tris(3-trimethoxysilylpropyl)isocyanurate on the shear bond strength of composite resin to titanium metal," *Dental Materials,* vol. 20, p. 804–813, 2004.

[113] J. P. Matinlinna, K. Laajalehto, I. K. T. Laiho, L. V. J. Lassila and P. K. Vallittu, "Surface analysis of Co–Cr–Mo alloy and Ti substrates silanized with trialkoxysilanes and silane mixtures," *SURFACE AND INTERFACE ANALYSIS,* vol. 36, p. 246–253, 2004.

[114] J. B. Z. Jovanovic, R. Jancic-Heinemann, M. Dimitrijevic and V. Miskovic-Stankovic, "Methacryloxypropyltrimethoxysilane films on aluminium: Electrochemical characteristics, adhesion and morphology," *Progress in Organic Coatings,* vol. 66, p. 393–399, 2009.

[115] P. Chaijareenont, H. Takahashi, N. Nishiyama and M. Arksornnukit, "Effect of different amounts of 3-methacryloxypropyltrimethoxysilane on the fl exural properties and wear resistance of alumina reinforced PMMA," *Dental Materials Journal,* vol. 31, no. 4, p. 623–628, 2012.

[116] J. P. Matinlinna, L. V. Lassila and J. E. Dahl, "Promotion of Adhesion Between Resin and Silica-coated Titanium by Silane Monomers and Formic Acid Catalyst," *Silicon,* vol. 2, p. 87–93, 2010.

[117] H.-I. Hsiang, Y.-L. Chang, C.-Y. Chen and F.-S. Yen, "Silane effects on the surface morphology and abrasion resistance of transparent SiO2/UV-curable resin nano-composites," *Applied Surface Science,* vol. 257, no. 8, p. 3451–3454, 2011.

[118] W. Posthumus, P. Magusin, J. Brokken-Zijp, A. Tinnemans and R. v. d. Linde, "Surface modification of oxidic nanoparticles using 3-methacryloxypropyltrimethoxysilane," *Journal of Colloid and Interface Science,* vol. 269, p. 109–116, 2004.

[119] M. R. T. Diodjo, L. B. Aragon, Y. Joliff and ‡. Lise Lanarde, "Silane Coupling Agent for Attaching Fusion-Bonded Epoxy to Steel," *ACS Applied Materials & Interfaces,* vol. 5, p. 6751−6761, 2013.

[120] M. Pantojaa, B.Diaz-Benitoa, F. Velascoa, J. Abenojara and J. d. Real, "Analysis of hydrolysis process of γ-methacryloxypropyltrimethoxysilane and its influence on the

formation of silane coatings on 6063 aluminum alloy," *Applied Surface Science,* p. 6386–6390, 2009.

[121] S.-j. Chen, "Transparent ZnO/Silicone nanocomposite film for UV shielding," National Central University Institutional Repository, Zhongli District, Taiwan, 2012.

[122] J. Matinlinna and P. Vallittu, "Silane based concepts on bonding resin composite to metals," *Journal of Contemporary Dental Practice,* vol. 8, no. 2, 2007.

[123] J. H. MacMillan, "Using Silanes as Adhesion Promoters," United Chemical Technologies, Inc., Bristol, PA, 1997.

[124] B. McMorrow, R. Chartoff, P. Lucas, W. Richardson and P. Anderson, "Particle surface treatment for nanocomposites containing ceramic particles," *Composite Interfaces,* vol. 13, no. 8-9, pp. 801-817, 2006.

[125] A. Blume, "Kinetics of the Silica-Silane Reaction," *Chemicke Listy,* vol. 105, pp. s261-s264, 2011.

[126] Z. S. Peng Liua, "Preparation and Characterization of PMMA/ZnO Nanocomposites via In-Situ Polymerization Method," *Journal of Macromolecular Science, Part B: Physics,* vol. 45, no. 1, pp. 131-138, 2006.

[127] I. Sondi, T. H. Fedynyshyn, R. Sinta and E. Matijević, "Encapsulation of Nanosized Silica by in Situ Polymerization of tert-Butyl Acrylate Monomer," *Langmuir,* vol. 16, no. 23, p. 9031–9034, 2000.

[128] S. C. J. Justin Gooding, "The molecular level modification of surfaces: from self-assembled monolayers to complex molecular assemblies," *Chem. Soc. Rev.,* vol. 40, pp. 2704-2718, 2011.

[129] M. Donleya, R. Mantz, A. Khramov, V. Balbyshev, L. Kasten and D. Gaspar, "The self-assembled nanophase particle (SNAP) process: a nanoscience approach to coatings," *Progress in Organic Coatings,* vol. 47, no. 3-4, p. 401–415, 2002.

[130] S. J. Curran and R. A. Black, "Oxygen transport and cell viability in an annular flow bioreactor: Comparison of laminar Couette and Taylor-vortex flow regimes," *Biotechnology and Bioengineering,* vol. 89, no. 7, p. 766–774 , 30 March 2005 .

[131] C. Bressy, V. G. Ngo, F. Ziarelli and A. Margaillan, "New Insights into the Adsorption of 3-(Trimethoxysilyl)propylmethacrylate on Hydroxylated ZnO Nanopowders," *Langmuir,* vol. 28, no. 6, p. 3290–3297, 2012.

[132] M. Z. Iqbal, M. S. Katsiotis, S. M. Alhassan, M. W. Liberatore and A. A. Abdala, "Effect of solvent on the uncatalyzed synthesis of aminosilane-functionalized graphene," *RSC Advances,* vol. 4, pp. 6830-6839, 2014.

[133] l. A. S. A. PradoI, M. SriyaiI, M. GhislandiI, A. Barros-TimmonsII and K. SchulteI, "Surface modification of alumina nanoparticles with silane coupling agents," *Journal of the Brazilian Chemical Society,* vol. 21, no. 12, pp. 2238-2245, 2010.

[134] A. Wang, C. Ge, H. Yin, M. Ren, Y. Zhang, Q. Zhou, Z. Wu, J. Huo, X. Li and T. Jiang, "Evolution of binary Fe2O3/SiO2 coating layers on the surfaces of aluminum flakes and the pigmentary performances," *Powder Technology,* vol. 221, p. 306–311, 2012.

[135] R. Ruggerone, V. Geiser, S. D. Vacche, Y. Leterrier and J.-A. E. Manson, "Immobilized Polymer Fraction in Hyperbranched Polymer/Silica," *Macromolecules,* vol. 43, no. 24, p. 10490–10497, 2010.

[136] W. Wanga and A. T. Dibenedettoa, "A Modified Silane Treatment for Superior Hydrolytic Stability of Glass Reinforced Composites," *The Journal of Adhesion,* vol. 68, no. 3-4, pp. 183-201, 1998.

[137] M. Arksornnukit, H. Takahashi and N. Nishiyama, "Effects of Silane Coupling Agent Amount on Mechanical Properties and Hydrolytic Durability of Composite Resin After Hot Water Storage," *Dental Materials Journal,* vol. 23, no. 1, pp. 31-36, 2004.

[138] T. Miyasaka, "Effect of Shape and Size of Silanated Fillers on Mechanical Properties of Experimental Photo Cure Composite Resins," *Dental Materials Journal,* vol. 15, no. 2, pp. 98-110, 1996.

[139] E. Tanga, B. Tian, E. Zheng, C. Fub and G. Cheng, "Preparation of zinc oxide nanoparticle via uniform precipitation method and its surface modification by methacryloxypropyltrimethoxysilane," *Chemical Engineering Communications,* vol. 195, no. 5, pp. 479-491, 2008.

[140] G. D. Combe, "Breakup of polystyrene particles in turbulent Taylor-Couette flow: Vallidation of a DNS model for asphaltene agglomeration," Delft University of Technology, 2013.

[141] M. F. Aljishi, M. Jhalaria and Y. L. Joo, "Development of Continuous Scalable Process for Production of Functionalized Metal Fillers via Taylor Couette Reactors," *(to be published),* 2016.

[142] S. Sheikh, "Antifouling and Antithrombogenic Ultrathin Surface Chemistry for Bioanalytical and Biomedical Applications," University of Toronto, Toronto, 2014.

[143] P. A. Heiney, K. Grüneberg and J. Fang, "Structure and Growth of Chromophore-Functionalized (3-Aminopropyl)triethoxysilane Self-Assembled on Silicon," *Langmuir,* vol. 16, no. 6, p. 2651–2657, 2000.

[144] E. H. W. A. V. Davydov, A. Motayed, S. G. Sundaresan, P. B. L. J. Richter, G. Stan, K. Steffens, R. Zangmeister, J. A. Schreifels and M. V. Raoc, "Immobilization of streptavidin on 4H–SiC for biosensor development," *Applied Surface Science,* vol. 258, p. 6056–6063, 2012.

[145] G. Mondin, "Functionalization of particles and selective functionalization of surfaces for the electroless metal plating process," Technical University Dresden, Technical University Dresden, 2014.

[146] Y. Nakamura, R. Yamazaki, K. Shitajima, N. Karyu and S. Fujii, "Aspects of Interfacial Structure of Silane Coupling Agents in Particulate-Filled Polymer Composites and the Reinforcement Effect: A Critical Review," *Reviews of Adhesion and Adhesives,,* vol. 3, no. 2, pp. 188-215, 2015.

[147] H. I. Noriyuki Suzuki, "A review on the structure and characterization techniques of Silane/Matrix Interphases," *MACROMOLECULAR SYMPOSIA,* vol. 108, pp. 19-53, 1996.

[148] R. H. Halvorson, R. L. Erickson and C. L. Davidson, "The effect of filler and silane content on conversion of resin-based composite," *Dental Materials,* vol. 19, no. 4, p. 327–333, 2003.

[149] G. Kickelbick, "Concepts for the incorporation of inorganic building blocks into organic polymers on a nanoscale," *Progress in Polymer Science,* vol. 28, no. 1, p. 83–114, 2003.

[150] Ying-Sing Li, N. E. Vecchio, Y. Wang and C. McNutt, "Vibrational spectra of metals treated with allyltrimethoxysilane sol–gel and self-assembled monolayer of allytrichlorosilane," *Spectrochimica Acta Part A,* vol. 67, p. 598–603, 2007.

[151] J. S. J. P. S. Valliappan, "Reactivity of aluminum nanopowders with metal oxides," *Powder Technology,* vol. 156, no. 2–3, p. 164–169, 2005.

[152] G. W. MM Demir, "Challenges in the preparation of optical polymer composites with nanosized pigment particles: a review on recent efforts," *Macromolecular Materials and Engineering,* vol. 297, p. 838–863, 2012.

[153] A. Sachse, V. Hulea, B. C. A. Finiels, F. Fajula and A. Galarneau, "Alumina-grafted macro-/mesoporous silica monoliths as continuous flow microreactors for the Diels–Alder reaction," *Journal of Catalysis,* vol. 287, p. 62–67, 2012.

[154] C. V. ,. T. B. Magnus Rueping, "Continuous Flow Organocatalytic C–H Functionalization and Cross-Dehydrogenative Coupling Reactions: Visible Light Organophotocatalysis for Multicomponent Reactions and C–C, C–P Bond Formations," *ACS Catalysis,* vol. 3 , no. 7, p. 1676–1680, 2013.

[155] M. Puska, L. Lassila, P. K. Vallittu, J. Seppälä and J. Matinlinn, "Evaluation of bis-GMA/MMA Resin Adhesion to Silica-Coated and Silanized Titanium," *Journal of Adhesion Science and Technology,* vol. 23, p. 991–1006, 2009.

[156] E. I. M. Vasilica Popescu, "Performances of Chitosan Grafted onto Surface of Polyacrylonitrile Functionalized through Amination Reactions," *Ind. Eng. Chem. Res.,* vol. 52 , no. 37, p. 13252–13263, 2013.

[157] J. B. Bajat, I. Milosev, Z. Jovanovic and V. B. Miskovic-Stankovic, "Studies on adhesion characteristics and corrosion behaviour of vinyltriethoxysilane/epoxy coating protective system on aluminium," *Applied Surface Science,* p. 3508–3517, 2010.

[158] L. Armelao, S. Gross, K. Muller, G. Pace, E. Tondello, O. Tsetsgee and A. Zattin, "Structural Evolution upon Thermal Heating of NanostructuredInorganic-Organic Hybrid Materials to Binary Oxides MO2-SiO2(M) Hf, Zr) as Evaluated by Solid-State NMR and FTIRSpectroscopy," *Chem. Mater.,* vol. 18, pp. 6019-6030, 2006.

[159] J. Luo, J. Lannutti and R. Seghi, "Solid-state NMR evaluation of the silane structure on nanoporous silica fillers," *Journal of Adhesion Science,* vol. 15, no. 3, p. 267–277, 2001.

[160] M. Oaten and N. R. Choudhury, "Silsesquioxane−Urethane Hybrid for Thin Film Applications," *Macromolecules,* vol. 38, no. 15, p. 6392–6401, 2005.

[161] G. B. ,. A. T. D. W. C. Selomulya, "Aggregation Mechanisms of Latex of Different Particle Sizes in a Controlled Shear Environment," *Langmuir,* vol. 18 , no. 6, p. 1974–1984, 2002.

[162] L. J. Forney, Z. Ye and A. Giorges, "Fast Competitive Reactions in Taylor-Couette Flow," *Ind. Eng. Chem. Res.,* vol. 44, pp. 7306-7312, 2005.

[163] O. Richter, H. Hoffmann and B. Kraushaar-Czarnetzki, "Effect of the rotor shape on the mixing characteristics of a continuous flow Taylor-vortex reactor," *Chemical Engineering Science,* vol. 63, no. 13, pp. 3504-3513, 2008.

[164] Q. Chang, Y. Mao, L. Zeng and C. Yu, "Flocculation Efficiency in Taylor-Couette Flow," *Journal of Materials Science and Chemical Engineering,* vol. 4, pp. 1-7, 2016.

[165] F.-C. Yu, N. Phalak, Z. Sun and L.-S. Fan, "Activation Strategies for Calcium-Based Sorbents for CO2 Capture: A Perspective," *Ind. Eng. Chem. Res.,* vol. 51, no. 4, p. 2133–2142, 2012.

[166] O. A. Jimoh, K. S. Ariffin, H. B. Hussin and A. E. Temitope, "Synthesis of precipitated calcium carbonate: a review," *Carbonates Evaporites,* no. 1-16, 2017.

[167] T. Jung, W.-S. Kim and C. K. Choi, "Effect of Nonstoichiometry on Reaction Crystallization of Calcium Carbonate in a Couette−Taylor Reactor," *Crystal Growth & Design,* vol. 4, no. 3, p. 491–495, 2004.

[168] D. W. Donigian, R. K. Resnik and M. G. McFadden, "Ink jet recording paper incorporating novel precipitated calcium carbonate pigment". United States Patent US5643631 A, 1 1997 July.

[169] H. Gupta and L.-S. Fan, "Carbonation−Calcination Cycle Using High Reactivity Calcium Oxide for Carbon Dioxide Separation from Flue Gas," *Ind. Eng. Chem. Res.,* vol. 41, no. 16, p. 4035–4042, 2002.

[170] R. Agnihotri, S. K. Mahuli, S. S. Chauk and L.-S. Fan, "Influence of Surface Modifiers on the Structure of Precipitated Calcium Carbonate," *Ind. Eng. Chem. Res.,* vol. 6, no. 38, p. 2283–2291, 1999.

[171] J.-H. Bang, Y. N. J. o. Kim, K. S. Song, h. W. Jeon, S. C. Chae, S.-W. Lee, S.-J. Park and M. G. Lee, "Specific surface area and particle size of calcium carbonate precipitated

by carbon dioxide microbubbles," *Chemical Engineering Journal,* vol. 198–199, p. 254–260, August 2012.

[172] P. A. Gane, J. Schölkopf, D. Gantenbein and D. E. Gerard, "Surface-reacted calcium carbonate and its use in waste water treatment". United States Patent US20140209831 A1, 31 July 2014.

[173] X. Guo, L. Liu, W. Wang, J. Zhang, Y. Wang and S.-H. Yu, "Controlled crystallization of hierarchical and porous calcium carbonate crystals using polypeptide type block copolymer as crystal growth modifier in a mixed solution†," *CrystEngComm,* vol. 13, pp. 2054-2061, 2011.

[174] J.-H. Yang, S.-M. Shih, C.-I. Wu and C. Y.-D. Tai, "Preparation of high surface area CaCO3 for SO2 removal by absorption of CO2 in aqueous suspensions of Ca(OH)2," *Powder Technology,* vol. 202, no. 1-3, p. 101–110, October 2010.

[175] S.-H. Wei, S. K. Mahuli, R. Agnihotri and L.-S. Fan, "High Surface Area Calcium Carbonate: Pore Structural Properties and Sulfation Characteristics," *Ind. Eng. Chem. Res.,* vol. 6, no. 36, p. 2141–2148, 1997.

[176] L. Xiang, Y. Xiang, Z. Wang and Y. Jin, "Influence of chemical additives on the formation of super-fine calcium carbonate," *Powder Technology,* vol. 126, no. 2, p. 129–133, July 2002.

[177] S. K. M. Rajeev Parmar, "Microbubble generation and microbubble-aided transport process intensification—A state-of-the-art report," *Chemical Engineering and Processing: Process Intensification,* vol. 64, p. 79–97, February 2013.

[178] J.-H. Bang, Y. N. Jang, W. Kim, K. S. Song, C. W. Jeon, S. C. Chae, S.-W. Lee, S.-J. Park and M. G. Lee, "Precipitation of calcium carbonate by carbon dioxide microbubbles," *Chemical Engineering Journal,* vol. 174, no. 1, p. 413–420, October 2011.

[179] M. Matsumoto, T. Fukunaga and K. Onoe, "Polymorph control of calcium carbonate by reactive crystallization using microbubble technique," *Chemical Engineering Research and Design,* vol. Volume 88, no. 12, p. 1624–1630, December 2010.

[180] J.-H. Bang, K. Song, S. Park, C. W. Jeon, S.-W. Lee and W. Kim, "Effects of CO2 Bubble Size, CO2 Flow Rate and Calcium Source on the Size and Specific Surface Area of CaCO3 Particles," *Energies,* vol. 8, no. 10, pp. 12304-12313, 2015.

[181] K. Wang, Y. J. Wang, G. G. Chen, G. S. Luo and J. D. Wang, "Enhancement of Mixing and Mass Transfer Performance with a Microstructure Minireactor for Controllable Preparation of CaCO3 Nanoparticles," *Ind. Eng. Chem. Res.*, vol. 46, no. 19, p. 6092–6098, 2007.

[182] K. Kędra-Królik and P. Gierycz, "Precipitation of nanostructured calcite in a controlled multiphase process," *Journal of Crystal Growth*, vol. 311, p. 3674–3681, 2009.

[183] K. Majerczak and P. Gierycz, "Analysis and simulation of monodispersed, nanostructured calcite obtained in a controlled multiphase process," *Nanomaterials and Nanotechnology*, vol. 6, p. 1–9, 2016.

[184] M. Wszelaka-Rylik, K. Piotrowska and P. Gierycz, "Simulation, aggregation and thermal analysis of nanostructured calcite obtained in a controlled multiphase process," *Journal of Thermal Analysis and Calorimetry*, vol. 119, no. 2, p. 1323–1338, February 2015.

[185] S. Sonawane, S. Shirsath, P. Khanna, S. Pawar, C. Mahajan, V. Paithankar, V. Shinde and C. Kapadnisa, "An innovative method for effective micro-mixing of CO2 gas during synthesisof nano-calcite crystal using sonochemical carbonization," *Chemical Engineering Journal*, vol. 143, p. 308–313, 2008.

[186] S. Shirsath, S. Sonawane, D. Saini and A. Pandit, "Continuous precipitation of calcium carbonate using sonochemical reactor," *Ultrasonics Sonochemistry*, vol. 24 , p. 132–139, 2015.

[187] G. Trippa and R. Jachuck, "Process Intensification: Precipitation of Calcium Carbonate Using Narrow Channel Reactors," *Chemical Engineering Research and Design*, vol. 81, no. 7, pp. 766-772, August 2003.

[188] Y. Liang, G. Chu, J. Wang, Y. Huang, J. Chen, B. Sun and L. Shao, "Controllable preparation of nano-CaCO3 in a microporous tube-in-tube microchannel reactor," *Chemical Engineering and Processing: Process Intensification*, vol. 79, p. 34–39, May 2014.

[189] B. Feng, A. K. Yong and H. An, "Effect of various factors on the particle size of calcium carbonate formed in a precipitation process," *Materials Science and Engineering A*, vol. 170–179, p. 445–446, 2007.

[190] J. Kuusisto, T. Tiittanen and T. C. Maloney, "Property optimization of calcium carbonate precipitated in a high shear, circulation reactor," *Powder Technology,* vol. 303, p. 241–250, December 2016.

[191] H. Casanova and L. P. Higuita, "Synthesis of calcium carbonate nanoparticles by reactive precipitation using a high pressure jet homogenizer," *Chemical Engineering Journal,* vol. 175, p. 569–578, November 2011.

[192] D. Gómez-Díaz, J. M. Navaza and B. Sanjurjo, "Analysis of mass transfer in the precipitation process of calcium carbonate using a gas/liquid reaction," *Chemical Engineering Journal,* vol. 116, no. 3, p. 203–209, March 2006.

[193] S. G. Lee, W. M. Jung, W.-S. Kim and C. K. Choi, "Gas-Liquid Reaction Precipitation of Calcium Carbonate in MSMPR and Couette-Taylor Reactors," *Journal of the Korean Institute of Chemical Engineers,* vol. 38, no. 1, pp. 67-74, 2000.

[194] W.-S. Kim, "Application of Taylor Vortex to Crystallization," *Journal of Chemical Engineerign of Japan,* vol. 47, no. 2, pp. 115-123, 2014.

[195] T. Jung, W.-S. Kim and C. K. Choi, "Effect of monovalent salts on morphology of calcium carbonate crystallized in Couette-Taylor reactor," *Crystal Research and Technology,* vol. 40, no. 6, p. 586–592, June 2005.

[196] W.-M. Jung, S. H. Kang, K.-S. Kim, W.-S. Kim and C. K. Choi, "Precipitation of calcium carbonate particles by gas–liquid reaction: Morphology and size distribution of particles in Couette-Taylor and stirred tank reactors," *Journal of Crystal Growth,* vol. 312, no. 22, p. 3331–3339, November 2010.

[197] E. Dluska, S. Wronski and T. Ryszczuk, "Interfacial area in gas–liquid Couette–Taylor flow reactor," *Experimental Thermal and Fluid Science,* vol. 28, p. 467–472, 2004.

[198] E. Dłuska, S. Wroński and R. Hubacz, "Mass transfer in gas–liquid Couette–Taylor flow reactor," *Chemical Engineering Science,* vol. 56, no. 3, p. 1131–1136, February 2001,.

[199] S. Wronski, E. Dluska, R. Hubacz and E. Molga, "Mass transfer in gas-liquid Couette-Taylor flow in membrane reactor," *Chemical Engineering Science,* vol. 54, pp. 2963-2967, 1999.

[200] I. T. Pineda and Y. T. Kang, "CO2 absorption enhancement by nanoabsorbents in Taylor–Couette absrober," *International Journal of Heat and Mass Transfer,* vol. 100, p. 39–47, 2016.

[201] J.-M. Kim, S.-M. Chang, J. H. Chang and W.-S. Kim, "Agglomeration of nickel/cobalt/manganese hydroxide crystalsin Couette–Taylor crystallizer," *Colloids and Surfaces A: Physicochemical andEngineering Aspects,* vol. 384 , p. 31– 39, 2011.

[202] E. Dluska and S. Wronski, "Mass Transfer Modelling in the Couette-Taylor Flow Reactor for the Oxidation Process of Organic Contaminants," in *Environmental Engineering Studies*, Boston, MA, Springer, 2003, pp. 43-52.

[203] X. Gao, B. Kong and R. D. Vigil, "CFD investigation of bubble effects on Taylor–Couette flow patterns in the weakly turbulent vortex regime," *Chemical Engineering Journal*, no. 270, p. 508–518, 2015.

[204] L. Xiang, Y. Xiang, Y. Wen and F. Wei, "Formation of CaCO3 nanoparticles in the presence of terpineol," *Materials Letters,* vol. 58 , p. 959– 965, 2004.

[205] K. Kędra-Królik and P. Gierycz, "Obtaining calcium carbonate in a multiphase system by the use of new rotating disc precipitation reactor," *Journal of Thermal Analysis and Calorimetry*, vol. 83, no. 3, pp. 579-582, 2006.

[206] S. Yamanaka, Y. Sugawara, T. Oiso, T. Fujimoto, Y. Ohira and Y. Kuga, "Phase transformation of mesoporous calcium carbonate by mechanical stirring," *CrystEngComm*, vol. 17, no. 8, pp. 1773-1777, 28 February 2015.

[207] J. Kontrec, M. Ukrainczyk, L. Brečević and D. Kralj, "Precipitation of mesoporous nanosized calcium carbonate," in *18th International Symposium on Industrial Crystallization*, Zurich - Switzerland, September, 2011.

[208] M. Ukrainczyk, J. Kontrec, V. Babić-Ivančić, L. Brečević and D. Kralj, "Experimental design approach to calcium carbonate precipitation in a semicontinuous process," *Powder Technology*, vol. 171 , p. 192–199, 2007.

[209] M. Polli, M. D. Stanislao, R. Bagatin, E. A. Bakr and M. Masi, "Bubble size distribution in the sparger region of bubble columns," *Chemical Engineering Science,* vol. 57, no. 1, p. 197–205, January 2002.

[210] A. García-Abuín, D. Gómez-Díaz, J. M. Navaza and I. Vidal-Tato, "CO2 capture by aqueous solutions of glucosamine in a bubble column reactor," *Chemical Engineering Journal,* vol. 162, no. 1, p. 37–42, August 2010.

[211] X. Gao, B. Kong and R. D. Vigil, "CFD simulation of bubbly turbulent Tayor–Couette flow," *Chinese Journal of Chemical Engineering,* vol. 24, no. 6, p. 719–727, June 2016.

[212] X. Gao, B. Kong, M. Ramezani, M. G. Olsen and R. D. Vigil, "An adaptive model for gas–liquid mass transfer in a Taylor vortex reactor," *International Journal of Heat and Mass Transfer,* vol. 1, p. 433–445, 2015.

[213] B. J. Azzopardi, "Sauter Mean Diameter," Thermopedia, February 2011.

[214] D. P. M. v. Gilsz, D. N. Guzman, C. Suny and D. Lohsey, "The importance of bubble deformability forstrong drag reduction in bubbly turbulent Taylor-Couette flow," *J. Fluid Mech.,* vol. 722, pp. 317-347, 2013.

[215] Y. Murai, "Frictional drag reduction by bubble injection," *Exp Fluids,* vol. 1773, no. 55, pp. 1-28, 2014.

[216] Y. Shiomi, H. Kutsuna, K. Akagawa and M. Ozawa, "Two-phase flow in an annulus with a rotating inner cylinder (flow pattern in bubbly flow region)," *Nuclear Engineering and Design,* vol. 141, no. 1-2, pp. 27-34, 2 June 1993.

[217] R. Maryami, S. Farahat, M. J. poor and M. H. S. Mayam, "Bubbly drag reduction in a vertical Couette–Taylor system with superimposed axial flow," *The Japan Society of Fluid Mechanics - Fluid Dyn. Res.,* vol. 46 , no. 055504 , 2014.

[218] K. Atkhen, J. Fontaine and J. E. Wesfreid, "Highly turbulent Couette-Taylor bubbly flow patterns," *J. Fluid Mech.,* vol. 422, pp. 55-68, 2000.

[219] H. Robert, "Classification of flow regimes in gas-liquid horizontal Couette-Taylor flow using dimensionless criteria," *Journal of Hydrodynamics,* vol. 27, no. 5, pp. 773-781, 2015.

[220] R.-y. Lin, J.-y. Zhang and Y.-q. Bai, "Mass transfer of reactive crystallization in synthesizing calcite nanocrystal," *Chemical Engineering Science,* vol. 61, p. 7019 – 7028, 2006.

[221] S. Lowell and J. E. Shields, Powder Surface Area and Porosity, London, New York : Chapman and Hall, 1991.

[222] V. Manovic and E. J. Anthony, "Sequential SO2/CO2 capture enhanced by steam reactivation of a CaO-based sorbent," *Fuel,* vol. 87, no. 8–9, p. 1564–1573, July 2008.

[223] J. H. Zou, Z. J. Zhou, F. C. Wang, W. Zhang, Z. H. Dai, H. F. Liu and Z. H. Yu, "Modeling reaction kinetics of petroleum coke gasification with CO2," *Chemical Engineering and Processing: Process Intensification,* vol. 46, no. 7, p. 630–636, July 2007.

[224] S. Kakaraniya, A. Gupta and A. Mehra, "Reactive Precipitation in Gas-Slurry Systems: The CO2−Ca(OH)2−CaCO3 System," *Ind. Eng. Chem. Res.*, vol. 46, no. 10, p. 3170–3179, 2007.

[225] D. R. Y. Kiho Park, "Modeling and Simulation for Feasibility Study of Taylor-Couette Crystallizer asCrystal Seed Manufacturing System," in *9th International Symposium on Advanced Control of Chemical Processes, The International Federation of Automatic Control*, Whistler, British Columbia, Canada, June 7-10, 2015.

[226] P. Ghosh, "Interfacial Reactions (Part III)," NPTEL - Chemical Engineering - Interfacial Engineering, IIT Guwahati - India, 2014.

[227] M. Schnebelen, M. Ricaud, A. Jakob, D. Sy, E. Plasari and H. Muhr, "Determination of Crystallization Kinetics and Size Distribution Parameters of Agglomerated Calcium Carbonate Nanoparticles during the Carbonation of a Suspension of Lime," *Crystal Structure Theory and Applications,* vol. 4, pp. 16-27, 2015.

[228] D. G. Leaist, P. Anderson and J. C. Elliott, "Diffusion Coefficients for the Ternary System Ca(OH)2-H,P04-Water," *Journal of the Chemical Society, Faraday Transactions,* vol. 86, no. 18, pp. 3093-3095, 1990.

[229] M. Olivares-Marín, E. Cuerda-Correa, A. Nieto-Sánchez, S. García, C. Pevida and S. Román, "Influence of morphology, porosity and crystal structure of CaCO3 precursors on the CO2 capture performance of CaO-derived sorbents," *Chemical Engineering Journal,* vol. 217, p. 71–81, 1 February 2013.

[230] M. Nieves-Remacha José, A. A. Kulkarni and K. F. Jensen, "Gas–Liquid Flow and Mass Transfer in an Advanced-Flow Reactor," *Ind. Eng. Chem. Res.*, vol. 52, no. 26, p. 8996–9010, 2013.

[231] X. Gao, B. Kong and R. D. Vigil, "Characteristic time scales of mixing, mass transfer and biomass growth in a Taylor vortex algal photobioreactor," *Bioresource Technology,* vol. 198, pp. 283-291, 2015.

[232] K. Ymawaki, H. Hosoi, T. Takigawa, M. N. Noui-Mehidi and N. Ohmura, "Gas-Liquid Two-Phase Flow in a Taylor Vortex Flow Reactor," in *ICheaP-8: the 8th Italian Conference on Chemical and Process Engineering*, Ischia Island, Naples, Italy, June 24-27, 2007.

[233] J. Dirksen and T. Ring, "Fundamentals of crystallization: Kinetic effects on particle size distributions and morphology," *Chemical Engineering Science,* vol. 46, no. 10, pp. 2389-2427, 1991.

[234] J. Elhajj, M. Al-Hindi and F. Azizi, "A Review of the Absorption and Desorption Processes of Carbon," *Industrial & Engineering Chemistry Research,* vol. 53, p. 2−22, 2014.

[235] M. K. H. Al-Mashhadani, H. C. H. Bandulasena and W. B. Zimmerman, "CO2 Mass Transfer Induced through an Airlift Loop by a Microbubble Cloud Generated by Fluidic Oscillation," *Industrial & Engineering Chemistry Research,* vol. 51, p. 1864–1877, 2012.

[236] L. Schultz, M.P.Andersson, K.N.Dalby, D.Muter, D.V.Okhrimenk, H. F. and S.L.S.Stipp, "High surface area calcite," *Journal of Crystal Growth,* vol. 371, p. 34–38, 2013.

[237] J. Fagerlund, "Carbonation of Mg(OH)2 in a pressurised fluidised bed for CO2 sequestration," Thermal and Flow Engineering Laboratory Department of Chemical Engineering Division for Natural Sciences and Technology Åbo Akademi University, Turku, Finland , 2012.

[238] M. Meeuwse, J. v. d. Schaaf and J. C. Schouten, "Multistage rotor-stator spinning disc reactor," *AICHE Journal,* vol. 58, no. 1, p. 247–255, 2012 .

[239] E. Aksamija, C. Weinländer, R. Sarzio and M. Siebenhofer, "The Taylor-Couette Disc Contactor: A Novel Apparatus for Liquid/Liquid Extraction," *Separation Science and Technology*, vol. 50, no. 18, pp. 2844-2852, 2015 .

[240] S. Vedantam, K. E.Wardle, T. V. Tamhane, V. V. Ranade and J. B. Joshi, "CFD Simulation of Annular Centrifugal Extractors," *International Journal of Chemical Engineering,* vol. 12, pp. 1-31, 2012.

[241] A. Racina, M. Pozarnik and M. Kind, "Experimental Investigations of Flow and Mixing in Taylor-Couette Reactor using PIV and LIF Methods," *International Journal of Dynamics of Fluids,* vol. 1, no. 1, pp. 37-55, 2005.

[242] D. Konopacka-Łyskawa, B. Kos´cielska and J. Karczewski, "Controlling the size and morphology of precipitated calcite particles by the selection of solvent composition," *Journal of Crystal Growth,* vol. 478, p. 102–110, 2017.

[243] D. Konopacka-Łyskawa, B. K. and J. Karczewski, "Effect of some organic solvent–water mixtures composition on precipitated calcium carbonate in carbonation process," *Journal of Crystal Growth,* vol. 418, pp. 25-31, 2015.

[244] A. J.Nieto-Sanchez, M. Olivares-Marin, SusanaGarcia, C. Pevida and E. M.Cuerda-Correaa, "Influence of the operation conditions on CO2 capture by CaO-derived sorbents prepared from synthetic CaCO3," *Chemosphere,* vol. 93, no. 9, pp. 2148-2158, November 2013.

[245] E. M. Flaten, M. Seiersten and J.-P. Andreassen, " Polymorphism and morphology of calcium carbonate precipitated in mixed solvents of ethylene glycol and water," *Journal of Crystal Growth, Volume,* vol. 311, no. 13, pp. 3533 - 3538, 2009.

[246] Q. Lia, Y. Dingb, F. Li, B. Xie and Y. Qian, "Solvothermal growth of vaterite in the presence of ethylene glycol, 1,2-propanediol and glycerin," *Journal of Crystal Growth,* vol. 236 , p. 357–362, 2002.

[247] J. R. Sanderson, W. A. Smith, E. T. Marquis and Kenneth P. Keating, "PURIFICATION OF PROPYLENE OXIDE BY TREATMENT WITH CALCUM HYDROXDE ENGLYCEROL OR SUGAR WATER". Texas, USA Patent 4,691,034, 1 Sept. 1987.

[248] J. Y. Kim, J. Choi, J. W. Namgoong, S. H. Kim, C. Sakong, S. B. Yuk, S.-a. Choi, W. Lee and J. P. Kim, "Synthesis and characterization of novel perylene dyes with new substituents at terminal-position as colorants for LCD color filter," *J Incl Phenom Macrocycl Chem,* vol. 82, p. 203–212, 2015.

[249] C. Yoon, H.-S. Kwon, J.-S. Yoo, H.-Y. Lee, J.-H. Bae and J.-H. Choi, "Preparation of thermally stable dyes derived from diketopyrrolopyrrole pigment by polymerisation with polyisocyanate binder," *Coloration Technology,* vol. 131, pp. 2-8, 2015.

[250] C.-H. Chen and W.-T. Cheng, "Fabrication and Characterization of Color Photosensitive Organic Compounds based on Copper Phthalocyanine having Acryloyl Group," *Journal of Photopolymer Science and Technology,* vol. 25, no. 4, pp. 409-413, 2012.

[251] G. E. Morsea, A. S. Patona, A. Loughb and T. P. Bender, "Chloro boron subphthalocyanine and its derivatives: dyes, pigments or somewhere in between?," *Dalton Trans.*, vol. 39, pp. 3915-3922, 2010.

[252] S. Ogawa, Y. Iwashita, S. Funakura, I. Oshiumi and K. Shimada, "Liquid crystal display device". Japan Patent US9441158B2, 13 Sept 2016.

Appendix A

8.1 Influence of Reactor Configuration on Calcium Carbonate Precipitation

Comparison of precipitation in CSTR and Taylor Couette reactor revealed that particles produced under Taylor Couette flow tend to be much smaller with finer morphologies and more uniform size distribution, as displayed in Figure 8.1.1 and Figure 8.1.3. Changing the geometry of the reactor to a narrower gap induced further control over the crystal growth processes, leading to the formation of smaller crystals, as displayed in Figure 8.1.5. Increasing the flowrate of the CO_2 feed into the reactor led to higher local supersaturation, which resulted in significant increase in nucleation rate. This was reflected in the reduction in particle size of PCC, as displayed in Figure 8.1.6. The BET surface area of PCC as well as the pore volume are more than doubled when formed under Taylor Couette flow than that of particles formed in CSTR configuration. This was especially true for the case of higher CO_2 flowrates, as displayed in Figure 8.1.7.

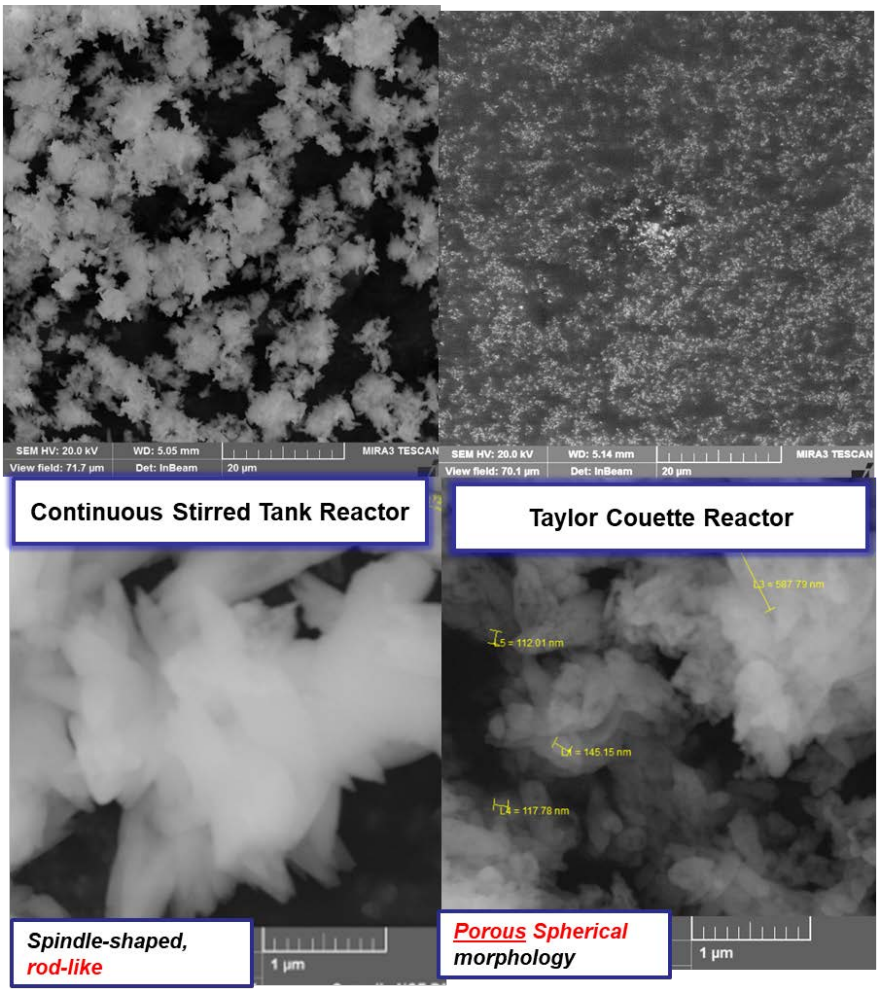

Figure 8.1.1 Particle morphology PCC formed under 800 RPM in CSTR and TCR with Large Gap r_1/r_2~0.8.

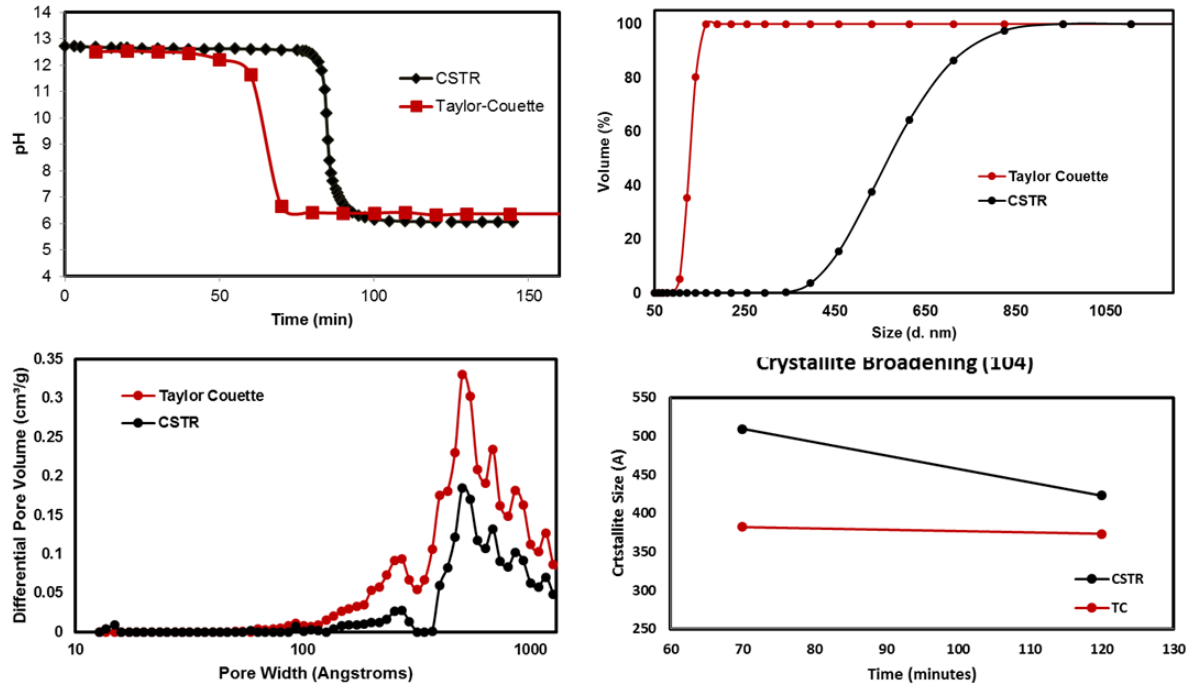

	Taylor Couette	CSTR
BET Surface Area (m²/g)	15.7	8.1
Cumulative Pore Volume (cm³/g)	0.15	0.07
Adsorption average pore width (Å)	378	333

Figure 8.1.2 Properties of PCC formed under 800 RPM in CSTR and TCR with Large Gap r_1/r_2~0.8.

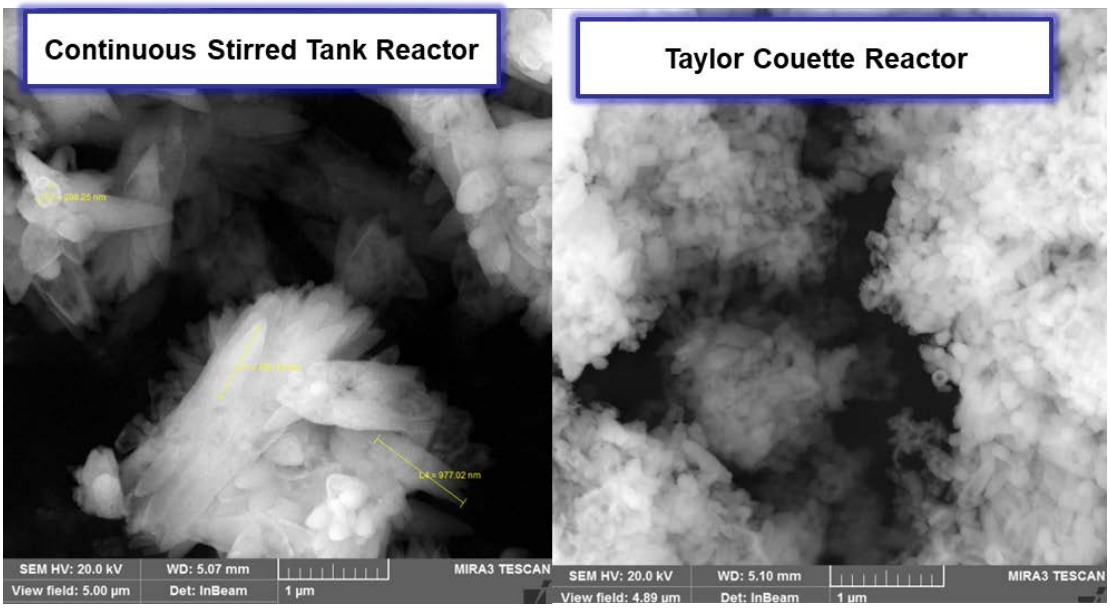

Figure 8.1.3 Particle morphology PCC formed under in TCR at 800 RPM with narrower Gap r_1/r_2~0.9.

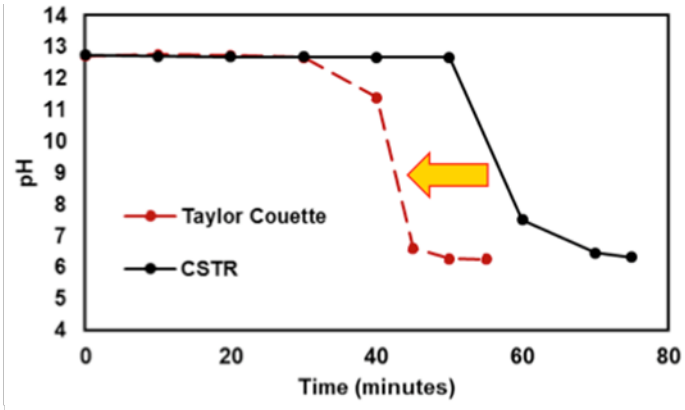

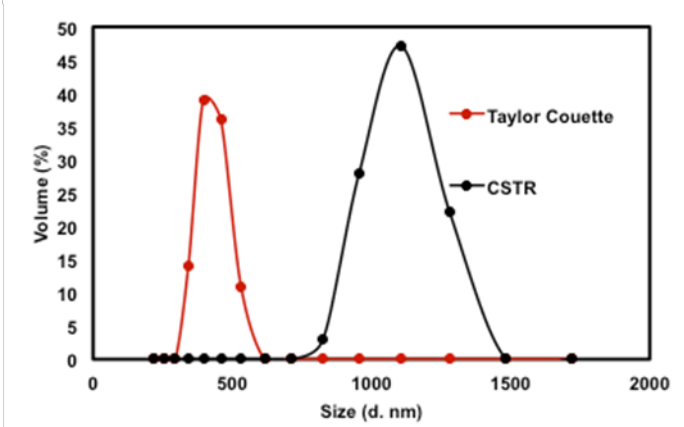

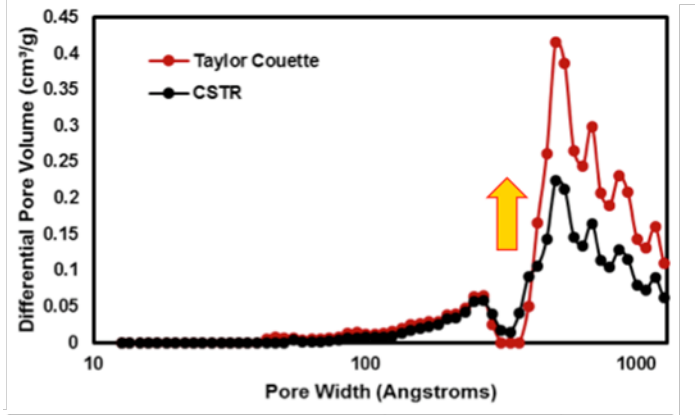

	Taylor Couette	CSTR
BET Surface Area (m²/g)	19.3	9.6
Cumulative Pore Volume (cm³/g)	0.16	0.09
Adsorption average pore width (Å)	325	389

Figure 8.1.4 Properties of PCC formed under 800 RPM in CSTR and TCR with Large Gap r_1/r_2~0.9.

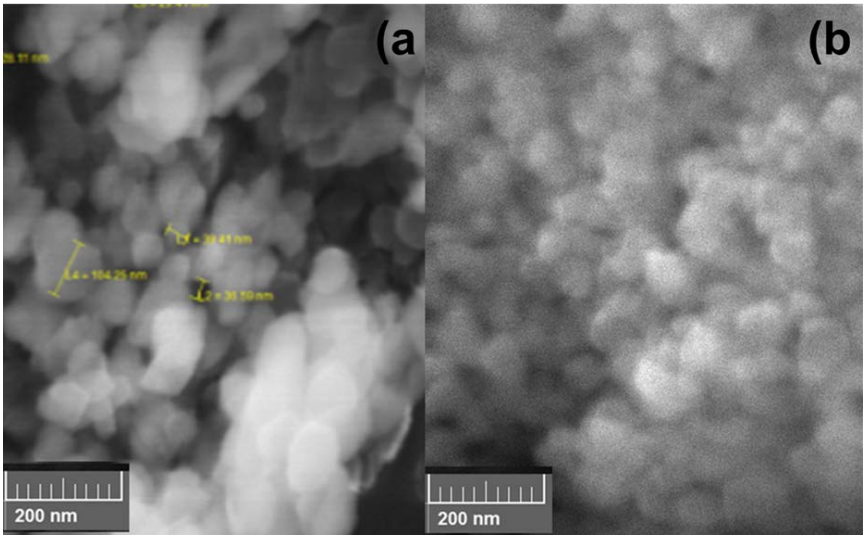

Figure 8.1.5 Particle morphology for PCC formed in TCR under configuration of a) Large Gap r_1/r_2~0.8 and b) narrower gap r_1/r_2~0.8 at 800RPM.

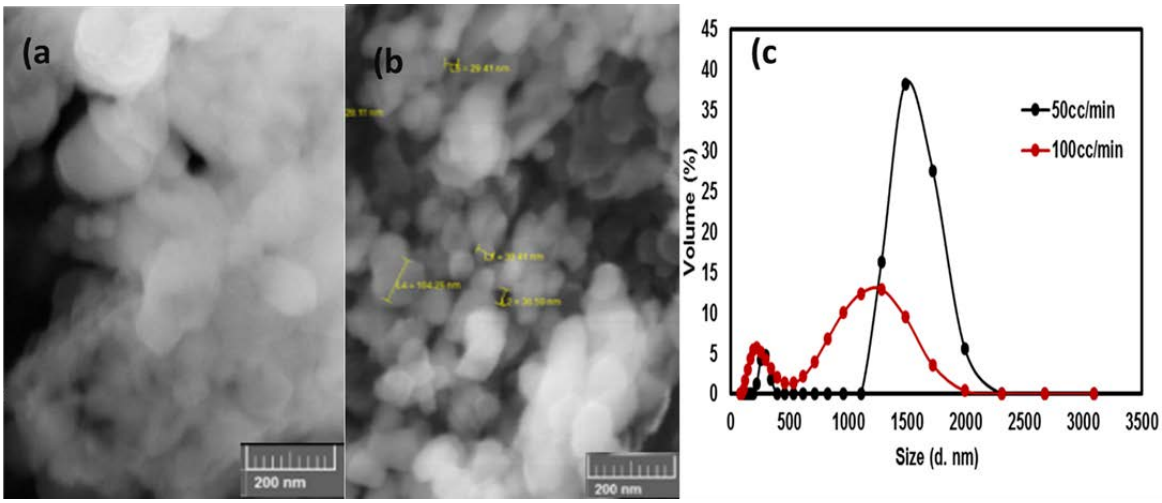

Figure 8.1.6 Change in PCC particle morphology and size with increasing CO_2 flowrates at 800RPM.

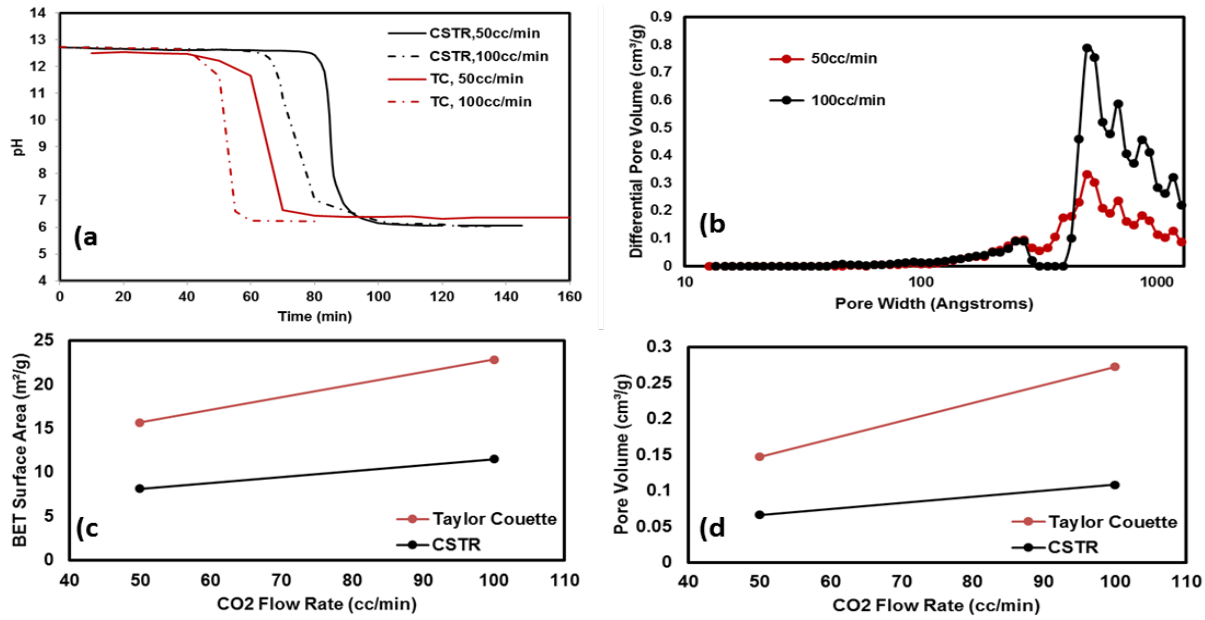

Figure 8.1.7 Change in properties of PCC with increasing CO_2 flowrates at 800RPM.

Appendix B

8.2 Controlling Particle Morphology with Glycerol

Solvent composition is among the factors that can play an important role in tailoring the specific characteristics of PCC particles. The addition of organic solvents modifies the viscosity of aqueous solutions, changes the rate of carbon dioxide absorption, solubility and diffusivity [242]. In particular, not only does the concentration of carbonate ions in the liquid phase changes, but also the solubility of $Ca(OH)_2$ and $CaCO_3$ [243]. When the three OH groups, which are considered to be the surface active molecules of glycerol, arrange themselves parallel to the hydrophilic surface of calcite particles, they can form a well-organized monolayer that facilitate interaction of active crystal growth sites with all OH groups [243].

Since precipitation strongly depends on local supersaturation values, and as both the $Ca(OH)_2$ and CO_2 supersaturation increase proportional to the glycerol content (see Figure 8.2.3 and Figure 8.2.2, respectively), it is anticipated that the precipitation would proceed faster with the presence of glycerol. This was the case for precipitations performed in the medium of glycerol concentration of <20wt %, as displayed in Figure 8.2.4. Such trends were also observed for the case of crystallite size, where it is anticipated that smaller crystallites will form with increasing glycerol concentration due to higher local supersaturation. As observed in Figure 8.2.11 and Figure 8.2.12, such initial reduction in crystallite size, at glycerol concentration of <20wt %, is associated with “the complex acting of glycerol”, through the stabilization of fine particles by the adsorption of glycerol molecules at PCC surfaces [242].

However, because the mass transfer is inversely proportional to the surface tension, which tends to be higher in less viscous liquids [243], the influence of supersaturation becomes rather compromised at higher glycerol concentrations. As displayed in Figure 8.2.1, the kinematic

viscosity of the precipitation medium increases significantly with higher glycerol content. Such trends explain the increase in precipitation acquisition time and crystallite size, where the significant increase in viscosity competes and rather suppresses the benefits of increased supersaturation.

Additionally, high local viscosity of the reaction medium containing glycerol can significantly limit the rate of diffusion for Ca^{2+} ions and effectively slow down the crystallization. Formed $CaCO_3$ crystal nucleuses tend to get connected by the glycerol reaction medium. The afterward crystallization happens on these crystal nucleuses. As a result, the PCC crystals tended to grow in separated dimensions, forming nano-rods, as displayed in Figure 8.1.5 and Figure 8.2.8. Higher glycerol content encouraged crystal growth to form bulk structures. The large, well-defined crystals may simply be an effect of viscosity. The elevated solution viscosity could have reduced secondary nucleation that might arise from crystal−crystal or crystal-stirrer/wall contacts, allowing the formation of better-shaped crystals of increased size. The larger crystals exhibited more perfect crystal structure, allowing for minimal formation of defects giving rise to the reduction in number of pores [244], reflecting significant reductions in the surface area, as displayed in Figure 8.2.13.

As depicted in Figure 8.2.2, with increasing viscosity the diffusivity of ions from the bulk solution to the crystal surface is reduced, which can lead to reductions in the growth rate constants. Slower growth is associated with the reduction of the diffusivity of calcium and carbonate ions from the bulk phase to the growing crystal [245]. The growth of ionic crystals can either be limited by the rate of diffusion or surface reaction, the former dominates when crystals are large, while the latter is important when the crystals are small [246].

The increase in scalenohedral morphology has been attributed to the stronger interaction of scalenohedral calcite with glycerol molecules [242], shifting eventually to the typical rhombohedral calcite with increased glycerol content. Such transition is said to happen through the corrosion of the scalenohedral faces of calcium carbonate particles to form rhombo scalenohedral elongated crystals [242].

PCC in this glycerol study formed porous microelipsoidal particles of uniform aspect ratio and dimensions. As displayed in Figure 8.2.5, PCC formed in the medium of 5wt% glycerol had a length of 1.5micron, a Width: 0.4micron, forming an aspect ratio of 3.75. Increasing the glycerol content to 15 wt% reduced the aspect ratio of the microelipsoidal particles to 2.37, with an average length of 2.3micron and an average width of 0.87micron.

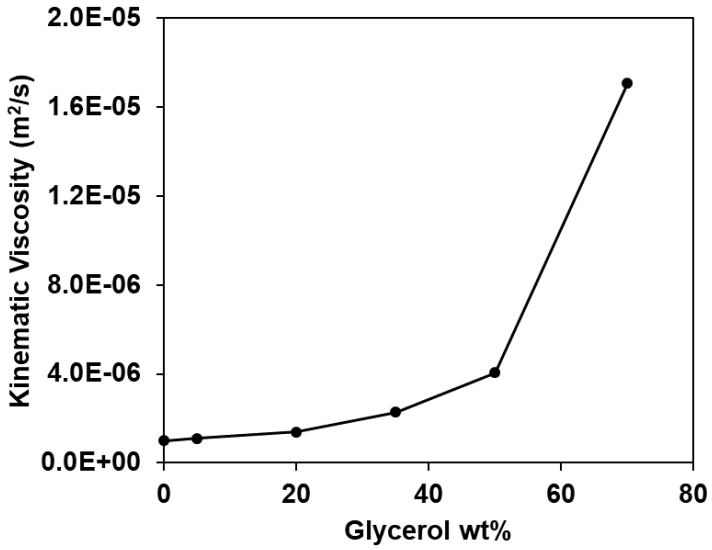

Figure 8.2.1 kinematic viscosity for glycerol solutions.

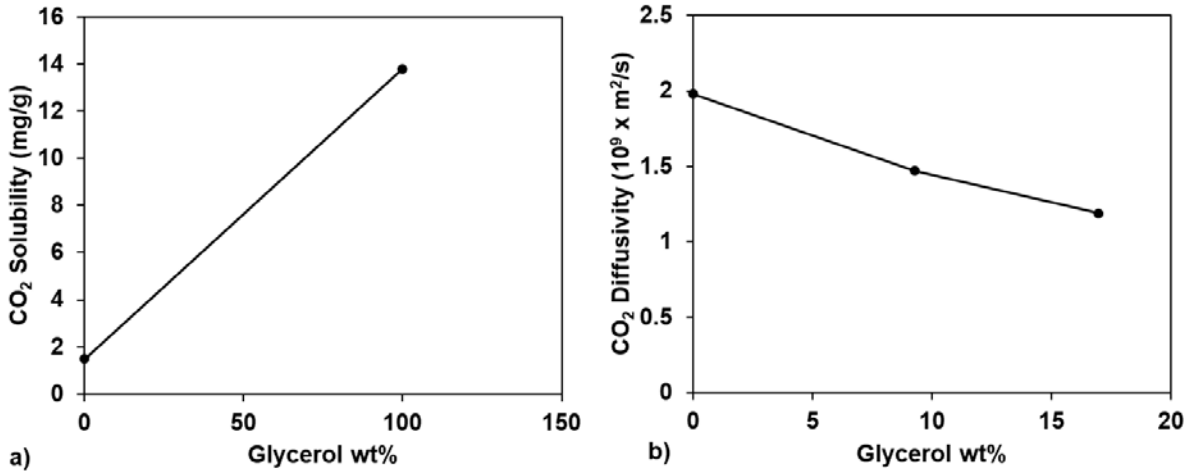

Figure 8.2.2) Increase in CO2 solubility due to glycerol, b) reduction of CO_2 diffusivity with increasing glycerol content.

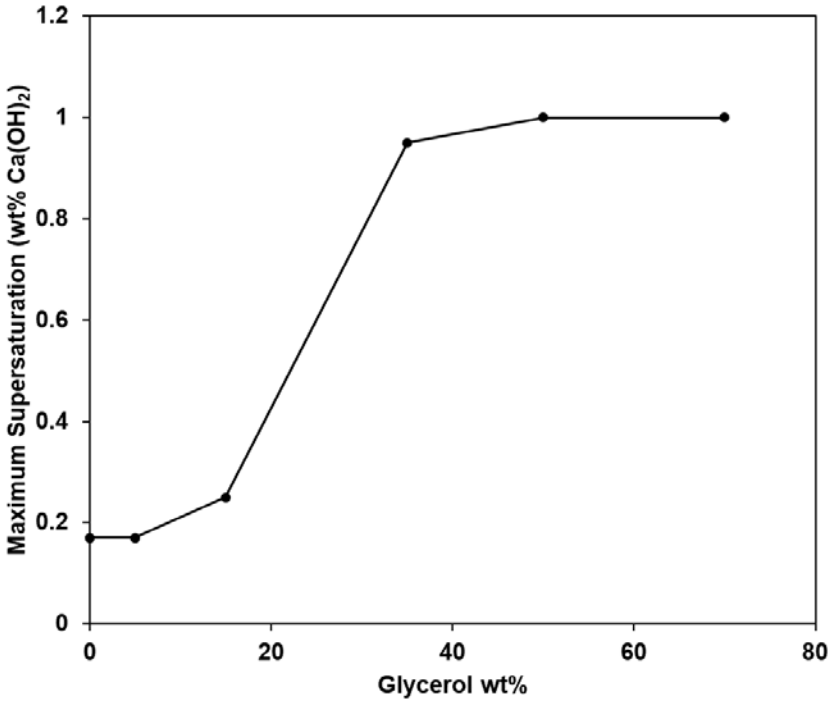

Figure 8.2.3 Increase in maximum supersaturation of $Ca(OH)_2$ aqueous solution, as obtained from [247].

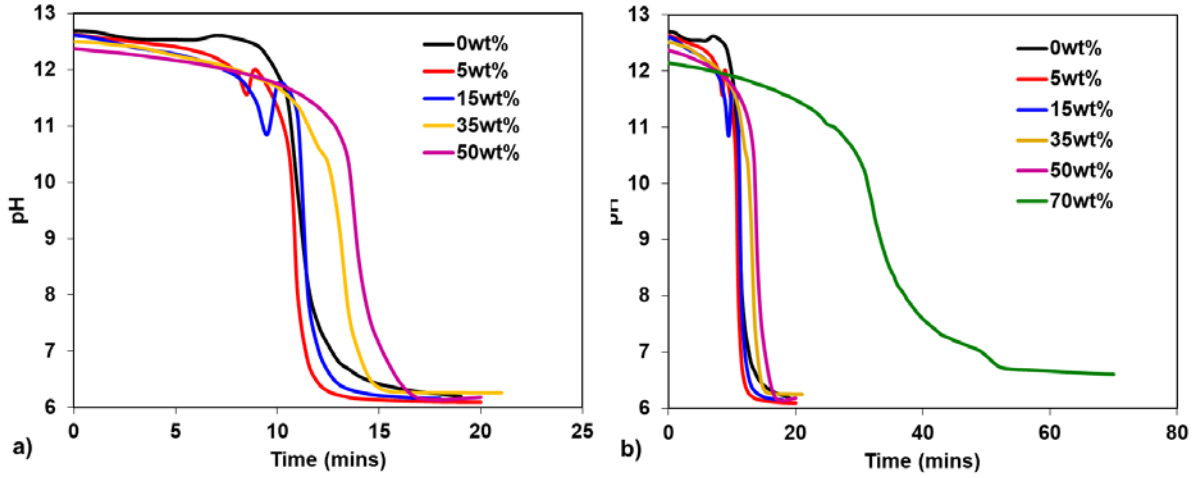

Figure 8.2.4 Influence of increasing glycerol content on shifting the pH curve during calcite precipitation.

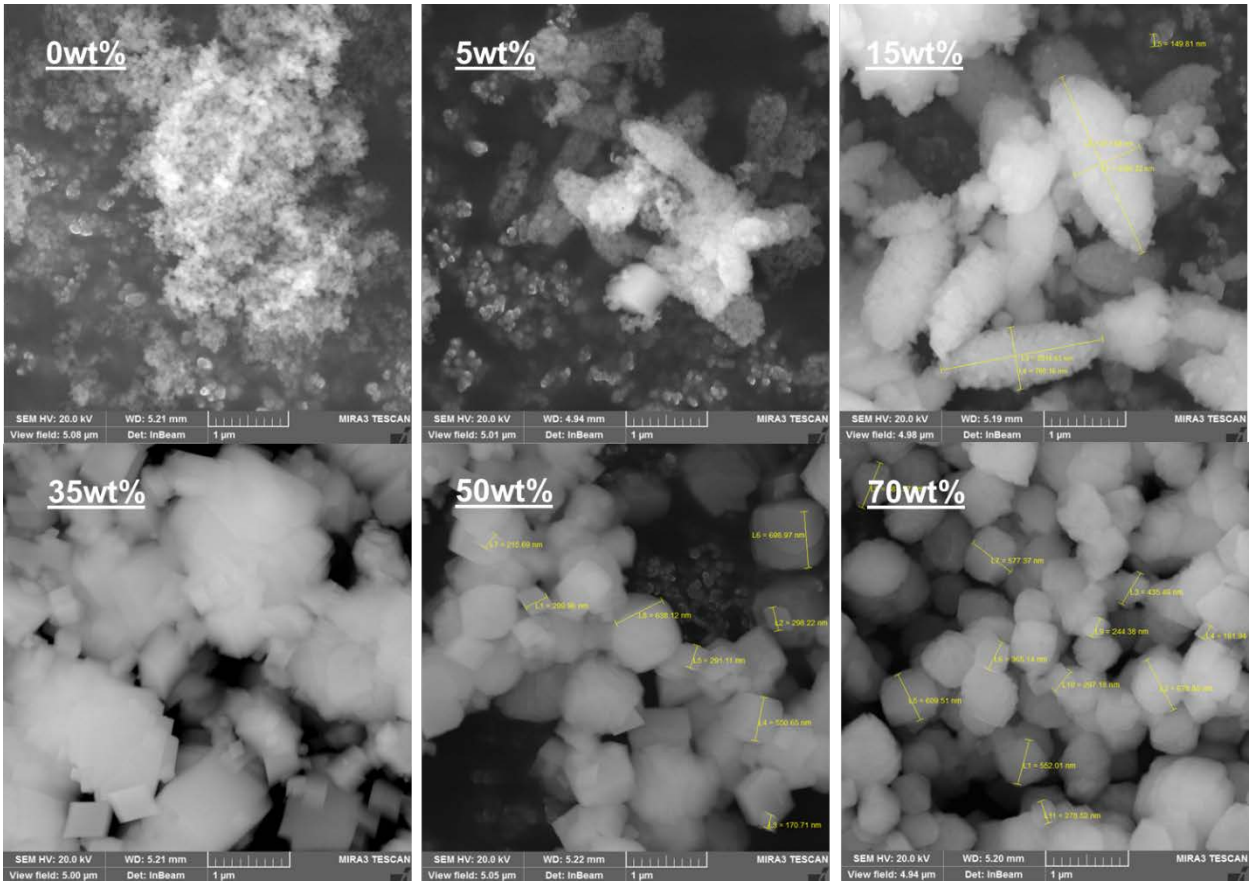

Figure 8.2.5 Influence of glycerol content on PCC morphology

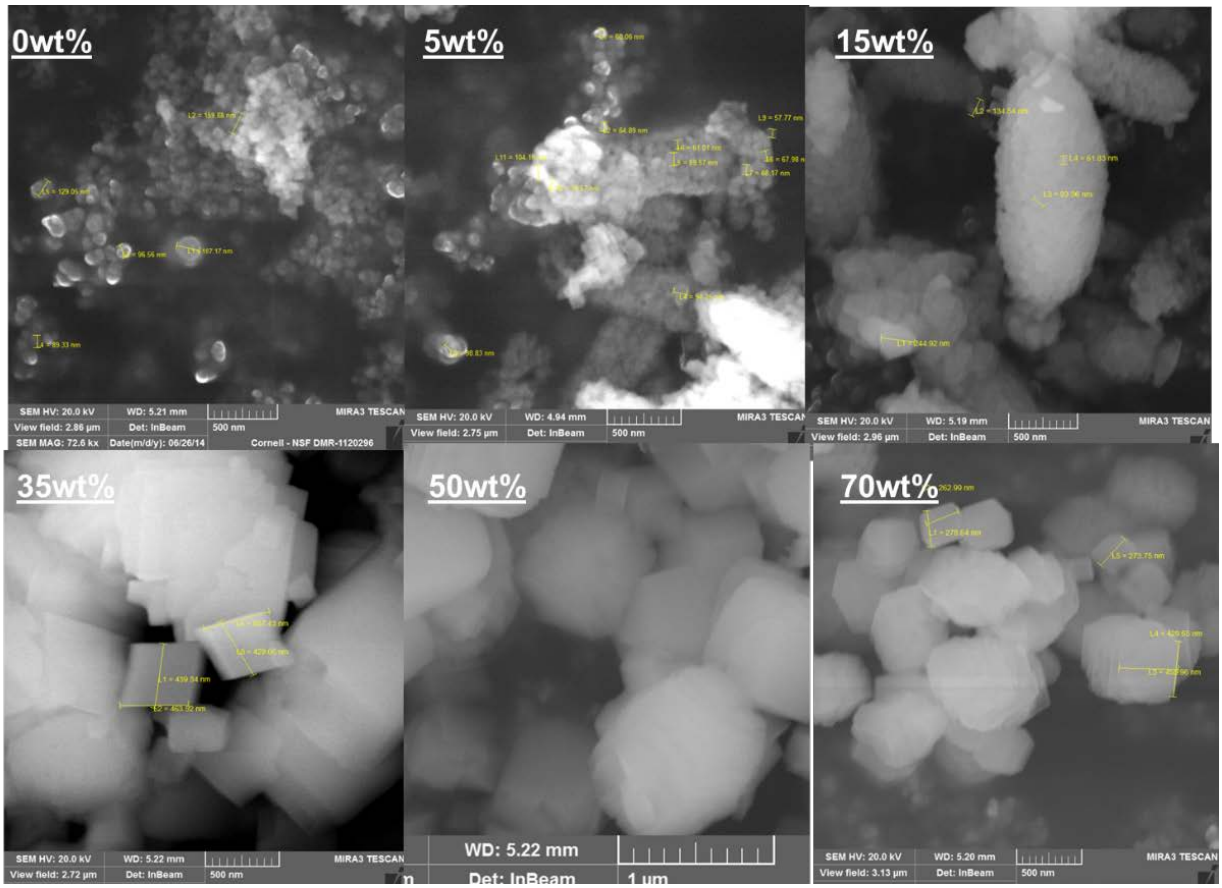

Figure 8.2.6 The large, well-defined crystals may simply be an effect of viscosity. The elevated solution viscosity could have reduced secondary nucleation that might arise from crystal−crystal or crystal-stirrer/wall contacts, allowing the formation of better-shaped crystals of increased size.

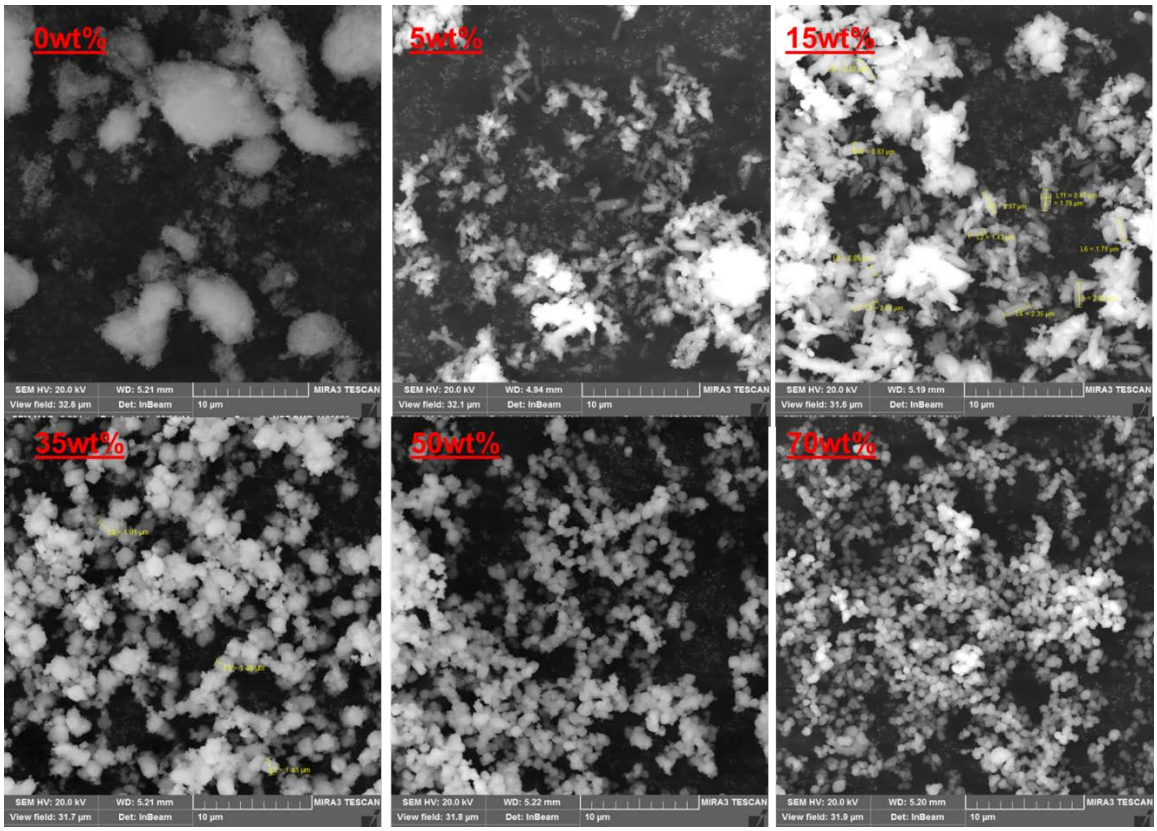

Figure 8.2.7 Porous nanorods vs solid spheres/cube.

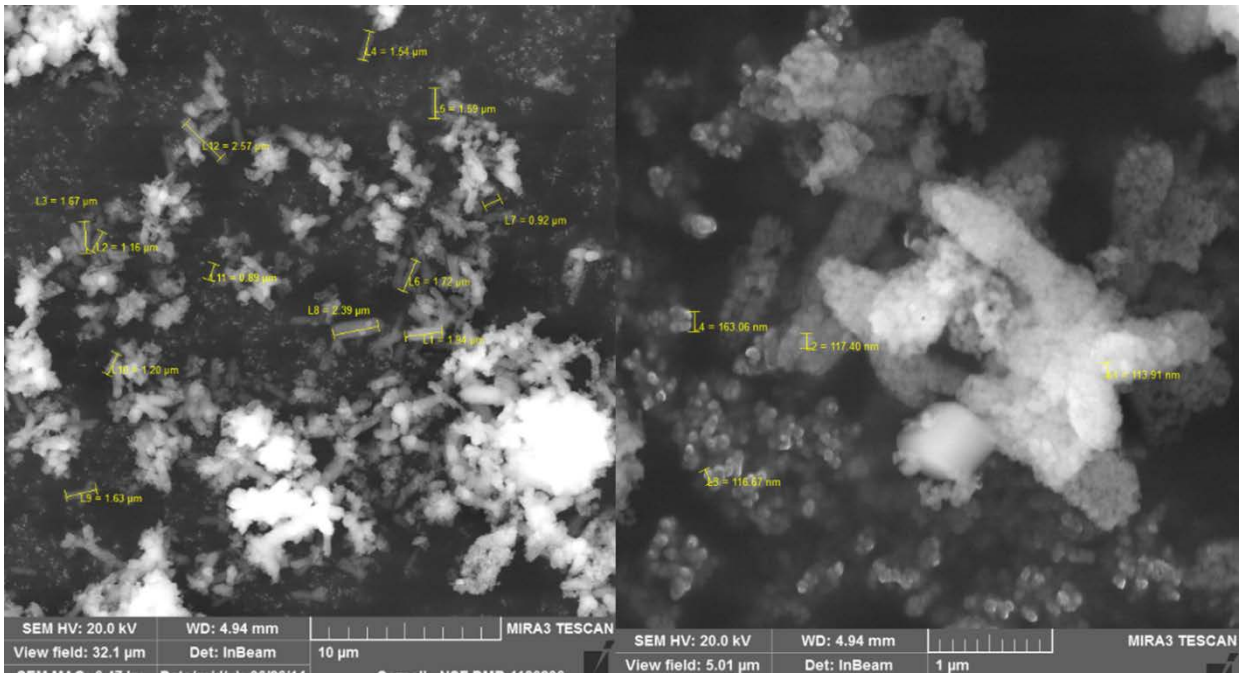

Figure 8.2.8 PCC micro-rods formed under 5wt% glycerol are made up of many (relatively uniform) nano-rods, and each rod is composed of smaller particles with diameters between 50 to 120 nm.

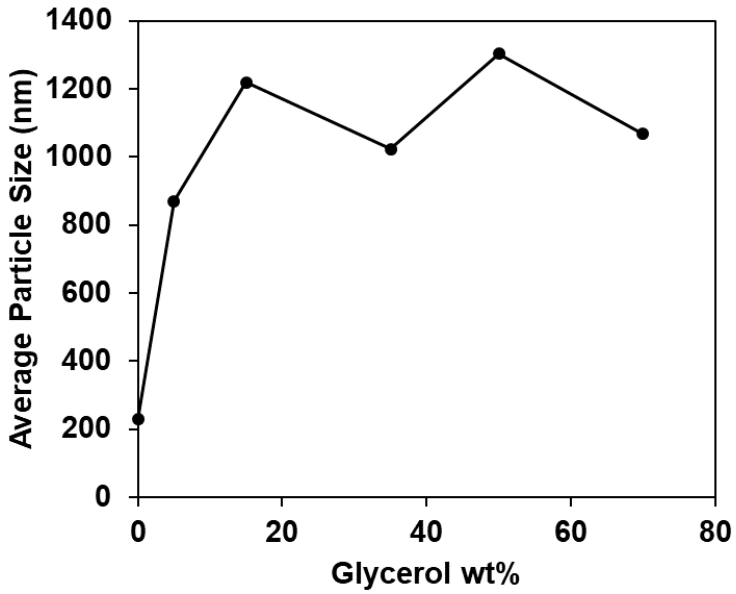

Figure 8.2.9 Increase in the average particle size as estimated via DLS measurements.

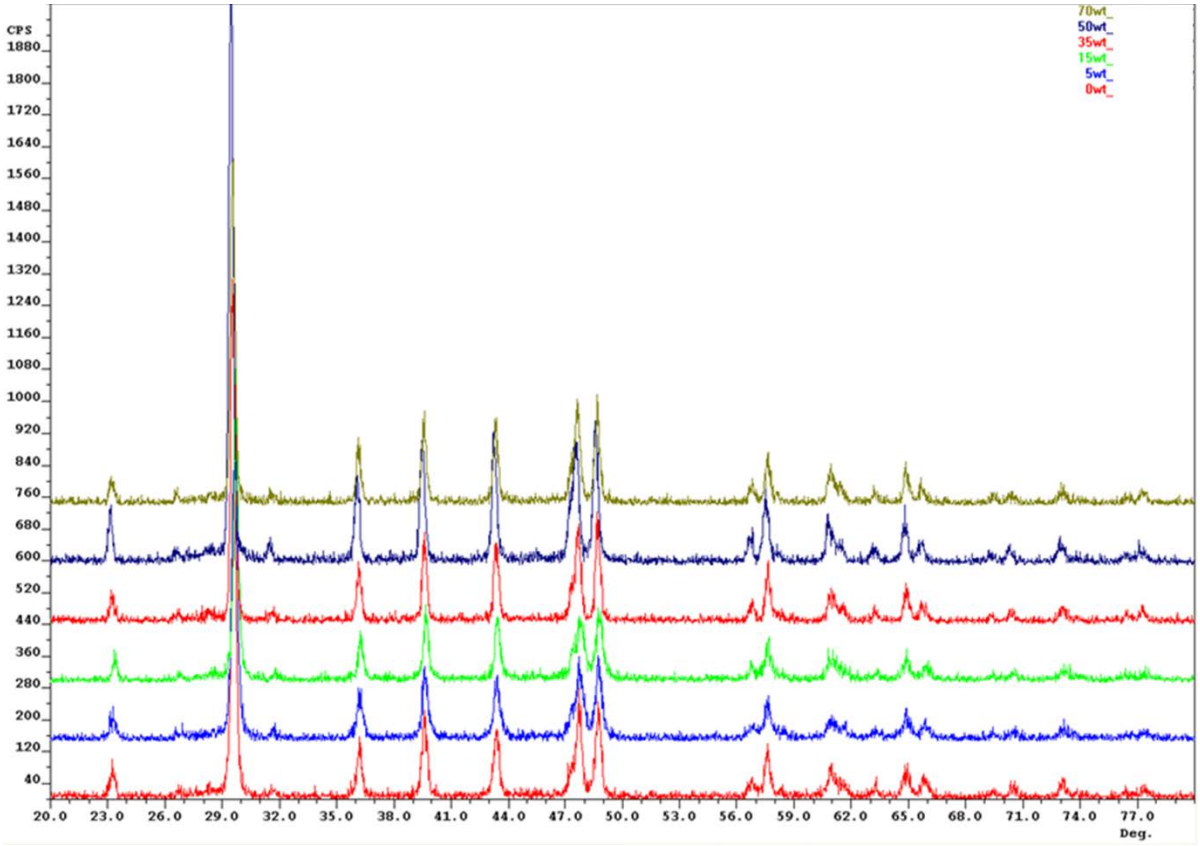

Figure 8.2.10 Glycerol affects the CaCO3, crystallite size, particle size, morphology (and growth rate) but no effect on the polymorph is observed, i.e.CaCO3 in the calcite form is produced in all experiments.

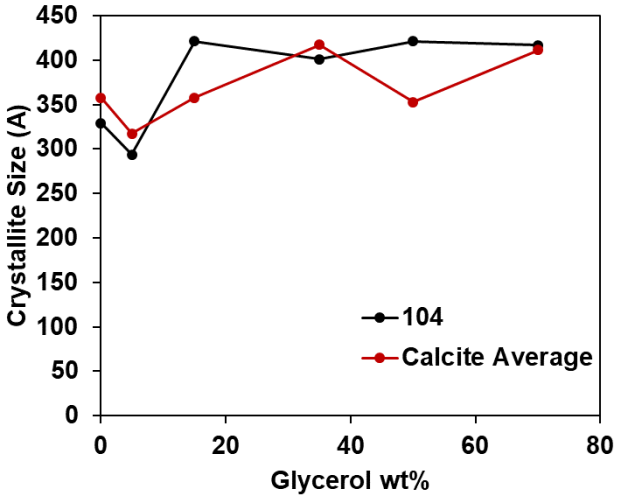

Figure 8.2.11 Change in PCC crystallite size with increasing glycerol concentration for the 104 peak, and the calcite average for 2.5wt% $Ca(OH)_2$.

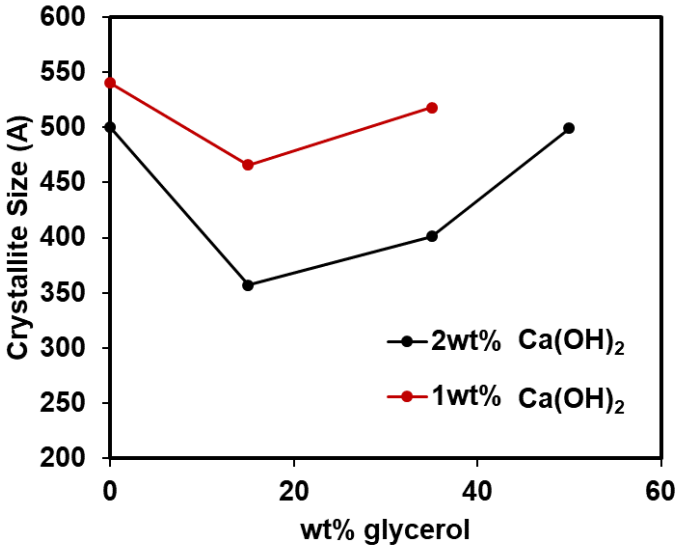

Figure 8.2.12 Change in crystallite size with the increasing glycerol content at different concentration of $Ca(OH)_2$

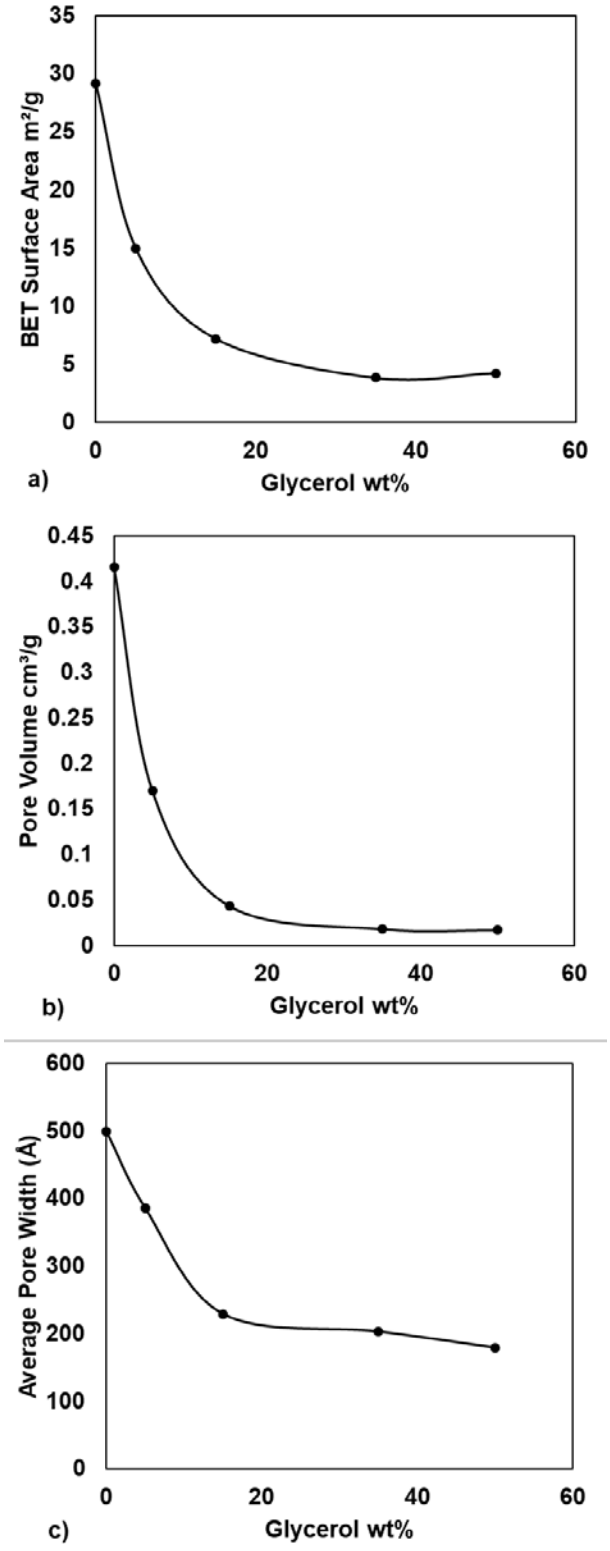

Figure 8.2.13 Adding Glycerol drastically decreases surface area (a), pore volume (b), and pore width (c).

Appendix C

8.3 Functionalization of ε-type Copper Phthalocyanine pigments

To produce photo-resist color filter with superior properties and lower cost competitive with dye-based color photo-resist, the desired properties for LCD color filters should have features such as: high solubility in organic industrial solvents such as (PGMEA), appropriate absorption-transmittance spectra, and sufficient thermal stability at industrial processing temperatures [248]. In this regard, dyes have better optical properties owing to reduced light scattering associated with small particle size in the film state, rendering color filters and displays to exhibit superior transmittance to pigment-based ones [249]. However, pigments have the advantage of excellent fatigue resistance [250], offering enhanced durability and better resistant to fading.

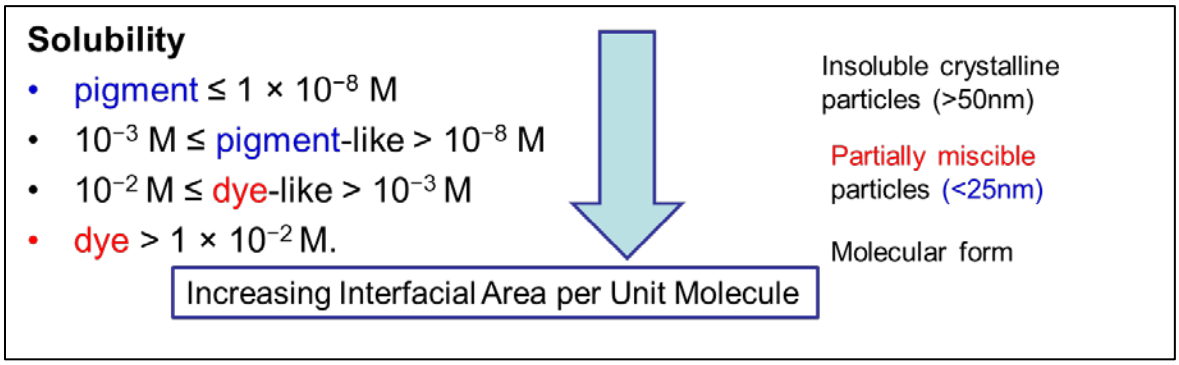

Figure 8.3.1 Classification in terms of particle solubility, as suggested in [251]

Considering the differences among pigments and dyes, as delineated in Figure 8.3.1, in order to transform pigments into dyes, substituents introduced to the terminal position of pigment crystals should preferably be electron releasing groups to observe the shift to shorter wavelengths. At the same time, they must be chosen to provide the desired transmittance spectra. Such coating on the exterior would induce the particles to repel one another and ultimately result in the formation of more discrete ligands.

The dyes and pigments used in traditional LCD filters include Red: C.I. Pigment Red 254, Green: C.I. Pigment Green 7 and/or 36 and Blue: C.I. Pigment Blue 15:6 [252]. The latter dye can be matched in color properties by ∈-copper phthalocyanine pigment, displayed in Figure 8.3.2.

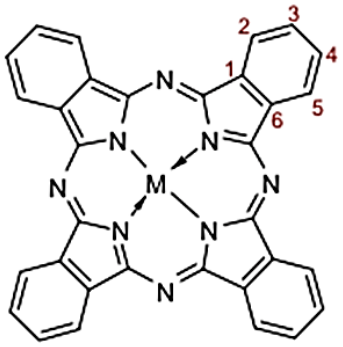

Figure 8.3.2 ∈-copper phthalocyanine pigment

For the application of improving the performance of ∈-copper phthalocyanine pigment, Soprophor, whose molecular structure is displayed in Figure 8.3.3 and Figure 8.3.4, fulfils such requirements and provides steric hindrance and electrostatic interaction that could enhance the degree of dispersion among the CuPc particles. Soprophor forms a stable emulsion at room temperature in Ethylene Glycol.

The functionalization ∈-copper phthalocyanine particles of with Soprophor was performed in the TCR with operating conditions as depicted in Figure 8.3.5. After an hour residence time, the product was collected and was subjected to post-processing that involves mixing with NaOH. Typical filtration was not effective in collecting the functionalized product due to the small size of the particles. Indeed, filtrate solution was observed to retain dark blue color even after 0.2 micron filtration. As a result, the samples were subjected to ultracentrifugation at

9000rpm for 1 hour, with a yield of about 1.5g per 50ml centrifuge tube. Starting with a wetcake of ∈-CuPc, which has 28wt% dry mass (~12g of wetcake) in each TCR experiment, 3.3g of functionalized ∈-CuPc were collected, and subjected to thermal treatment at 120 ^{o}C for 8 hours. Thermogravimetric analysis was performed on a TA Instruments TGA device, where 2 mg samples were placed on aluminum DSC pans. All data were collected in dynamic mode under flowing nitrogen (60ml/min) from room temperature to 580°C at a rate of 10°C/min. The results, as displayed in Figure C.8.3.6, confirm that the degree of functionalization in the TCR was superior to that of commercially available ∈-CuPc. This was also reflected by the more prominent peaks in the FTIR spectra, as displayed in Figure 8.3.7 and Figure 8.3.8.

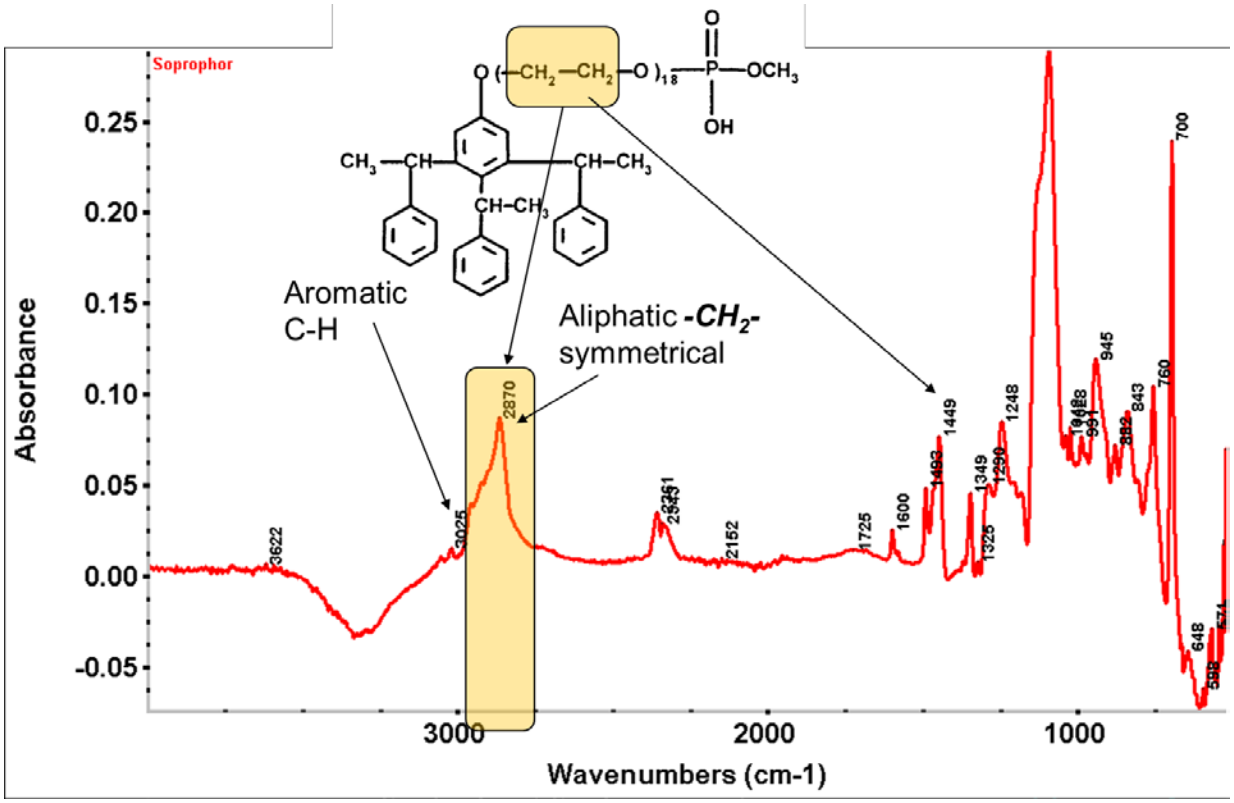

Figure 8.3.3 FTIR spectra for Soprophor.

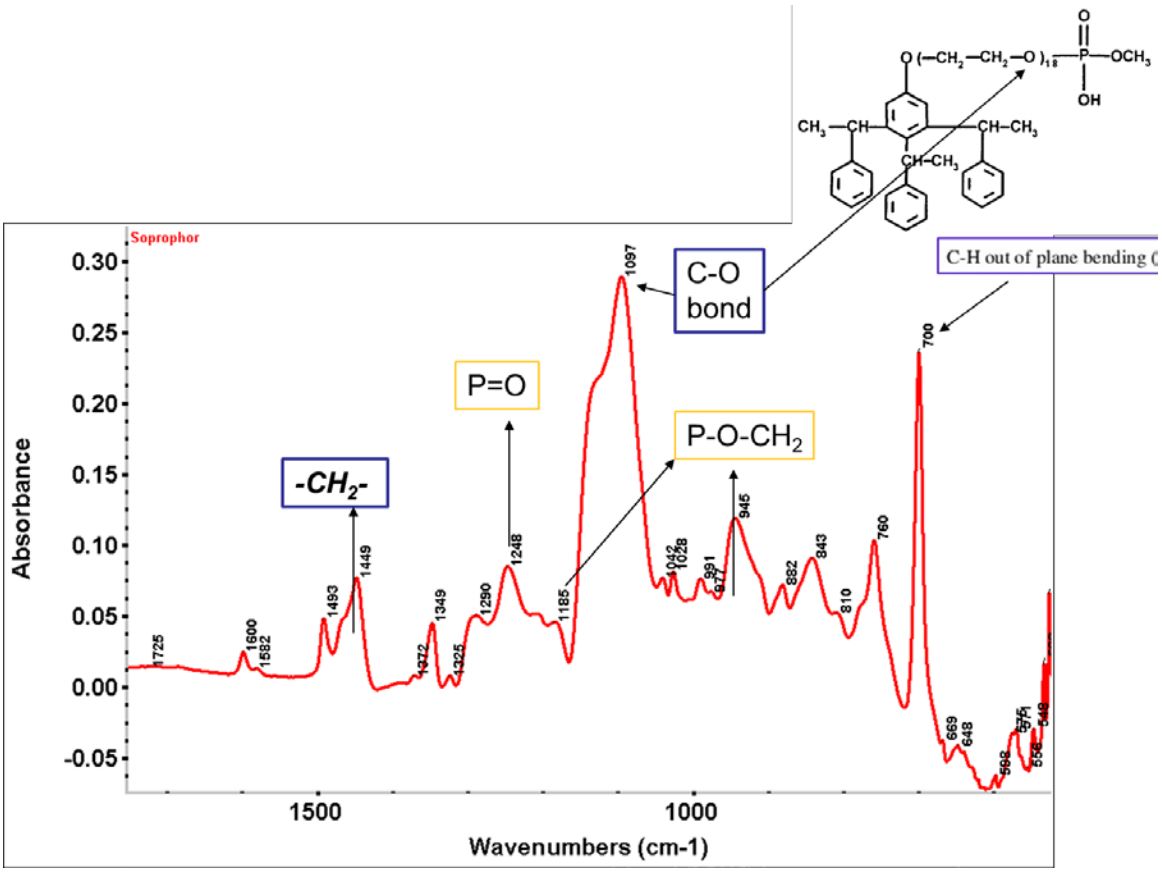

Figure 8.3.4 FTIR spectra for Soprophor.

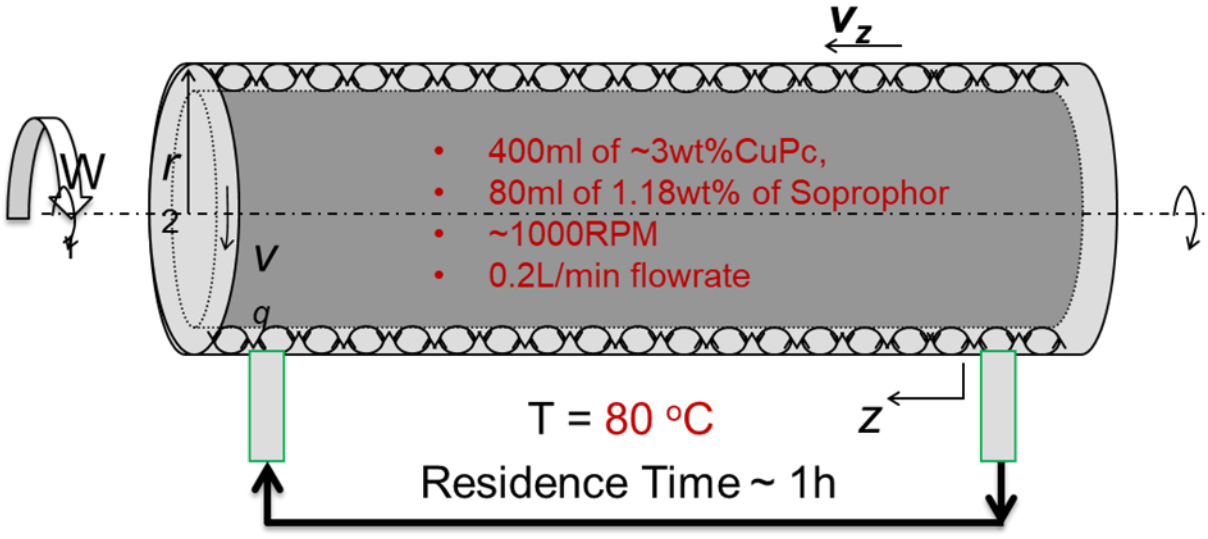

Figure 8.3.5 Configuration of TCR for the functionalization of ε-CuPc particles with Soprophor.

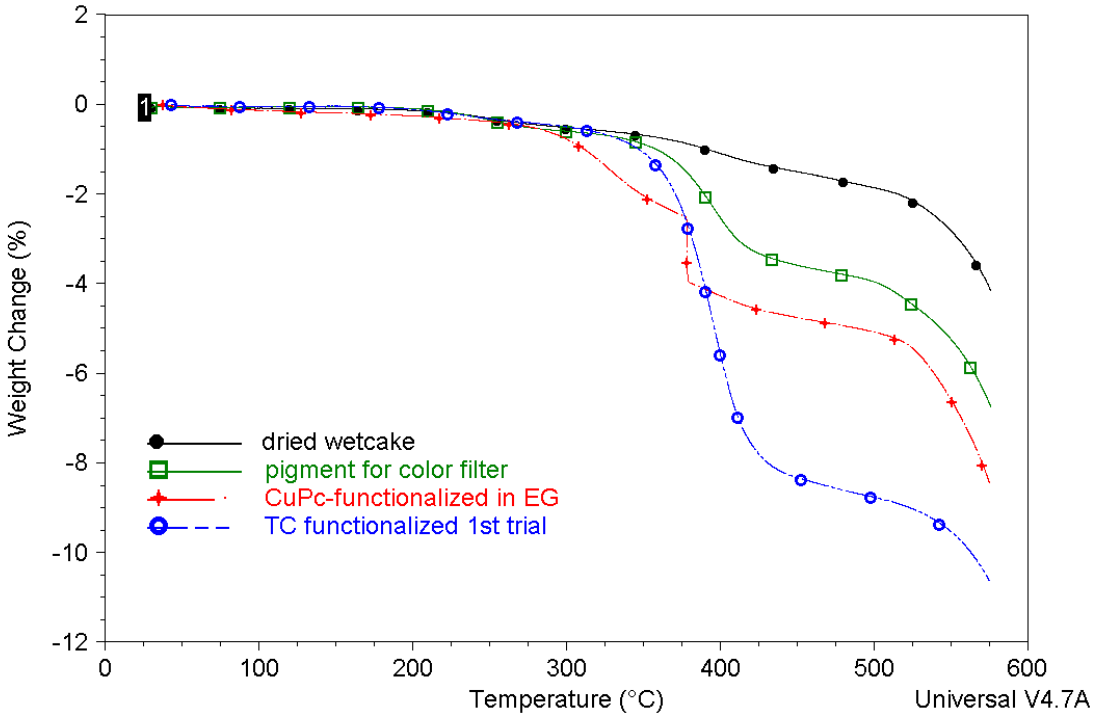

Figure C.8.3.6 Thermal degradation under nitrogen of ε-CuPc functionalized with Soprophor.

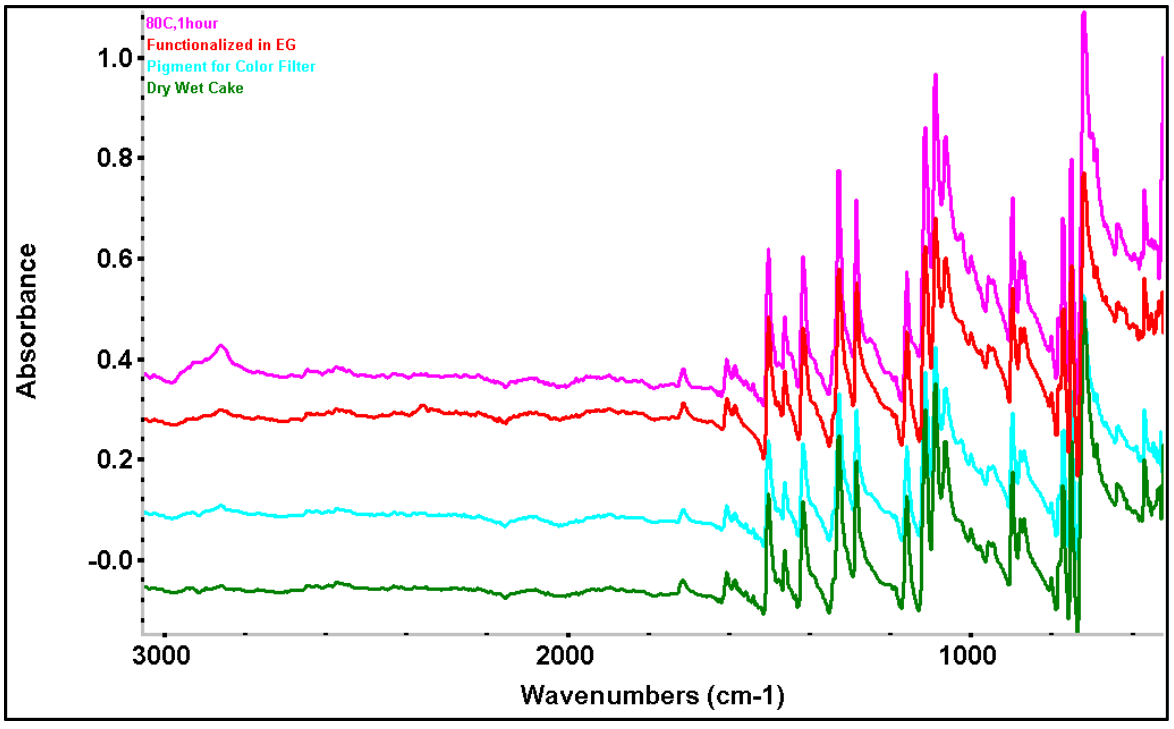

Figure 8.3.7 FTIR spectra for ε-CuPc functionalized with Soprophor.

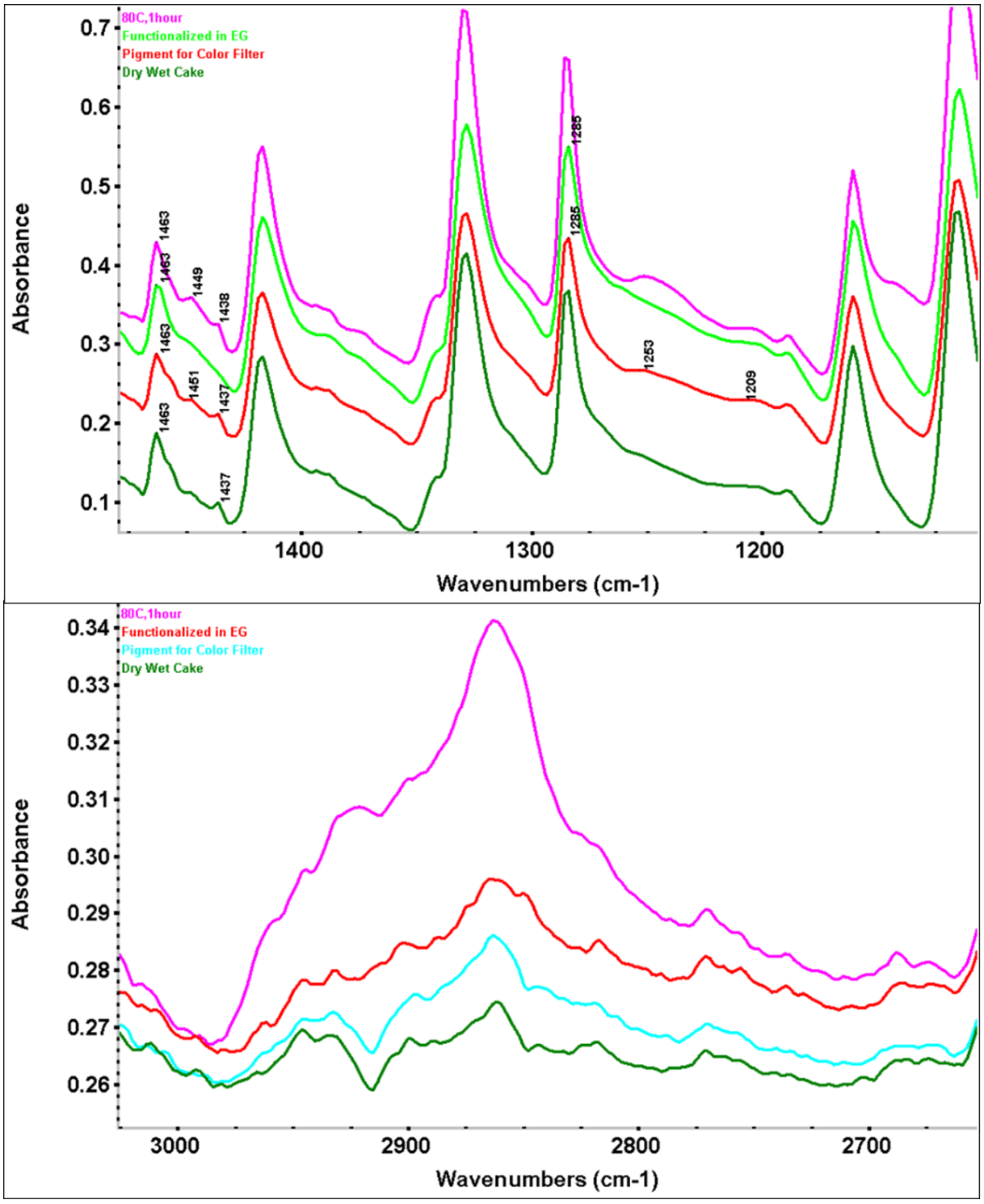

Figure 8.3.8 FTIR spectra for ε-CuPc functionalized with Soprophor.